Alma Mater Studiorum – Università di Bologna

DOTTORATO DI RICERCA IN

Ingegneria Civile, Chimica, Ambientale e dei Materiali

Ciclo XXX

Settore Concorsuale: 09/D1

Settore Scientifico Disciplinare: ING-IND 22

ATMOSPHERIC CORROSION OF OUTDOOR BRONZE:
MECHANISM OF DECAY AND CONSERVATION STRATEGIES

Presentata da: Giulia Masi

Coordinatore Dottorato

Prof. Luca Vittuari

Supervisore

Prof. Maria Chiara Bignozzi

Co-Supervisore

Dott. Cristina Chiavari
Dott. Elena Bernardi
Prof. Carla Martini
Dott. Luc Robbiola

Esame finale anno 2018

ATMOSPHERIC CORROSION OF OUTDOOR BRONZE: MECHANISM OF DECAY AND CONSERVATION STRATEGIES

A Pina e Agnese
Madri, Nonne, lottatrici con dolcezza:
la mia Ispirazione

Abstract

Application of protective coatings is the most widely used conservation treatment for outdoor bronzes. Innovative, eco-friendly and non-hazardous coatings are currently needed to enlarge the batch of efficient advanced formulations for conservation of outdoor bronze monuments. To meet the requirements of the conservation practice, protective coatings need to be selected in accordance with specific properties, such as ease of application, minimal aesthetical impact, excellent protective performance and long-term durability, non-toxicity and reversibility. For this reason, anti-corrosion protection currently developed for industrial applications can only partially transfer to the field of Cultural Heritage. To fulfil the need of new efficient conservation strategies for outdoor bronzes, the M-ERA.NET European research project B-IMPACT (Bronze-IMproved non-hazardous PAtina CoaTings) aimed at assessing the protectiveness of innovative organic coatings for historical and modern bronze monuments.

In this PhD thesis, elaborated in the framework of B-IMPACT project, the assessment of novel, eco-friendly and non-hazardous protective coatings was carried out. Different organosilane and fluoropolymer coatings were purposely developed as promising candidates for protection of outdoor bronzes. They were compared to Incralac®, one of the most used protective coatings in the conservation practice. A multi-analytical approach was adopted considering electrochemical evaluation, artificial ageing and metal release, as well as the morphological and structural evolution of the coated surfaces induced by the simulated outdoor exposure. In addition, to bring the conservation of artistic objects in line with proper engineering practice and Cultural Heritage regulations, the standardisation of the artificial patination procedures is still needed, so as to obtain artificially patinated surfaces representative of the natural ones for the application of innovative protective treatments. To this aim, a comparative study of patinated quaternary bronze (Cu-Sn-Zn-Pb) samples produced by accelerated ageing tests, simulating the unsheltered and sheltered exposure conditions mainly affecting outdoor bronze monuments, was performed. In detail, the effects of runoff in a Dropping test (unsheltered condition) and the exposure to stagnant acid rain in a Wet&Dry test (sheltered condition) on a bronze surface were investigated. It was evidenced that the corrosion layers, forming a nano-porous structure, were caused by the decuprification process owing to the preferential dissolution of Cu and Zn and the formation of a Sn-O species network within the barrier layer. The artificially patinated samples well represented natural corrosion structures observed for outdoor bronzes.

The best performance as a non-toxic alternative to the conventional Incralac® protective treatment was exhibited by a fluoroacrylate blended with methacryloxy-propyl-trimethoxy-silane to improve the coating adhesion (FA-MS) applied on Cu-Sn-Zn-Pb bronze, patinated by Dropping test and a 3-mercapto-propyl-trimethoxysilane (PropS-SH) coating applied on Cu-Si-Mn bronze, black patinated by "liver of sulphur" procedure (based on the use of K_2S aqueous solution). A two-step approach was applied for comparing the different promising coatings to Incralac®. In the first step, the accelerated corrosion test by Dropping was

carried out and surface characterization of the exposed samples was performed by colorimetric measurements, X-ray photoelectron spectroscopy (XPS), X-ray diffraction (XRD) and Focused Ion Beam Scanning Electron Microscopy (FIB-SEM) with Energy Dispersive Spectrometry (EDS). Furthermore, metal release in the weathering solution was monitored by Atomic Absorption Spectrometry (AAS), as a function of the exposure time, to calculate the inhibiting efficiency. In the second step, a non-destructive electrochemical monitoring of corrosion behaviour of coated and uncoated patinated bronze was performed during 30 days of total immersion in concentrated synthetic acid rain. In this second step, the characterisation of the toxicity level of the selected coatings was measured by occupational exposure test, by the evaluation of the volatile organic compounds (VOCs) concentration in the tested formulations.

Finally, this PhD thesis also presents an XPS and Electron Microscopy (FEG-SEM+FIB) characterization of a thin PropS-SH film on casting bronze. In particular, in order to better understand the influence of alloying elements on the coating performance, PropS-SH was studied first on pure Cu and Sn substrates and then on bronzes with increasing alloy additions: Cu8Sn, as well as a quinary Cu-Sn-Zn-Pb-Sb bronze. Moreover, in view of the real application of this coating on historical bronze substrates, previously artificially patinated bronze samples were prepared and a comparison in terms of bare and patinated quinary bronzes was performed. In the case of coated quinary bronze, the free surface of samples was analysed by High Resolution Photoelectron Spectroscopy using Synchrotron Radiation (HR-SRPES) at ANTARES (Synchrotron SOLEIL), which offers a higher energy and lateral resolution than conventional instruments. By compiling complementary spectroscopic and imaging information, a deeper insight into the interactions between the protective coating and the bronze substrate was achieved.

Keywords

Artificial ageing; Atmospheric corrosion; Bronze; Coatings; Cultural Heritage; FIB; Protective coatings; Fluoropolymer; Organosilane; XPS.

Acknowledgements

Getting a PhD was my first choice since the amazing experience at the Curtin University (Western Australia) where I developed a strong passion in performing research for the preparation of my Master Thesis. So, this Thesis is the results of this three hard and crazy PhD years and for this achievement I have to strongly acknowledge many people I met, I shared a moment with and who always believes in me.

I would like to acknowledge my advisor **Prof. Bignozzi** for the opportunity of developing my research in the frame of B-IMPACT project during these three years. A big thank you goes to **Dr. Cristina Chiavari**, **Prof. Carla Martini** and **Dr. Elena Bernardi** for being the co-supervisors that really guide me in the scientific adventure of the PhD. Thank you very much for welcoming me in your labs!

I am sincerely grateful to **Dr. Luc Robbiola** for the possibility to visit TRACES Laboratory (Toulouse, France) not once but twice during my PhD and for his constant encouragement, guidance and friendship. It has been a great privilege to work with you!

In addition, I express my gratitude to **Dr. Jerome Esvan** for his precious help and tutorials in XPS analyses, **Dr. Claudie Josse** for her time and expertise in performing FIB / SEM observations, **Dr. Maëlenn Aufray** for her help at CIRIMAT and finally **Mr. Patrick Costans** for his kindness, coffees in the morning and French lunches during my stay in Toulouse.

Therefore, I would like to acknowledge **Prof. Cecilia Monticelli** and **Dr. Tadeja Kosec** for their precious help and appreciation during the revisions process of this Thesis. I also want to thank all the B-IMPACT people (most of them in the pictures). It has been the best multidisciplinary and stimulating team I could ever be part of!

Project meeting in Toulouse, 2016

Project meeting in Bologna, 2017
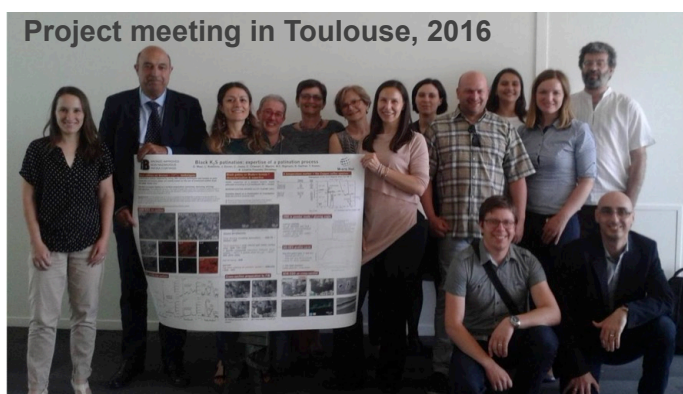
I also wish to deeply thank **Lorenza** for being such a perfect PhD mate! We shared all the nice, funny but also difficult and stressful moments of the last three years and we support each other as great friends. I have also to thank **Enrico** for his invaluable support and advices and **Gabriela** for her friendship, help and support. You are the best colleagues ever!

I would also acknowledge all the students, technicians and researchers helping me in the experimental work, especially **Dr. Iuri Boromei** (Metallurgy Laboratories at DIN, University of Bologna), **Mr. Paolo Carta** (LASTM Laboratories at DICAM, University of Bologna) and **Dr. Jose Avila** and **Dr. Maria Carmen Asensio** (ANTARES beamline at Synchrotron Soleil, France).

Last but not least, I have to deeply thank all **my family**. First of all, I would sincerely thank **"my Pirate"** who always supports me in every moment of these last three years. He has enthusiastically participated with his wise "scientific" suggestions and has always listened to my PhD tales and adventures. We lived many beautiful and difficult experiences together and this manuscript is also Fede's PhD Thesis. **Thank you for always being next to me!**

Finally, I want to thank my parents, **Mauro** and **Stefania** and my brother **Enrico** with **Sara**, **Riccardo** and **Bianca** for their support, unconditional love and for always believing in me. A big thank you goes to all **my friends** for the funny and happy moments spent together.

List of contents

Acronyms and abbreviations

AR	Acid Rain solution
at%	atomic per cent
β-CD+MPT	β-CycloDextrin + Mercapto-Phenyl-Tetrazole
B-IMPACT	Bronze-IMproved non-hazardous PAtina CoaTings
BTA	Benzotriazole
CuO	Tenorite
Cu_2O	Cuprite
$Cu_4(SO_4)(OH)_6$	Brochantite
$Cu_3(SO_4)(OH)_4$	Antlerite
$Cu_4(SO_4)(OH)_6H_2O$	Posnjakite
$Cu_2Cl(OH)_3$	Atacamite or Paratacamite
$Cu_2(CO_3)(OH)_2$	Malachite
$Cu_2NO_3(OH)_3$	Gerhardite
Cu-Si-Mn	Ternary bronze for contemporary art
Cu-Sn-Zn-Pb	Quaternary bronze alloy (traditional bronze)
Cu-Sn-Zn-Pb-Sb	Quinary bronze alloy (traditional bronze)
E_{cor}	Corrosion potential
EL	Exposure Limit
FA	Fly Ash
FA-MS	Fluoro-Acrylate - Methacryloxy-propyl-trimethoxy-Silane
FIB	Focused Ion Beam
FZP	Fresnel Zone Plates
GD-OES	Glow Discharge - Optical Emission Spectroscopy
i_{cor}	Corrosion current density
MMA	Methyl MethAcrylate
NO_x	Nitrogen oxides
PE	Protective Efficiency
PM	Particulate Matter
PropS-SH	3-mercapto-propyl-trimethoxy-silane
R_p	Polarization resistance
rsd	Relative standard deviation
SCE	Saturated Calomel Electrode
SEM-EDS	Scanning Electron Microscopy – Energy Dispersive x-ray Spectroscopy
SME	Small and Medium Enterprises
SO_x	Sulphur oxides

SR-HRPES	Synchrotron Radiation-High Resolution PhotoElectron Spectroscopy
ToW	Time of Wetness
VOC	Volatile Organic Compound
wt%	weight per cent
XPS	X-ray Photoelectron Spectroscopy
XRD	X-Ray Diffraction
XRF	X-Ray Fluorescence

Introduction

CHAPTER 1 PRESENTS THE MAIN OBJECTIVES OF THE STUDY AND THE STRUCTURE OF THE THESIS.

CHAPTER 2 REPORTS THE CONTEXT OF THE RESEARCH AND THE LITERATURE REVIEW ABOUT CORROSION MECHANISM OF OUTDOOR BRONZE AS WELL AS THE MAIN CONSERVATION STRATEGIES

1. GENERAL OVERVIEW

1.1. B-IMPACT project

The B-IMPACT (Bronze-IMproved non-hazardous PAtina CoaTings) project, financed in the frame of M-ERA.NET Transnational Call 2013, aimed at developing innovative, eco-friendly and non-hazardous protective coatings with specific properties tailored for improving the protection of outdoor bronzes [1].

Bronze artefacts and monuments exposed outdoors are prone to degradation processes, especially in polluted environments. Their protection and maintenance is a great challenge, requiring on-going investment. This is why in the field of Cultural Heritage preservation, tailored "right off the shelf" formulations based on advanced protection strategies are needed for the reduction of maintenance costs and the provision of efficient conservation solutions for end-users, including local authorities and other stakeholders (architects, artists, museums, etc.). The project has taken into account: (i) the typical nature of substrates for treatment testing, based on the real patinas of outdoor bronzes and (ii) the non-hazardous nature of the protective materials used. Different types of coatings have been developed in order to improve current and new formulations, from the following coating groups: particle-containing silanes, inhibitor-charged multilayer self-healing coatings, spray sol-gels and fluoropolymers. Surface tests have been performed on typical bronze samples supplied by the sub-contracting foundry: a modern silicon bronze (Cu-Si-Mn) that is used in contemporary art, artificially patinated as commonly required by artists, and a traditional quaternary bronze (Cu-Sn-Zn-Pb), patinated by typical ageing procedures. Their performance have been assessed by electrochemical tests in artificial acid rain and, in the case of the most promising ones, by severe accelerated ageing involving environmental parameters (runoff, UV radiation, ...). The fulfilment of the strict requirements needed in the case of Cultural Heritage practice have been verified by means of advanced surface characterization techniques. Specific toxicity tests have addressed the compliance of coatings with European health and safety regulations. After validation at the bench scale, the feasibility of the best coatings has been assessed at the upscale level by industrial partners who are also involved in the coating formulation and reversibility investigations. B-IMPACT project involved eight partners (4 SMEs, 1 research, and 3 academic institutions), as shown in Figure 1.1.
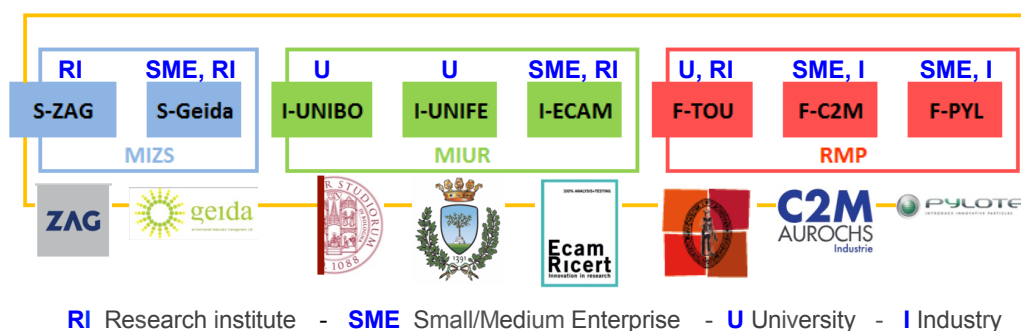
Figure 1.1: Representation of project members grouped in National groups (Slovenian, Italian and French).

The SME partners were fully integrated within the project realization. Two coating producing SMEs (F-C2M and F-PYL) were working in connection with three research institutions (S-ZAG, I-UNIBO and I-UNIFE) and with the research SME (S-Geida) in tuning the formulation of each functional coating at the lab-scale and in the pre-production stage. The other academic partner (F-TOU) was in charge of the interface characterisation of the different coated bronze samples before and after ageing. The fourth SME (I-ECAM) was mainly involved in the validation of coatings by carrying out toxicity tests. The plans for the exploitation of project research results were also performed by SME S-Geida. According to the Cultural Heritage requirements, a SME subcontractor (Livartis d.o.o.) provided suitable typical alloys.

Relevant outputs were obtained from B-IMPACT. Improved knowledge in the field of the protection of metals was gained through a multidisciplinary collaborative exchange between the partners. Innovative development of effective coatings with assessed limited environmental impact was also carried out.

1.2. Research objectives and method

This PhD thesis presents the experimental work performed in the framework of the B-IMPACT project. In particular, the aim of this work was to assess through artificial ageing methods the protectiveness of promising innovative, eco-friendly and non-hazardous coatings tailored for the application on patinated traditional bronze (Cu-Sn-Zn-Pb), as well as on a modern silicon bronze (Cu-Si-Mn) that is used in contemporary art, artificially patinated as commonly required by artists. A schematic of the working plan adopted is reported in Figure 1.2.
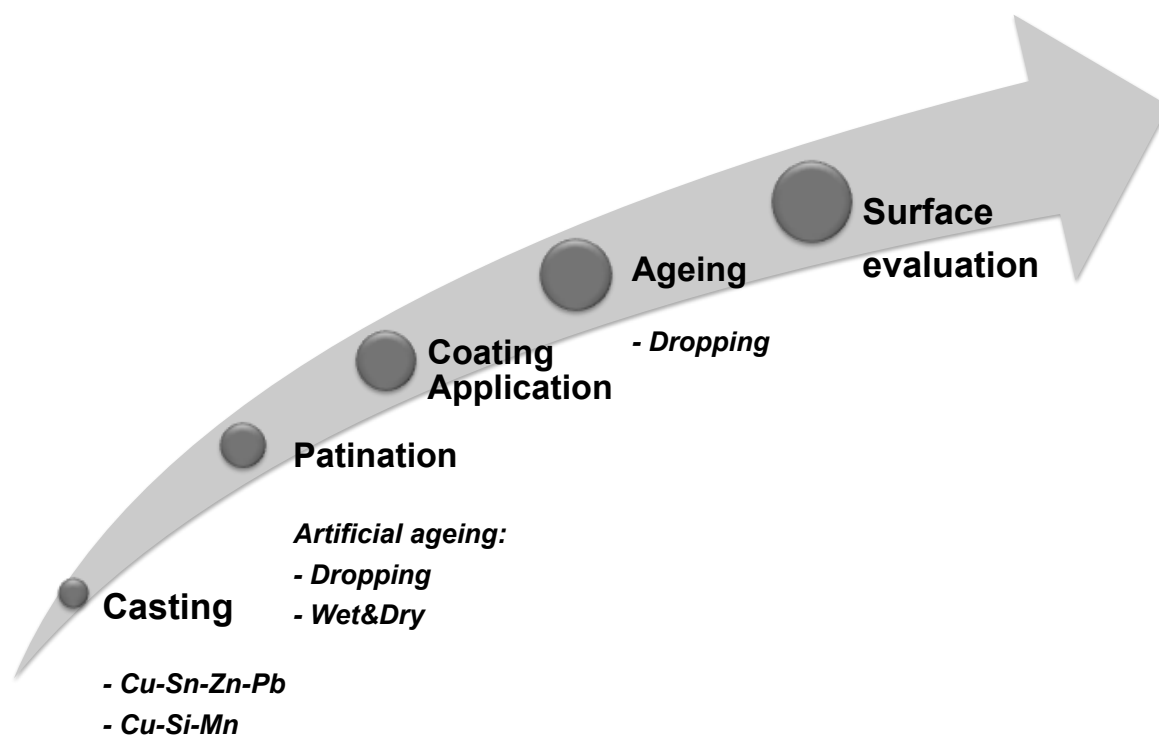
Figure 1.2: Schematic of the working plan adopted during this PhD research project.

Firstly, to produce representative substrates for coating application, a patination campaign was carried out on Cu-Sn-Zn-Pb applying both Dropping and Wet&Dry tests, thus taking into consideration the main exposure geometries of outdoor bronze monuments. In particular, implementation of the Dropping device was carried out, in order to age a larger batch of sample in the same experimental conditions. A multi-scale approach was adopted in order to monitor and characterise the surface evolution of the patinated Cu-Sn-Zn-Pb substrates, as well as to investigate the morphology of the artificial patina applied by the artistic foundry (by K_2S solution) on Cu-Si-Mn (Figure 1.3). The microstructural and chemical analyses of the patinated substrates were performed during a three-months visiting period at the Laboratoire TRACES of the Université Jean Jaurès in Toulouse (February-May 2016).
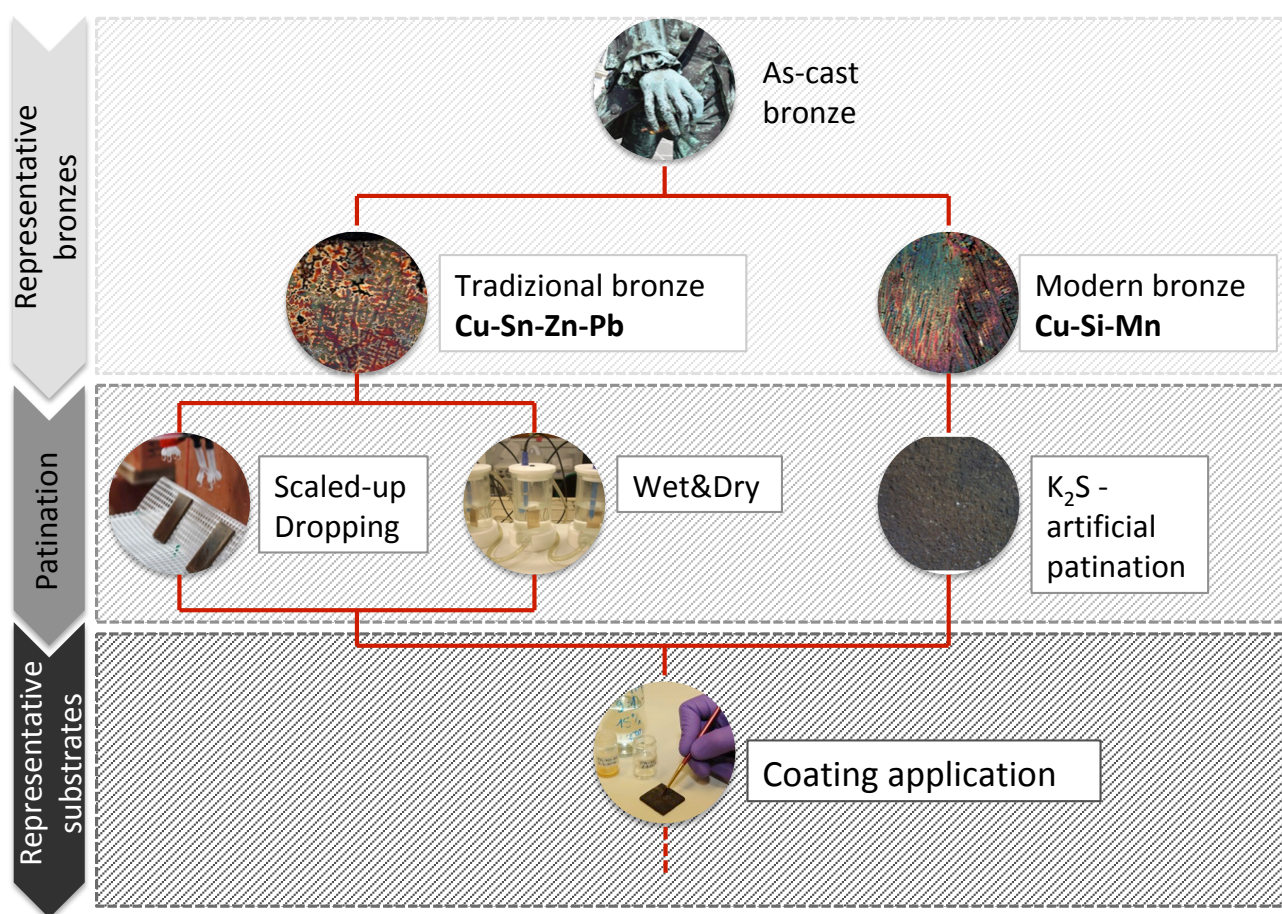
Figure 1.3: Methodology applied for the patination of both the bronzes and the characterization of the patinated substrates.

Figure 1.4 reports the methodology used in the second step of the research, in which the goal was to assess the protectiveness of different protective coatings for the protection of patinated traditional Cu-Sn-Zn-Pb and modern Cu-Si-Mn alloys. A multi-analytical approach was applied and the performance of the coatings was evaluated after ageing (Dropping test) considering both the evolution of the uncoated and coated surfaces and the metal release in the ageing solutions. Also in this case, the morphological and structural characterisation of the coated substrates was carried out in a second three-months visiting period at the Laboratoire TRACES of

the Univeristé Jean Jaurès in Toulouse (January – April 2017), financed by the Department of Civil, Chemical, Environmental and Materials Engineering (DICAM) in the framework of "Marco Polo" scholarship. In order to show a more complete vision of B-IMPACT project, the main results performed by the other partners are also discussed. In particular, the main results from the electrochemical tests performed by coating developers (I-UniFE and S-ZAG) to select the most promising innovative coatings are collected, as well as the main results of the eco-toxicity in terms of occupational exposure tests carried out by I-ECAM, as one of the main property for the developed coatings, required by B-IMPACT project. In addition, in order to deeply investigate the interaction of one of the selected silane coating in the B-IMPACT project, X-Ray Photoelectron Spectroscopy (XPS) was performed coupling conventional XPS and high-resolution techniques thanks to the use of synchrotron radiation. This study was carried out in the framework of the international scientific project accepted by Soleil Synchrotron (Saint Aubin, France) "Outdoor bronze corrosion: nanoscale XPS investigation of protective coating on representative substrates" (Proposal no. 2016149) and performed by one week measurements in Antares beamline in February 2016.
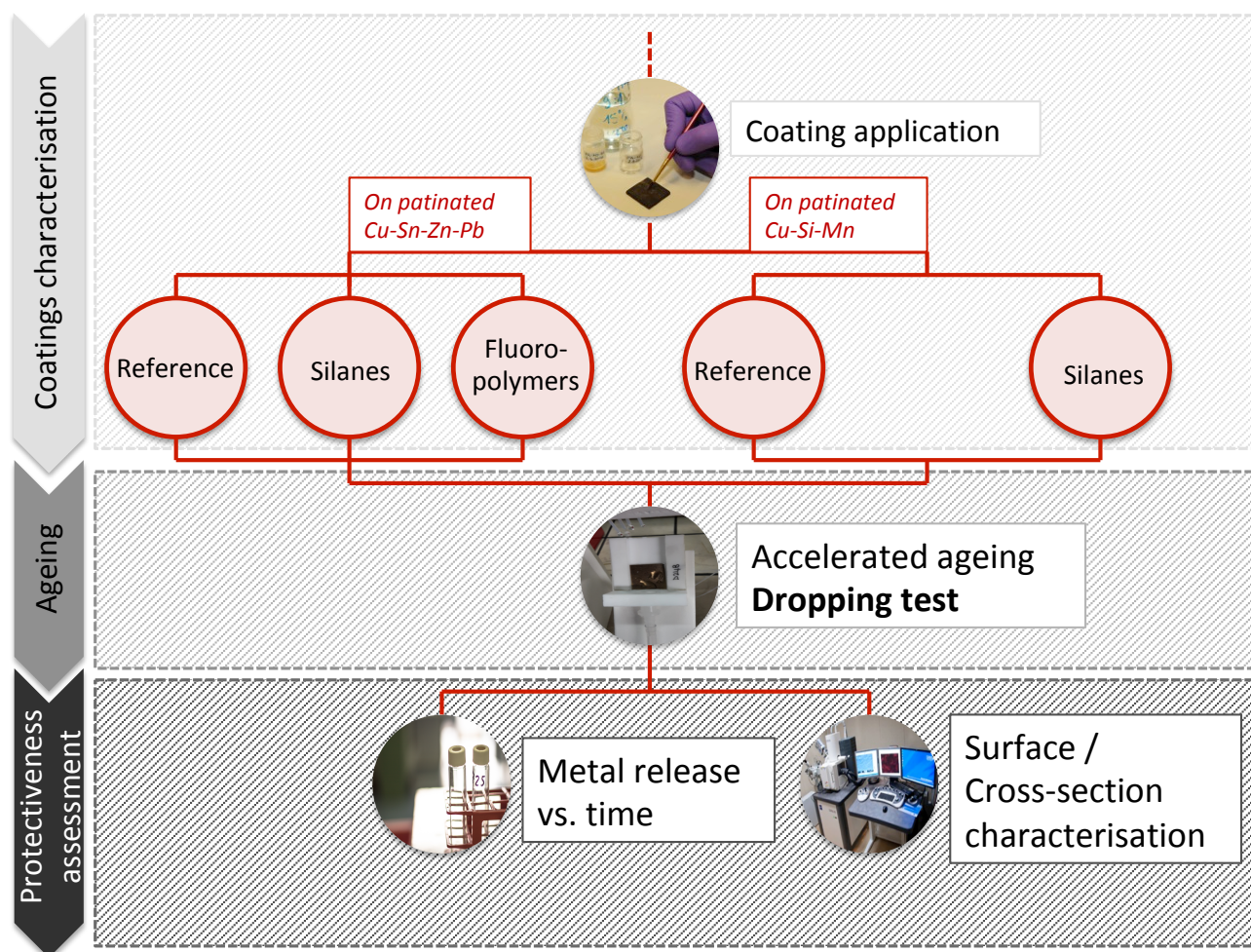
Figure 1.4: Schematic of the methodology applied for the assessment of the selected innovative coatings applied on patinated substrates.

1.3. Organisation of the thesis

A conventional thesis format has been used. A literature review of corrosion of outdoor bronzes and of the protective treatments currently investigated, as well as the strategy for the evaluation of their performances is covered in chapter 2.

In chapter 3 the experiment section details the investigated materials, the experimental methods and the equipment used.

"Results and discussion" section is organised in three chapters. In particular, chapter 4 reports a comparative study about the differences between patinated traditional quaternary bronze (Cu-Sn-Zn-Pb) produced by accelerated ageing tests simulating sheltered and unsheltered conditions in outdoor exposure. In addition, the assessment of the protectiveness of promising protective coatings (silanes and fluoropolymers) for the conservation of Cu-Sn-Zn-Pb alloys is also discussed. Chapter 5 collects a deeper insight into the interactions between a protective coating (organosilane) and the bronze substrates, by compiling complementary spectroscopic and imaging information. In chapter 6, the main properties of black patina (formed by K_2S aqueous solution) are presented, as well as the performance of the protective silane coating is evaluated as a possible alternative to commercial products currently used in restoration practice.

Finally, chapter 7 contains the conclusions including the perspectives and the suggestions for future research.

2. LITERATURE REVIEW

Cultural objects and monuments represent footprints, developments and events of a society, offering a bridge to the past and providing important markers for the worldwide cultures [2]. For this reason, conservation of Cultural Heritage is an important goal for the society. The aim of conservation is normally the preservation of an object using minimum intervention. In addition, the purpose of conservation is to maximise the object utility. So, usability and longevity need to be achieved with conservation practice [3]. Metals conservation involves different approaches that can be split into interventive methods and preventive techniques. Interventive methods aim at adding or removing something from the object in order to preserve it, while the scope of preventive methods is to prevent corrosion by controlling the environment. For both the approaches, an understanding of the physical and chemical structure of metal alloys, their interactions with environmental variables and the properties of their corrosion products. In particular, in the field of Cultural Heritage the selection of a conservation strategy therein requires taking into account the following key points:

(i)   a basic understanding of the corrosion mechanism;

(ii)   testing the efficiency and the aesthetical impact of the candidate treatments on representative substrates, which reproduce in a reliable way the complexity of real surfaces.

In order to follow this approach, this chapter includes the literature review about the main corrosion mechanisms occur for outdoor bronze monuments and for coupons at the laboratory scale, as well as the main types of protective coatings applied for their conservation. For the sake of clarity, basics of atmospheric corrosion and casting bronze metallurgy are also reported. Finally, the main experimental studies about the assessment of the protectiveness of protective coatings are also collected and presented in this chapter.

2.1. Basics of corrosion

2.1.1. Definitions of Corrosion

Several definitions have been proposed for the term corrosion. The International Standard Organization defined corrosion in the following way [4]:

"Corrosion is the physicochemical interaction between a metal and its environment that results in changes in the properties of the metal, and which may lead to significant impairment of the function of the metal, the environment, or the technique system, of which these form a part."

From this definition it is possible to state that in the corrosion phenomena the important factors are the metal, the environment and the interface between the metal and the environment. In particular, regarding the metal, its composition, the atomic structure and its heterogeneities and the stresses may determine different corrosion phenomena. In addition, parameters of the environment, such as temperature and pressure, chemical nature

and concentration of the reactive species, are also relevant to understand the corrosion process. Finally, the interaction between the metal and the environment induces reactions at the metal/environmental interface and the kinetics of the metal oxidation and dissolution, as well as the reduction of the species in solution are the main factors ruling the corrosion process [5]. Corrosion covers a broad range of processes and corrosive environments and for this reason a broad classification into "wet" and "dry" corrosion is commonly accepted: "wet" corrosion includes all the reactions involving an aqueous solution in the reaction mechanism, while the "dry" corrosion happens in absence of water or of an aqueous solution.

2.1.2. Corrosion as a chemical reaction

The corrosion is an electrochemical process which occurs as an oxidation-reduction (redox) reaction: the dissolution of the metal is due to the development of an oxidation reaction, while the reduction part refers to the species that gain these electrons. Both reactions simultaneously occur on the metal surface.

Due to the electrochemical nature of the process, the chemical reactions occurred involved the electron transfer. So the anodic reaction is the one occurring as metal oxidation (anode) (Equation 2.1). This reaction produces electrons that pass through the conducting metallic substrate to other sites (cathode) of the metal surface, where the cathodic reaction occurs and the oxidant is reduced (Equation 2.2).

$$M \longrightarrow M^{2+} + 2e^-$$

$$M^{2+} + 2H_2O \longrightarrow M(OH)_2 + 2H^+$$

$$(2.1)$$

$$\tfrac{1}{2} O_2 + H_2O + 2e^- \longrightarrow 2OH^- \tag{2.2}$$
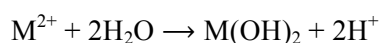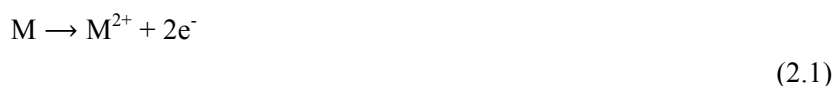
So the whole corrosion process can be described by the following reaction (Equation 2.3):

$$M + \tfrac{1}{2} O_2 + H_2O \longrightarrow M(OH)_2 \tag{2.3}$$

These chemical reactions described the corrosion mechanism in neutral solutions. However in acid environments (pH $\leq$ 2), metals react with H$^+$ ions of the solution producing hydrogen (Equation 2.4).

$$2H^+ + 2e^- \longrightarrow H_2 \tag{2.4}$$
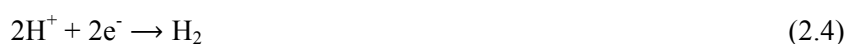
This means that, compared with neutral water solutions, low-pH acidic water accelerates corrosion by supplying hydrogen ions to the corrosion process. Oxygen reduction and hydrogen ion reduction are the most

common cathodic reactions, while metal ion reduction and metal deposition are less common but can cause severe corrosion attacks.

Many anodic and cathodic reactions can occur during corrosion. Indeed, in corrosion processes of alloys, all metal components can be dissolved as ions in the solution and then be oxidized. In the same way, more than one cathodic reaction can occur at the metal surface which means that, for instance, acid solutions that contain dissolved oxygen or that are exposed to air are generally more corrosive than de-aerated acids.

2.1.3. Thermodynamic approach to corrosion reaction

The corrosion of a metal in contact with an electrolyte deeply depends on the environment pH and on its oxidizing or reducing power. Generally, a metal can exhibit three different behaviours: inert, active or passive. A metal is inert when it does not react with the environment ($\Delta G < 0$). In this case corrosion mechanisms do not occur. When, instead, a metal has an active behaviour ($\Delta G > 0$) it reacts with the environment, corrosion mechanisms occur, and the resulting corrosion products are soluble. On the contrary, when the metal is passivated corrosion mechanisms forms corrosion products that are insoluble and protective.

A useful tool to predict in which condition a metal is inert, active or passive is given by potential-pH diagrams, commonly called Pourbaix diagrams. The pH represents the acidity or alkalinity of the electrolyte while the potential represents its oxidative power. By the use of these diagrams it is possible to foresee if corrosion can occur and to estimate the composition of the corrosion products. Figure 2.1 reports the partial Pourbaix diagram of Cu and reveals that the corrosion of Cu immersed in de-aerated acid water is not likely to occur (unless in presence of high concentration of specific complexing ions). The H^+/H_2 equilibrium potential represented by line a is always lower than the Cu^{2+}/Cu equilibrium potential. The H^+ ions are stable in contact with Cu metal, which cannot corrode (is immune) in water solutions free from oxidizing agents [6].
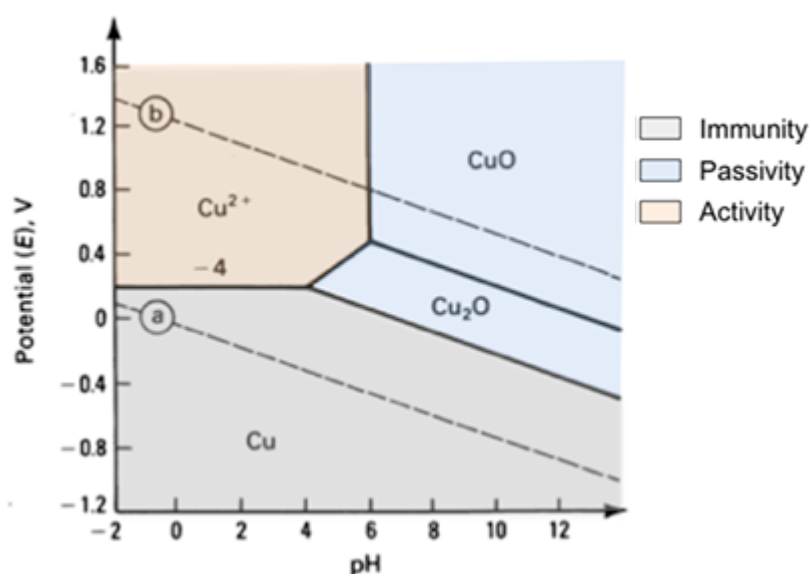
Figure 2.1: Partial E-pH diagram for Cu [6].

22

2.1.4. Types of corrosion

Corrosion can affect the metal in a various ways depending on the nature of the metal and the environmental conditions prevailing. Therefore, a broad classification of the various forms of corrosions is as follows and then reported in Figure 2.2:

- general corrosion;
- localised corrosion;
- selective corrosion.

General corrosion usually affects the whole surface of the metal and all the areas of the metal corrodes at similar rate. Depending on the uniformity of the corrosion attack, it is possible to define uniform and non-uniform corrosion. Localised corrosion usually involves local areas of the metallic surface, which corrode at higher rates than others due to heterogeneities in the metals, in the environmental or in the geometry of the structure. So it induces the formation of cavities that depending on the ratio between the diameter and the depth form different morphologies, as craters, pits or cracks. In particular, cracks are defined intergranular or transgranular if they preferentially follow the grain boundaries or not, respectively. In particular, in the case of pitting highly localised corrosion attack at specific areas results in small pits that penetrate into the metal and may lead to perforation

Selective corrosion determines the preferential dissolution of particular parts of the metallic surface, which can be attacked more easily, due to their chemical and/or metallurgical reason. It is possible to distinguish crystallographic, intergranular and interdendritic corrosion depending on the fact that crystalline species, the grain boundaries or the interdendritic phases are preferentially attacked. Dealloying corrosion consists of the preferentially dissolution of one or more alloying elements (*e.g.* denzincification of brass or decuprification of bronze alloys).

Finally, the conjoint action of corrosion and mechanical factors induced localised attack or fracture due to the synergistic action of a mechanical factor and corrosion. In bronzes, most prevailing corrosion morphology is general corrosion in atmospheric condition.
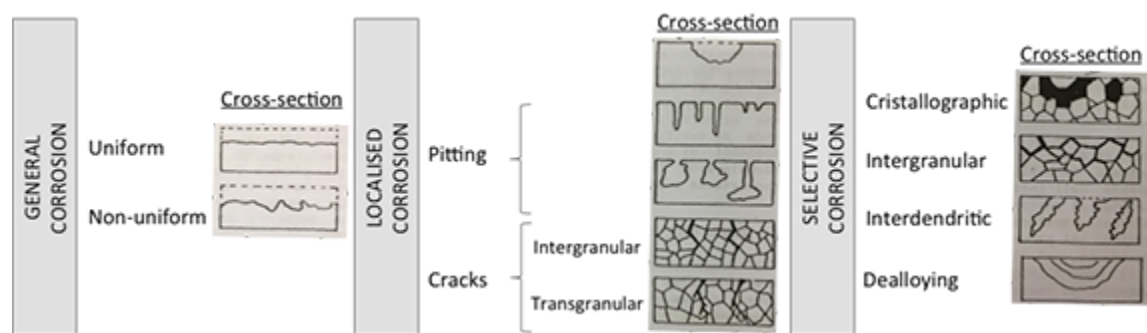
Figure 2.2: Classification of the main corrosion morphologies [7].

23

2.2. Atmospheric corrosion of bronzes

2.2.1. Metallurgy of casting bronzes

Cu and Cu-based alloys constitute one of the major groups of commercial metals. They are widely used because of their excellent electrical and thermal conductivities, outstanding resistance to corrosion, ease of fabrication, and good strength and fatigue resistance. They are generally nonmagnetic. They can be readily soldered and brazed, and many Cu and Cu-based alloys can be welded by various gas, arc, and resistance methods. For decorative parts, standard alloys having specific colours are readily available. Cu alloys can be polished and buffed to almost any desired texture and luster. They can be plated, coated with organic substances, or chemically coloured to further extend the variety of available finishes [8].

Classification of both wrought and cast bronze alloys are reported in Table 2.1 and 2.2, respectively. In all classes of Cu alloys, certain alloy compositions for wrought products have counterparts among the cast alloys. In particular, wrought alloys are defined from C1XXXX to C7XXXX, while cast alloys are classified from C8XXX to C9XXXX.

Table 2.1: Classification of wrought Cu-based alloys in accordance to UNS nomenclature [8].

Generic name	UNS numbers	Composition
Wrought alloys		
Coppers	C10100-C15760	>99% Cu
High-copper alloys	C16200-C19600	>96% Cu
Brasses	C20500-C28580	Cu-Zn
Leaded brasses	C31200-C3890	Cu-Zn-Pb
Tin brasses	C40400-C49080	Cu-Zn-Sn-Pb
Phosphor bronzes	C50100-C52400	Cu-Sn-P
Leaded phosphor bronzes	C53200-C54800	Cu-Sn-Pb-P
Copper-phosphorus and copper-silver-phosphorus alloys	C55180-C55284	Cu-P-Ag
Aluminum bronzes	C60600-C64400	Cu-Al-Ni-Fe-Si-Sn
Silicon bronzes	C64700-C66100	Cu-Si-Sn
Other copper-zinc alloys	C66400-C69900	…
Copper-nickels	C7000-C79900	Cu-Ni-Fe
Nickel silvers	C73200-C79900	Cu-Ni-Zn

Table 2.2: Classification of wrought Cu-based alloys in accordance to UNS nomenclature [8].

Generic name	UNS numbers	Composition
Cast alloys		
Coppers	C80100-C81100	>99% Cu
High-copper alloys	C81300-C82800	>94 Cu
Red and leaded red brasses	C83300-C85800	Cu-Zn-Sn-Pb (75–89% Cu)
Yellow and leaded yellow brasses	C85200-C85800	Cu-Zn-Sn-Pb (57–74% Cu)
Manganese bronzes and leaded manganese bronzes	C86100-C86800	Cu-Zn-Mn-Fe-Pb
Silicon bronzes, silicon brasses	C87300-C87900	Cu-Zn-Si
Tin bronzes and leaded tin bronzes	C90200-C94500	Cu-Sn-Zn-Pb
Nickel-tin bronzes	C94700-C94900	Cu-Ni-Sn-Zn-Pb
Aluminum bronzes	C95200-C95810	Cu-Al-Fe-Ni
Copper-nickels	C96200-C96800	Cu-Ni-Fe
Nickel silvers	C97300-C97800	Cu-Ni-Zn-Pb-Sn
Leaded coppers	C98200-C98800	Cu-Pb
Miscellaneous alloys	C99300-C99750	…

As pure Cu is difficult to cast and it is prone to cracking, gas porosity and internal cavities, usually it is alloyed with other elements in order to improve its castability, except if excellent electrical conductivity properties are required [9]. So several alloying elements can be added impacting the main properties, such as:

- Sn is the oldest known alloying element in Cu and the key alloying element in many bronzes. It gives solid-solution strengthening, improves corrosion resistance, reduces the melting temperature of Cu and improves fluidity, making the alloy more easy to cast.
- Zn is relatively inexpensive and imparts strength and hardness through solid solution strengthening. It is the major alloying element for brasses.
- Pb is insoluble in Cu but help to seal the normal shrinkage porosity forward during cooling due to the fact that Pb solidifies last and it is found at the grain boundaries or in the interdendritic areas. It also improves machinability.
- Al improves the strength of Cu and if added in small concentrations it can improve the fluidity of Cu-based alloys.
- Si forms a solid solution with Cu and improves the fluidity so as these alloys are used for art and mould casting.
- Ni improves corrosion resistance, as well as the quality, strength and creep resistance of Cu-Sn alloys.

- Be provides strength by forming an interdendritic precipitate without compromising other properties as electrical and thermal conductivity.

- Cr increases strength with a minor loss in electrical conductivity.

- Fe is not miscible in Cu and increases the melting temperature of Cu-based alloys.

- P is a very common element at high Cu-based alloys, it is resistive to cracking and deoxygenated Cu.

In particular, bronze is a Cu alloy, which can vary widely in its composition. It is often used where a material harder than Cu is required, where strength and corrosion resistance is required and for ornamental purposes. The variations in bronze (both in proportion and elemental composition) can significantly affect its weathering characteristics. Usually bronze is defined as a combination of approximately 90% Cu and 10% Sn, however there are three major classes or types of "bronzes" used in sculpture and construction [10]:

- Statuary Bronze - approximately 97% Cu, 2% Sn and 1% Zn; this composition is the closest to the definition of bronze. Also Pb and Sb can be in the alloy to form quaternary and quinary bronze respectively.

- Architectural Bronze - actually more of a "leaded brass", this composition is commonly composed of approximately 57% Cu, 40% Zn and 3% Pb.

- Commercial Bronze - composed of approximately 90% Cu and 10% Zn.

However, nowadays bronze composition may vary significantly and bronzes may contain Si, Mn, Al, Zn and other elements, with or without Sn.

In order to represent the different phases in an alloy at the equilibrium, phase diagram are usually considered. Figure 2.3 reports the Cu-Sn phase diagram that shows an eutectoid structure characterised by the transformation of a solid solution into two distinct solids. So, the eutectoid constituent is made up two phases, α-phase (Cu-rich solid solution) and δ-phase (an intermetallic compound of fixed composition $Cu_{31}Sn_8$). This phase is light blue, hard and brittle material with a jagged appearance [11].

So tin bronze can be divided into two regions depending on the composition, as follows:

- low-tin bronze contains less than 15.8 wt% of Sn that corresponds to the solubility limit as a function of temperature;

- high-tin bronze.
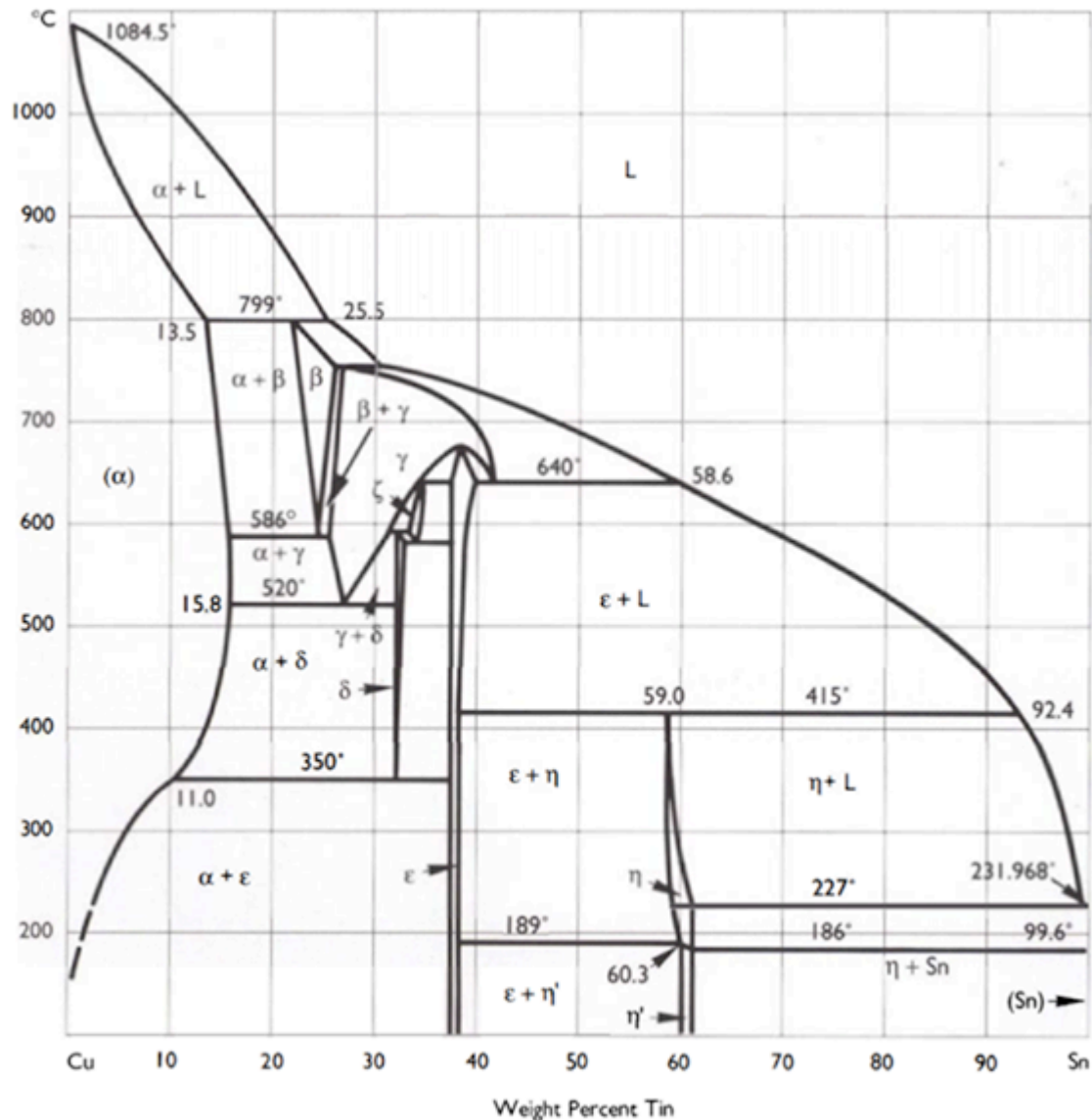
Figure 2.3: Cu-Sn phase diagram [11].

The Cu-Sn phase diagram reported in Figure 2.3 could be more el×aborated. In Figure 2.4, the different Cu-Sn phase diagrams at the equilibrium in the annealed and casting conditions show different features. In particular, due to the fact that the higher rate of solidification corresponds to the lower solubility of Sn in Cu, the highest Sn content is in the case of equilibrium due to the slowest cooling rate. Another difference between these different conditions is that the α+ε phase is not present in the annealing and casting cases, due to the fact that a very slow solidification rate has to be applied to obtain this phase. So, in two-phase alloy like tin bronze microsegregation is present due to the different compositions localised in different places in the microstructure. In addition, the corrosion process depends on the kind of alloy and the different phases can be selectively corroded.

27
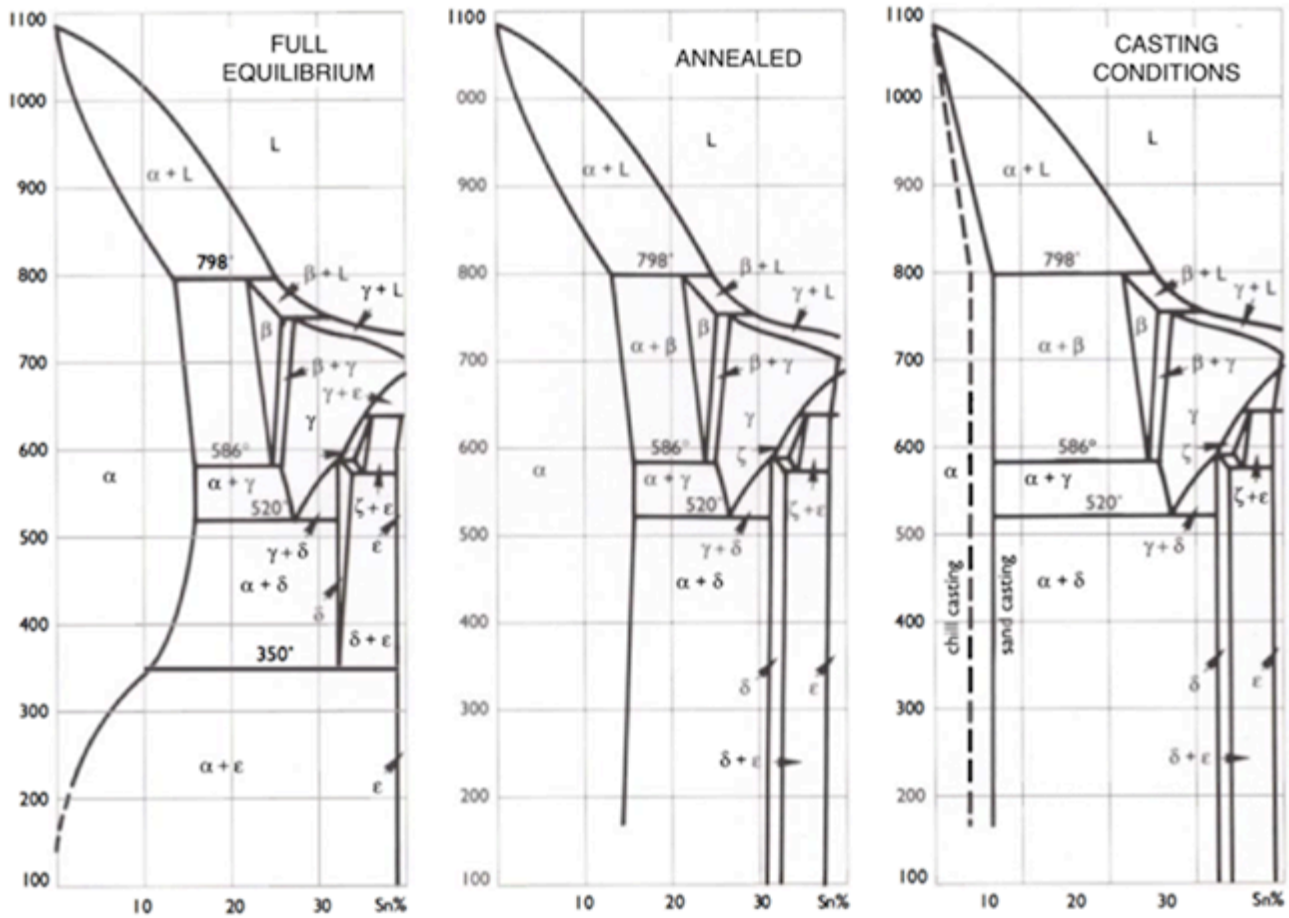
Figure 2.4: Part of the Cu-Sn diagram (until 40 wt% Sn) at different conditions [11].

In addition, the binary phase diagram of Cu-Si systems is reported in Figure 2.5. The phase diagram at the equilibrium is quite complex with 8 intermetallic compounds in a very small range of Si concentration (4-26 wt% Si). It shows that there are 3 stable intermetallic phases at room temperature in the Cu-Si system. In the literature, these phases are mostly named as follows: η (Cu3Si), ε (Cu15Si4) and γ (Cu5Si). Cu3Si phase has two high temperature modifications η (556-802 °C) and η' (467-556 °C) beside the room temperature stable η'' intermetallic (stable below 467 °C).
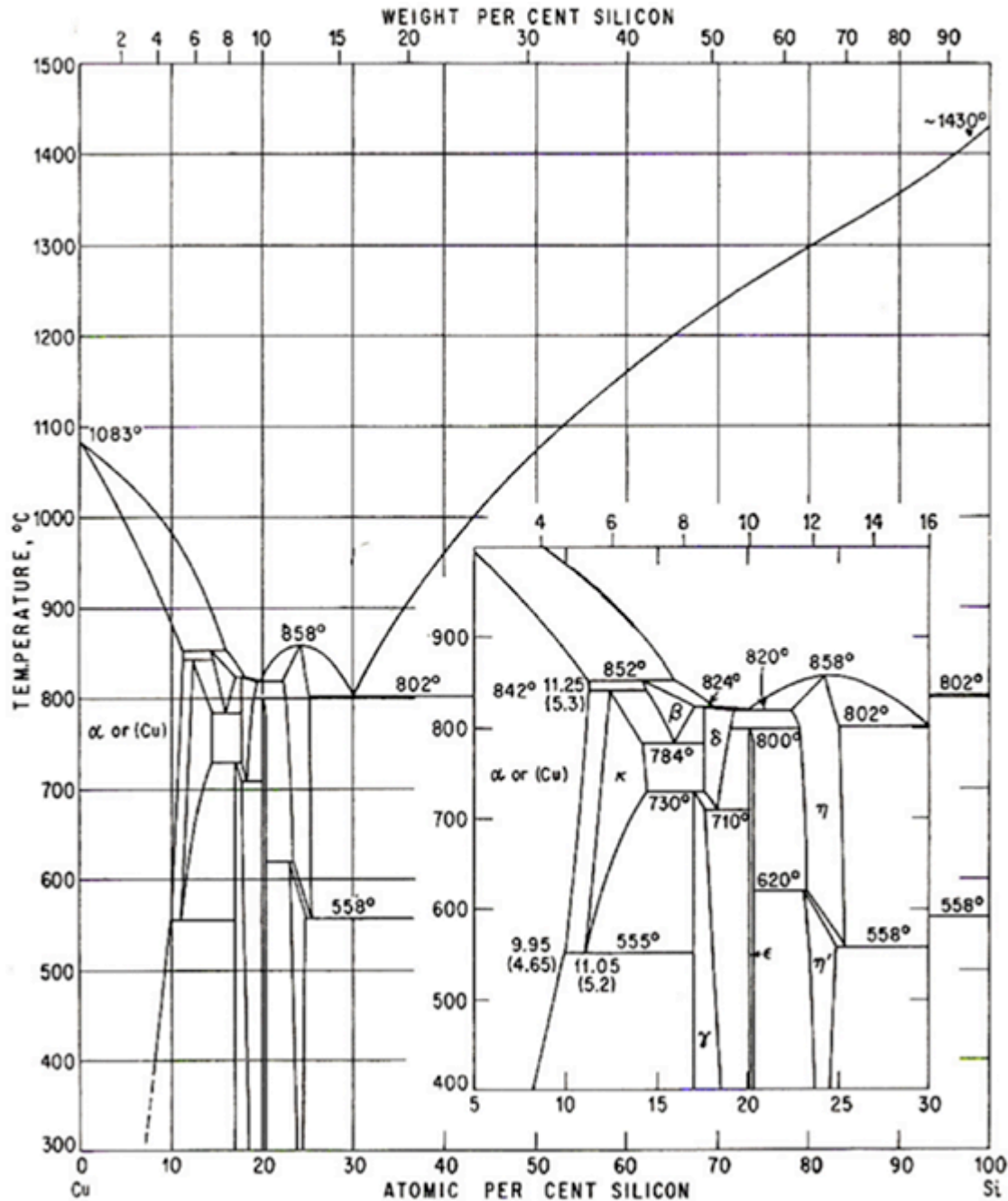
Figure 2.5: Cu-Si phase diagram [12].

Finally, the microstructure of cast bronze is typically dendritic, as shown in Figure 2.6. Dendrites look like fernlike growth scattered at random throughout the metal. They continue to grow until they touch each other. In addition, dendrites are composed of different type of arms as reported in Figure 2.6 a and by measuring the space between these arms, it could be possible to find the mould or the conditions used for casting the metal [11]. The size of dendrites depends on the cooling rate of the alloy: the faster the cooling rate, the smaller the dendrites. In the case of slow cooling, the dendrites can sometimes be observed at naked eye or under a binocular bench microscope at low magnification (×10 or ×20).
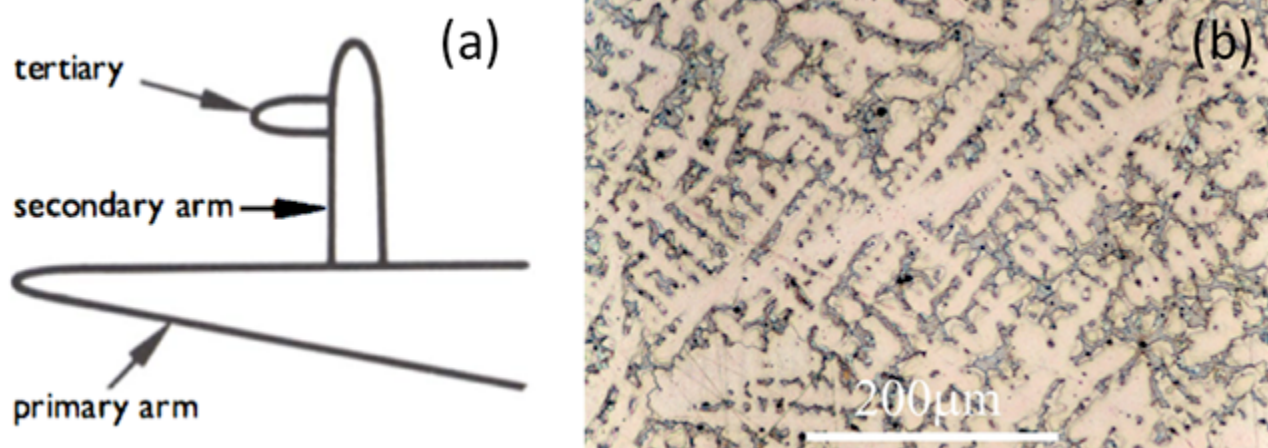
Figure 2.6: (a) schematic of dendritic arms [11]*; (b) dendritic structure of a bronze with 15 wt% of Sn observed by optical microscopy* [13]*.*

2.2.2. Outdoor environment

The atmosphere is a thin layer gas around the Earth [14]. The composition of atmosphere reported in table 2.3 is almost constant for all locations except for the water vapour content that varies according to the climatic region, season of the year and time of the day. For atmospheric corrosion only oxygen, carbon dioxide and water vapour need to be considered [5].

Table 2.3: Chemical composition of the main components of the atmosphere at 10 °C (impurities are not considered) [5]*.*

Constituents	g/m^3	Weight (%)	Constituents	mg/m^3	ppm by weight
Air	1172	100	**Neon**	14	12
Nitrogen	879	75	**Krypton**	4	12
Oxygen	269	23	**Helium**	0.8	0.7
Argon	15	1.26	**Xenon**	0.5	0.4
Water vapour	8	0.70	**Hydrogen**	0.05	0.04
Carbon dioxide	0.5	0.04			

Water vapour is essential for the formation of an electrolyte solution, which is responsible of the electrochemical corrosion reactions and its concentration is expressed by relative humidity (R.H.), defined as the percentage ratio of the water vapour pressure in the atmosphere compared to the concentration needed for saturating the atmosphere at the same temperature. In addition, oxygen from the atmosphere dissolves in the electrolyte and provides the cathode reactant in the corrosion process.

Atmospheric pollutants may ne defined as those substances present in atmosphere that can have adverse effects on health or the environment [14]. They usually come from gases and black particles and strongly influence the atmospheric corrosion. Pollutants from natural sources including lighting, volcanic eruptions,

natural microbiological process in soil, wind-blown soils and animals, while contaminants from the anthropogenic sources include sulphur oxides (SO_x), nitrogen oxides (NO_x), hydrocarbons and heavy metals. Most atmospheric pollutants have both natural and anthropogenic nature [14].

Sulphur oxides (SO_2 is the most frequently encountered oxide) are strong stimulators of the atmospheric corrosion and derive from the aerial oxidation of H_2S produced naturally and from the combustion of S-containing fuel. Nitrogen compounds also arise from both natural and anthropogenic sources, as are produced in the atmosphere during electrical storms but also are due to the use of artificial fertilisers. Both SO_2 and NO_x form acids where the weather is wet, while in dry areas the acid chemicals can concentrate and be incorporated in dust or smoke [5,14]. Another gas, ozone (O_3), influences the atmospheric corrosion process. Ozone is a variety of oxygen with three oxygen atoms and it is the major component of photochemical smog and it is produced from burning coal, gasoline and other fuels. Finally, particulate matter (PM) is a mixture of several components that includes dust, soot and other bits of solid materials produced by many anthropogenic sources. The particulate matter can cause the increase of corrosion and it is a source of the black matter on the surfaces exposed outdoor [14].

Several environmental factors can simultaneous influence the atmospheric corrosion process, such as UV radiation or light, temperature and rainfalls conditions and act on outdoor exposed objects in a synergetic way. In particular, temperature affects the rate of chemical reaction, as well as the time the surfaces remain wet. In addition, temperature affects the emission of atmosphere pollutants through the management of heating during cold seasons and cooling of living space for comfort. This impacts energy use and thus fuel consumption.

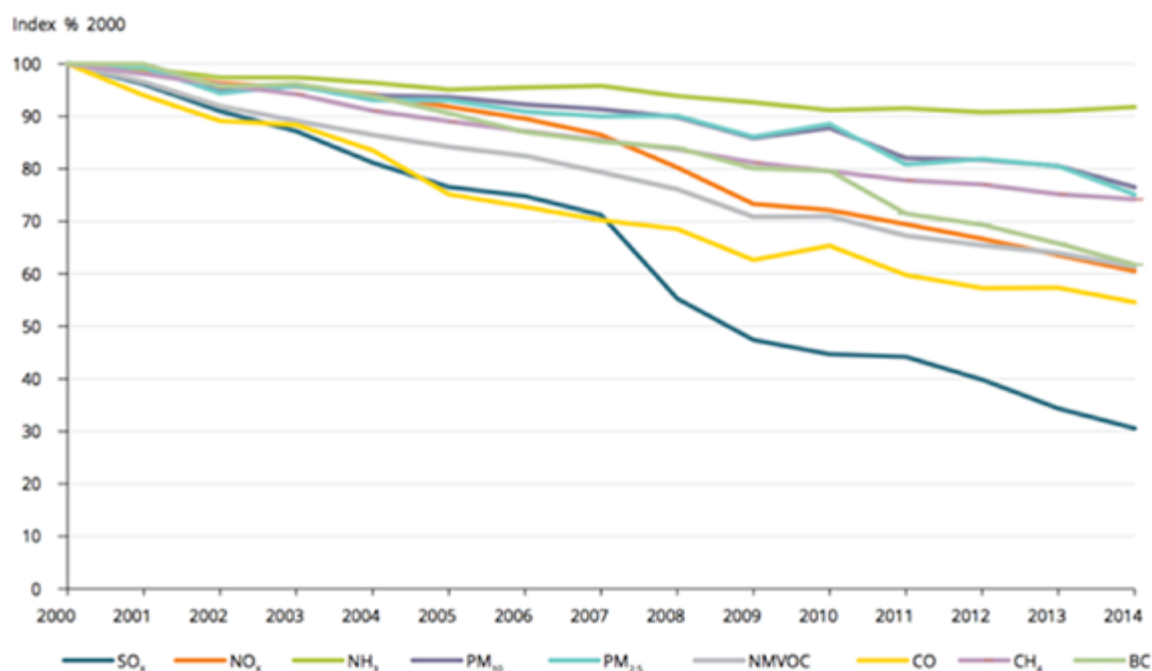*Figure 2.7: Development in EU-28 emissions of the main air pollutants from 2000 to 2014 (% of 2000 levels): sulphur oxides (SO_x), nitrogen oxides (NO_x), ammonia (NH_3), particulate matter (PM_{10} and PM_{25}), non-methane volatile organic compounds (NMVOC), carbon monoxide (CO), methane (CH_4), black carbon (BC) [15].*

The European Environment Agency reports that the quality of the air is continuously improved in Europe in the last decade, due to reduced emissions in particular regarding SO_x and NO_x, as highlighted in Figure 2.7. However, concentration of atmospheric particulate matter (PM) continues to exceed the EU limit and target values in large parts of Europe in 2014 [15]. So even if the decrease of SO_x and NO_x concentrations induces a lower acidity of rainfalls, the presence of air pollutants, particularly particulate matter, is still the main responsible of the atmospheric corrosion process.

2.2.3. Corrosion mechanisms of bronze

When a bronze is exposed to the outdoor environment, corrosion processes occur and *patina*, which is a layer containing several corrosion species, forms on the metal substrate. Usually, a thin layer of brown-red oxide patina forms spontaneously on copper and its alloys, protecting them from further corrosion. Patina on a bronze sculpture not only protects the substrate metal, but also enhances the aesthetic of art objects. In particular, it is possible to distinguish two kinds of patina. The first one is natural patina formed spontaneously during long time exposure to atmospheric environment. The structure and composition of this kind of bronze patina are specific to each alloy and depend on the environment to which the bronze is exposed. The second type is synthetic or artificial patina with a defined chemical composition that can be formed in laboratory or artistic workshop, allowing appropriate accelerated surface treatment of bronze with peculiar aesthetical features. However, over time, bronze surfaces undergo secondary corrosion processes, which are influenced by environmental conditions, gradually changing colour to dark brown until the formation of green patinas [16–19]. This has been particularly observed in outdoor monuments [16–19] both in the case of ancient natural patinas and recent artificial patinas. In particular, areas directly washed by rainfalls tend to appear light green, while areas sheltered from the rain tend to black [20].

A patina that has developed over many years in outdoor environment contains a large number of different species that together provide a complex structure and the overall appearance. This includes corrosion products, but also deposited material, such as aerosol particles, wind blown dust and soot [20]. Regarding the chemical composition of Cu-based corrosion products, the following compounds can be found in Cu specimens weathered in atmosphere [20–22]:

- *CUPRITE (Cu_2O):* is the most common corrosion product on Cu-based alloys exposed outdoors. It has a red, brown or black appearance and it is insoluble in water and slightly soluble in acid;
- *TENORITE (CuO):* is rarely detected on outdoor objects;
- *BROCHANTITE [$Cu_4(SO_4)(OH)_6$]:* nearly always the most common component of the green patina formed on Cu after long atmospheric exposure. This mineral is the most common Cu hydroxyl-sulphate occurring in nature, so as it is reported to be stable under a wide variety of chemical conditions;

- *ANTLERITE [Cu$_3$(SO$_4$)(OH)$_4$]*: a common patina constituent and it is mainly identified in rain-sheltered areas on objects that are older than several decades. It is stable in more acidic conditions than brochantite. There is some evidence that antlerite may occur at earlier stages of the patination process than brochantite. Anterlite has been also found on the Cu skin of the Statue of Liberty. It is suggested that acid rain is converting brochantite to the less protective anterlite, which is more susceptible to erosion;

- *POSNJAKITE [Cu$_4$(SO$_4$)(OH)$_6$·H$_2$O]*: may co-exist with or undergo transformation to brochantite because of its structural similarity (hydrated form of brochantite). Indeed it has been suggested to be a metastable precursor to brochantite formation.

- *ATACAMITE or CLINOATACAMITE [Cu$_2$Cl(OH)$_3$]*: soluble in weak acid. It has been found to be as abundant or more abundant than brochantite in patinas formed near the sea due to the influence of sea-salt aerosols. It is not found on specimens exposed for short times;

- *PARATACAMITE [Cu$_2$Cl(OH)$_3$]*: its presence is transitory and it eventually converts to atacamite. It is not found in patinas corresponding to long exposures;

- *MALACHITE [Cu$_2$(CO$_3$)(OH)$_2$]*: atmospheric conditions do not favour the formation of this type of patina, but this basic carbonate is sometimes unexpectedly found in practice;

- *GERHARDTITE [Cu$_2$NO$_3$(OH)$_3$]*: also found in some locations.

The concentrations of air pollutants and the chemistry of the precipitation have strongly changed during the XIX century due to the anthropogenic activity, inducing a lower stability of the patinas on the bronze substrates mainly due to the presence of aggressive environmental species, as SO$_2$ and NO$_x$. In particular, dry deposition of air pollutants plays an important role in the degradation of patina layers by the conversion of the patina species in new phases which are more susceptible to the dissolution to rain, as reported in [20,22–24]. Tenorite reacts rapidly with SO$_2$ in humid air, absorbing all SO$_2$ supplied, mainly forming brochantite. This explains the rare presence of tenorite in outdoor exposure. The reaction of Cu$_2$O with SO$_2$ in humid air is slight and corresponds to the formation of a chemisorbed sulfite layer on the surface. In addition, when O$_3$ is present together with SO$_2$, the oxidation of the adsorbed sulfite was rapid and antlerite and brochantatite form. Finally a mixture of atacamite and clinoatacamite react in humid SO$_2$-containing air forming soluble CuSO$_4$·xH$_2$O and CuCl$_2$·xH$_2$O solution. Adding O$_3$ to the humid air, the rate of the sulfation increases. So the reaction between Cu hydroxyl chloride and SO$_2$ implies the release of chloride ions and protons, which may cause severe corrosion on outdoor bronze by formation of an acid electrolyte [20].

Krätschmer et al. [25] proposed a schematic representation of all the results about the evolution of the different corrosion products of a sheltered Cu patina over the time and in different dominated environments (sulphate- or chloride- dominated), reported in Figure 2.8. The central part of the scheme (Figure 2.8) shows that cuprite is the first compound formed on the patina. It appears quite instantaneously and it is followed by the formation of copper hydroxi-sulphates, which result from amorphous copper sulfate. When Cu is in an

acid environment (high SO_2/SO_4^{2-} concentration), this amorphous phase transforms into strandbergite, while posnjakite and langite tend to form in a less acidic environment. These compounds form in a restricted period of time (months). Years are needed if we want these precursors to transform into brochantite or antlerite. Moreover, for obtaining atacamite, a Cl^- rich environment is necessary, preceded by the formation of nantokite.
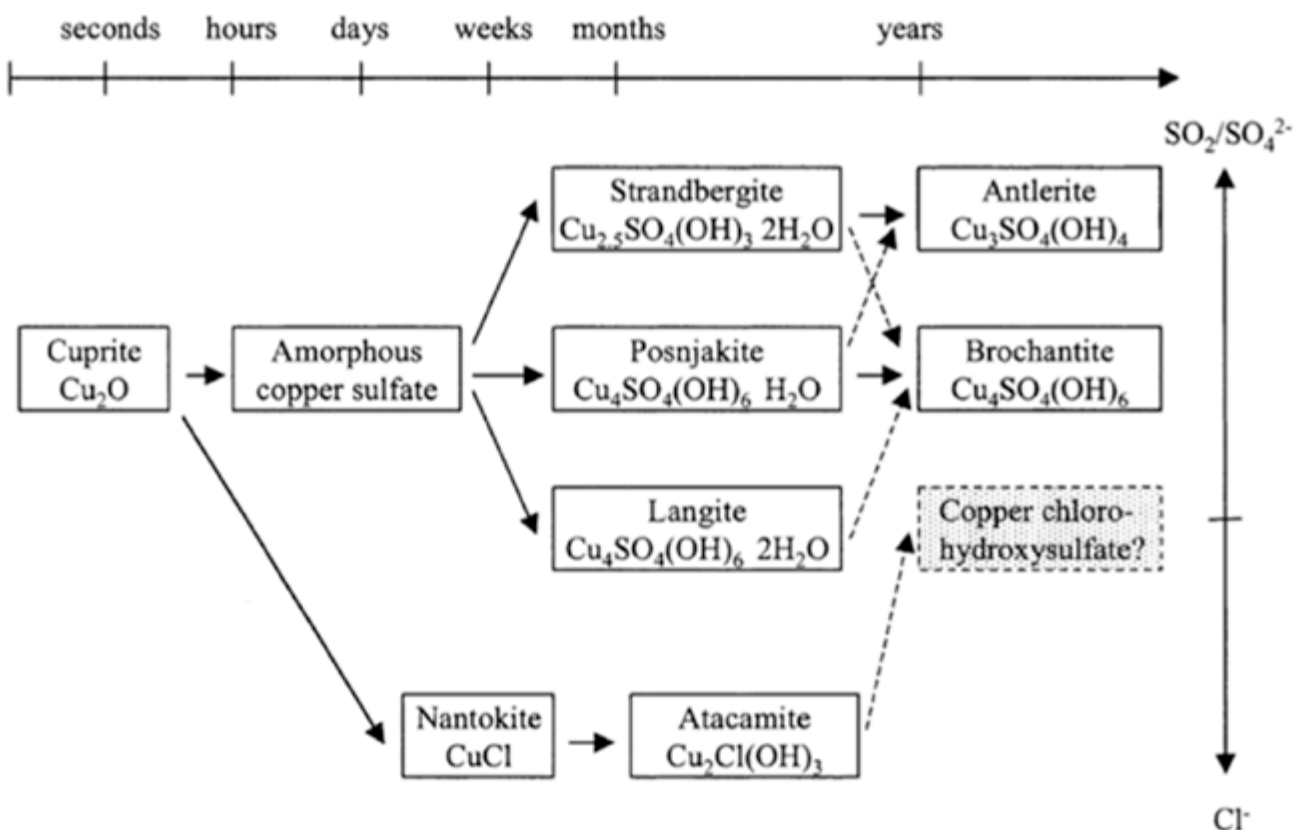
Figure 2.8: Schematic of patina evolution of sheltered Cu [25].

Another fundamental parameter ruling the corrosion processes of the outdoor bronzes and the consequent formation of patina layers is the geometry of exposure. In particular, for outdoor bronzes which are exposed to rain events, if the surface is under stagnant conditions then the patina acts as a multilayer system where a Sn-enriched layer is covered by Cu and Pb compounds and Zn dissolves completely. Conversely, in the case of runoff conditions, the patina is a thin porous layer strongly enriched in non-soluble Sn oxides across which Cu, Zn and Pb cations migrate and most of them are leached into the environment [26,27]. More in detail, as summarize by Jouen et al. [28] in the schematic representation reported in Figure 2.9, the corrosion behaviour of Cu and Zn appears relatively similar in the unsheltered exposure in a French industrial atmosphere since the mass curves exhibited a parabolic time dependence. The increase of mass observed in the first stage occurs from the formation of a corrosion layer over the surface, while the mass loss recorded thereafter is explained by the continuous dissolution by rainwater of a relatively large fraction of the corrosion products. On a Cu surface cuprite layer can be identified within a few days of exposure, then a mixture of the basic Cu sulphates $Cu_4SO_4(OH)_6 \cdot H_2O$ with $Cu_4SO_4(OH)_6$, is commonly formed over this oxide layer. The proportion of non-

hydrated form is increasing with time to the detriment of the hydrated one. Depending on the coupons and the exposure time, basic Cu nitrate $Cu_2(OH)_3NO_3$, basic Cu chloride $Cu_2(OH)_3Cl$, cuprous chloride $CuCl$, and Cu sulphate $CuSO_4 \cdot xH_2O$ were also identified in lower proportion [28]. Concerning Zn substrate, the corrosion layers formed on the surface are thin as a consequence of the washing and dissolution process by rainfalls during the testing period. Basic Zn carbonates $Zn_5(OH)_3(CO_3)_2$ and $Zn_4CO_3(OH)_6 \cdot H_2O$ and basic Zn sulphates $Zn_4SO_4(OH)_6 \cdot xH_2O$ appear as main corrosion products on all points analysed over the surface [28].
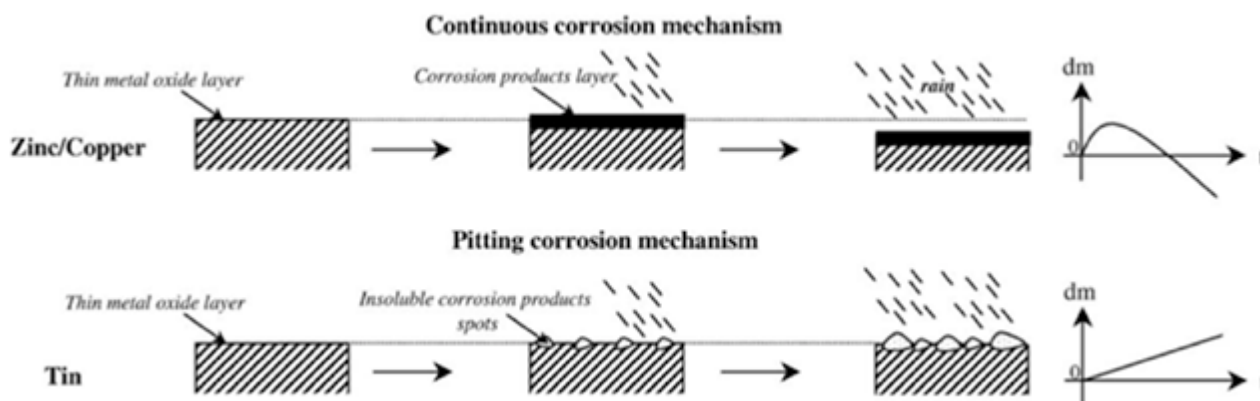
Figure 2.9: Schematic representation of Zn, Cu and Sn behaviour and mass variation (dm) along the exposure under unsheltered conditions [28]*.*

Mass variations become negative after few months. On the other hand, Sn mass variation curve exhibited a rather linear trend throughout the exposure time. This increase is attributed to a pitting corrosion mechanism and the growth of mainly insoluble clusters of corrosion products formed on the surfaces. The corrosion layers of Sn coupons consist of a complex mixture of corrosion products. Hydrated stannic oxide $SnO_2 \cdot xH_2O$ not well crystallised is the main constituent. Other forms of Sn(IV) and Sn(II) compounds were also detected in the form of sulphate, carbonate and chloride phases, but were poorly identified. No significant change in the corrosion product proportions was observed with exposure time [28].

2.2.4. Case Studies: real monuments and bronze coupons

The understanding of corrosion processes occur on outdoor bronzes was possible thanks to the investigation of real patina layers [17,19,26,29]. Robbiola et al. [27] established a model of the process involved in the outdoor bronze corrosion on the basis of several investigations of outdoor bronze sculptures such as Rodin's bronze, a Stanislas statue in Nancy (France) and other bronzes exposed to urban environments. From the analysis of the nature of real patinas and their chemical characteristics, two types of surfaces may be distinguished. The surfaces exposed to rainfall are usually made of pale green products and black areas, which stand as isletsts surrounded by the pale green products. The analysis of these corrosion products revealed a high Sn content and the Cu corrosion species are mainly brochantite. On the other hand, the areas protected by the action of rain showed generally green deposits and/or opaque black crusts, containing various atmospheric

particles. These compounds have a low or very low Sn elemental concentration and contain both antlerite and brochantite [27]. The described features can be easily identified in Figure 2.10 from the observation of different areas of the Rodin's statues *"Ugolin et ses enfants"* and *"Le Penseur"*, as reported in [17]. In particular, in Figure 2.10a black spots are surrounding by green pale corrosion products, which are porous and unprotective. The original surface of the bronze is corresponding to the external surface of the black spots, while in Figure 2.10b pale green area is in the centre of the picture. On the foot and on the right, black areas are surrounding by pale green areas. On the left rainfall unexposed area can be observed characterised by opaque black and green areas.
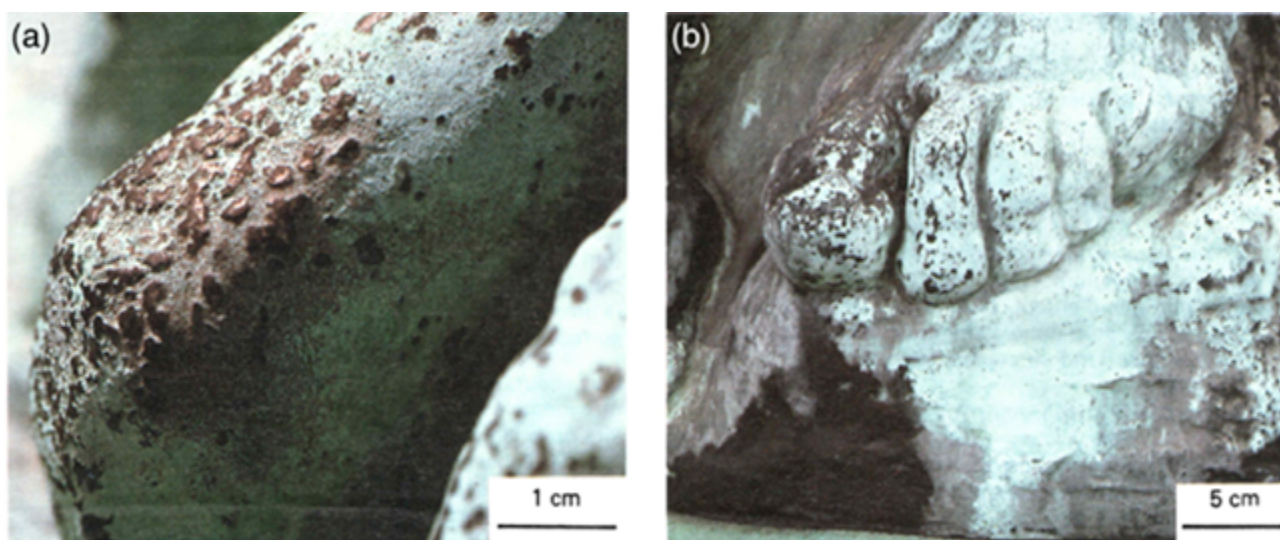
Figure 2.10: View of the corroded surfaces: (a) black spots surrounding by green pale corrosion on the finger of the Ugolin's hand, Rodin Museum, Paris; (b) detail of the foot of "Le penseur", Rodin Museum, Paris [17].

In the schematic representation reported in Figure 2.11 three main steps were outlined regarding the corrosion products of outdoor bronzes [27]. In particular,

1) SELECTIVE DISSOLUTION OF Cu

In contact with the electrolyte (water surface) the oxidation of the alloy can occur as follows (Equations 2.5 and 2.6):

$$Sn + O_2 + nH_2O \longrightarrow SnO_2 \cdot nH_2O \tag{2.5}$$

$$Cu \longrightarrow Cu^+ + e^- \text{ and } Cu^+ \longrightarrow Cu^{2+} + e^- \tag{2.6}$$

Sn oxide is stable in aerated conditions and over a large pH range it is cathodic compared to Cu-rich regions. The Cu ions produced during this first step may build a layer of Cu compounds such as cuprous oxide on the top surface, while the Sn compounds are in the inner part of the corrosion layer.

2) <u>INCREASE OF THE THICKNESS OF Cu DEPOSIT</u>

Several Cu(II) species form and their nature generally depends on the local environment, i.e. mainly brochantite in urban atmosphere or chloride-containing species in a marine environment. In particular, the controlling step of the process is the migration of Cu ions from the alloy to the atmosphere through the deposit.

3) <u>DEPENDING TO SURFACE EXPOSURE GEOMETRY</u>

The acidity of rain and atmospheric pollutants can both solubilize the outermost Cu-based corrosion compounds and promote the transformation of minerals. It is possible to distinguish surfaces directly washed by rainfall (runoff condition) and surfaces, which are not exposed to rainwater (stagnant exposure):

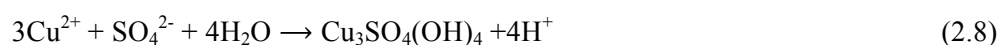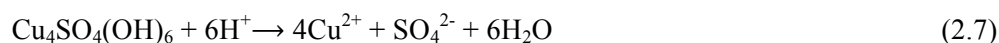 I.   <u>RUNOFF CONDITION:</u> soluble Cu compounds are leached from the rain-exposed surface and the deposit described in the second step is progressively destroyed. So, the corrosion process proceeds from a cyclic mechanism that is strongly correlated with the rainfall frequency. In addition, the heterogeneities of the metallurgical structure locally enhance the formation of the electrochemical coupling. This was also observed by Chang et al. [30] in relation to the inclusions embedded in the metallic Cu. In particular, they observed that the historic naturally patinated sheet Cu showed an inhomogeneous patina and the thickness ratio between the brochantite (outer layer) and cuprite (inner layer) sub-layers seems to be related to the maximum size of the inclusions found in the historic material [30].

  II.   <u>STAGNANT EXPOSURE:</u> the deposit of Cu species on surfaces protected from rainfall may be stable, but acidic waters can promote the transformation of brochantite into antlerite. The increase of the acidity of the water film leads to a dissolution of brochantite followed by antlerite precipitation in accordance with the following reactions (Equations 2.7 and 2.8):

$$Cu_4SO_4(OH)_6 + 6H^+ \rightarrow 4Cu^{2+} + SO_4^{2-} + 6H_2O \qquad (2.7)$$

$$3Cu^{2+} + SO_4^{2-} + 4H_2O \rightarrow Cu_3SO_4(OH)_4 + 4H^+ \qquad (2.8)$$

However, the antlerite formation needs an acidic electrolyte for a sufficiently long period of time. Conversely, brochantite can reform on the surface. It is expected that antlerite forms preferentially on the unexposed areas of sculptures that have lower evaporation rates than exposed surfaces [27].

ATMOSPHERE

(1)

water film

soluble species (H^+, O_2, SO_4^{--} ...)

corrosion products

Cu^+, Cu^{++}

bronze (Cu-Sn alloy)

Basic mechanism

reduction of soluble species
oxidation of the alloy :

- formation of insoluble tin compounds ($SnO_2.nH_2O$), and migration of copper ions to the surface.
- formation of copper species

(2)

corrosion products

Cu^+, Cu^{++}

Increase in the corrosion layer:
formation of copper II minerals (outermost layer) on a inner corrosion layer rich in tin compounds

Surfaces washed by the rainwater
(leaching out of copper II ions)

(3.I)   **(3.II)**

Surfaces not washed by the rainwater

corrosion products

Cu^+, Cu^{++}

corrosion products

Cu^+, Cu^{++}

outermost layer :
mainly $Cu_4SO_4.(OH)_6$, and tin compounds ($SnO_2.nH_2O$)

outermost layer :
mainly copper species
$Cu_4SO_4(OH)_6$, $Cu_3SO_4(OH)_4$

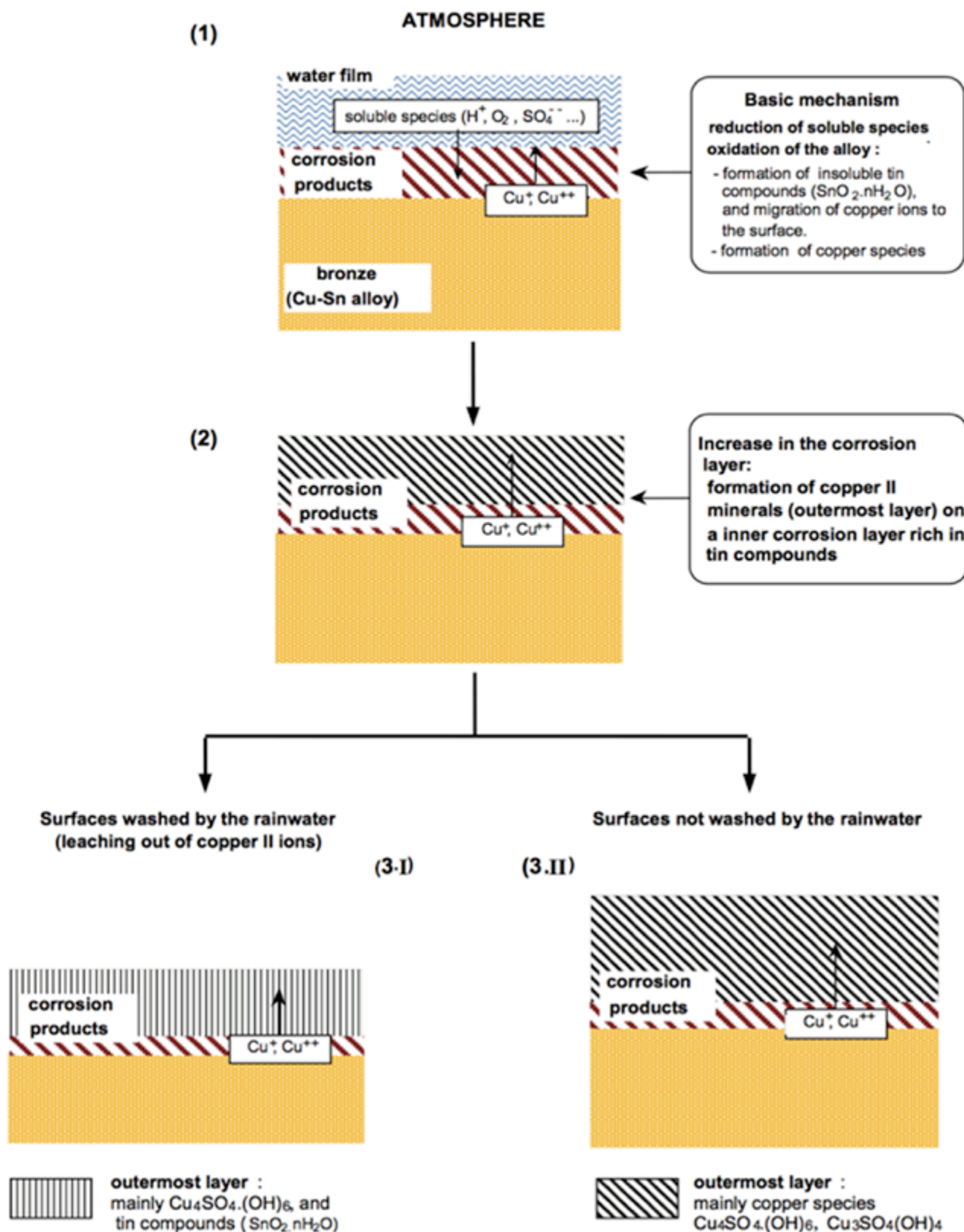*Figure 2.11: Schematic representation of the process involved in outdoor bronze corrosion* [17,27].

The investigation of the patina surfaces of Louis XIV's equestrian statue exposed in Versailles (Figure 2.12) [19,26] confirms that the external pale green layer is relatively homogeneous in composition and contains high amount of Sn compared to the other alloying elements (Cu, Zn and Pb), as expected. The corrosion

products analysed are characterised by poor crystallised nature and the black islets show lower Sn content and high Cl concentration [19]. A following study allowed the comparison between real corrosion products samples from the sculpture of King Louis XIV and those obtained from artificially corroded coupons [26].

Figure 2.12: The statue of King Louis XIV at the Palace of Versailles, France (bottom image). Detail of the unsheltered pale green sample area of the plume on the statue (top image) [19,26].

39

It was found that in stagnant conditions, the patina is a multi-layer system, made of a Sn-enriched layer covered by Cu and Pb compounds, while Zn dissolves completely. In runoff conditions the patina is a rather porous and thin layer, enriched in insoluble Sn oxides, across which Cu, Zn and Pb can migrate. Finally, a strong agreement was found between the results obtained by laboratory tests (Dropping and Wet&Dry test) demonstrating that patinas have different features according to the exposed areas.

In most of the cases, the assessment of coatings or of the corrosion inhibitors has been performed on bare metallic surfaces. Pure Cu-containing compounds were applied or electrochemically produced on the bronze surface to simulate real natural patinas [31,32]. However, artificial patination based only on the deposition of Cu-based compounds is insufficient to reproduce the complexity of natural patinas. In order to develop effective protection strategies, better understanding of the corrosion process on ancient materials was developed from specifically adapted ageing tests. In particular, the impact of artificial acid solutions used for simulated natural rainwaters highlighted the behaviour of alloying elements that release in different ways from the bronze surface, revealing the absence of dissolved tin [33,34]. In this context, an approach based on two specific exposure conditions has been set up on artificial quaternary bronze coupons exposed to synthetic rain, with a monitored time of wetness (ToW) [34,35]. For simulating the effect of runoff (typical of the unsheltered parts of outdoor monuments), the rainfall is replicated by periodically dropping acid rain onto a surface coupon (Dropping test) [34]. On the other hand, for replicating the ageing conditions typical of sheltered areas, the action of stagnant water is reproduced by alternating immersions inducing wet and dry cycles (Wet&Dry test) [35]. Very similar features are found for patinas produced by these artificial ageing methods and for natural patinas [18]. This global procedure is a further advancement for developing testing procedures and new protective treatments, overcoming the difficulties of simulating natural bronze patinas formed upon exposure to outdoor atmospheric environments.

2.3. Conservation methods for outdoor bronzes: protective coatings

In general, coatings for conservation are normally applied with the aim of forming a barrier to inhibit the entrance of gaseous, aqueous or particulate agencies of decay. For Cu-based alloys, resistance to vapours, as well as some volatile pollutants, is important. The characteristics of the coating, the environment in which it must be effective and the nature of the metal surfaces at the moment of coating application impose the choice of the coating. In particular, in order to be applied for Cultural Heritage applications, conservation coatings need to fulfil several requirements [2], such as:

- ease of application;
- minimal aesthetical impact;
- predictive performance and long-term durability;
- non-toxicity;
- reversibility and re-applicability.

Coating performance in its operational environment is of crucial importance, as it determines its maintenance requirements and life-span. In particular, one of the critical parameter is the application method that it is as important as the intrinsic properties of the coating. Spraying is often the favoured application method, while brushing is known to offer preferential failure in defects created by the brush stroke. In addition, the nature of the surface of the object may also favour different methods of application, as well as the coating itself can dictate which application modes are possible to use [2]. In addition, before coating application, cleaning of the surfaces is necessary and for outdoor statuary the cleaning methods are chosen in accordance to the goal of the conservation process, taking into account that they will influence the effectiveness of the coatings, due to the fact that leaving corrosion products and patina influence their adhesion and distribution [2].

Due to the presence of a large amount of specific studies about tailored coatings for outdoor bronze protection, the main investigated types of protective coatings are presented in the following paragraphs in accordance with their chemical affiliation.

2.3.1. Acrylic coating

The Paraloid^{TM} range of acrylics is commonly used within conservation practice. Other acrylics are used according to availability, meaning that geography can impose the choice of materials. However, only few coatings are commonly used with Paraloid B72^{TM} being one of the most popular general purpose surface coatings for cultural metals [2].

In particular, for the protection of Cu-based alloys conservators adopted an acrylic-based formulation containing resin Paraloid^{TM} B-44, named Incralac$^{®}$, from industry, that was found to be the best option for the protection of Cu alloys, even if it was formulated for polished or clean Cu alloys surfaces. Due to the fact that Incralac$^{®}$ is clear, have good adhesion to the bronze, do afford good protection and is removable, it is a popular choice also today. In particular, Incralac$^{®}$ was firstly developed between 1960 and 1965 based on a research initiated jointly by the International Copper Research Association (INCRA) and a cohort from the British Non-Ferrous Metals Research Association (BNFMRA). Both institutions discover that ParaloidTM B44 gave superior protection on Cu alloys and had good appearance and working properties. In particular, they found that spray application performed better than brush application and had nicer appearance with better film formation [36]. Paraloid^{TM} B44 is a methyl methacrylate (MMA) copolymer with minor copolymer units of ethyl acrylate and butyl methyl acrylate [36–38]. INCRA and BNFMRA developed formulations that contained 30 wt% B-44 in toluene and butyl acetate (or ethyl alcohol), benzotriazole (BTA) as a corrosion inhibitor and either silicone fluid or epoxidized soybeam oil (ESBO) as a leveling agent [36,38].

There have been several studies published over the years demonstrating the performance of Incralac$^{®}$ in conservation. The performance can vary depending on the chemical patinas [39] and the coating formulation. In addition, the performed studies are very specific and covered a broad range of methodologies and surface

treatment. In a recent review [36], Wolfe and Grayburn summarised the main studies carried out in the last decades and it was highlighted that there have been studies that present the performance of Incralac® as fairly good, as well as showing that it has poor performance. In addition, one of the crucial issue of the use of Incralac® is linked to the toxicity and the health risks. Many components of the formulation, such as the BTA that is suspected of carcinogenicity [40], the leveling agent added, either Paraplex G-60 (epoxidized soybean oil) or silicone oil and some of the solvents (toluene), show considerable level of eco-toxicity. For this reason some studies explored different solvents that lead to less toxic formulations in order to reduce health risks. In particular, a comparative study about different Incralac® formulation (solvent- and water-based) applied on naturally aged brass coupons showed that a lab-made low-toxicity Incralac® using 1-methoxy-2propanol can provide similar protection as the commercial product. However, the water-based Incralac® showed worse performance [38]. Finally, some studies also investigated the susceptibility of Incralac® to biodeterioration [41,42], suggesting that the solvent trapped in the resin could be a source of carbon energy for microorganisms.

2.3.2. Waxes

Microcrystalline waxes are currently applied on outdoor monuments in order to coat and smooth the patinated surfaces. The most common commercial waxes are Cosmoloid 80H™ and Renaissance™. Compared to acrylic coatings, waxes are considered a better solution for the protection of outdoor bronzes. Due to their hydrophobic nature, low vapour permeability and transparency waxes could be considered valid candidate for the treatment of heritage metals. However, several studies have demonstrated that their use should be carefully evaluated. Reversibility issues can be experienced and the application of wax coatings for archaeological objects has been discouraged [43]. Furthermore, waxes used on outdoor monuments have a short lifetime, poor barrier properties, and susceptibility to photodegradation, as well as a high volatile organic compound (VOC) content and removal difficulties [44,45]. Another study gave recommendations to conservator-restorers as the reapplication of waxes at an interval of less than 9 months and application of thick films, 100-200 μm ideally or as thick as possible [46]. Also, aged wax films contained oxidation products that could enhance the corrosion of the underlying metal since they are polar and more acidic than fresh waxes. In addition, microcrystalline waxes are also often used as topcoat for underlying acrylic layer. The multilayer Incralac® + wax system has proven to be a better coating system compared to the wax alone because of the synergy between a corrosion inhibitor used as primer, usually BTA, a central acrylic layer, mainly Incralac®, and a microcrystalline wax as top coat.

2.3.3. Silanes

As regards protective treatments, organosilane coatings attracted a significant research attention in recent years, due to their protective efficiency towards the corrosion of several alloys in outdoor conditions. Research studies on the protection of Cu and Cu-based alloys were mainly carried out on octadecyl-

trimethoxy-silane [47], glycidoxy-propyl-trimethoxy-silane [48] and γ-aminopropyltriethoxysilane (γ-APS) [49]. However, outstanding results were obtained with silanes containing sulphur or mercapto- groups, such as 3-mercapto-propyl-trimethoxy-silane (PropS-SH) [49–57].

PropS-SH coating preparation involves a step of silane hydrolysis in hydroalcoholic solution that determines the formation of silanol (Si-O-H) groups, then the hydrolysed solution is on the metal surface to be protected where silane chemisorption occurs. In particular, strong adhesion on the substrate is ensured by formation of metal siloxane (Me-O-Si) [58] and, on Cu and Cu-based alloys, also metal thiolate (Me-S-C) bonds [51]. A coating curing treatment follows, to allow the condensation of silanol groups (Si-OH) in a polymeric dense siloxane (Si-O-Si) network with barrier properties against aggressive environments [58]. This curing process, often carried out at temperatures of 100 °C [49,51,59] or more [60], can be also effectively carried out at lower temperatures, *e.g.* at room temperature [35,55,56,61], more compatible with the protection of artworks. A simplified schematic of bonding mechanism (adsorption and curing) between silane molecules and metallic surface, proposed by Zhu et al. [62] is reported in Figure 2.13.
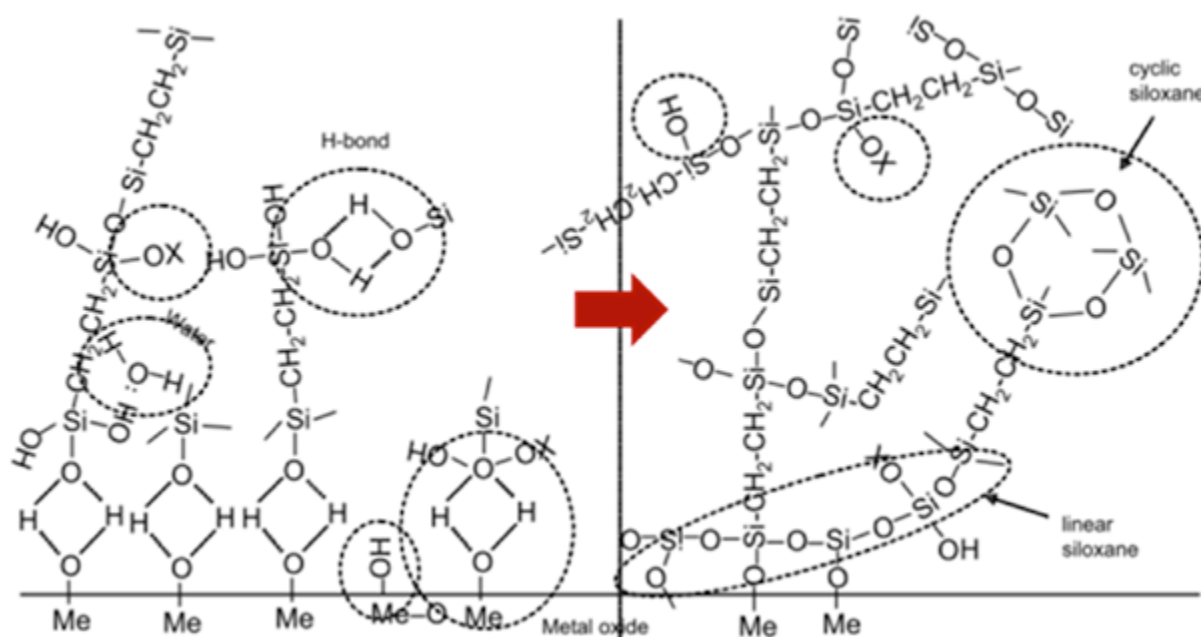

Figure 2.13: Silane adsorption and curing on a generic metallic substrate [62].

PropS-SH coatings effectively protect bare Cu and Cu-based alloys in NaCl solution [59,60,63,64] and in synthetic acid rain [56]. Their protectiveness is enhanced by the addition of nanoparticles [65]. PropS-SH was also applied on quaternary bronze, pre-patinated by exposure to acid rain under runoff conditions simulated in laboratory through the Dropping test [27, 28]. It also exhibits good performance against bronze corrosion during subsequent analogous Dropping exposures [57].

However, exposure of organic coatings to UV radiation can produce degradation of the polymer structure [66]. In particular, as concerns silanes, after UV-irradiation for 30 min in air, PropS-SH films applied on

silicon substrate undergo Si-C break and SiOH groups formation, while irradiated PropS-SH undergoes to −COOH formation [67]. So irreversible structural changes occur in the polymer chains, as under UV exposure they are subjected to photo-oxidation [68,69]. The photo-stability of silane coatings can be improved by the addition of nanoparticles. Accelerated weathering tests have shown that silane modification with TiO_2 nanoparticles permitted the preparation of transparent UV-protective coatings for polycarbonate substrates [70], as well as TiO_2 was found to be an effective UV absorber [56,71]. Other nanoparticles, such as CeO_2 and La_2O_3, were also added to silane coatings in order to improve its photo-stability performance and it was found that the measured improvement under UV exposure is connected to the capability of the selected nanoparticles to act as network formers and to prevent the film deterioration [56].

In addition, hybrid (organic-inorganic) polymer system formed by hydrolysis and condensation reactions of alkoxy compounds have been tested on bronze substrate as ORMOCER[TM] (ORganically Modified CERamic) [72,73]. This hybrid materials were synthesized from 3-glycidoxy-propyl-trimethoxy-silane or γ–methacryloxy-propyl-trimethoxy-silane and modified with a second or a third reactive silane. It was found that these ORMOCER[TM] lacquers well performed in outdoor conditions [72]. Finally, several silane coatings were developed in the frame of the EU-ARTECH project (6th EU-Framework Program 2004-2009) showing that some of the selected treatment showed comparable behaviours to the reference treatment (Incralac[®]) [74].

2.3.4. Fluoropolymers

Only few studies report the performance of fluoropolymers for the protection of Cu-based alloys in the conservation practice, despite fluoropolymer coatings usually show outstanding performance in outdoor applications, such as excellent exterior durability and chemical resistance, good flexibility, low dirty retention and good moisture and fungus resistance. One of the most used fluoropolymer is polyvinylidene fluoride (PVDF), which contains alternating carbon/fluorine bonds and carbon/hydrogen bonds. This structure provides chemical inertness that enables the formation of coating that resist environmental degradation. However, this feature hinders adhesion to metallic and patinated substrates. To solve this issue, an acrylic or silane-base resin is blended to the fluoride copolymer to improve coating adhesion. Iezzi et al. developed a new polymerization process in which the acrylic is mixed to the fluoropolymer during the polymerization procedures, producing a fluoropolymer-acrylic mixture on a micro-molecular scale. This new process improved the solvent-based dispersion properties [75]. Another study blended PVDF with the 40 wt% of Paraloid[TM] B44 (the acrylic base of Incralac[®]) in order to improve the adhesion of the coating, taking into account the removability properties of both PVDF and the acrylic resin [76]. It was found from electrochemical testing that this fluorocarbon-acrylic blend shows promising barrier properties indicating the potential to be a high resistance coating for the protection of outdoor Cu-based alloys.

2.3.5. Eco-friendly coatings

Recently, research gives emphasis to the development of eco-friendly and sustainable approaches for the preservation of Cultural Heritage. For this reason few specific studies proposed innovative treatments for the conservation of outdoor bronze. However, the lack of systematic investigations about the performance of these new coatings makes difficult the evaluation of the goodness of them in the real conservation practice. Albini et al. [77,78] investigated the performance of an innovative biological treatment based on a specific fungal strain of *Beauveria bassiana* as an alternative treatment for the stabilisation of Cu-based alloys. The protective mechanism is based on the capability of Cu-resistant fungi to transform soluble Cu corrosion products into more stable Cu oxalates, which, due to their inorganic nature, are compatible with the original patina. In addition, this treatment showed interesting properties for environmental and health issue, as the selected treatment is already used in organic agriculture. It was found that the interaction between Sn-enriched bronze surfaces (unsheltered areas) and the studied treatment was efficient and produced Sn- and Cu-based oxalates. The presence of these compounds were found also after severe runoff conditions indicating good adhesion of the treatment [77]. Finally, the authors suggested an improvement of the layers that are quite porous in order to improve the efficiency of the treatment for which a higher Cu release than the reference samples was detected.

Another study developed new renewable and bio-compatible polymers from lactic acid, a natural resource produced from the sugar fermentation [79]. In addition, they performed the reaction without solvents following a green chemical approach and benzotriazole (BTA) group was added in order to improve the corrosion inhibition. They observed promising results as protective coatings but further studies needed to be carried out to better understand the efficiency of anticorrosive coating.

Finally, preliminary studies promotes the application of different inorganic coatings such as Ca oxalates [80] and Diamon-Like Carbon (DLC) by plasma-enhanced chemical vapour deposition (PECVD) [81], as promising alternatives for the conservation practice of outdoor and archaeological Cu-based artefacts.

2.3.6. Corrosion inhibitors

Inhibitors are chemical substances that when present in the corrosion system at a suitable concentration, decreases the corrosion rate, without significantly changing the concentration of any corrosive agent [4]. In general, corrosion inhibitors are efficiently in small concentrations and their efficiency is enhanced by increasing inhibitor concentrations. Combinations of different inhibitors are commonly used in commercial formulations for industrial applications to improve corrosion resistance and reduce concentrations that would be necessary in the case of single additions. Inhibitors act by several mechanisms and the main ones are reported, as follows:

–   anodic mechanism of inhibition;

–   cathodic mechanism of inhibition;

–   mixed mechanism of inhibition.

In conservation practice no inhibitors have been specifically developed, but they are borrowed from industrial contexts, where they have been tailored for use in specific, operational environments on particular alloys. So, inhibitors are used purposely and sometimes empirically in conservation practice, mainly in combination with coatings particularly for outdoor objects [2]. As in combination with protective coatings inhibitors are required to be effective in the presence of corrosion products, this represents issues due to the fact that soluble corrosion agents (*e.g.* chlorides) normally interfere with their action. In addition, low toxicity of inhibitors is also a requirement, as the objects are for the public domain and have to be handled by restorers and operators.

Benzotriazole (BTA)

Benzotriazole is the most successful commercial corrosion inhibitors used in conservation practice. Several studies were carried out in particular on its performance for the protection of Cu-based alloys [76,82–86]. It is mainly used for the stabilization of Cu-based artefacts, especially for the treatment of chloride corrosion. There is some discussion about the mechanism of BTA if a real inhibition occurs or if the Cu-BTA film acts only as barrier layer. BTA is a mixed-type inhibitor as it was found to retard metal oxidation as well as the cathodic process. BTA is often embedded into coatings, as for example in Incralac® as an anti-corrosion additive and for its UV absorption properties [76,87]. However, BTA shows some toxicity issues and is suspected of carcinogenicity and for this reason innovative solutions are demanded. A solution proposed by Casaletto et al. consists of encapsulating BTA in nano-carriers of halloysite. Halloysite is a natural cylindrical clay, thus naturally available, biocompatible, low-cost and environmental friendly. In addition, it can be easily processed with many polymeric materials. Promising results were highlighted in term of protection efficiency in terms of surface coverage, as well as selective release of BTA during the corrosion process. However, only preliminary tests on bare bronze were performed and the interaction of this protective system with patinas has to be investigated [88]. Other authors proposed the application of another kind of azole, imidazole, having a similar molecular structure, but generally less toxic [89]. In this study moderate protective efficiency was recorded and for this reason further investigation was necessary.

2.4. Assessment of protective coatings

The lack of standardized procedures for testing coating effectiveness on Cultural Heritage metals hinders the assessment of innovative products through the published literature for comparatively identifying the most suitable coating for specific use. In particular, qualitative and quantitative assessment of coating performance for conservation applications usually employ specific experimental methods, such as electrochemical tests, natural and artificial ageing and eco-toxicity investigations applying the most advanced tools and an increased

collaboration within corrosion scientists. Laboratory testing is useful for establishing which coatings are unsuitable for use and for comparative performance testing in specified conditions. For this reason, laboratory studies, instrumental analysis and electrochemistry can establish intrinsic performance characteristics of coatings according to a set of fixed variables. However, they cannot offer quantitative assessment of real-time *in situ* performance within outdoor environments.

Electrochemical techniques have a long tradition in testing protective treatments, as reported in many studies from the published literature. Different electrochemical tests, such as potentiodynamic polarization curves measuring corrosion current density (i_{cor}) and polarization resistance (R_p) were performed in different aggressive solutions, such as sodium chloride solution, simulated concentrated acid rain, as reported in [85,90–93]. In addition, electrochemical impedance spectroscopy (EIS) has only been used recently and it is suitable for testing coatings suitable for conservation practice. It can be used in specially prepared coupons or *in situ* on the artefacts to evaluate the protective performance of the coatings or the natural or the artificial patinas [94,95]. The electrochemical approach well represented the comparative protective performance of different coatings and corrosion inhibitors; however it did not simulate accurately the exposure geometries and conditions as in the real monuments. For this reason artificial ageing tests are necessary to better simulate the exposure condition, in terms of exposure geometry and aggressive environment.

2.4.1. Artificial ageing

Only few studies investigate the coating performance when applied on patinated bronze substrates [57,65,72] or consider the coating resistance to environmental stresses, such as UV radiation, temperature or wet/dry cycles [56,57,65,76,77,79,96].

Compared to natural ageing that allows the assessment of the protected surfaces by long-term exposure [74], artificial ageing allows the assessment of the different protective treatments monitoring the different environmental parameters and their influences by accelerated exposures [54,57,77]. Organosilane coatings were assessed under simulated acid rain conditions considering the different exposure geometries of unsheltered and sheltered conditions to the rainfall [54,57,77]. In particular, the performance of a silane coating (3-mercapto-propyl-trimethoxy-silane, PropS-SH) was evaluated on bronze pre-patinated through Wet&Dry (stagnant) and Dropping tests (runoff), in order to simulate actual application conditions in the field of conservation. The comparison of the corrosion behaviour between uncoated and coated pre-patinated bronze in stagnant and runoff conditions shows that PropS-SH is effective in protecting bronze from corrosion, because it reduces both the specimen weight loss and the metal release. It also limits the formation of corrosion products and the colour alteration of the exposed surfaces [57]. A recent study aimed to evaluate the feasibility of a biological treatment on unsheltered areas and it was demonstrated that this treatment (*Beauveria bassiana*) is efficient on tin-enriched surfaces producing tin and copper oxalates. Moreover, their

presence was observed even after severe runoff condition indicating a good adhesion, showing promising protective performance [77].

As organic coatings suffer degradation processes induced by UV radiation, such as oxidation of double bonds, polymer segment scission and cross-linking, while high temperature can induce thermal degradation and hydrolysis [66]. The effect of different nano-particles addition, such as CeO_2, La_2O_3 and TiO_2, in organosilane coatings was investigated by the exposure under UV radiation and to temperature cycles under humid conditions and their performance was compared to naturally weathered samples exposed in the coastal town of Rimini (Italy) [56]. It was found that on plane silane coatings micro-scale cracking and spalling phenomena occur during natural exposure, partly limiting their protective efficiency, while the addition of nano-particles slightly reduced the tendency to degradation, especially in the case of TiO_2. In addition, exposure to temperature/UV cycles showed that while thermal cycles in humid atmosphere stimulate silane reticulation, UV radiation is responsible of the degradation process of the silane net and the impairment of the coating performances. These tests indicate that the improvement of the PropS-SH coating stability under UV exposure afforded by dispersed oxide particles is mainly connected to their capability to act as network formers.

In another study, some new renewable and biocompatible polymers obtained from lactic acid were applied on bronze coupons and their performance was evaluated after photochemical ageing in Solar box and accelerated thermo-hygrometric ageing in a climatic chamber. It was shown that due to the fact that end-capped poly-lactic acid coatings exhibited high stability after thermo-hygrometric ageing and photochemical ageing, they are promising candidates for the protection of outdoor bronzes [79].

2.4.2. Eco-toxicity and occupational hazard

The comprehensive eco-toxicological testing is one of the main current requirements necessary for the development of new advanced formulations. The traditional approaches are based on the chemical determinations of hazardous compounds. Usually the concentration of a limited range of specific substances is generally measured in leachates obtained from real or simulated treatment conditions. These traditional analytical methodologies are typically very sensitive and designed to be selective for specific chemical species, but are often also expensive and time-consuming. In addition, they base also on the reductionist assumption that the overall toxicity of a complex formulation can be inferred as the simple sum of toxic effects due to their individual components. Still, this premise is essentially wrong in realistic scenarios and can lead to underestimate the biological effects of a product [97].

Conversely, bioassay methods are a valuable approach to understand the eco-toxicological behaviour of innovative products. Bioassays assess the effect of the release of a chemical in the environment by exposing representative organisms, chosen as bioindicators, to a range of concentration of the substance. The Organisation for Economic Co-operation and Development (OECD) proposed guidelines for the testing of

Chemicals proposing several assays for aquatic organisms [98]. Bioindicators for aquatic risk assessment studies belong to different phila (microalgae, cyanobacteria, crustaceans, mollusks, plants and fishes) and have the advantage of being sensitive to a wide range of bio-available substances, and represent the entire trophic chain. If the assays are carried out using microorganisms, the drawback of time consumption is overcome because microbiotests are cheap, use small test volume and are available as kit; that is an advantage for toxicity screening and assessment [99]. Due to the application of control conditions, the bioassays reported in the OECD guidelines are standardized, and allow obtaining comparable data and complete toxicity curves, which are useful to evaluate end-points such as mortality, growth or reproduction.

The most widely used microbiotest for toxicity assessment is based on the inhibition of the bioluminescence of *Vibrio fischeri* or *Photobacterium phosphoreum,* a luminescent marine bacterium whose light production is directly proportional to the metabolic status of the cell. The *Vibrio fischeri* test has the advantage of being sensitive to a wide range of chemicals compared to other bacterial assays, is rapid, reproducible and shows good correlations with other standard acute toxicity test [100]. However, Farré et al. [101] mentioned that the test presents also some disadvantages because *Vibrio fischeri* is a marine bacteria, and thus can be used only in saline solution, a medium which can enhance the insolubility of some organic compounds. In addition, the test works with a maximum tolerable level of methanol of 10%. Therefore, the use of *Daphnia* and *Ceriodaphnia* as species for toxicity testing is widely reported in aquatic risk assessment studies [101–110]. The tests are standardized and are carried out by exposing the organisms to toxic substances under controlled conditions. Results are usually expressed using the concentration EC_{50} defined as the 50 % equivalent concentration value. The use of *Daphnia* and *Ceriodaphnia* for toxicological assessment has many advantages: they are freshwater organisms representative of an intermediate level of the trophic chain, and this allows obtaining integrated information because the presence or absence of these crustaceans in an ecosystem (*i.e.* water bodies or soil) influence both primary producers and secondary consumers. Moreover, *Daphnia* and *Ceriodaphnia* are suitable for laboratory-scale tests because they are small, with a short reproductive cycle and are highly sensitive to a wide range of substances.

However, dedicated applications of bioassay methods to the specific task of outdoor bronze conservation are not available yet. Limited and often incomplete eco-toxicological data can be found in the literature regarding individual components of the formulations, still unrelated to the Cultural Heritage field.

Even if Incralac® is one of the most used commercial product for the protection of copper alloys, only few information about its eco-toxicity are available for some of its hazardous ingredients, particularly benzotriazole and the organic solvents (*e.g.* toluene), but the overall ecotoxicology of Incralac® has not been specifically assessed. Wu et al. [111] reported data on benzotriazole toxicity derived from tests on several plant species (alfalfa, poplar, pumpkin, corkscrew, horseradish) and all except horseradish died within 4 weeks after the *application* of the compound. Pillard et al. [112] compared the toxicity of benzotriazole, two methyl-benzotriazoles and a butyl-benzotriazole on three widely used test microorganisms (*Ceriodaphnia*

dubia, *Pimephales promelas* and *Vibrio fischeri*). *Vibrio fischeri* showed to be more sensitive than the other organisms to all the tested substances, while *C. dubia* was less sensitive than *P. promelas*, except to butyl-benzotriazole. The latter induced acute toxicity at a concentration of ≤ 3.3 mg/l to all organisms, thus being proved as the most toxic amongst the tested compounds. Kim et al. [40] selected nine widely used benzotriazole-based UV stabilizers and tested them on *Daphnia pulex*. No acute toxic effects were observed for all compounds within the applied dosage (< 10 mg/l), but the authors raised concerns about the potential bioaccumulation and hazardous chronic effects on the aquatic ecosystem. In addition, toluene is a well-known substance and ecological information about its interaction with fishes, aquatic invertebrates and algae are available. For example, an EC_{50} of 8 mg/l for test carried out on *Daphnia magna* in 24 hours has been reported in the Toluene Safety Data Sheet from Sigma-Aldrich. However, producers state that ecological injuries are not known or expected under normal use of this solvent.

Another test to evaluate the eco-toxicity level is the Occupational Exposure test and it is to determine the potential toxicity on restorers of released substances from the coatings during their application (in particular to Volatile Organic Compounds (VOCs)). These measurements were carried in accordance to UNI EN 689 (1997) "Workplace atmosphere. Guidance for the assessment of exposure by inhalation to chemical agents for comparison with limit values and measurement strategy" and to UNI EN 16017-1 (2002) "Indoor, ambient, workplace air. Sampling and analysis of volatile organic compounds by sorbent tube/thermal desorption/capillary gas chromatography. Pumped sampling".

At last, it must be highlighted that the scientific literature lacks of studies and data concerning the eco-toxicological behaviour of the inhibitors for the conservation of bronze, regardless the products are traditionally or newly developed.

Experimental

CHAPTER 3 GIVES AN OVERVIEW OF THE
DIFFERENT INVESTIGATED MATERIALS
AND THE DIFFERENT ANALYTICAL
TECHNIQUES USED THROUGHOUT THIS
WORK.

3. MATERIALS AND METHODS

This chapter reports details of the materials used in this study, as well as the description of ageing methods used for the preparation of the patinated samples as well as the investigation of the performance of the coated systems. The techniques used for the characterisation are also listed and brief details of the principles behind the technique are additionally included where considered appropriate. Finally, in order to propose a complete view of the characterisation methods used in B-IMPACT project to assess the performance of the different coatings, the procedures used for the electrochemical evaluation carried out by I-UniFE (Italy) and S-ZAG (Slovenia), as well as the evaluation of the toxicity in terms of exposure limit performed by I-ECAM (Italy) are also reported.

3.1. Bronze

Two different types of bronzes were used as the substrates for the application of artificial patinas. In particular, a quaternary Cu-Sn-Zn-Pb and a ternary Cu-Si-Mn bronze alloy were used in the whole study.

3.1.1. Cu-Sn-Zn-Pb

A quaternary cast Cu-Sn-Zn-Pb alloy was selected in accordance with the composition of last centuries bronzes commonly used for sculptures by artistic foundries and always used up nowadays [19,113]. The elemental composition of this bronze is: 6.9±0.6 Sn, 3.1±0.4 Zn, 2.0±0.9 Pb (wt%), also containing Al, P Mn and Si in traces (Cu to balance). The microstructure of this bronze is dendritic typical of cast bronzes, as showed in Figure 3.1a and b. The dendrites are several hundred microns in length, which corresponds to slow cooling rate, as usually observed on traditional bronzes obtained from sand casting. As shown in Figure 3.1a and b, the large network of dendrites includes shrinkage cavities, due to cooling step during casting procedure. Cast Cu-based alloys are sensitive to coring, inducing micro- but also macro-segregation of the alloying elements [114], as highlighted in Figure 3.1c, where the x-ray maps showed the microsegregation of Sn. Conversely, Zn, soluble in the Cu solid solution, has a distribution overlapping that of Cu. For Pb, this large variation has to be ascribed to Pb globules that are not miscible in the Cu matrix.
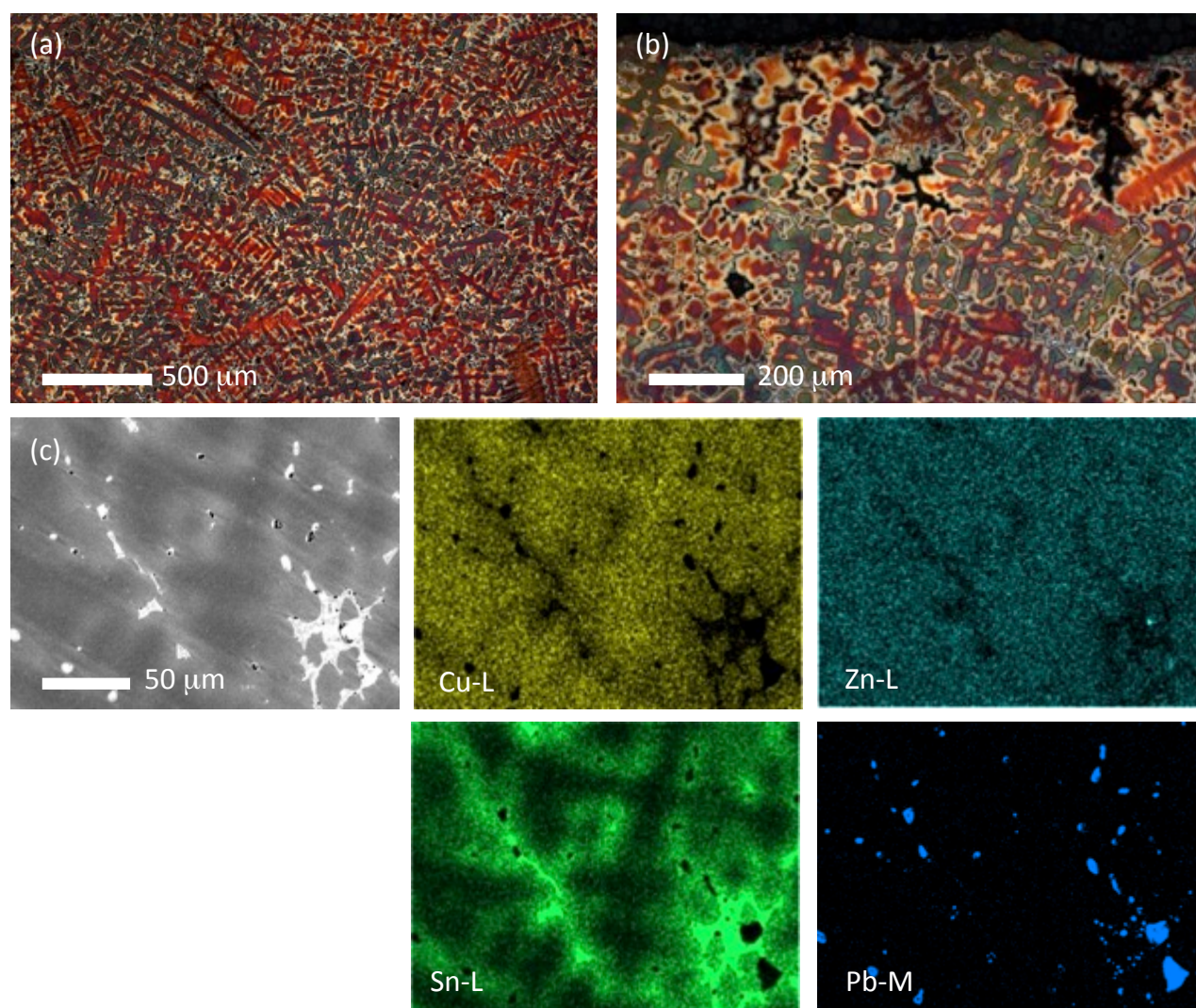
Figure 3.1: Optical examination of as-cast quaternary alloy (tint etchant Klemm III): (a) as-cast alloy with large dendritic structure (mm size); (b) cross-section with vertical preferential orientation of the dendrites linked to cooling temperature gradient within the thickness of bronze plate and (c) X-ray maps of the bulk of as-cast alloy (Cu, Zn, Sn and Pb).

3.1.2. Cu-Si-Mn

The as-cast bronze alloy is a silicon manganese bronze (Cu-Si-Mn), with 3.1 ± 0.4 Si and 0.9 ± 0.1 Mn (wt%) as major alloying elements, while Sn and Zn (< 0.1 wt%) and P (0.02 wt%) are the main trace elements. It corresponds to Cu cast alloy UNS C87300 international reference [115]. Due to its excellent corrosion resistance, good weldability, remarkable castability and golden colour, Cu-Si-Mn bronze is now widely applied by artistic foundries for bronze monuments [9]. As-cast plates of 5 mm thick were obtained by sand casting. Metallographic examination revealed a typical dendritic microstructure with Si and Mn coring and a few shrinkage cavities within the interdendritic spaces (Figure 3.2). Cu-Si-Mn plates were cut to obtain 50 × 25 mm coupons.
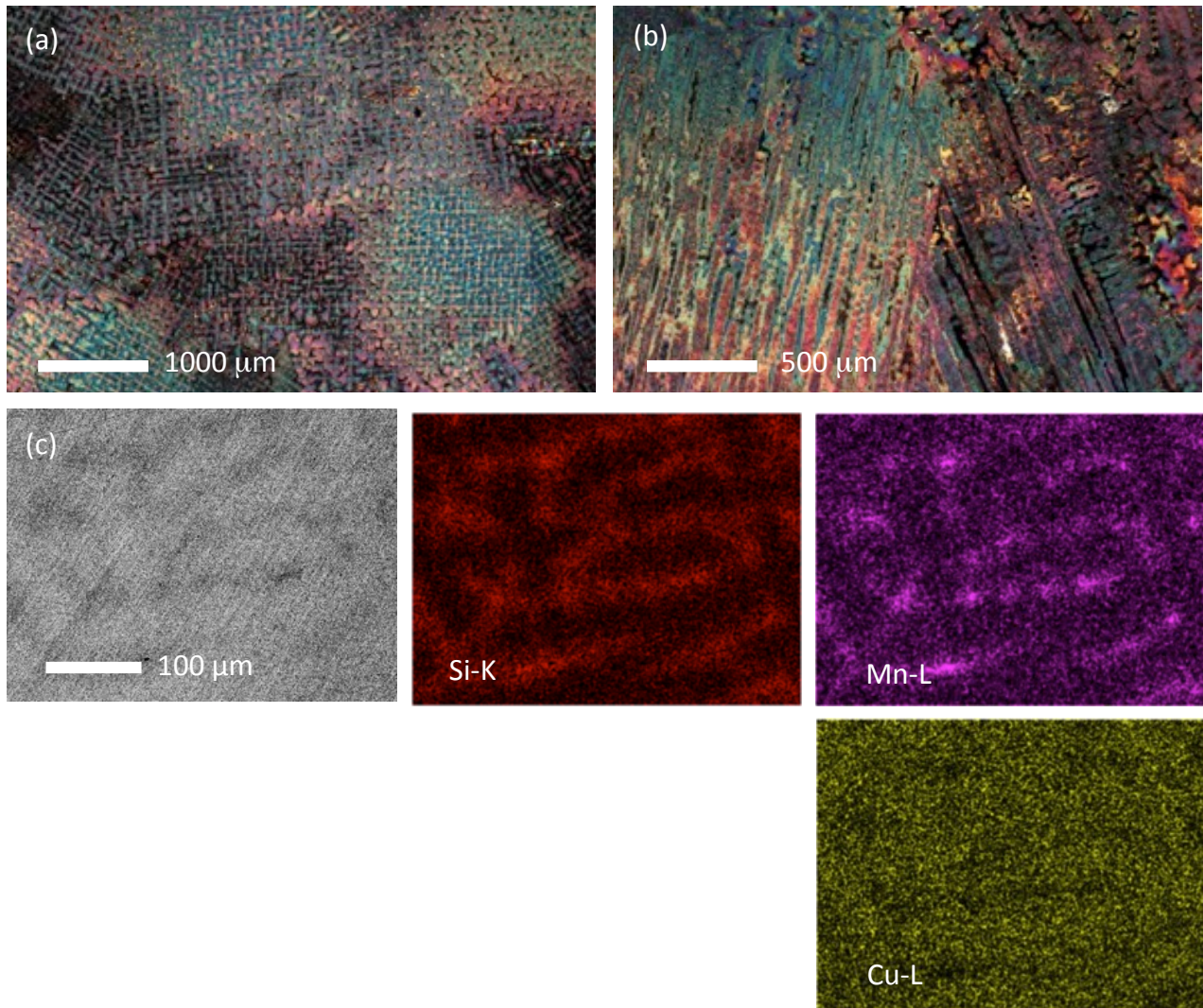
Figure 3.2: Optical examination of as-cast Cu-Si-Mn plate (tint etchant Klemm III): (a) top view of the surface revealing large dendrites; (b) cross-section showing the preferential crystalline orientation of the dendrites linked to cooling temperature gradient from the top to the plate centre; (c) X-ray maps of the Cu-Si-Mn surface (Si, Mn and Cu).

3.1.3. Artificial patination

Cu-Sn-Zn-Pb alloy was artificially patinated by two different ageing methods, Dropping [34] and Wet&Dry [35], simulating unsheltered and sheltered exposure of outdoor monuments, respectively. The ageing systems were detailed in paragraph 3.3 (Accelerated ageing methods).
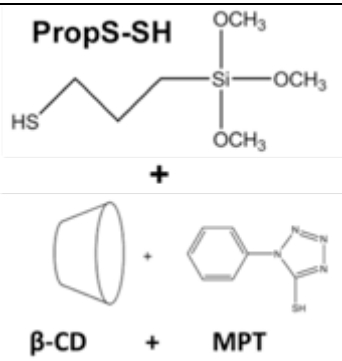
Traditional black patina was applied on the Cu-Si-Mn alloy coupons by the torch technique [116,117]. The patination process was performed by the Livartis Foundry d.o.o, Slovenia (www.livartis.si/en) according to the good practice typical of artistic foundries. Before patination, coupons were mechanically polished applying sandblasting directly on the as-cast surface. The bronze surface was then preheated with a torch up to 50-60°C. Then an aqueous solution of potassium sulphide (3.0 wt% K_2S) was applied with a brush until a black colour appeared. Heating and application cycles were repeated until the typical black colour was fully developed and then the metal was allowed to dry and was rinsed with tap water. The free surface of K_2S-

55
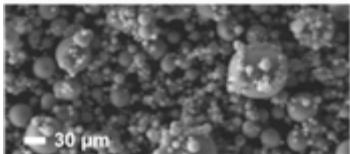
patinated Cu-Si-Mn was analysed by Glow Discharge-Optical Emission Spectroscopy (GD-OES) and the concentration profiles were measured after gentle rising with ethanol, so as to remove surface contamination. GD-OES analysis was carried out with a Grimm-style glow discharge lamp in DC mode, as detailed in [118]. With a relatively high current density of 50 to 500 mA/cm^2, the penetration rate in a Grimm-type GD is typically in the range of 1 to 10 μm/min. The result is a crater with a nearly flat bottom. Thus, by recording the optical emission signals as a function of sputtering time, an elemental depth profile is obtained. In addition, the spectrometer must be able to sample the emission spectrum at a rate of at least 100 times per s and a so-called multi-channel spectrometer is the most commonly used [119].

3.2. Coatings

Coatings were applied to patinated bronze substrates by spraying or brushing technique in order to simulate the realistic coating application during restoration procedures. The selected coatings were developed in two different laboratories. In particular, silane coatings were developed at the University of Ferrara (I-UniFE, Italy) under the responsibility of the investigators Dr. Andrea Balbo and Prof. Cecilia Monticelli. Fluoropolymer coatings were developed at the Slovenian National Building and Civil Engineering Institute (S-ZAG, Slovenia) under the responsibility of Luka Škrlep and Dr. Erika Švara Fabjan. The detailed presentation of coatings preparation applied in B-IMPACT project is reported in [120]. In the following paragraphs information about application procedures on the two patinated bronze substrates related to the selected coatings reported in Table 3.1 are detailed. In addition, Table 3.1 reports a schematization of the coating molecules as well as the application methods used for each type of coating.

Table 3.1: Type of coatings applied on the two different patinated substrates. Application methods are also specified for each coating type.

Substrates	*Coatings*	*Acronyms*	*Molecules*	*Application methods*
	Incralac®	Incralac®	Commercial reference	Spraying
Patinated Cu-Sn-Zn-Pb	3-mercapto-propyl-trimethoxy-silane with β-cyclodextrin with mercapto-phenyl-tetrazole	PropS-SH+ β-CD+MPT		Spraying

3-mercapto-propyl-trimethoxy-silane with fly ash	PropS-SH+FA	**PropS-SH** Fly ash (FA): amorphous alumino-silicates 30 µm	Spraying
FluoroAcrylate-Methacryloxy-propyl-trimethoxy-silane	FA-MS	**FA** **MS**	Brushing
Patinated Cu-Si-Mn	Incralac®	Incralac®	Commercial reference	Spraying
	3-mercapto-propyl-trimethoxy-silane	PropS-SH	**PropS-SH**	Spraying

3.2.1. Commercial reference: Incralac®

Incralac® was purchased from Bresciani s.r.l. (www.brescianisrl.it) and was applied on both the patinated substrates. It was considered as a commercial reference, due to the fact that it is one of the most used protective coatings currently applied in restorations practices. It was used as a 3 % solution in ethyl acetate solvent and applied by spraying. This application method produces a final specific weight of 5.6 g m^{-2} on average.

3.2.2. Organosilane coatings

3-mercapto-propyl-trimethoxy-silane (PropS-SH, purity 95%, Aldrich) was dissolved in a hydroalcoholic solution (90/5/5 v/v ethanol/water/PropS-SH), acidified to pH 4 by addition of some drops of diluted sulphuric acid solution. After 24 hours hydrolysis at room temperature, the solution was used for coating preparation.

In order to improve the performances of PropS-SH, different additives were added in the coating solution prior to application. In particular fly ash (FA) was used as microparticles in a concentration of 250 ppm. Fly ashes, a waste product of thermal power plants, are amorphous aluminosilicates. The composition of the main oxides of the fly ash used for this study is the following: SiO_2 51.8 wt%, Al_2O_3 27.8 wt%, Fe_2O_3 6.2 wt%,

CaO 4.6 wt%, SO$_3$ 0.7 wt%, K$_2$O 2.5 wt%, Na$_2$O 0.6 wt%, TiO$_2$ 1.4 wt% and MnO 0.06 wt%. The microstructure of fly ash is characterised by spherical particles with a particle dimension lower than 30 μm. In addition, a corrosion inhibitor complex made of β-cyclodextrin with mercapto-phenyl-tetrazole (β-CD+MPT) was also added to plain PropS-SH in a range of concentration between 0.5 and 1 mM.

So plain PropS-SH coating was applied on K$_2$S-patinated Cu-Si-Mn, while PropS-SH with fly ash (FA) as additives, as well as β-cyclodextrin with mercapto-phenyl-tetrazole (β-CD+MPT) added to PropS-SH were applied on patinated Cu-Sn-Zn-Pb. In order to be more consistent with the practices adopted by restorers, spraying was used as application method for all the silane coatings, which permitted to produce coatings with a constant specific weight of 6±1 g m^{-2} (similar to that achieved for Incralac$^{®}$). All coatings were cured at 50°C for 24 hours, before exposure to the aggressive environments.

Finally, in order to investigate the interaction between PropS-SH and bronze substrate as well as the role of the alloying elements (the results are discussed in paragraph 4.2), PropS-SH was applied on pure copper (Cu) and tin (Sn) metals (purity higher than 99.99 wt%), as well as a binary bronze alloy with 8 wt% Sn (Cu8Sn) and the quinary bronze (Cu-Sn-Zn-Pb-Sb) in both bare and patinated conditions. The composition of quinary bronze is: 91.9 Cu, 2.4 Sn, 1.0 Pb, 2.9 Zn and 0.8 Sb (wt%). It has a typical dendritic as-cast microstructure with cored α-solid solution (*i.e.* local enrichment of Sn and Sb elements in the interdendritic spaces) also including non-miscible lead globules as detailed in [55,57]. Shrinkage due to cooling during the casting process was also observed, inducing the formation of micro-cavities.

Moreover, in order to investigate coating properties in the absence of interactions with bronze elements, also a non-metallic, ceramic substrate (zirconium nitride, ZrN) was prepared. In this case, before coating application, the surfaces of bare samples were prepared by emery papers, then polished by using diamond spray with decreasing particle size (down to 1 μm), washed with deionized water and degreased with acetone. Instead, the rough artificially patinated surface (quinary bronze) was silane coated without any surface preparation. In order to prepare thin coatings suitable for XPS analysis of coating/metal interfaces, bare samples of Cu, Sn, Cu8Sn and quinary bronze were immersed ("dip-coated") for short times (150 s) in hydrolysed silane solution (90/5/5 v/v ethanol/water/PropS-SH) at pH= 4, followed by fast withdrawal (Table 3.2).

Table 3.2: Samples on which XPS measurements were carried out: summary of sample acronyms and coating application conditions [121].

Sample name	Substrate	Coating	Application mode
ZrN	Zirconium nitride	PropS-SH (thick layer)	Dip-coating (1h immersion in silane sol.)
Cu	Pure copper	PropS-SH	Dip-coating (fast immersion in silane sol.)
Sn	Pure tin	PropS-SH	Dip-coating (fast immersion in silane sol.)
Cu8Sn	Binary bronze (8wt% Sn)	PropS-SH	Dip-coating (fast immersion in silane sol.)
Q	Quinary bronze	PropS-SH	Dip-coating (fast immersion in silane sol.)
Q_PAT	Patinated quinary bronze	PropS-SH	Dip-coating (1h immersion in silane sol.)

Then, the samples were washed by ethanol to eliminate physisorbed silane molecules. The obtained coatings were few nanometers thick as evaluated by weight gain measurements, assuming a density value of 1.1 g.cm^{-3} for PropS-SH. By prolonging to 1 hour the immersion time in hydrolysed silane solution, thicker coatings on ZrN were prepared (Table 3.2). 1 h dip-coating is often adopted for PropS-SH to protect efficiently bronzes from corrosion [54–57]. Therefore on patinated quinary bronze, these thicker coatings were also applied to analyse their cross-sections stratigraphy and for surface XPS and HR-SRPES investigations. All the coated samples were cured at room temperature for at least 10 days before analyses.

3.2.3. Fluoropolymer coatings

A copolymer of fluoroacrylate (FA) blended with methacryloxy-propyl-trimethoxy-silane (MS), used to improve the adhesion of the coating, was applied on patinated Cu-Sn-Zn-Pb substrate by brushing. FA copolymer was prepared from Remmers Funcosil AG available on the market that was dried and then dissolved in N-butyl acetate to obtain a solution of 10 wt% FA. MS was synthesised in acetone to obtain a solution of 20 wt% MS in diethyl succinate. The final FA-MS solution was prepared mixing 5 wt% of FA and 10 wt% of MS in solvent mixture solution (50 wt% n-butyl acetate and 50 wt% diethyl succinate).

3.3. Accelerated ageing methods

Accelerated ageing was applied on different substrates during the whole study. In particular, in order to prepare representative bronze surfaces for coating application, both Dropping and Wet&Dry ageing tests were used, simulating unsheltered and sheltered areas typical of outdoor exposure, respectively. Only for this step, Dropping device was implemented in order to simultaneously age several samples in the same experimental conditions. Secondly, the coated samples were aged by Dropping to assess the protectiveness of the applied coatings. Table 3.3 reports detail information about the ageing methods applied on the different samples.

Table 3.3: Purpose of the application of the different ageing device on the different samples. Amount and dimensions of the aged samples are also reported.

Purpose	Ageing methods	Number of samples	Samples dimension
Patination of Cu-Sn-Zn-Pb bronze	Scaled-up Dropping	52	50x25 mm
	Wet&Dry	6	50x50 mm
Ageing of coated samples			
On patinated Cu-Sn-Zn-Pb:		At least 2 samples	
– Uncoated samples	Dropping	for each uncoated	25x25 mm
– Incralac®		substrate/coating	
– PropS-SH+β-CD+MPT			
– PropS-SH+FA			
– FA-MS			

On K$_2$S-patinated Cu-Si-Mn:

– Uncoated samples
– Incralac$^{®}$
– PropS-SH

3.3.1. Artificial acid rain solution

The acid rain solution (AR) was prepared according to natural acid rain collected in winter months in a monitoring atmospheric station in Bologna. The chemical composition of the artificial rain used in the ageing process is SO_4^{2-} 1.90 mg L^{-1}, Cl$^-$ 1.27 mg L^{-1}, NO_3^- 4.62 mg L^{-1}, CH_3COO^- 0.23 mg L^{-1}, $HCOO^-$ 0.05 mg L^{-1}, NH_4^+ 1.05mg L^{-1}, Ca^{2+} 0.34 mg L^{-1}, Na^+ 0.53 mg L^{-1} and the measured pH is 4.35 [61]. The same synthetic rain solution was used during all the ageing for the whole study.

3.3.2. Dropping and Wet&Dry test for artificial ageing

The Dropping test, reported in Figure 3.3 simulating exposure to runoff conditions was used to age the different coated samples in order to assess the protectiveness of the applied coatings [26,34,57,61]. In order to expose only the coated surface of all the samples, epoxy resin was used for protecting the other faces of the samples. The cycles consisted of periods when the artificial acid rain solution is dropped onto the samples and periods when the samples are allowed to dry. In particular, two weekly cycles of 3 days of Dropping / 1 days of dry and 2 days of Dropping / 1 day of wet were performed up to a total Time of Wetness (ToW) of 10 days for each sample.
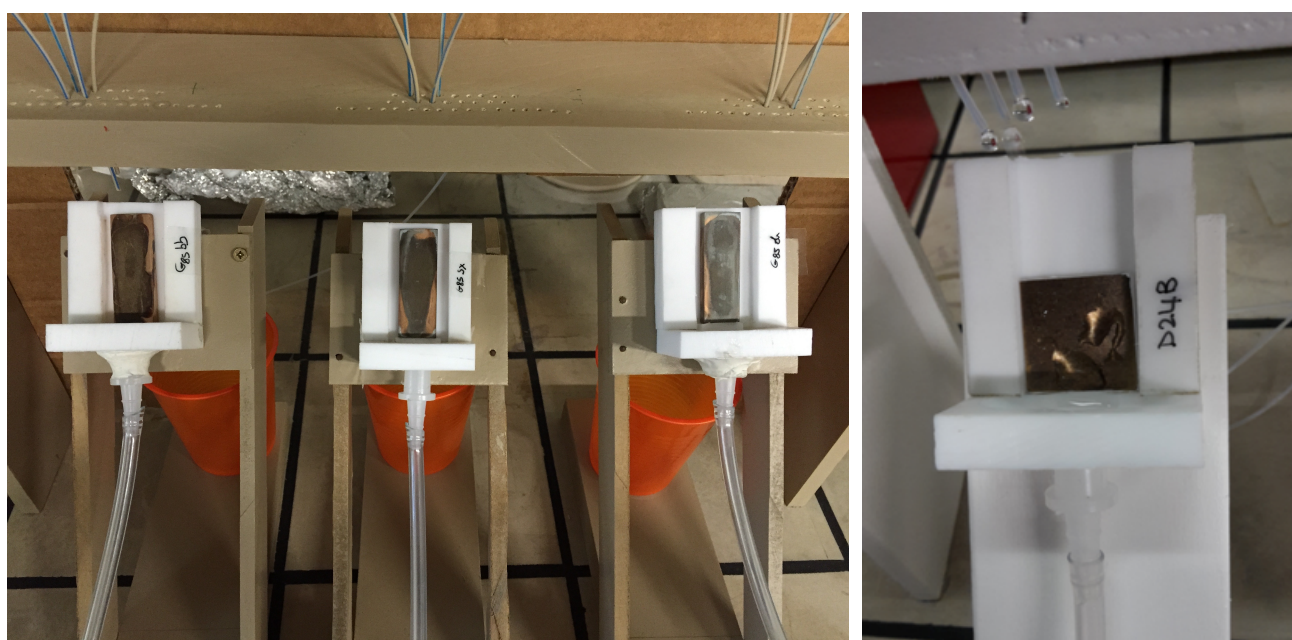
Figure 3.3: Dropping device with a detailed view (on the right) during the Dropping of synthetic acid rain on a sample.

Within the installation designed for the ageing test six samples were placed at a 45° angle on plastic supports. A peristaltic pump dropped artificial acid rain solution on the samples by means of capillary tubes with an almost constant dropped volume of 60 ml/h on each sample. Mass measurements were carried out using a digital balance KERN AGB210_4 with repeatability of ± 0.1 mg. The mass variation was calculated by the difference between the initial weight of the sample and the weight of the corroded samples at different ageing times during weathering.

The Wet&Dry test (Figure 3.4), simulating exposure to stagnant conditions, was used both to patinated Cu-Sn-Zn-Pb. The test was organised in alternate immersion cycles: one hour-cycles composed of wetness period of 20 min and dry period of 40 min were performed, as detailed in [35,122,123]. Considering 20 min for the sample to get dry, Time of Wetness (TOW) of 40 min is assumed to correspond to an hourly cycle and so in this experiment the total TOW for Wet&Dry test was of 87 days. In addition, pH of the synthetic solutions was periodically measured. The weathering solution, 350 mL per cell (pH of 4.35), was renewed twice a week when the pH becomes neutral.
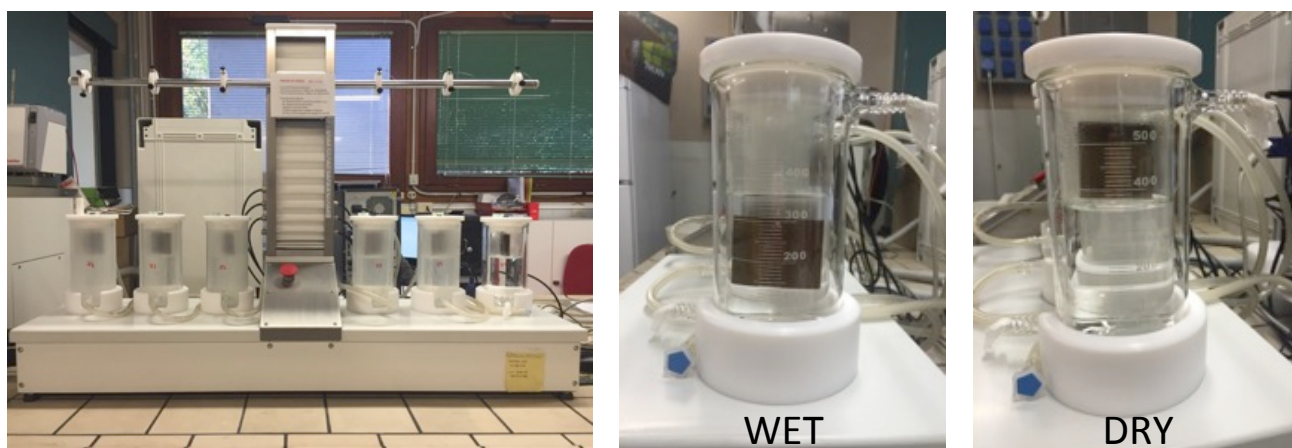
Figure 3.4: Wet&Dry device with a detailed view (on the right) of a cell during wet and dry cycle.

3.3.3. Implementation of Dropping device for patination

For patination of Cu-Sn-Zn-Pb, the Dropping test was specifically adapted to produce a large set of corroded samples. This test device has been improved from the one previously used, described in paragraph 3.3.2 (Dropping and Wet&Dry for artificial ageing): similarly to the set up used in [61] the largest aged areas have been provided by splitting the rain flux Dropping on each sample into four drops and a higher number of samples could be obtained at the same time. However, at this stage this implemented system is not suitable for the assessment of the protectiveness of coatings, as it is not possible to collect the ageing solutions of each sample due to the fact that one drain system was designed for the entire Dropping device. Figure 3.5 shows a schematic of the unit in which two water pumps for each line distributed the weathering solution on the bronze coupons. So, two Dropping units were applied and 52 bronze samples were aged in the same batch.

Artificial rain was guttered in four drops over the samples, inclined at 45°, with an average drop height of 3.5 cm and an average Dropping rate per sample of 270 cm^3/h; 12 h of Dropping was continuously alternated with 12 h of dry phase until a total ToW of 37 days was completed. Considering the annual average rain in Bologna (800 mm) and the size of the samples (50x25mm), the volume of solution used corresponds to about 300 years of rain in Bologna. In order to ensure a constant Dropping rate for each sample, a rotation of 180° for each sample during the Dropping test was made every day.
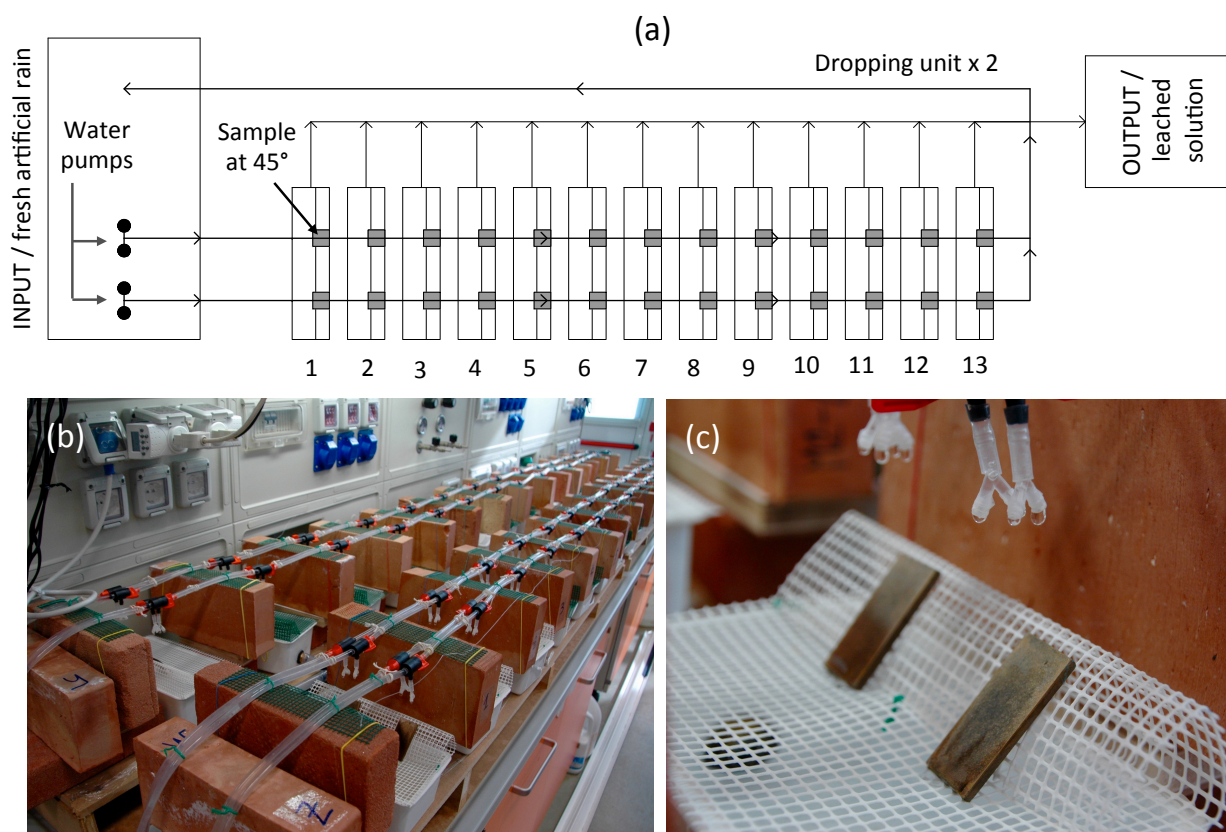
Figure 3.5: (a) Schematic mode of the implemented Dropping test device; (b) general view of the Dropping system and (c) detail showing the bronze samples placed at 45° during the ageing [124].

The implementation was carried out starting from an existing Dropping system used for the artificial ageing of marble in order to assess the resistance of inorganic protective coatings to simulated rain, as reported in [125]. Compared to this apparatus that consists in two lines of nozzles, other two lines were designed and each nozzle was split in order to have two drops for each nozzle. In addition an automatic drain system collecting the weathering solutions were added in order to facilitate the ageing procedures.

3.4. Inhibiting efficiency in terms of metal release in the ageing solutions

The runoff solution dropped on each sample was separately collected in canisters and volume and pH of the collected solutions were measured. An amount of each solution was stored in HDPE bottle in order to analyse the metallic ions release. These solutions were acidified with HNO$_3$ 65% suprapur, in order to prevent

62

absorption of metals on the interior of the bottles and dissolve any metal complexes present, and stored at 4 °C. The concentration of alloying elements (Cu, Zn and Pb for Cu-Sn-Zn-Pb bronze and Cu, Si and Mn for Cu-Si-Mn bronze) cations in the weathering solutions was analysed through Atomic Absorption Spectrometer (AAS) Perkin-Elmer AAnalyst 400, provided with Flame Atomization and Perkin-Elmer PinAAcle 900Z, provided with Transversely Heated and longitudinal Zeeman background correction, reaching a Limit of Detection equal to 0.3 µg/L for Cu, 1.0 µg/L for Zn, 0.6 µg/L for Pb and to 0.2 µg/L for Mn. Si concentration was measured by Microwave Plasma-Atomic Emission Spectrometer (MP-AES) Agilent 4210 with a Limit of Detection of 18 ppb. The protective efficiency of the tested coatings was quantified through the metal release in the ageing solutions. In particular, the Inhibiting Efficiency in terms of metal release (h_M) was calculated using Equation 3.1:

$$\eta_M = \left(\frac{M_{sol,NC} - M_{sol,C}}{M_{sol,NC}} \right) \times 100 \tag{3.1}$$

where M_{sol} is the amount of metal in the ageing solution (Cu, Mn or Si concentrations in µg cm^{-2}); NC is the uncoated sample and C is the coated sample as reported in [123].

3.5. Surface and cross-section characterisations of the aged samples

Several analytical techniques were adopted in order to characterise the patinated substrates, as well as the coated systems after ageing. A clear vision of which characterisation was carried out on which samples is reported in Table 3.4.

Table 3.4: Analytic techniques used for the characterisation of patinated samples, as well as coated systems after Dropping.

Samples	Colorimetry	SEM on surfaces	FIB cross-section	XRD	µ-Raman spectroscopy	XPS
Cu-Sn-Zn-Pb						
Patinated by Dropping	✓	✓	✓	✓	✓	✓
Patinated by Wet&Dry	-	✓	✓	✓	✓	✓
Coated samples						
Incralac®	✓	✓	-	-	-	✓
PropS-SH + β-CD+MPT	✓	✓	-	-	-	✓
PropS-SH + FA	✓	✓	-	-	-	✓
FA-MS	✓	✓	-	-	-	✓
Coated samples after Dropping						
Incralac®	✓	✓	✓	-	-	✓
PropS-SH + β-CD+MPT	✓	✓	✓	-	-	✓
PropS-SH + FA	✓	✓	✓	-	-	✓
FA-MS	✓	✓	✓	-	-	✓

Cu-Si-Mn						
Black patinated	✓	✓	✓	✓	✓	✓
Coated samples						
Incralac®	✓	✓	-	-	-	✓
PropS-SH	✓	✓	-	-	-	✓
Coated samples after Dropping						
Incralac®	✓	✓	✓	-	-	✓
PropS-SH	✓	✓	✓	-	-	✓

3.5.1. Colorimetry

Patinated uncoated and coated samples were characterized before and after Dropping by visual observation and by measurement of the colour coordinates in the CIELab colour space on the uncovered surface of the samples at three different areas. These measurements were carried out by using a Datacolor D400 spectrophotometer with a D65 illuminant, a 10° observer, a measure area of $\varnothing$ 6.6 mm and specular component excluded. In the CIELab space, each colour is defined by three coordinates: L*, corresponding to lightness, ranges from 0 (black) to 100 (white), a* and b* corresponding to the chromatic coordinates, have not specific numerical limits (+a* is red, -a* green, +b* yellow, -b* blue). Total colour change (ΔE^*) is calculated through Equation 3.2:

$$\Delta E^* = \sqrt{(\Delta L^*)^2 + (\Delta a^*)^2 + (\Delta b^*)^2}$$

(3.2)

For each sample, ΔE^* was calculated by averaging the ΔE^* of the three measured areas.

In general, ΔE^* values lower than 3 can be assumed as not appreciable and, in the field of Cultural Heritage ΔE^* in the range between 3 and 5 are considered acceptable, while $\Delta E^* > 5$ are considered clearly perceivable [126].

3.5.2. Scanning electron microscopy (SEM)

Surface observation was carried by Scanning electron Microscope using the apparatus FEI Helios NanoLab 600i prior to perform *in situ*-cross-sections.

Cross-sections of patinated bronze samples, as well as coated samples after Dropping, were investigated after applying the Focused Ion Beam (FIB) apparatus (FEI Helios NanoLab 600i). The FIB uses Ga$^+$ ions to remove material with a very high spatial precision. Ga$^+$ ions are emitted as a result of field ionization and post-ionization and then accelerated down the FIB column. The use of Ga$^+$ is advantageous as it has a low melting point, exists in the liquid state near room temperature and it can be focused to a very fine probe size

(< 10 nm). When a Ga^+ ion is accelerated to the target sample, it enters the sample and allows the ejection of sputtered particles (which may be an ion or a neutral atom). In addition, this sputtering process induces the implantation of Ga^+ ions into the sample [127]. In this way, cross-sections can be made at a specific location after surface observation and representative sampling area. For this operation, the sample is positioned in the SEM chamber, tilted at 52°, and a platinum (Pt) layer of 2-μm thickness is first laid down for surface protection, as reported in Figure 3.6. FIB milling is then applied to etch the sample.
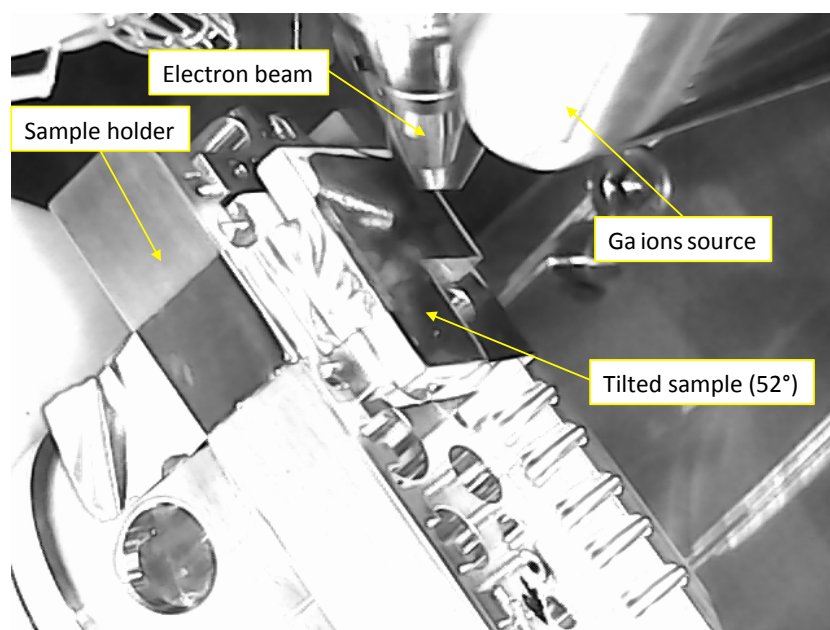
Figure 3.6: *Picture inside the microscope chamber showing the geometry during FIB milling.*

In particular, representative portions of each sample were selected in order to prepare FIB cross-section shown the main and most representative features. For example, corroded dendrites surrounded by a eutectoid were selected as typical areas of interest for the FIB cross-sections of patinated Cu-Sn-Zn-Pb bronze. The FEG-SEM imaging, X-ray maps and line-scans (Aztec Oxford system with SSD detector, WD 4mm) were performed using different applied energies of electrons (10 KeV) in order to detect all possible elements. Under these conditions, the X-ray emission depth for the O $K\alpha$ (0.53 keV), Cu $L\alpha_1$ (0.93 keV) and Zn L α_1 (1.01 keV) lines is roughly of the order of 100 nm, while it is at least twice as much for Sn L α_1 (3.44 keV). Thus, the X-ray intensity values of the X-ray maps and the line-scans obtained for these elements are related to different analysed volumes.

3.5.3. X-ray diffraction (XRD)

X-ray diffraction (XRD) makes use of coherent scattering of x-rays by atomic electron clouds and the constructive interference that occurs between x-rays scattered by regularly placed series of atoms [128]. One of the light-material interactions in the case of x-rays is the elastic scattering or Rayleigh diffusion. In that case, no energy is lost in the process and the wavelength (energy) of the scattered radiation remains

unchanged. Regular arrays of atoms in a crystal lattice interact elastically with radiation of sufficiently short wavelengths. Due to the order of the atoms, the interference of the scattered x-rays is constructive in some directions and destructive in others. These interactions yield a diffraction spectrum in which the peaks' angles and intensities are sensitive functions of the crystal structure. Bragg's law (Equation 3.3) states that the interferences are constructive if [129]:

$$n\lambda = 2d \sin \theta \qquad (3.3)$$

wher d is the distance between two layers of atoms, θ is the angle between the incident beam and the layer, n is the diffraction integer order and λ is the wave lengths, as defined in Figure 3.7.
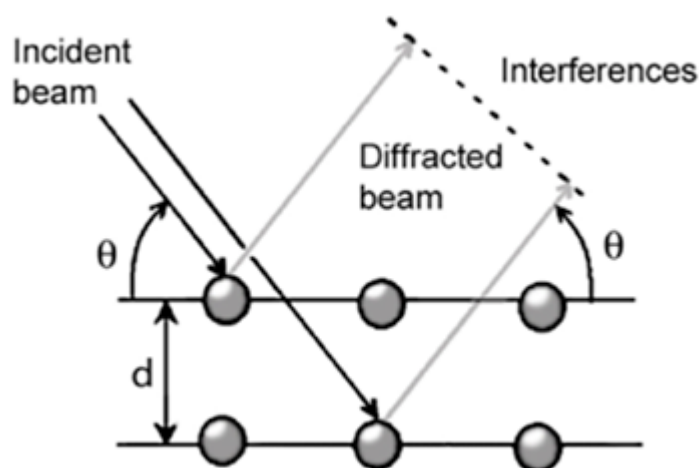
Figure 3.7: Bragg's setup for reflections from uniformly spaced layers [129].

X-ray Diffraction (XRD) was performed using a DRX D8 Advance (Bruker) apparatus (Cu-Kα, λ= 0.15418 nm) with a fast detector (LynxEye). The samples were analysed in grazing-incidence mode (GXRD) to better analyse the thin corrosion layer (incident angle fixed at 1°, pattern acquisition from 10° to 80°, 2θ, step of 0.03° and step time of 24 s) on a surface area of ~0.5 cm².

3.5.4. µ-Raman Spectroscopy

Raman spectroscopy is nowadays one of the most used non-invasive techniques in the field of Cultural Heritage to obtain the molecular and mineralogical composition of samples [130]. The working principle is based on the "Raman effect". In particular, the resonance Raman effect consists in the excitation of a molecule by using radiation characterized by a frequency belonging to one of its absorption bands. Fluorescence may also disclose vibrational states of a molecule in its electronic ground state. Molecules which are irradiated with light quanta whose energy is sufficiently high to allow transitions of valence electrons to excited states, may return to the ground state by emitting light quanta of lower energy. Such fluorescence

spectra may show sub-bands arising from a transition of the electronic excited state to different vibrational states of the electronic ground state [131].

μ-Raman spectroscopy was performed in order to determine the composition of the surface species at the micro-level, in addition to the X-ray diffraction performed on a larger surface scale. Measurements were carried out on the artificially aged Cu-Sn-Zn-Pb bronze surfaces with a Horiba Jobin Yvon LabRAM HR 800 apparatus (grading resolution of 600 lines/mm, excitation wavelength 532.0 nm (Ar diode), with an Olympus objective ×100 (NO 0.9) allowing a theoretical lateral resolution of 0.7 μm at a maximum depth of 2.61 μm). The alignment was calibrated for the first order of a pure Si crystal (520.7±1 cm^{-1}). The scan number and the accumulation time (usually 60 s) were adapted according to the intrinsic signal intensity (specifically here, 30 s × 3 acquisition, at an energy < 5 mW). The acquisition and treatments of the spectra were performed with LabSpec software.

3.5.5. Conventional X-ray photoelectron spectroscopy (XPS)

X-ray photoelectron spectroscopy (XPS) involves the irradiation of a sample with x-rays. The absorption of a high-energy x-ray photon causes the ionization of an electronic level. The use of an x-ray source, usually Al Kα or Mg Kα, permits the ejection of electrons from all electronics levels, especially core levels (within the energy range of the x-ray beam). The Al Kα and the Mg Kα radiations with energies hv = 1486.6 and 1253.6 eV have a line width of 1.0 and 0.8 eV, respectively. This line width restricts in many cases the spectral resolution. It can be improved by an x-ray monochromator to 0.5 eV or less with a strong loss of the intensity of the exciting beam. This loss can be compensated for modern spectrometers by the use of magnetic lenses and of more sensitive detectors [119].

The electron is ejected from its level by absorption of an x-ray photon to the vacuum with the kinetic energy $E_{kin,S}$ and $E_{kin,A}$ with respect to the sample and the analyzer. These different values are a direct consequence of the difference of the work functions $e\Phi_S$ and $e\Phi_A$ of the specimen and the analyzer, which causes a contact potential difference and thus two different vacuum levels. Equation 3.4 describes the energy balance for the photoelectrons, showing that with a known energy hv of the radiation source the measured kinetic energy $E_{kin,A}$ and the work function $e\Phi_A$, E_B may be calculated. Usually the constant work function of the analyzer is calibrated by measurements of well-characterized standards and then compensated internally:

$$hv = E_B + E_{kin,A} + e\Phi_A \qquad (3.4)$$

The energy spectrum of the ejected electrons is characteristic for the element involved in the process [119]. So, XPS is an essential method to study the chemical composition of surfaces by qualitative and quantitative analysis. Most materials are not affected by x-rays and they may be examined with no change of the

composition of their surfaces, as well as the conservation of the oxidation state of the specimen, if an appropriate sample preparation is performed. In addition, the chemical shift measured by XPS signal provides detailed information on the distribution of the chemical composition, including their oxidation state and the chemical binding of the species.

XPS analyses were carried out by using a monochromatised Al Kα (hν = 1486.7 eV) source on a ThermoScientific K-Alpha system. The X-ray spot size was about 400 μm. The pass energy was fixed at 130 eV with a step of 1 eV for surveys and 40 eV with a step of 0.1 eV for core levels. Ionic Ar^+ sputtering of the surfaces was applied using an Ar^+ ion beam acceleration of 200 eV and a low current for 30s, in order to clean the top surface of the examined specimen from pollutants and contaminations. The analysed core levels were calibrated against C 1s binding energy (conventionally BE=284.6±0.1 eV). XPS data were fitted by using Thermo Scientific™ Avantage Software and the background signal was removed by using Shirley method. Flood gun was also applied for avoiding charge effects.

3.5.6. Synchrotron radiation-High resolution Photoelectron Spectroscopy (SR-HRPES)

A synchrotron is a large electron-magnetic instrument used to increase the speed of elementary particles to high energy. In the case of SOLEIL Synchrotron these particles are electrons. Figure 3.8 reports a simplified schematic of a synchrotron to explain its working principle. First, the electrons are emitted from an electron gun in a 16 m LINear ACcelerator (the LINAC) to reach an energy level of 100 MeV. They are transmitted in a second (circular) accelerator, the booster. This brings the electrons to the functional energy of SOLEIL, 2.75 GeV.
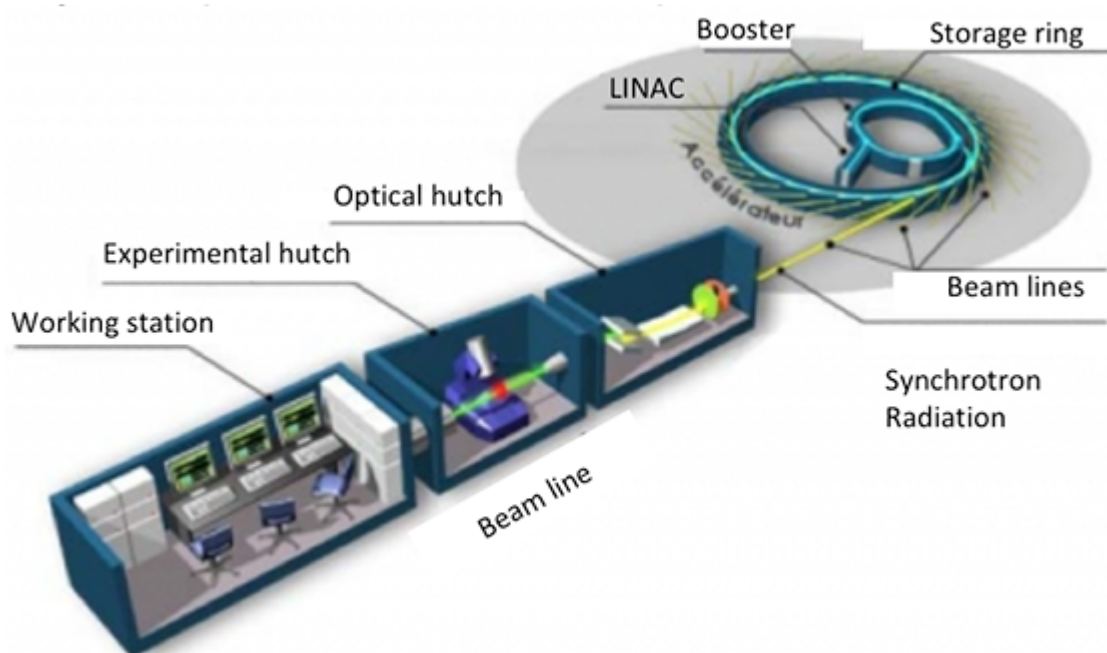
Figure 3.8: Scheme of the SOLEIL Synchrotron configuration with a beamline disposition [132].

From there, they are injected in the storage ring (diameter 113 m), where they turn for hours. Different elements exist on the ring: the dipoles (bending magnets), the undulators and the wigglers (succession of alternating magnets) are used to control the trajectory of the electrons or make them oscillate. When changes in this trajectory occur, the electrons lose energy in the form of light. This light is the synchrotron radiation. Other elements present on the ring are the radio-frequency cavities. They compensate the electron energy loss when emitting the synchrotron radiation. This radiation is selected and directed by optic systems (in the radio-protected area and the optical hutch) towards the experimental hutch. Completed by the working station, this is what is called a beamline. Laboratory facilities and sample preparation rooms support the beamlines [132].

Bare and patinated quinary bronze samples carrying PropS-SH coatings were also investigated by High Resolution Photoelectron Spectroscopy using Synchrotron Radiation (HR-SRPES) with excitation energy of 700 eV, as already detailed in [118]. A schematic representation of the basic components of Antares beamline is shown in Figure 3.9.
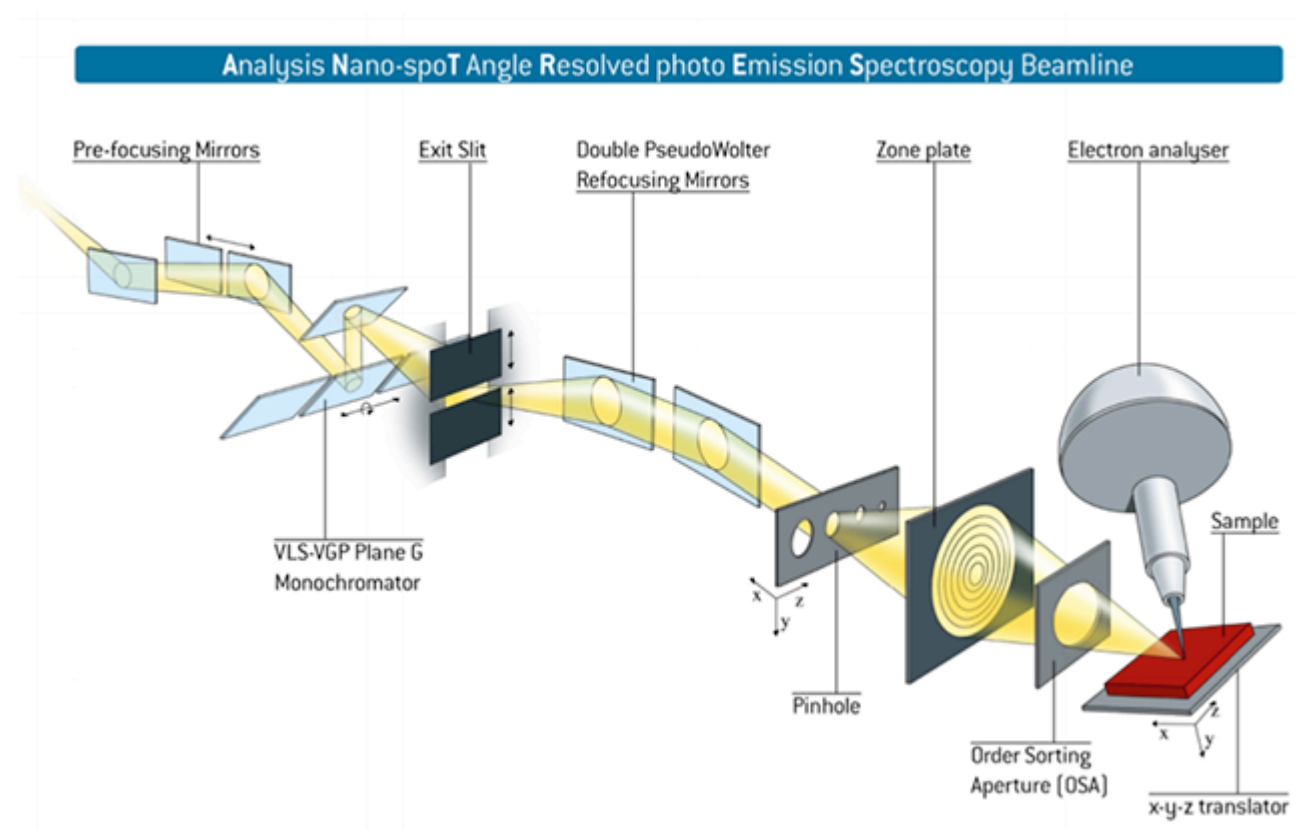
Figure 3.9: *Schematic representation of the basic components of the Antares beamline* [133].

The main difference of the ANTARES microscope from other conventional ARPES instruments is that the specimens can be mounted on a high-precision plate that ensures their nanoscale positioning in the x, y and z directions [118,133,134]. The pass energy was fixed at 100 eV with a step at 0.05 eV for core levels. Investigated core levels were limited to a few localised spots, due to the available synchrotron beamtime, which was mostly used for time-consuming high-resolution photoelectron spectroscopy (HR-SRPES) maps. A

surface cleaning using He ion bombardment was applied prior XPS measurements. Imaging of the free coated surface was carried out using the R4000 Scienta hemispherical analyser with a set of Fresnel Zone Plates (FZP), able to focalise the beam spot up to a few tenths of nanometres in spatial resolution [133,134].

HR-SRPES experiments were conducted in the ANTARES beamline at the SOLEIL synchrotron. HR-SRPES chemical imaging maps were recorded on the same surface areas where EDS maps were subsequently collected.

3.6. Other analytical techniques to assess coatings performance in the B-IMPACT project

3.6.1. Electrochemical evaluation

Electrochemical tests were performed by I-UniFE (Italy) and S-ZAG (Slovenia) in accordance to a shared procedure detailed in [135]. The electrochemical tests were performed in a tenfold concentrated synthetic acid rain solution (ARx10, pH 3.30), to achieve accelerated corrosion conditions. The electrochemical cell consisted in a poly-methyl-methacrylate tube with internal diameter of 20 mm and height 80 mm which was glued onto 50 mm x 50 mm x 5 mm uncoated or coated K_2S- or Dropping-patinated bronze coupons by an epoxy adhesive (Figure 3.10).
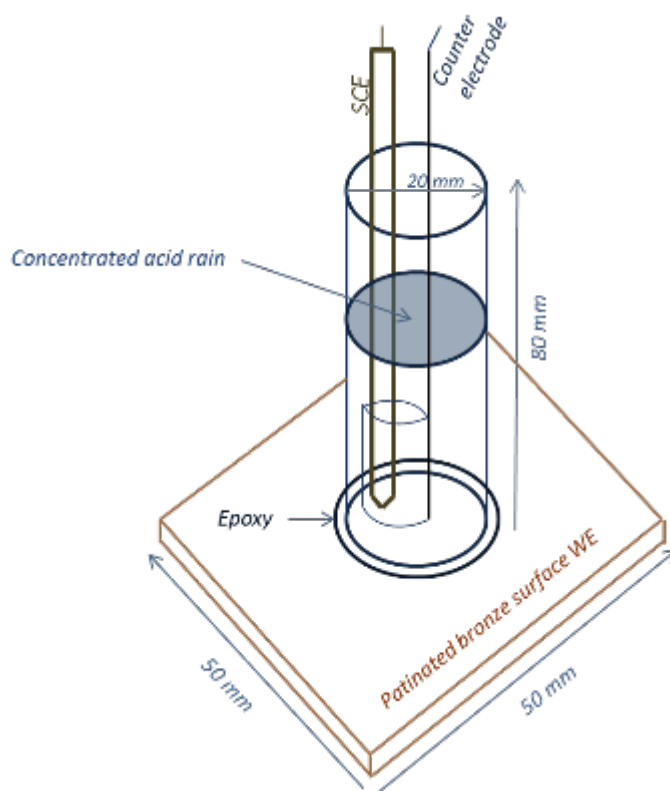
Figure 3.10: Electrochemical cell adopted to assess coatings protectiveness [135,136].

In this tube, filled by ARX10, a Pt wire and a saturated calomel electrode (SCE) were introduced to act as counter and reference electrodes respectively, while the bronze specimen underneath was the working electrode for electrochemical measurements. With the aim to limit the effects of water evaporation (concentration of aggressive species and pH changes in ARX10), the solution was renewed after 1, 2 and 3 weeks (168, 336 and 504 h), just after the scheduled electrochemical measurements. The tests were performed by a PAR/ AMETEK PARSTAT2273 Potentiostat/Galvanostat.

The evolution of the bronze corrosion process was monitored over 30 days of exposure by electrochemical impedance spectroscopy (EIS), under the following experimental conditions: ± 10 mV rms alternating potential signal, 100 kHz–1 mHz frequency range and 10 frequencies/decade. Polarization resistance (R_p) values were measured from the spectra in Nyquist form, by circle fitting the low frequency arc. In particular, R_p corresponded to the low frequency intercept of the circle with the real axis, after subtraction of the solution resistance (R_s) value. The tests were performed in triplicate and the time evolution of average R_p and corrosion potential (E_{cor}) values were obtained.

IR-compensated polarization curves were collected after 1 h, 24 h and 30 days of immersion. Separate anodic and cathodic potential scans, always starting from E_{cor}, were carried out at a rate of 0.1667 mV/s^{-1}. These tests were performed in triplicate and representative curves were discussed. The corrosion protection efficiency, PE, was calculated according to Equation 3.5:

$$PE = \frac{i_{cor0} - i_{cor}}{i_{cor0}} x \, 100 \qquad (3.5)$$

where i_{cor0} and i_{cor} are the corrosion current densities obtained by the Tafel method from the polarization curves, recorded on uncoated and coated bronze electrodes, respectively. All the potentials quoted in the text are related to the SCE reference electrode.

3.6.2. Potential toxicity of coatings: determination of the Exposure Limit (EL)

The detailed description of the procedure used by ECAM (Italy) for the determination of the exposure limit (EL) is reported in [137].

Simulation of coating application and Volatile Organic Compounds (VOCs) sampling and analysis

The selected coatings were applied by brushing on 700x700 mm glass plates (about 0.5 m^2) on both the surfaces. Applied coatings lasted 1 h for an average applied volume of 500 mL. These tests were performed in triplicate.

Active, pumped sampling was performed to sample VOCs released from the coatings during application on glass plate. In accordance with UNI EN 16017-1:2002, sampling device (Gilian AirPlus RECOM) was positioned at the level of the operator collar bone and air was collected for 1 h with a flow rate of 0.5 L/min, for a total volume of 30 L of air. VOCs were collected in the charcoal desorption tubes, stored at -20 °C at the end of the sampling. Then they were extracted with carbon disulphide (CS_2) and analyzed by the gas chromatography-flame ionization detector (GC-FID) Thermo Trace 1300 with autosampler, DB-WAX 60 mm x 0.32 mm and 0.50 µm column. A characteristic chromatogram, with calibrated and uncalibrated peaks, was obtained for each coating. The amount of specific VOC (ethanol, toluene, xylene, etc.), corresponding to calibrated peaks, were directly calculated while uncalibrated peaks (other VOCs) were considered as n-hexane and pooled together.

Occupational exposure test: potential toxicity in terms of Exposure Limit

Threshold limit value (TLV) of a chemical substance is the level to which it is believed a worker can be exposed day after day for a working lifetime without adverse effects. Considering the application of coating formulations to bronze work-of-art during the standard workday (8 h), Time-Weighted Average TWA was applied. TLV-TWA is an airborne concentration of a gas or particle to which most workers can be exposed on a daily basis for a working lifetime without adverse effect (assuming an average exposure on the basis of a 8h/day, 40h/week work schedule). TLV-TWA is specific for each analyzed substance (ethanol, methanol, etc.) and their values are calculated according to Equation 3.6:

$$TLV - TWA = \frac{t_1 c_1 + t_2 c_2 + \cdots + t_i c_i}{8h} \tag{3.6}$$

where t_i is the duration and c_i is the concentration during the ith interval. However, for complex mixture of chemicals, such as the tested coatings, it is necessary to consider the simultaneous exposure to multiple chemicals. To determine mixture (coating solution) exposure limits (EL), Equation 3.7 was applied:

$$EL = \frac{c_1}{TVL_1} + \frac{c_2}{TVL_2} + \cdots + \frac{c_n}{TVL_n} \tag{3.7}$$

where C_n is the 8 h-measure Time-Weighted Average (TWA) concentration of compound n and TVL_n is the TLV for compound n. C_n values were calculated by normalizing the compound n concentration obtained during 1 h application simulation for a 8 h application. To be compliant, the EL of a mixture must be < 1 to be considered not hazardous for the operator.

Results and Discussion

CHAPTER 4 REPORTS THE CHARACTERISATION OF PATINATED SURFACES AND THE ASSESSMENT OF THE PROTECTIVENESS OF THE SELECTED PROTECTIVE COATINGS APPLIED ON PATINATED Cu-Sn-Zn-Pb.

THE AIM OF **CHAPTER 5** IS TO PRESENT THE RESULTS ABOUT THE INTERACTION BETWEEN A SILANE COATING AND THE BRONZE SUBSTRATE.

CHAPTER 6 REPORTS THE ASSESSMENT OF THE PROTECTIVENESS OF THE SELECTED PROTECTIVE COATINGS APPLIED ON BLACK-PATINATED Cu-Si-Mn.

This section is based on the results of the following published articles:

- G. Masi, J. Esvan, C. Josse, C. Chiavari, E. Bernardi, C. Martini, M.C. Bignozzi, N. Gartner, T. Kosec, L. Robbiola, *Characterization of typical patinas simulating bronze corrosion in outdoor conditions*, Materials Chemistry and Physics 200 (2017) 308-321.
- G. Masi, A. Balbo, J. Esvan, C. Monticelli, J. Avila, L. Robbiola, E. Bernardi, M.C. Bignozzi, M.C. Asensio, C. Martini, C. Chiavari, *X-ray Photoelectron Spectroscopy as a tool to investigate silane-based coatings for the protection of outdoor bronze: the role of alloying elements*, Applied Surface Science 433 (2018) 468-479.
- G. Masi, C. Josse, J. Esvan, C. Chiavari, E. Bernardi, C. Martini, M. C. Bignozzi, C. Monticelli, F. Zanotto, A. Balbo, E. Svara Fabjan, T. Kosec, L. Robbiola, *Evaluation of the protectiveness of an organosilane coating on patinated Cu-Si-Mn bronze for contemporary art*, submitted to Corrosion Science on the 22nd December 2017.

4. PROTECTIVE COATINGS FOR HISTORICAL BRONZES (Cu-Sn-Zn-Pb)

4.1. Artificial patinas: unsheltered and sheltered outdoor exposure

4.1.1. Surface observation and elemental analysis

Optical observations of the bronze samples, artificially aged by Dropping and Wet&Dry tests, are reported in Figure 4.1a and b, respectively. Artificial ageing highlighted the typical dendritic structure of the as-cast bronze alloy.
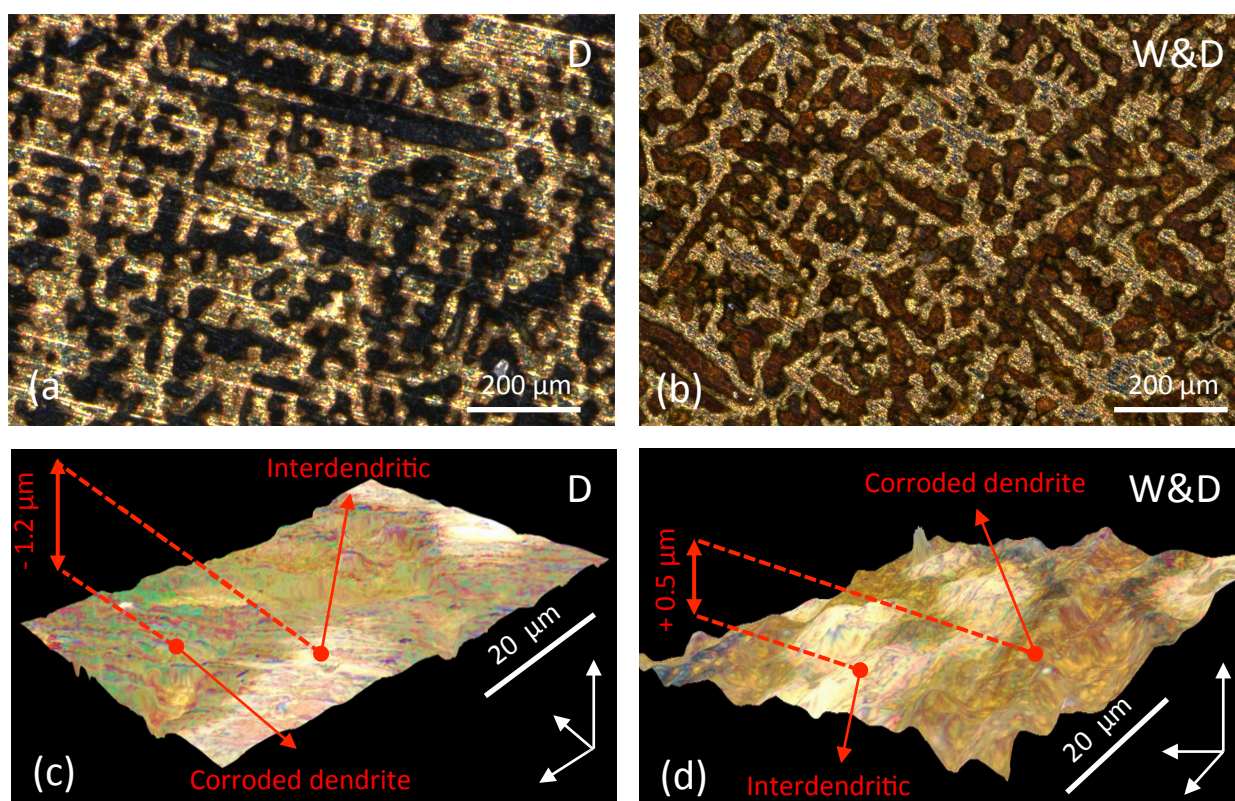
Figure 4.1: Corroded surfaces obtained by Dropping (D) and by Wet&Dry (Wet&Dry): (c, d) Optical bright-field observation and (e, f) 3-D digital microscopy topographic images of bronze samples after artificial corrosion by the Dropping and Wet&Dry tests, respectively [124]*.*

The corrosion attack is not uniform and more deeply affects the Cu-rich centre part of the dendrites: black for Dropping (Figure 4.1a) and reddish for Wet&Dry (Figure 4.1b). The interdendritic areas with eutectoid, corresponding to the bright gold surfaces, are less modified by the corrosion attack than the dendrite core. However, the two ageing systems induced different surface morphologies, as revealed by the 3D digital microscopy topographic images (Figure 4.1c and d). In particular, for Dropping (Figure 4.1c), due to the runoff of acid rain, a slight erosion (~ 1 µm) of the central part of the dendrite is revealed. For Wet&Dry (Figure 4.1d), the presence of a deposit of corrosion compounds is found on the dendrites, inducing a slight increase of the thickness (< 1 µm) and an increased roughness by comparison with the original surface.

Detailed observations by SEM are shown in Figure 4.2. In both ageing tests (Figures 4.2a and d), the corroded dendrites (in dark grey) are surrounded by the interdendritic region, which includes the eutectoid (in light grey) but also black spots, which represent porosities due to solidification shrinkage during casting. It is confirmed that the corrosion attack is heterogeneous: α-Cu solid solution with an initially lower Sn content is more severely corroded, whereas the dendrite borders with a higher tin content and the (α+δ) eutectoid (white area) are not attacked by corrosion. This is confirmed from elemental characterisation carried out by EDS coupled with SEM.
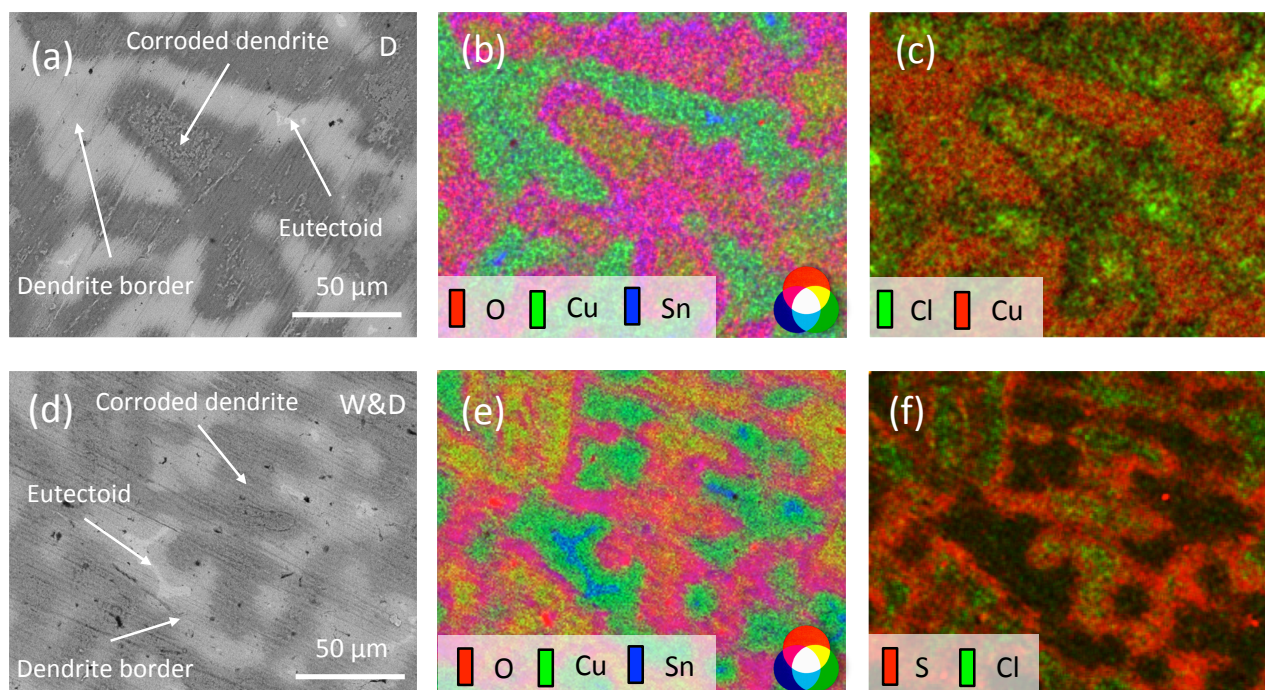
Figure 4.2: SEM observation and X-ray maps of surfaces aged by Dropping (a-c) and Wet&Dry (d-f): (a) and (d) BSE images; (b) and (e) Composite X-ray map image (O in green, Cu in magenta and Sn in blue); (c) Composite X-ray map image (Cl in green and Cu in red); (f) Composite X-ray map image (S in red and Cl in green) [124].

The composite images relative to the X-ray emission of O K (red), Cu K (green) Sn L (blue) signals are reported in Figures 4.2b and e for Dropping and Wet&Dry, respectively. The eutectoid (in light blue) and dendrite borders (in blue-green) are poorly attacked (no or a very low O signal detected). In contrast, the corroded dendrite areas can be observed by the high O and low Cu emissions, defining two main areas: purple (blue + red) in the external part (high Sn emission) and yellow in the central part (low Sn emission). For both ageing tests, this result highlights the substantial Cu dissolution relative to tin content in the alloy, according to the preferential dissolution of Cu. However, a different behaviour within the corroded dendrites was observed, depending on the exposure conditions. For Dropping, as shown in Figure 4.2c, Cl (in green) is locally observed in very small amount in the centre of the dendrites. It is also related to a more important Cu emission (in yellow in Figure 4.2b). For Wet&Dry, as shown in Figure 4.2f, both Cl and S are detected in small amounts all over the corroded areas: Cl (in green) mainly in the centre of the dendrites, but also S (in

red) more to the edge of the corroded dendritic parts. For Wet&Dry, this has to be related to the incorporation of S- and Cl-containing compounds within the corrosion deposit, previously evidenced in Figure 4.2b.

Elemental quantification of the different surface regions of the dendrites was performed on the basis of EDS analyses. The results are reported in at% in Table 4.1. Adjacent to the eutectoid, the dendrite borders exhibit a comparable chemical composition between the two samples. Sn content is, as expected, close to the limit of solubility of the α-Cu solid-solution atomic ratio (Cu/Sn ~ 12). However, oxygen is detected in a small amount: the dendrite borders are weakly attacked and are covered by a thin corrosion layer.

Table 4.1: Chemical composition of quaternary bronze artificially patinated through Dropping and Wet&Dry (EDS – Beam energy 15 kV). The reported results are an average obtained from different areas [124].

at%	O	S	Cl	Cu	Zn	Sn	Pb	Cu/Sn
Dendrite border close to eutectoid								
Dropping	11±4	-	-	80±4.0	2.6±0.2	6.6±0.3	0.1±0.1	12.1
Wet&Dry	14.7±0.5	-	-	76.4±0.3	2.3±0.1	6.5±0.1	-	11.8
corroded dendrite : external part								
Dropping	60±1	0.1±0.1	0.3±0.1	31±2	0.6±0.1	7.5±0.7	0.2±0.1	4.1
Wet&Dry	54±3	0.8±0.1	0.7±0.1	37±3	0.4±0.1	7.1±0.1	0.7±0.1	5.2
corroded dendrite: central part								
Dropping	48±3	0.2±0.1	-	46±4	1.1±0.3	4.5±0.4	0.2±0.1	10
Wet&Dry	39±5	0.6±0.1	1.0±0.3	55±5	0.9±0.4	3.6±0.4	0.4±0.1	15.3

In the corroded parts of the dendrites, the main differences between all the areas, previously highlighted by X-ray maps, are linked to the variation of the Cu content. For both the ageing methods, a trend in the chemical composition is observed. It is confirmed that a small quantity of environmental elements (Cl and S) were detected, but in larger amounts for Wet&Dry.

In particular, the differences between these corroded areas are mainly linked to Cu dissolution coupled to the relative Sn enrichment. Interestingly (Table 4.1), the Cu/Sn ratio is markedly higher within the centre of the corroded dendrites. This can be related to the deposition of the Cu species, but it can also be linked to the initially low Sn concentration in the centre of the dendrites due to casting, as shown later. The results reported in Table 4.1 also confirm that the aged surfaces obtained by the Dropping method exhibit lower Cu/Sn ratios compared to the surface aged by Wet&Dry, in good agreement with previous results [12,13]. In fact, the combined chemical and mechanical action induced by the Dropping method generated a higher Cu dissolution rate and limited the growth of Cu deposits in comparison to the Wet&Dry procedure.

A low Zn content was observed in all the corroded areas due to its preferential dissolution in bronze, as already reported [8,11]. For Pb, a significant amount was detected on the surfaces aged by Wet&Dry, whereas only traces were detected in the dropped surface. In the case of Wet&Dry, the Sn/Pb atomic ratio is found to

be almost constant at around 10 for all of the analysed areas. This is probably due to the tetravalent nature of Pb, that spread all over the surface and easily formed compounds with environmental elements within the corrosion layer [25]. Thus, these results confirm that the artificial ageing induced corrosion with surface oxidation, forming a thin corrosion layer. This patinated structure will be assimilated to thin natural patina, representative of its initial formation, according to their detailed composition and structure, as described below.

4.1.2. Structural characterization

The X-ray diffraction patterns performed on large surface area (around 0.5 cm²) at low diffraction angles for artificially patinated surfaces are shown in Figures 4.3a and b, respectively, for the Dropping and Wet&Dry tests. In addition to the Cu solid solution, cuprous oxide (Cu_2O) was also identified for both ageing tests. Moreover, the surface aged by Wet&Dry (Figure 4.3b) also revealed posnjakite, a Cu hydrated hydroxysulphate ($Cu_4(OH)_6SO_4.H_2O$). This compound is a precursor of brochantite, which forms for longer exposure times on Cu [25,138]. This behaviour confirms the difficulty of forming stable corrosion compounds for the Dropping system due to the runoff regime at the surface.
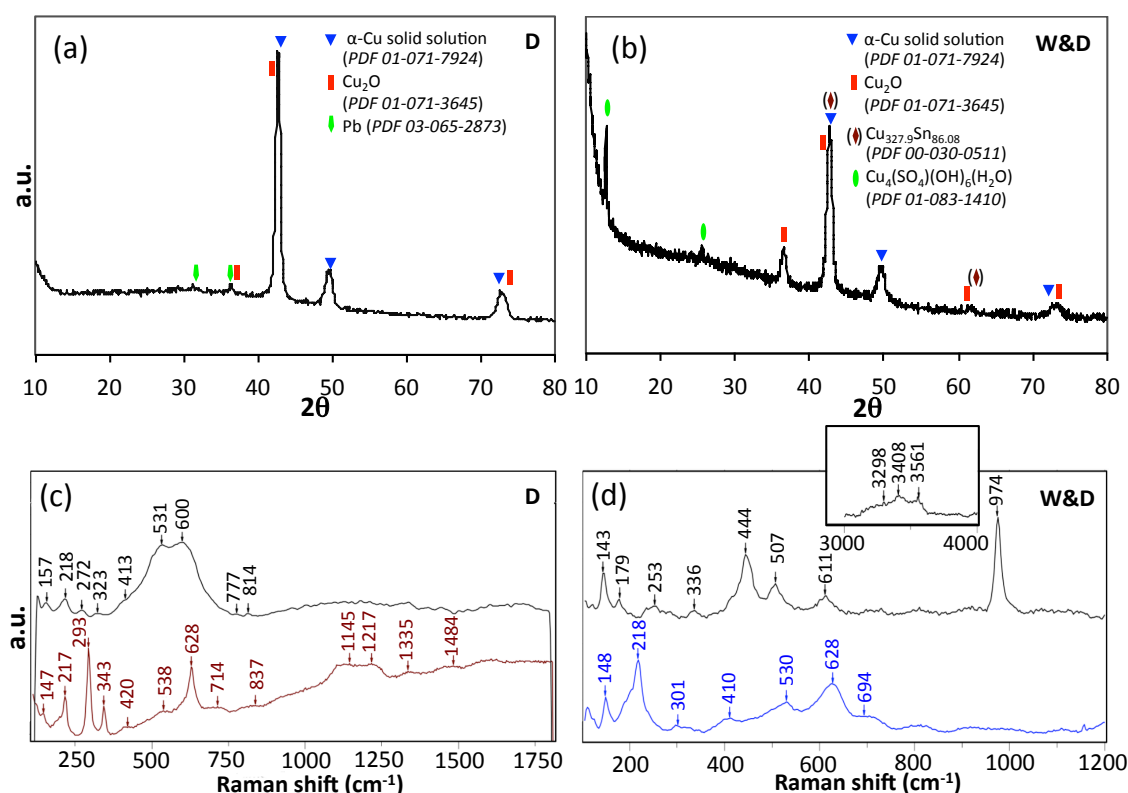
Figure 4.3: Grazing-angle X-ray diffraction (GXRD) of the corroded surface by (a) Dropping and (b) Wet&Dry; Raman spectroscopy performed on corroded dendrite of artificial quaternary bronze patinated surface by (c) Dropping (top spectrum: metal-O stretching vibration / bottom spectrum: cuprous oxide) and by (d) Wet&Dry (top: posnjakite / bottom: cuprous oxide) [124].

The X-ray diffraction analyses performed on large surface areas were completed at a micrometric level by applying Raman spectroscopy. Even though Raman spectroscopy is a very sensitive method for the characterization of oxidized metallic surfaces, processing the spectra was rather difficult, mainly due to the very low thickness and due to the poor crystallisation of the surface compounds. Typical spectra of the identified compounds by Raman spectroscopy are reported in Figures 4.3c and d. The phase-composition determination of the aged surfaces using the Dropping or Wet&Dry tests proved to be rather different.

For the Dropping tests, unlike for the Wet&Dry, Raman spectroscopy measurements gave poorly resolved signals. Raman spectroscopy performed on different areas of the corroded surface confirmed the formation of cuprous oxide (Figure 4.3c, bottom spectrum). In this spectrum a doublet at 293–343 cm^{-1} was also observed. It is difficult to ascribe, but it could correspond to the M-O stretching vibration, such as for CuO (305–350 cm^{-1}), and not expected here. The black spectrum in Figure 4.3c (top) exhibits intense, but very broad, peaks at 531 and 600 cm^{-1}, characteristic of M-O stretching vibrations, probably indicating the presence of several compounds mixed together, which could be related to Cu but also to Cu and/or Sn oxides [139–142]. In this spectrum, the peak at 218 cm^{-1} indicates the presence of Cu_2O, marked by a large band in the 1100–1230 cm^{-1} region. A characteristic Raman fingerprint is the 272–323 cm^{-1} doublet linked to the peaks in the 200–600 cm^{-1} region. These fingerprints do not exactly correspond to the pure cuprite (Cu_2O), tenorite (CuO) and chalcocite (Cu_2S), but could be compatible with a mixture of these Cu-containing phases [142]. Furthermore, the attribution of the strong $\sim$ 530 cm^{-1} peaks forming a broad structure associated with weak bands at $\sim$ 750 and 777 cm^{-1} (Figure 4.3c, top spectrum) does not correspond to the cassiterite fingerprint. This result could be linked to a non-stoichiometric tin oxide, probably hydrated, which could correspond to the SnO_{2-x} or substituted $Sn(M)O_2$ oxide (where M is a bronze alloying element) but also hydroxyl tin oxide [139,141,142].

For the Wet&Dry tests, two compounds were punctually identified by Raman spectroscopy, fully confirming the X-ray diffraction measurements: cuprous oxide and posnjakite. In Figure 4.3d, the spectrum of cuprous oxide Cu_2O (bottom spectrum in blue) exhibits the characteristic features of well-crystallised compounds marked by the 215 –220 cm^{-1} and 620–630 cm^{-1} peaks [140–142]. It should be noted that the poorly resolved cuprous oxide was also detected in the border of the dendrites, forming a thin corrosion film, as later confirmed from the FIB SEM observations. The spectrum on the top of Figure 4.3d corresponds to posnjakite [140], small, green-blue crystallites, localized in the centre of the dendrites. The stretching of the hydroxyl units in the posnjakite produced bands in the 3300–3600 cm^{-1} region. The sulphate group stretched symmetrically at 974 cm^{-1}, while the 200–600 cm^{-1} region with the 445 cm^{-1} peak is typical of Cu-O stretching. No evidence of tin-containing compounds was found for the Wet&Dry sample. This could be attributed to the fact that the tin oxide species could be non-stoichiometric, but also hydrated, and could be hindered by the higher Raman signals relative to the deposit of crystalline Cu species.

These results, summarized in Table 4.2, confirmed the differences in the main features of the surfaces aged with these two methods, previously highlighted by SEM and EDS analyses. Dropping allows the formation of

poorly crystallised tin compounds (the top Raman spectrum in Figure 4.3c), related to selective Cu dissolution. For Wet&Dry, the alternate immersion action leads to the formation of thin corrosion layers of cuprous oxide with Cu sulphate corrosion products. It should be noted that chlorides, nitrates and carbonates were not detected.

Table 4.2: Corrosion products on the patinated surfaces by Dropping and Wet&Dry identified by μ-Raman spectroscopy and XRD (compounds identified by XRD are labelled with (*)).

	Cuprous oxide Cu_2O	SnO_x	*Posnjakite* $Cu_4(OH)_6SO_4.H_2O$
Dropping	X* (variable crystallinity)	X	-
Wet&Dry	X*	-	X*

In order to define more precisely the top corrosion layers that can interact with the protective coating, XPS analyses were carried out on the artificially patinated surfaces. Figure 4.4 shows XPS surveys of the corroded surfaces before (in black) and after (in grey) Ar$^+$-ion sputtering (30 s with Ar$^+$ ions accelerated to 200 eV).

Compared with the EDS analysis (Table 4.1), no Cl peaks on both the samples and no Zn on the Wet&Dry aged surface were found, indicating that chlorides (Cl element) is located in the inner part of the corrosion layers (hence non-detectable by XPS) and Zn is fully dissolved out of the top layer of the surface aged by Wet&Dry.
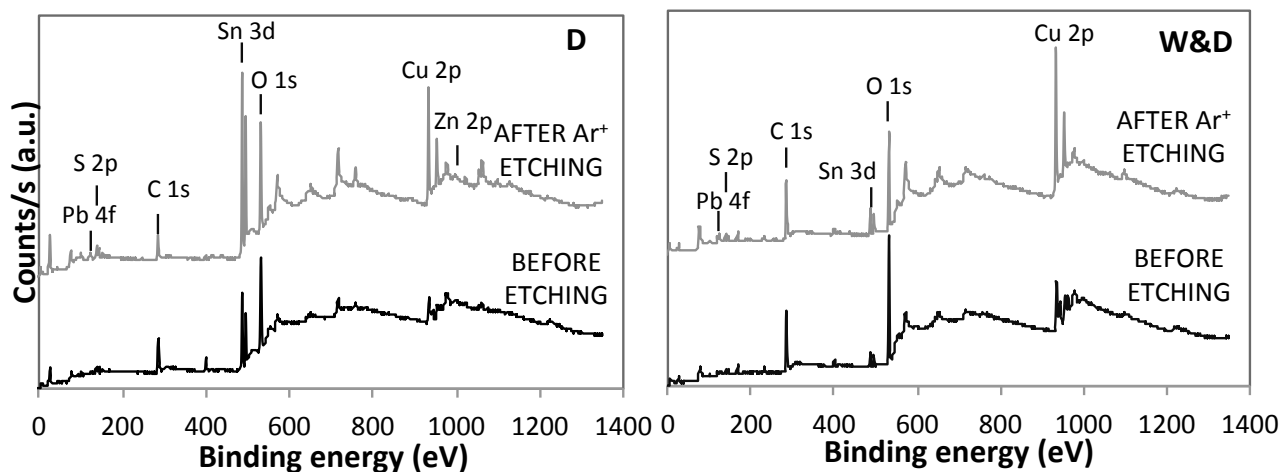
Figure 4.4: XPS survey of the corroded surfaces by Dropping and Wet&Dry before and after Ar$^+$ ion etching [124].

The short and slight etching applied on the samples is very effective for these surface compounds. As shown in Figure 4.4, it allowed surface cleaning with respect to carbon contamination (C 1s peak decreasing), enhancing the global XPS signals of the main elements (O 1s, Zn 2p in the surface aged by Dropping, Sn 3d and Pb 4f). Only the Cu 2p and S 2p exhibited a few changes. Specifically, the Cu 2p spectrum shows typical

shake-up satellites before etching, which significantly decrease in intensity after ion sputtering, enhancing the main Cu 2p peaks at lower BE. Regarding S 2p, new contributions at lower BE are observed when the corroded surfaces were etched. This indicates Cu 2p and S 2p reduction under Ar^+ sputtering, as reported in [143]. The O 1s, Cu 2p core levels and the S 2p curve fitted regions of the surfaces aged by the Dropping (in black) and Wet&Dry (in grey) tests showed a similar behaviour (Figure 4.5).
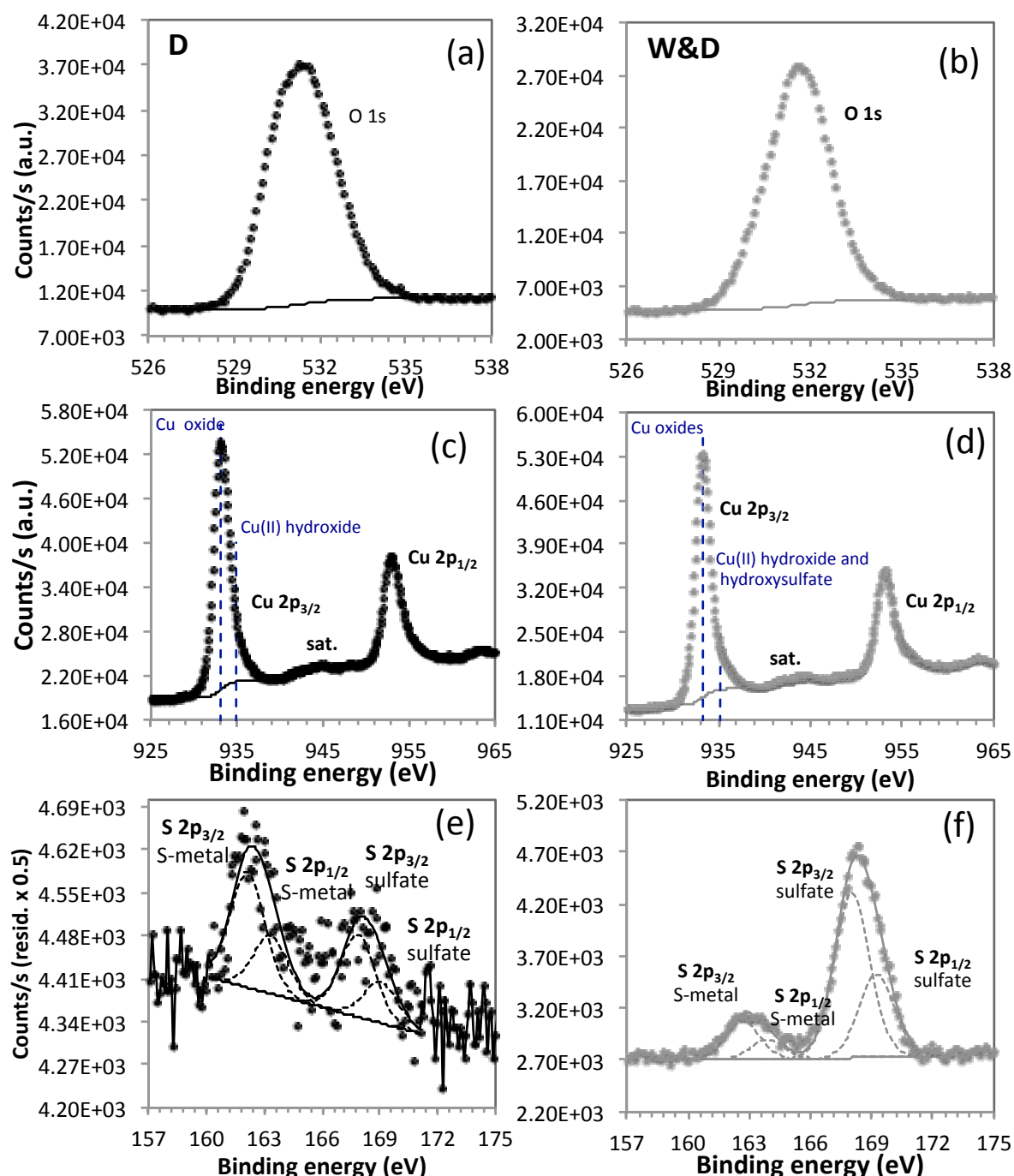
Figure 4.5: XPS core levels of O 1s, Cu 2p and S 2p curve fitted regions, after Ar^+ ion etching, on the bronze surface corroded by Dropping (a, c and e, respectively) and Wet&Dry (b, d, f, respectively) [124].

The main Cu 2p peaks are observed at BE=933.3 eV (Cu $2p_{3/2}$, α'=1848.4 eV), probably due to a mix of Cu oxides. Other contributions were detected at about 935.0 eV (BE); they can be ascribed to Cu (II) hydroxyl-species [143–146]. Also, the O 1s core level showed a broad peak, with similar features between the two samples. An O 1s deconvolution was not performed, due to the presence of several contributions in the range of a few eV, which could correspond to different metal oxides and hydroxyl species. The main differences between the two samples are related to the S 2p signals (Figure 4.5e and f). In particular, for both the samples two S 2p contributions were detected: S $2p_{3/2}$ BE = 168.5 eV, ascribed to sulphates, and S $2p_{3/2}$ = 163.0 eV, attributed to the S-metal bond, also linked to etching effects [143,145,146]. However, for the Dropping test, the S 2p signal is characterized by a low intensity and a high signal noise, confirming the EDS results. This might not just be related to Cu, but also to the minor amount of Pb(II) [146]. On the top surface, all the other metallic elements in smaller contents, Sn 3d, Zn 2p and Pb 4f, formed mostly oxides and/or hydroxides. As such, the environment of the different Cu 2p oxidation states for the dropped samples is mainly oxides and hydroxides, whereas, added to this for Wet&Dry surfaces, the S is mainly linked to Cu-developing hydroxysulphates.

Table 4.3 reports the atomic quantification of an artificially patinated surface using the Dropping and Wet&Dry tests for the main alloying elements as well as for C 1s, O 1s and S 2p.

Table 4.3: XPS atomic quantification on corroded surface by Dropping and Wet&Dry before and after Ar$^+$ ion etching [124].

	Cu $2p_{3/2}$	Sn $3d_{5/2}$	Zn $2p_{3/2}$	Pb $4f_{7/2}$	C 1s			O 1s	S 2p	
		Sn(IV)	oxide	Pb(II)	CC, CH	C-O	O-C=O		S- metal	Sulfates
Before etching										
Dropping										
Peak BE (eV)	934.7	486.8	1022.2	138.6	284.9	286.5	288.4	531.8	161.8	167.8
at%	5.6	5.1	0.1	0.4	25.0	10.2	11.9	40.9	0.3	0.5
Wet&Dry										
Peak BE (eV)	935.2	486.7	-	138.6	284.5	286.2	288.0	531.7	163.0	168.5
at%	8.6	0.7	-	0.2	34.8	7.1	4.3	35.5	0.3	8.5
After etching										
Dropping										
Peak BE (eV)	933.2	486.8	1022.1	138.5	284.8	286.4	288.4	531.3	162.1	167.9
at%	16.9	10.7	0.5	0.8	17.7	4.5	4.6	43.4	0.5	0.4
Wet&Dry										
Peak BE (eV)	933.3	486.7	-	138.6	284.5	286.2	288.0	531.7	163.0	168.5
at%	11.8	1.3	-	0.3	37.1	4.9	3.6	31.3	1.8	7.9

On the top surface corroded by Dropping, not only Cu compounds are present. The concentrations of Sn $3d_{5/2}$, Pb $4f_{7/2}$ and Zn $2p_{3/2}$ are higher compared to the Wet&Dry aged surfaces, coupled with an higher oxygen

content. The Sn is present as Sn(IV), probably as tin oxides or hydroxides, but the broad and poorly resolved Sn LMM Auger at around 105.3 eV cannot aid in further refinement of Sn spectrum interpretation. These observations confirm the difficulty of forming Cu-based corrosion deposits, due to the runoff during the Dropping tests. Conversely, on the Wet&Dry aged surface, the Sn, Pb and Zn are almost completely absent. The surface is essentially covered with Cu compounds, mainly hydroxysulfates, but also oxides and a S-metal bond (after ion sputtering). In particular, the Cu $2p_{3/2}$ concentration (at%) is in almost the same ratio as the S $2p$ sulphate, indicating that nearly all the sulphates are bonded to Cu, in agreement with the detection of posnjakite by GXRD and the Raman spectroscopy results.

Relationships between the surface corrosion and the bulk bronze alloy were investigated by FIB analysis. Typical areas of interest were selected in order to obtain a representative section of both the centre of a corroded dendrite and the adjacent inter-dendritic space (Figure 4.6a and b for the Dropping and Wet&Dry samples, respectively). The corresponding FIB cross-sections are shown in Figures 4.6c and d.
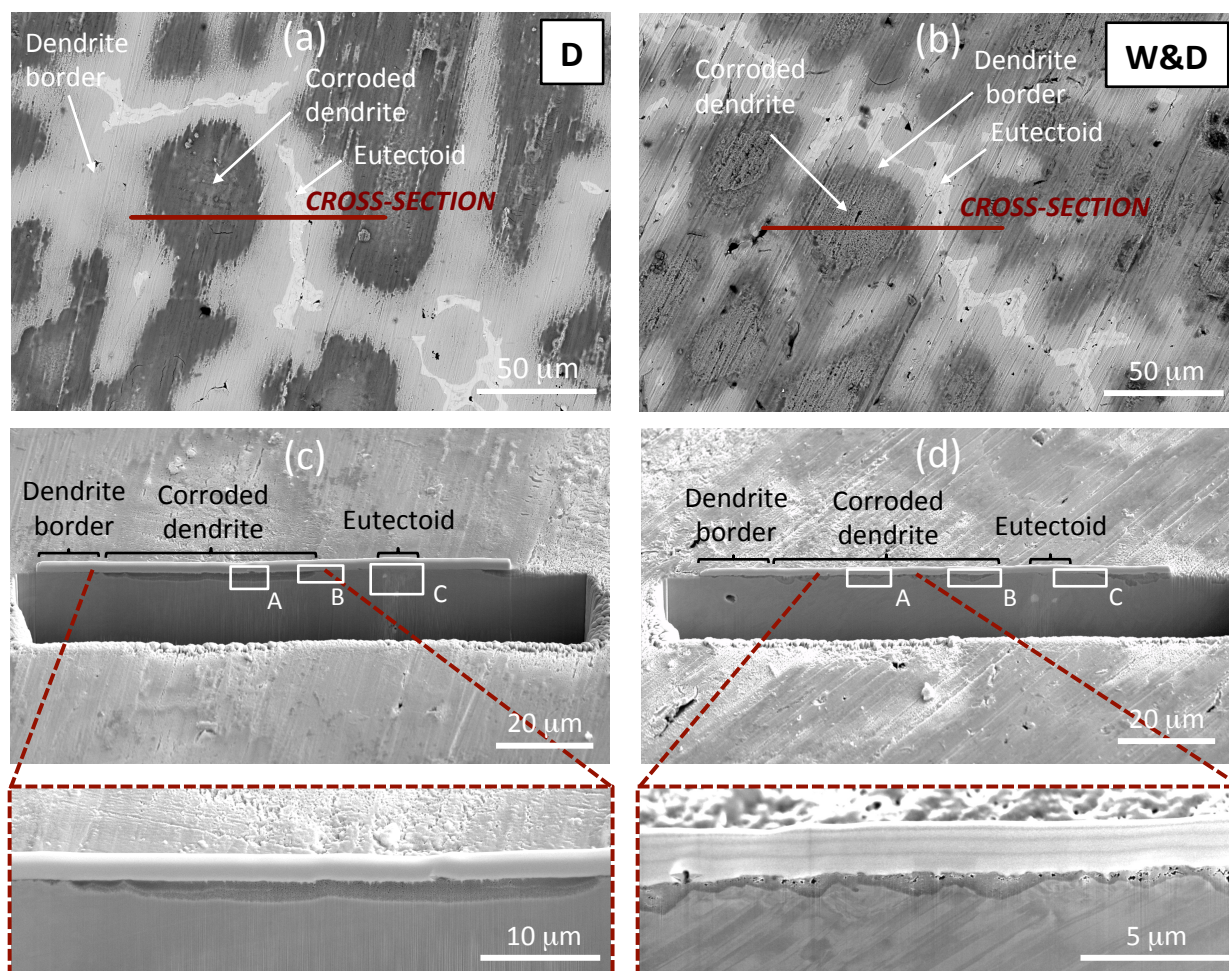
Figure 4.6: Images of the corroded surface and cross-sections prepared by FIB milling of samples obtained by Dropping and Wet&Dry: (a) and (b) surface areas corresponding to cross-section obtained by FIB milling; (c) and (d) general views of the cross-section after FIB milling (rectangles are corresponding to details shown in Figure 4.7) [124]*.*

According to the previous reported results, the dendrites are more corroded than the dendrite borders, which are poorly attacked and the eutectoid is not corroded at all, as detailed in Figure 4.7.
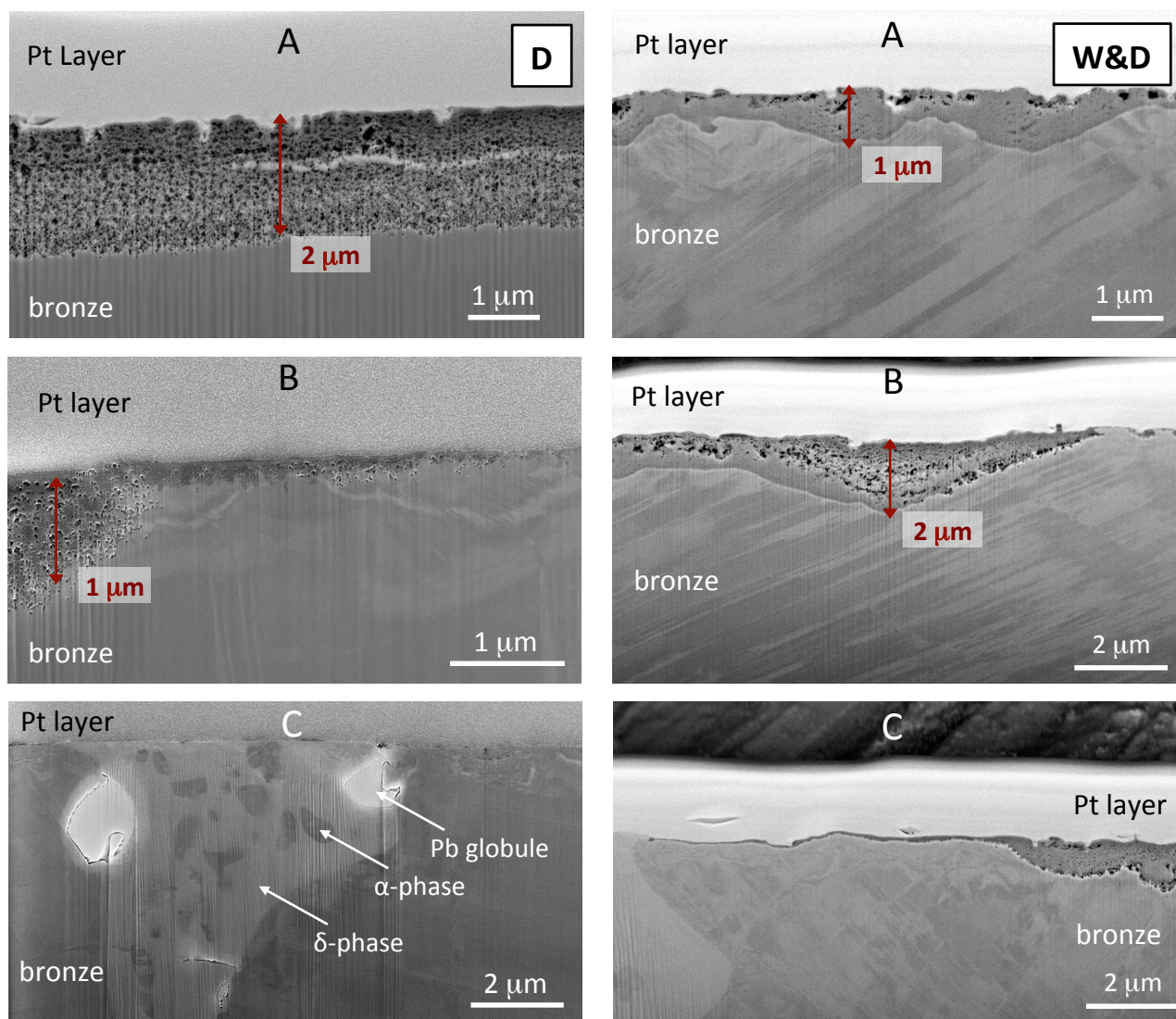
Figure 4.7: Cross-sections prepared by FIB milling of samples obtained by Dropping and Wet&Dry, corresponding to areas defined in Figure 4.6c-d: (A) dendrite centre, (B) dendrite borders corresponding to the transition corroded dendrite / eutectoid area and (C) interdendritic space (eutectoid) [124]*.*

Figures 4.6c and d provide a detailed view of the most corroded parts corresponding to the dendrites, characterised by a low tin content in comparison to the interdendritic spaces with here also contain the high tin content stable delta phase ($Cu_{41}Sn_{11}$). Different corrosion structures between the Dropping and Wet&Dry samples are revealed: thicker for the Dropping samples and thinner for the Wet&Dry samples, with a diverse distribution of nano-porosities. In particular, for the Dropping samples (Figures 4.6c and 4.7A), the corrosion of the dendrites is uniform with a homogeneous thickness (about 2 μm), while for the Wet&Dry samples (Figures 4.6d and 4.7C), the corrosion layer is irregular and thinner: less than 1 μm in the dendrite core, and up to 2 μm close to the border parts. For Wet&Dry, this could be linked to the lateral junction of several

localized attacks. In addition, for the Dropping sample (Figure 4.7A) nano-porosities of a few tens of nm are observed throughout the whole corrosion layer. For the Wet&Dry sample (Figure 4.7B), the nano-porosities are essentially observed only in the outermost part of the layer.

A detailed view of the nano-porosities is shown in Figure 4.8. It is important to mention that the porous structure shown was hypothesised for several years for bronze patinas formed in natural environments [16,18,27]. In fact, according to the process of decuprification leading to an internal oxidation of the alloy, it was found that the selective release of Cu ions and the formation of patinas involved the presence of a porous structure, through which cations migrate outwards from the alloy to the corrosive environment, while the anions migrate inwards [16]. This fundamental point of the presence of a nano-porous structure is revealed thanks to the nm spatial resolution achieved using the FIB FEG-SEM technique. It has to be coupled to nano-precipitates of the tin-containing species (tin hydroxyl- and/or hydrated tin oxides) forming a stabilizing network within the corrosion structure. Thus, for both ageing tests, the main corrosion process involved is relative to the decuprification of bronze, like that observed for natural patinas. As also revealed in the EDS maps hereafter, it corresponds well to an internal oxidation of the alloy, with a preferential release of Cu ions (including also Zn) and marked by the formation of tin-insoluble species within a corrosion layer.
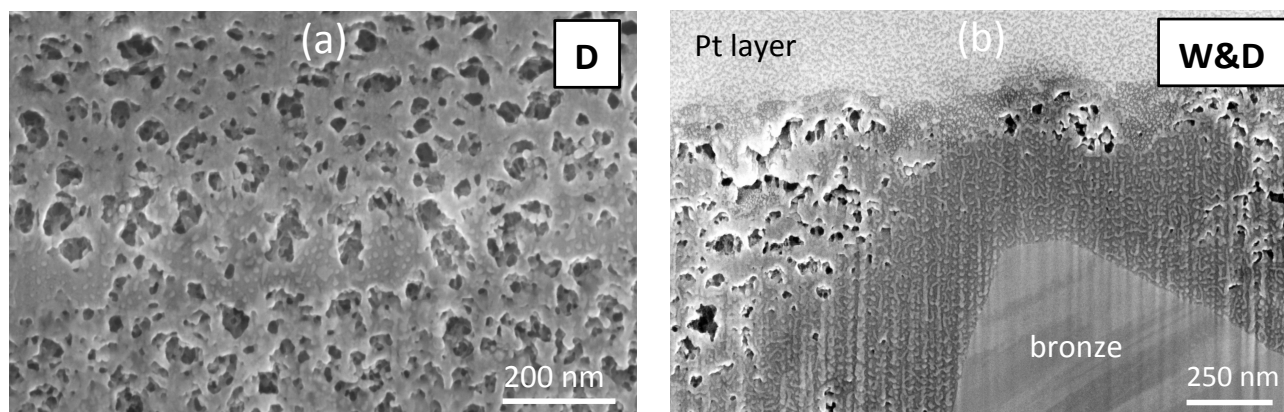
Figure 4.8: High-magnification observation of the corrosion layer revealing the porosity of bronze patinas on a nanometre scale obtained with FIB cross-sections of (a) the Dropping and (b) the Wet&Dry samples [124].

As regards the nano-porosity distribution within the corroded dendrite (Figure 4.8), a difference appears between the Dropping and Wet&Dry samples. This has to be related directly to the ageing process applied. In fact, for the Dropping test, the dendrites are attacked more severely due to the permanent leaching of the alloy, inducing a permanent release of the Cu and Zn ions in relation to the internal oxidation. As a consequence, the developed network of nano-porosities has to be related to the formation of a porous barrier layer that is more pronounced for the Dropping than for the Wet&Dry samples. In fact, for Wet&Dry samples, the corrosion is less developed and a more efficient barrier layer can be built up, limiting the alloy dissolution, the species migration throughout the layer and then consequently the nano-porosity network.

As previously pointed out through surface images, corrosion mainly affects the central part of the dendrites. Thus as revealed in Figure 4.7C for both samples, a marked transition between the centre and the border of the dendrites is revealed: the dendrite borders are poorly attacked and a corrosion film of a few tens of nm is emphasised. Investigations to identify this abrupt transition were carried out by recording EDS line-scans within the alloy, parallel to the surface. Representative X-ray profiles of the alloying elements in the Wet&Dry sample are shown in Figure 4.9, where the profiles are centred relative to the corroded dendrite.

A strong relationship between the Sn content in the alloy and the corrosion morphology was observed, validating the previous surface characterisation. As shown in Figure 4.9, the marked transition between the highly corroded core and the relatively unaltered border of the dendrites is linked to the transition from lower to higher Sn contents in the alloy, respectively, due to the Sn micro-segregation during cooling in the casting procedure.
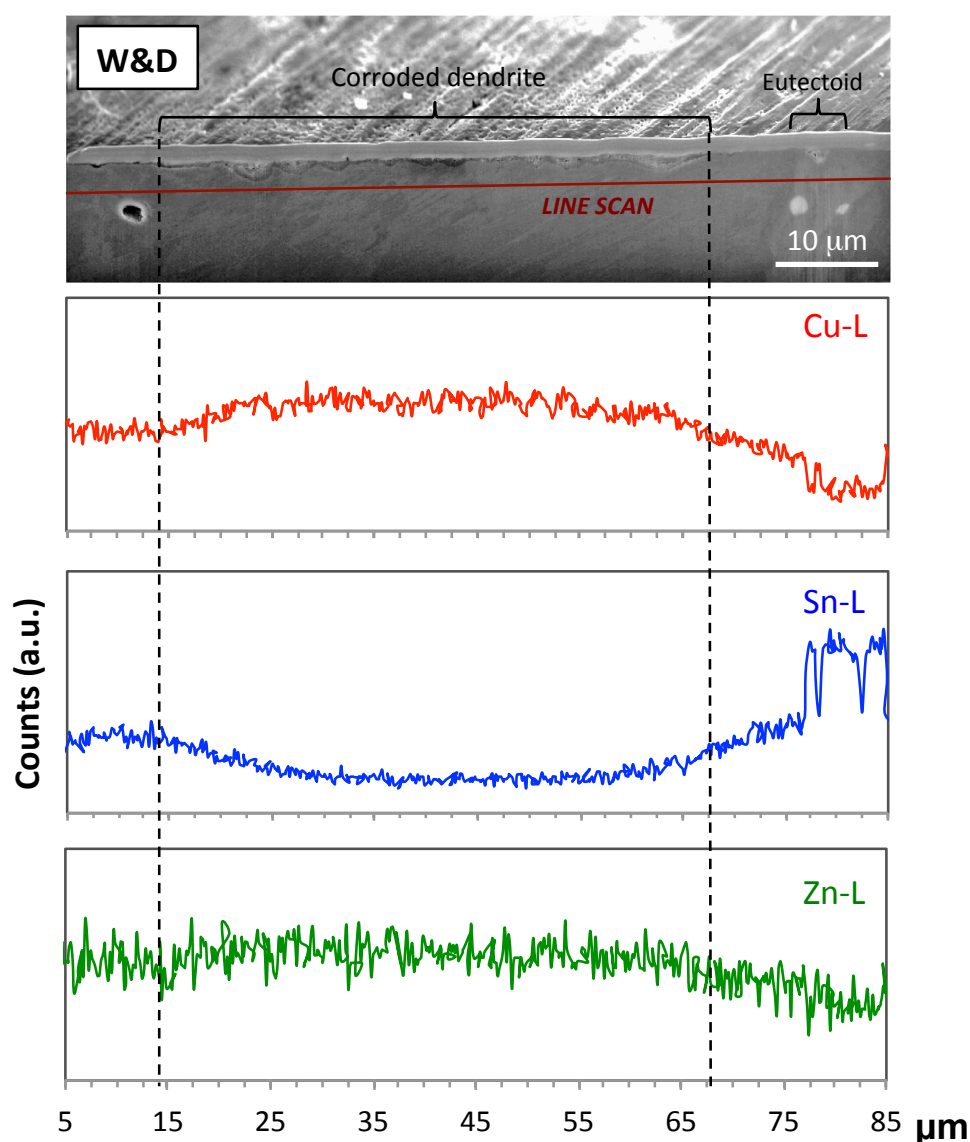
Figure 4.9: Representative EDS line-scan profiles of the Cu-Sn-Zn-Pb alloy, located on the bulk alloy parallel to the corrosion layer and centred on the corroded dendrite [124].

In particular, corrosion preferentially affects the dendrite areas with lower Sn contents (*i.e.*, the core): an effect of galvanic coupling, linked to Sn segregation between the core of dendrites (anodic) and the border (cathodic, due to Sn passivation), is clearly revealed from the observation of the cross-sections.

Within the corroded dendrites, the corrosion process induced a preferential Cu and Zn dissolution linked to the presence of O element within the whole thickness of the corroded layer. This is shown by elemental X-ray maps within the corrosion layer (1 μm) obtained from the Wet&Dry tests (Figure 4.10). Furthermore, for the Wet&Dry tests, the distribution of S is not reported due to its very low emission signal. Also, small amounts of Cl were detected, but only in the internal part of the corrosion layer, confirming the EDS results in Table 4.1 (surface analysis,) but also the XPS results, in which Cl was not detected on the top surface.
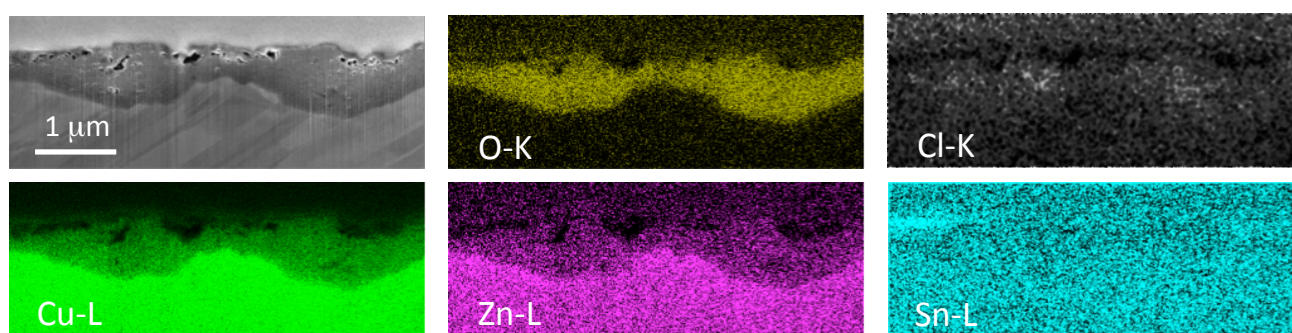
Figure 4.10: X-ray maps of the corrosion layer produced by Wet&Dry test in the centre of dendrite obtained by FIB cross-section (A right-hand image of Figure 4.7) [124].

For a better understanding of the elemental distribution within the corrosion layers, EDS line-scans were performed vertically through the corrosion layers produced by the two ageing methods, as shown Figure 4.11 a-c. For the thick corrosion layers, the EDS profiles (Figure 4.11a and b) show a similar trend for Cu, Zn, O and Sn, characterised by a decrease of Cu and Zn within the corrosion and a relatively high and constant amount of O and Sn. For the very thin corroded layer (< 200 nm) reported in Figure 4.11c, only O, Cu and Sn were detected (the Zn signal was not resolved, so it is not reported). Also in this case, the corrosion features are comparable to the previously described thicker layer. In particular, a homogeneous decrease in the Cu signal coupled with the presence of O and a slight increase in Sn is shown, in accordance with the previous observation in Figures 4.11a and b. Thus, the preferential dissolution of Cu and Zn coupled with a relative Sn enrichment (decuprification) is confirmed, not only for the thickest corrosion layers, but also for the film of a few hundred nanometres. For both aged surfaces, the S signal was very low and no information can be reported. In particular for the Wet&Dry outer layer, no S element (such as in posnjakite) was detected in the cross-section, in contrast to the surface analysis. This is probably due to the non-uniform distribution on the Wet&Dry surface. As regards Cl element, a different behaviour is highlighted between the Dropping and the Wet&Dry samples, but only for thick corrosion layers. Within the 2-μm-thick Dropping corrosion layer (Figure 4.11a), the presence of the chlorine content seems linked to a compact compound within the porous layer. For the Wet&Dry samples (Figure 4.11b), an enrichment of Cl is found at the corrosion/bronze

interface, as a typical consequence of the selective action of this anion on anodic zones (the core of the dendrites) during the corrosion attack.
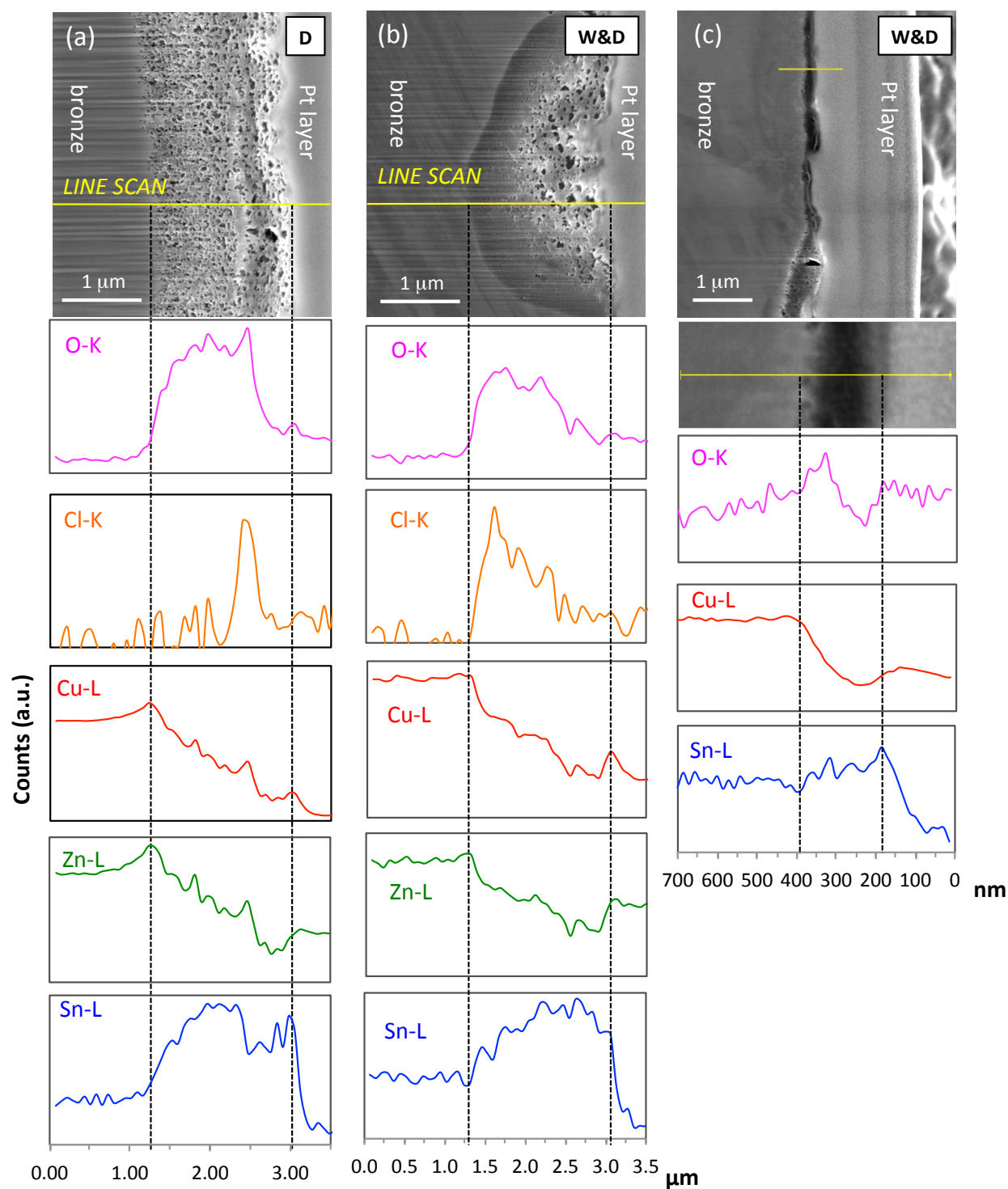
Figure 4.11: Elemental line profiles (X-ray intensity vs distance) obtained by cross-section prepared by FIB milling within the corrosion layer produced by Dropping: (a) centre of corroded dendrite, and by Wet&Dry: (b) thicker part of the corroded dendrite and (c) thin layer in the dendrite border [124].

This confirms the specific role of Cl anions in the corrosion process of bronze in the presence of a cuprous oxide membrane, as already pointed out for other natural environments [16]. In particular, Cl anions can act either as "passive" anions, not directly involved in the corrosion mechanism [147] (included in stable corrosion compounds within the layer as for the Dropping samples), or the Cl⁻ can act as an "active" anion, directly involved in the corrosion process in relation with cuprous oxide layer, as revealed by their enrichment at the corrosion layer/alloy interface of the Wet&Dry sample.

4.2. Surface characterisation of the coated samples

Surface characterisation of the patinated Cu-Sn-Zn-Pb samples in terms of colour variation, surface observation by SEM and surface chemistry analysis by XPS are presented.

The application by spraying of PropS-SH charged with β-CD+MPT and fly ash (FA), as well as Incralac® induced a relevant colour variation at the limit of acceptability for Cultural Heritage applications ($\Delta E^* \leq 5$), as reported in Table 4.4. In particular, a strong variability in the lightness component (ΔL^*) was recorded for Incralac®, while for both the silane coatings an increase of the yellow component as well as a darkening of the patinated surface were detected after the application of these coatings. However, the application by brushing of the FA-MS did not induce a relevant colour variation ($\Delta E^* \leq 1$), indicating that the application of fluoropolymer coating do not produce a noticeable aesthetical variation of the patinated bronze surfaces.

Table 4.4: Colour variation measurements in CIELab 1976 colour space induced by coating application on patinated Cu-Sn-Zn-Pb.

	Δa*	*Δb**	*ΔL**	*ΔE**
Incralac®	-0.4±0.6	0.1±0.7	0.7±7.3	**5±1**
PropS-SH+β-CD+MPT	-0.01±0.37	5±1	-3.2±2.3	**6.3±0.2**
PropS-SH+FA	-0.1±0.2	2.1±0.3	-6±3	**6±3**
FA-MS	0.5±0.1	2.5±0.2	-2±1	**0.6±1.6**

The morphology of the coated patinated surfaces on Cu-Sn-Zn-Pb bronze is shown in Figure 4.12. The application of all the selected coatings induced the formation of a continuous layer that well covered the patinated substrates. However, the surface coated by Incralac® reveals some uncovered areas of the samples, as highlighted in the inlay of Figure 4.12a. These uncovered portions could be area of preferential attack of aggressive agents, inducing corrosion. Moreover, the addition of fly ash in the PropS-SH layer is observable in the coating layer and it results in some inhomogeneity of the coated surface (Figure 4.12c). Similarly, on the top surface of FA-MS coating some heterogeneity in the chemical composition is highlighted in Figure 4.12d. In particular, circular lighter spots rich in F element (as detected by EDS) are detected, indicating some issue in the preparation of the coating to obtain an homogenous mix of the fluoroacrylate copolymer with the silane MS.
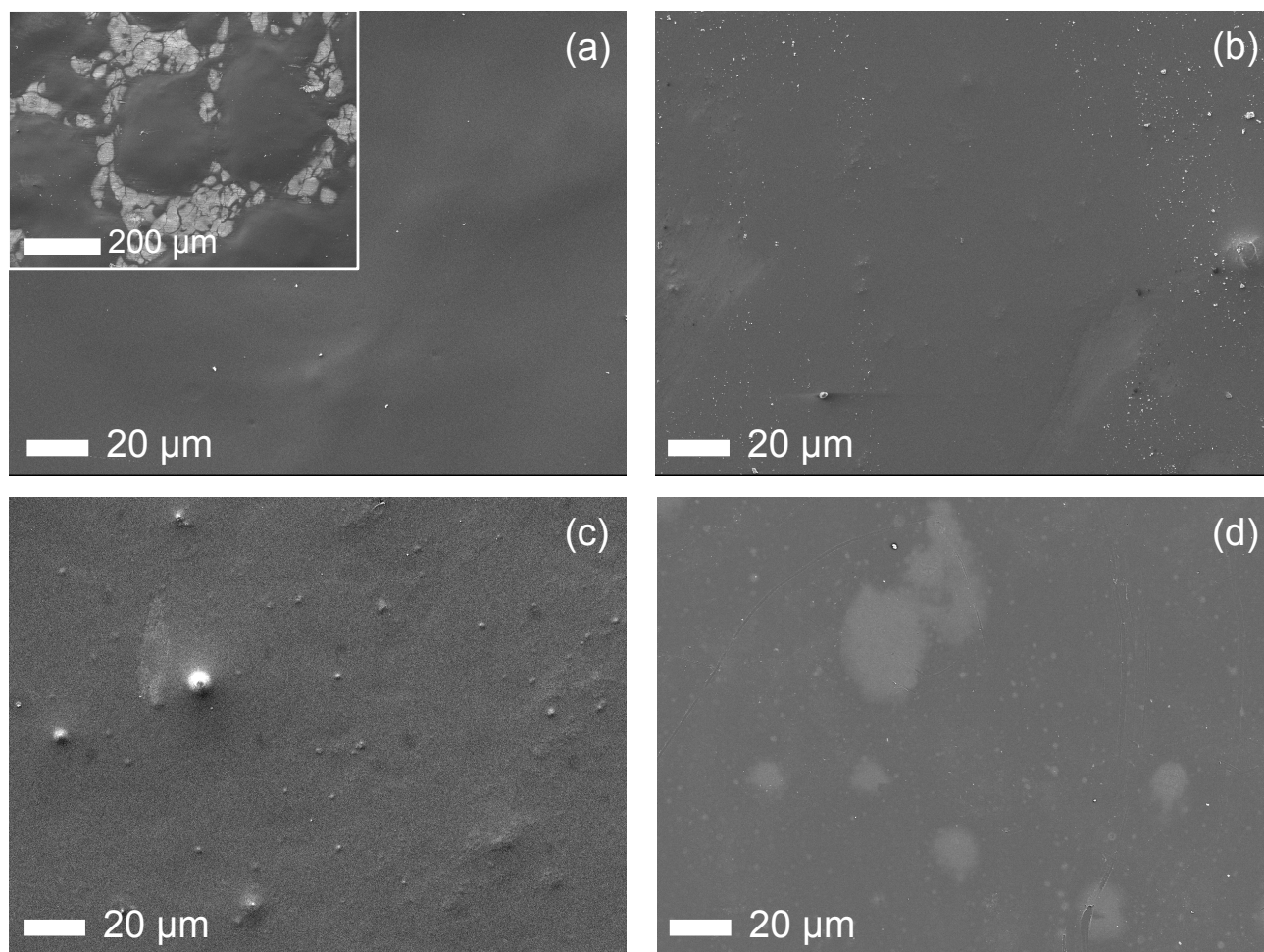
Figure 4.12: Surface observation of the coated samples by (a) Incralac[®] (in the inlay: sample portion in which the coating is not able to homogenously covered the patinated substrate); (b) PropS-SH+ β-CD+MPT; (c) PropS-SH+FA and (d) FA-MS.

The XPS surface analysis of the selected coatings on patinated Cu-Sn-Zn-Pb coatings are reported in Table 4.5. Results were obtained after a slight Ar^+ etching for limiting the detection of C pollution. For Incralac[®] the top surface mainly consists of C and O with a minor contribution of N and Si. In particular, C 1s shows and intense peak at BE=284.7±0.1 eV characteristic of the C-C and C-H chain of the methyl-methacrylate and ethyl-methacrylate present in the coating formulation. Two minor peaks were also detected at BE=286.3±0.1 eV and BE=288.5±0.1 eV linked to C-O and O-C=O species, respectively. Atomic quantification reported in Table 4.5 reports the atomic quantification measured on the top surface of the selected coatings and shows that for Incralac[®] the O present in the coating is completely linked to C, showing an atomic C/O ratio of about 1. N was detected in low concentration (< 1 at%) highlighting the presence of BTA corrosion inhibitor within the organic layer [85,86,148]. Regarding the silane coatings, only the atomic quantification of the top surface of PropS-SH+ β-CD+MPT is reported in Table 4.5. The main detected elements are C, O, Si and S, as expected. In particular, C 1s showed an intense peak at BE=284.8±0.1 eV characteristic of the aliphatic chain of the coating and also two other small contributions (BE=286.2±0.1 eV and BE=288.7 eV) linked to C-S/C-

O and O-C=O species, respectively. O-C=O bond is connected to a limited oxidation of the coating, already observed on organic thiol compounds, like for PropS-SH exposed to atmosphere [56,149,150]. In addition, an intense Si 2p peak was observed at BE=102.4±0.1 eV ascribed to the silane (C-Si-O and Si-O-Si), as detailed in [52,53]. Moreover, a relevant concentration of SiO_2 (BE=103.1±0.1 eV) was found related to the presence of the corrosion inhibitor β-CD+MPT. The analysis of S 2p signal takes into account the presence of a doublet structure of the core level with a spacing of 1.2 eV (S $2p_{1/2}$ - S $2p_{3/2}$ = 1.2 eV) and a theoretical intensity ratio of 2 (I(S $2p_{3/2}$) / I(S $2p_{1/2}$) = 2). In particular, S 2p peak is centred at BE=163.4±0.1 eV, characteristic of S-C bonds and thiol groups and presents a minor contribution centred at BE=168.1±0.1 eV to be ascribed to sulphate [52,53,151–153]. From the atomic quantification reported in Table 4.5, the calculated atomic ratios are Si/C=0.32, Si/O=0.60 and Si/S=1.00, by considering only the concentration of Si 2p centred in the representative value for silane at BE=102.4 eV. These values agree quite well with the theoretical values: Si/C=0.33, Si/O=0.67 and Si/S=1.00. This indicates that the Ar^+ ion sputtering is quite efficient in removing contamination without damaging the polymer. The slightly lower value of the Si/O ratio than the theoretical one could be linked to surface contamination of SiO_2 species found on this coated substrate. Conversely to what found in [121] where the thiol group in PropS-SH obtained by dip-coating can be partially oxidized to sulphate, the application of silane coating by spraying did not induce a loss of sulphur from the silane top layer after thiol group oxidation. Finally, FA-MS coating shows on the top surface the presence of intense C 1s, O 1s and F1s peaks with minor Si 2p, S 2p and N 1s features. Compared to the other samples, the effect of the Ar^+ sputtering is more evident, as O 1s, F 1s and S 2p showed a strong decrease in peak intensity, while Si 2p was detected just after etching. In particular, after etching C 1s showed higher intense peak at lower BE values (C-C, C-H) and the features at higher BE centred at 291.4 eV and 293.8 eV linked to F 1s were not detected. In addition, O 1s and F 1s showed a less intense peak, as well as S 2p that showed just a small peak centred at 163.4 eV and no more sulphate features were found as it was for the core level before etching, while Si 2p was revealed just after Ar^+ sputtering. This is probably due to the inhomogeneity of the coating, already revealed by EDS observation of the surface reported in Figure 4.12, in which lighter compounds richer in F element were found. So on the top surface the coating showed enrichment in F 1s (intense peak at BE=688.6±0.1 eV related to the bond with C) [154], which mostly disappeared after etching for an increase of C 1s in correspondence with C-C and C-H compounds (BE=284.2±0.1 eV), reported in Table 4.5. This peak strongly decreased after etching while small Si 2p at BE=102.2±0.1 eV to be ascribed mainly to silane was found, indicating the presence of the silane MS.

Table 4.5: XPS atomic quantification (at%) of top coated surfaces before and after Dropping test. The XPS measurements are carried out after Ar^+ sputtering (200 eV for 30s).

	C 1s			N 1s	O 1s	F 1s			Si 2p			S 2p	Cu 2p	Sn $3d_{5/2}$	Pb $4f_{7/2}$
	CC, CH, CN, C-Si	C-O, C-S	C=O, O-C=O	N-C, N-O		F-Cu	F-C	$F_{(x)}$-C	O-Si-C, Si-O-Si	SiO_2	C-S	Sulphates	Cu(I)	Sn(IV)	oxide
Before ageing															
Incralac®															
Peak BE (eV)	284.7	286.3	288.5	399.4	532.1	-	-	-	101.8	-	-	-	-	-	-
at%	56.5	12.4	8.5	0.9	21.1	-	-	-	0.6	-	-	-	-	-	-
PropS-SH															
Peak BE (eV)	284.8	286.2	288.7	400.3	532.3	-	-	-	102.4	103.1	163.4	168.1	-	-	-
at%	33.5	2.9	0.7	0.7	32.3	-	-	-	10.6	8.6	9.7	0.9	-	-	-
FA-MS															
Peak BE (eV)	284.2	286.2	288.3	400.0	532.1	-	687.3	688.5	102.2	-	163.3	168.2	-	-	-
at%	63.7	12.4	3.3	3.1	10.8	-	2.9	2.6	0.4	-	0.4	0.4	-	-	-
After dropping															
Incralac®															
Peak BE (eV)	284.8	286.4	288.8	399.5	532.4	-	-	-	102.2	-	-	168.1	932.9*	486.2	137.9
at%	59.5	5.6	11.7	1.4	20.2	-	-	-	0.5	-	-	0.1	0.2	0.1	0.1
PropS-SH															
Peak BE (eV)	284.8	286.2	288.1	399.8	532.2	-	-	-	102.1	103.1	163.4	168.1	-	-	-
at%	37.4	6.6	0.7	1.3	30.2	-	-	-	8.7	6.4	6.6	2.2	-	-	-
FA-MS															
Peak BE (eV)	284.2	286.2	288.9	399.5	532.0	684.1	687.2	688.6	102.1	-	163.1	167.8	932.9*	-	-
at%	65.3	7.0	12.4	2.4	9.5	0.7	1.3	3.7	0.5	-	0.4	0.4	0.2	-	-

* KE (Cu LMM) = 915.8 eV; α' = 1848.7 eV Cu(I) - component.

4.3. Assessment of the coatings protectiveness: inhibiting efficiency after Dropping

The gravimetric measurements reported in Figure 4.13 shows that the uncoated Cu-Sn-Zn-Pb exhibits a marked parabolic trend ($R^2 = 0.996$) of mass decrease as a function of the Time of Wetness (ToW), while the coated samples reveal a very limited mass variations. These results confirm the protective barrier effect of the selected coatings. In particular, both the charged silanes act similarly showing a slight mass decrease almost constant during the Dropping exposure, while FA-MS exhibits a mass increase at the first stage of the ageing test (ToW=3 d). However for Incralac® a slight increase of mass was measured at the end of Dropping (ToW=10 d), probably linked to localised corrosion at the coating/substrate interface.
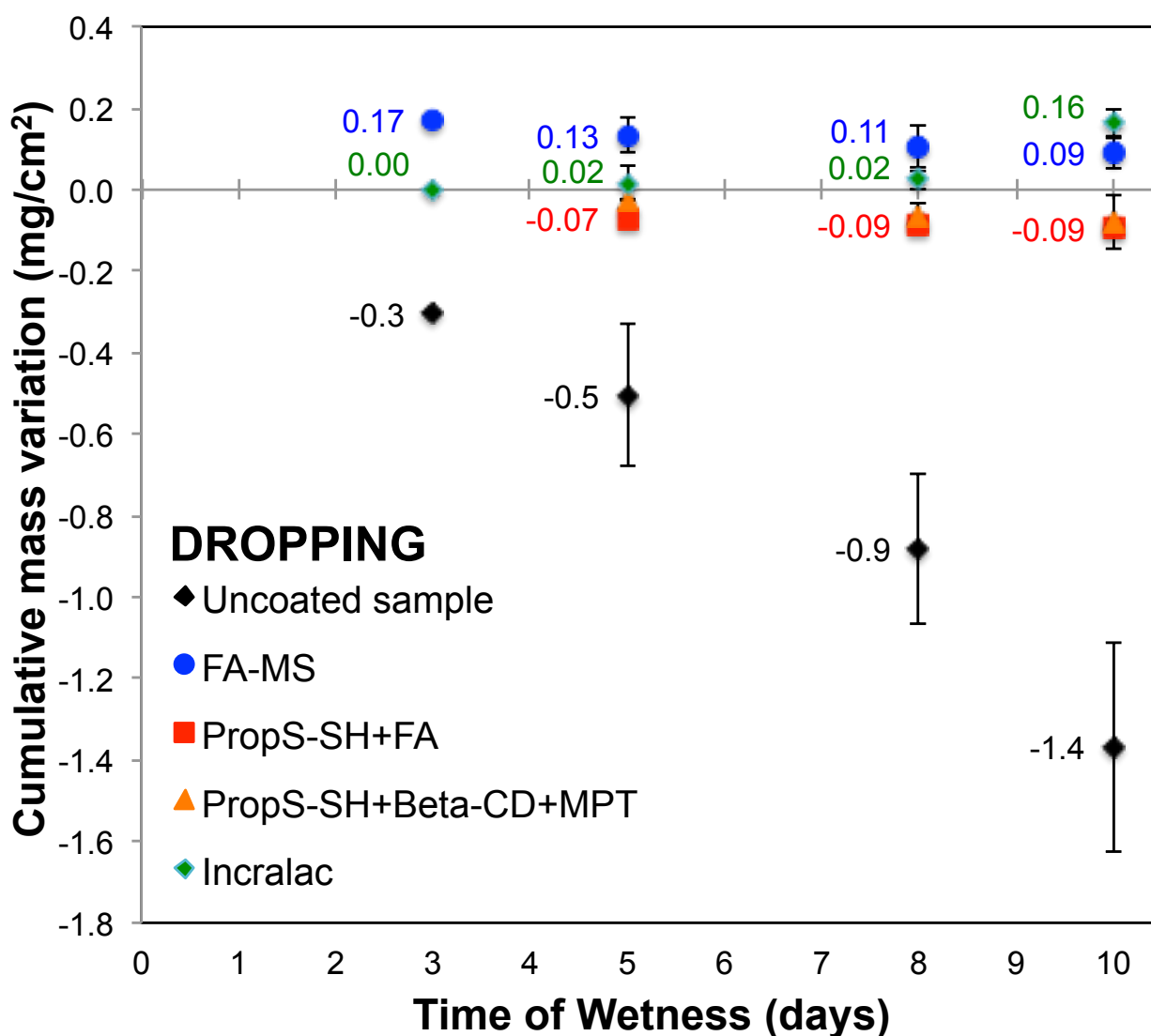
Figure 4.13: Mass variation for uncoated (in black) and coated patinated Cu-Sn-Zn-Pb samples (PropS-SH+β-CD+MPT in orange, PropS-SH+FA in red, FA-MS in blue and Incralac® in green).

The evolution of Cu, Zn and Pb cations, released in the weathering solutions, was measured as a function of ToW and results are reported in Figure 4.14. The measurement of the release of Sn soluble cations were under the Limit of Detection (LoD) in all the samples, as observed in previous studies [17,57,155]. For the uncoated

sample (in black), a linear Cu, Zn and Pb ions release trends were detected. In particular, the Cu/Zn ratio (about 20) is of the same magnitude order of the one measured from the alloy composition (about 28), indicating a similar tendency of Cu and Zn to dissolve under Dropping conditions, as previously observed in [34]. Conversely, the Cu/Pb ratio (about 17) is 2.5 times lower the value measured from the alloy (about 44), due to local Pb species precipitation. These results highlight that Dropping test always leads to a significant leaching of the surface of the unprotected samples inhibiting the formation of a protective barrier layer of Cu-based corrosion products. However, all the coated samples showed a lower dissolution rate of Cu, Zn (under the LoD for all the coatings and for this reason not displayed in Figure 4.14) and Pb compared to the uncoated ones, revealing a clear difference between uncoated and coated samples.
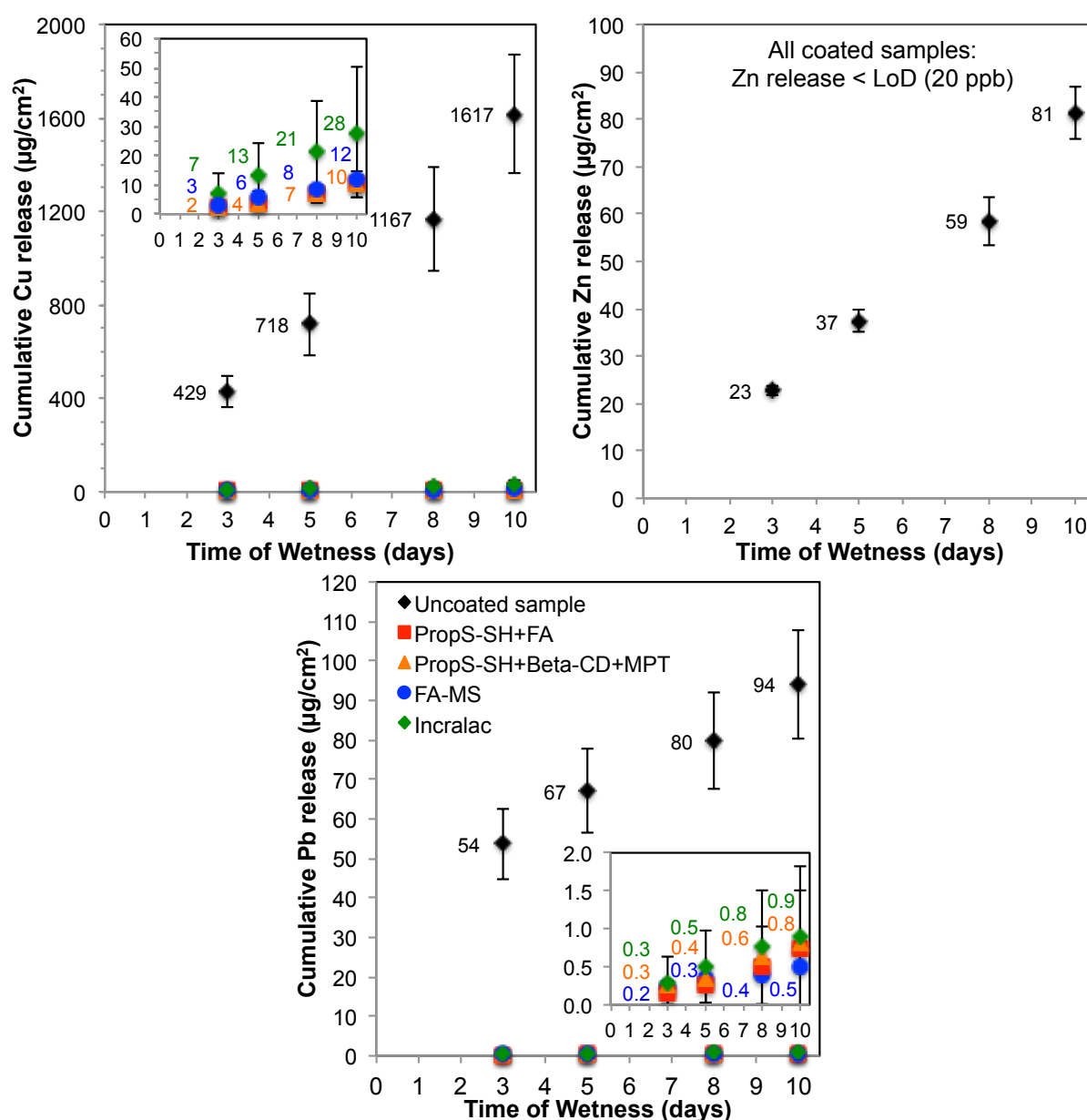
Figure 4.14: Cumulative Cu, Zn and Pb ions release (μg/cm^2) from patinated Cu-Sn-Zn-Pb bronze (uncoated and coated) in weathering synthetic solution, as a function of exposure time, for a total Time of Wetness (ToW) of 10 days of Dropping test (all the coated samples give a Zn release lower of the Limit of Detection (LoD=20 ppb)).

This clearly confirms the high protectiveness of these selected coatings. So, inhibiting efficiency values η calculated in accordance with Equation 3.1 highlight the high protective performance of the selected coatings. In particular, all the coatings afforded an average η_{Cu} of 99% (rsd = 22%) and η_{Pb} of 99% (rsd = 15%), except for Incralac[®] for which a η_{Cu} of 98% (rsd = 23%) was calculated.

4.4. Surface examination after Dropping

After Dropping test, uncoated and coated surfaces were analysed using the same methodology presented in paragraph 4.2 with the addition of the observation of *in situ* FIB cross-sections.

Colour measurements reported in Table 4.6 revealed that the appearance of the uncoated patinated Cu-Sn-Zn-Pb showed marked colour variations (ΔE^* = 12), mainly due to an increase of lightness component (ΔL^* = 11.5) and to chromatic variation toward green and blue. On the contrary, the coated samples do not significantly change after the Dropping test (ΔE^* < 3), indicating no evident visual alteration of the coatings in the test conditions occurred. This observation has to be related to a good protectiveness performance without patina evolution and formation of corrosion products at the interface between patinated bronze and the coatings.

Table 4.6: Colour variation measurements in CIELab 1976 colour space induced by accelerated ageing (Dropping) on coatings applied on patinated Cu-Sn-Zn-Pb.

	Δa^*	Δb^*	ΔL^*	ΔE^*
Uncoated sample	-2.5±0.8	-1.4±1.8	11.5±0.6	**12±1**
Incralac[®]	-0.2±0.3	-0.7±0.2	-0.3±0.2	**0.8±0.3**
PropS-SH+β-CD+MPT	0.31±0.03	-0.3±0.3	-0.6±0.4	**0.8±0.4**
PropS-SH+FA	0.0±0.4	0.6±0.7	-0.4±2.2	**1.7±0.7**
FA-MS	-0.11±0.03	-0.4±0.2	-0.2±0.6	**0.65±0.02**

Due to the fact that both PropS-SH charged with β-CD+MPT as corrosion inhibitor and with fly ash as micro-particles act in a comparable way under Dropping exposure, examination of the samples coated by PropS-SH+ β-CD+MPT is only reported in the following part of this results section.

Surface examination of uncoated patinated Cu-Sn-Zn-Pb after Dropping, reported in Figure 4.15a, confirms an extensive degradation of the surface induced by the ageing compared to the coated surfaces showed in Figure 4.15b-d, as already highlighted from gravimetric and metal release as well as colour variations measurements. In particular, corrosion products of the uncoated sample are non-homogenous, highlighting the bronze microstructure. In particular, dendrite borders showed strong corrosion and several cracks on corrosion products. The corrosion attack is preferentially developed between the Cu-rich core and the Sn-rich areas of eutectoid. In addition, the presence of the polishing grooves is revealed on the micrograph reported in Figure

4.15a. This indicates that corrosion attack is linked to an internal phenomenon inducing a corrosion patina of Sn-rich products (decuprification) and Dropping facilitates the leaching of Cu metal ions rather than the deposit of corrosion products, as already observed in [34]. On the contrary, no evident modifications were observed on the surfaces of the coated samples after Dropping (Figure 4.15 b-d), confirming the high protectiveness of the selected coatings.
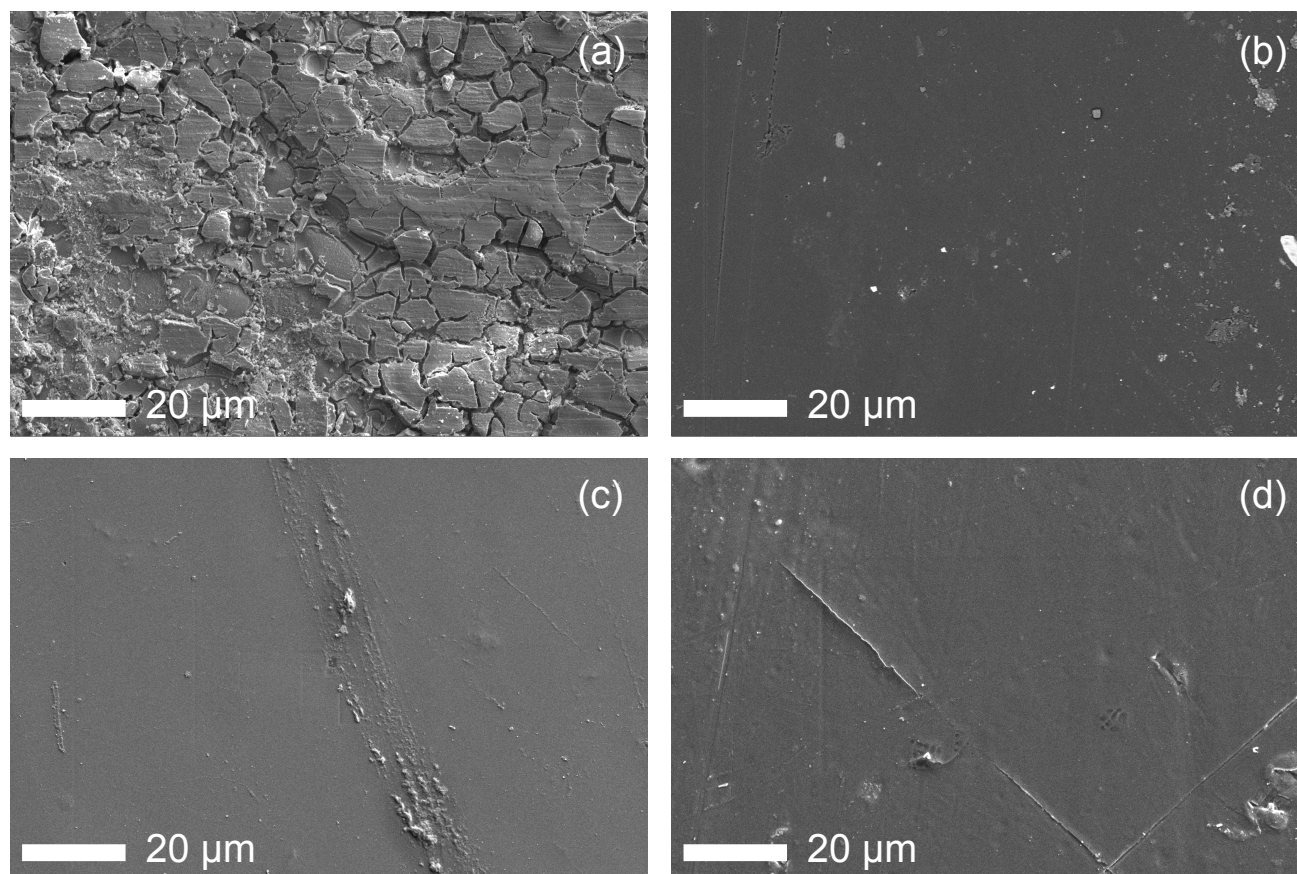
Figure 4.15: Surface morphology after Dropping: (a) uncoated patinated Cu-Sn-Zn-Pb sample; (b) patinated bronze coated by Incralac®; (c) patinated bronze coated by PropS-SH+β-CD+MPT; (d) patinated bronze coated by FA-MS.

The influence of Dropping on the coatings was also analysed by XPS measurements and the atomic quantification is reported in Table 4.5. These results showed that no significant variations occurred, except a slight increase of N and sulphates (centred at BE=168.1±0.1 eV) on the top surface of Incralac®. In addition, signals of the alloying elements appeared after the Dropping exposure. In particular, Cu 2p presents a main contribution centred at BE=932.9±0.1 eV (with the Auger peak centred at KE=915.8±0.1 eV with a modified parameter α'=1848.7 eV), indicating the presence of Cu(I) compounds related to Cu_2O species [146]. Moreover, also Sn and Pb were detected as oxide species in very low concentration: Sn 3d (BE=486.2±0.1 eV) showed the typical signal of Sn(IV) oxides, as reported in [147,156–159], while Pb 4f shows the main contribution centred at BE= 137.9 assigned to oxide [86,118].

Investigation of the microstructure of the interface between the coating and the patinated bronze after Dropping was performed thanks to the preparation of *in situ* FIB cross-section and the FEG-SEM observation.

The results for the uncoated sample are shown in Figure 4.16. Internal cracks within the corrosion (patina) were detected and some of the corrosion products forming surface patches were lost after the ageing process. The corrosion structure is not uniform within the whole cross-section, and it is more developed in correspondence with the interdendritic borders. In particular, a thick corrosion layer of about 3 μm is observed in the interdendritic areas, exhibiting a two-layer structure also highlighted by x-ray maps (Figure 4.16): a thin internal corrosion layer (< 300 nm) rich in Cu-O species and an external homogenous and dense outermost layer of Sn-O compounds, but with some nano-metric porosities close to the external/internal layers interface. However in the dendrite core, corrosion produces a thinner layer of about 1.5 - 2 μm, also characterised by a two layer structure but with an external one revealing an homogenous distribution of nano-metric interconnected pores, as observed for the pre-patinated quaternary bronze [160]. The observed corrosion behaviour is in good accordance with previous results achieved in quaternary bronze with different compositions, as reported in [34]. The α+δ eutectoid only reveals a thin corrosion film on the Cu-rich α-phase close to the surface.
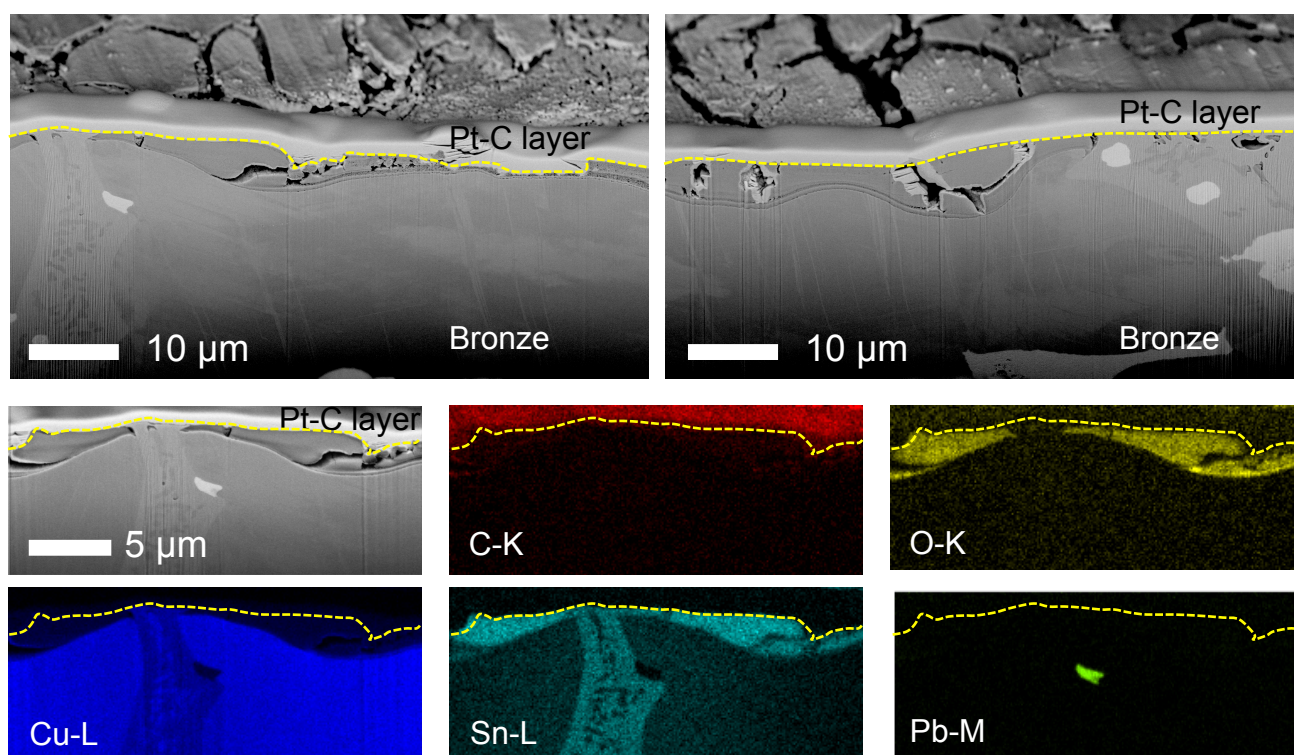
Figure 4.16: FIB cross-section of the uncoated patinated Cu-Sn-Zn-Pb after Dropping. X-ray maps of the cross-section showing the distribution of the main elements (Zn is not reported due to the not well-resolved EDS maps).

As regards the coated samples, observations of FIB cross-section are reported in Figure 4.17 - 4.19. In general, all the coatings fully cover the patinated Cu-Sn-Zn-Pb substrates and the polymer layers are quite homogenous in thickness. More in detail, Incralac® layer (Figure 4.17) exhibits an average thickness higher than 5 μm and it is characterised by the presence of few micro-pores entrapped inside the layer. This porosity should reduce with time the protective performance of Incralac® as barrier layer against the aggressive

particles present in atmosphere. Figure 4.17 also presents x-ray maps of C and O characteristic of the coating, as well as Cu, Zn and Sn signals of the alloy, confirming the homogenous chemical composition of the commercial reference, already observed from XPS data reported in Table 4.4.
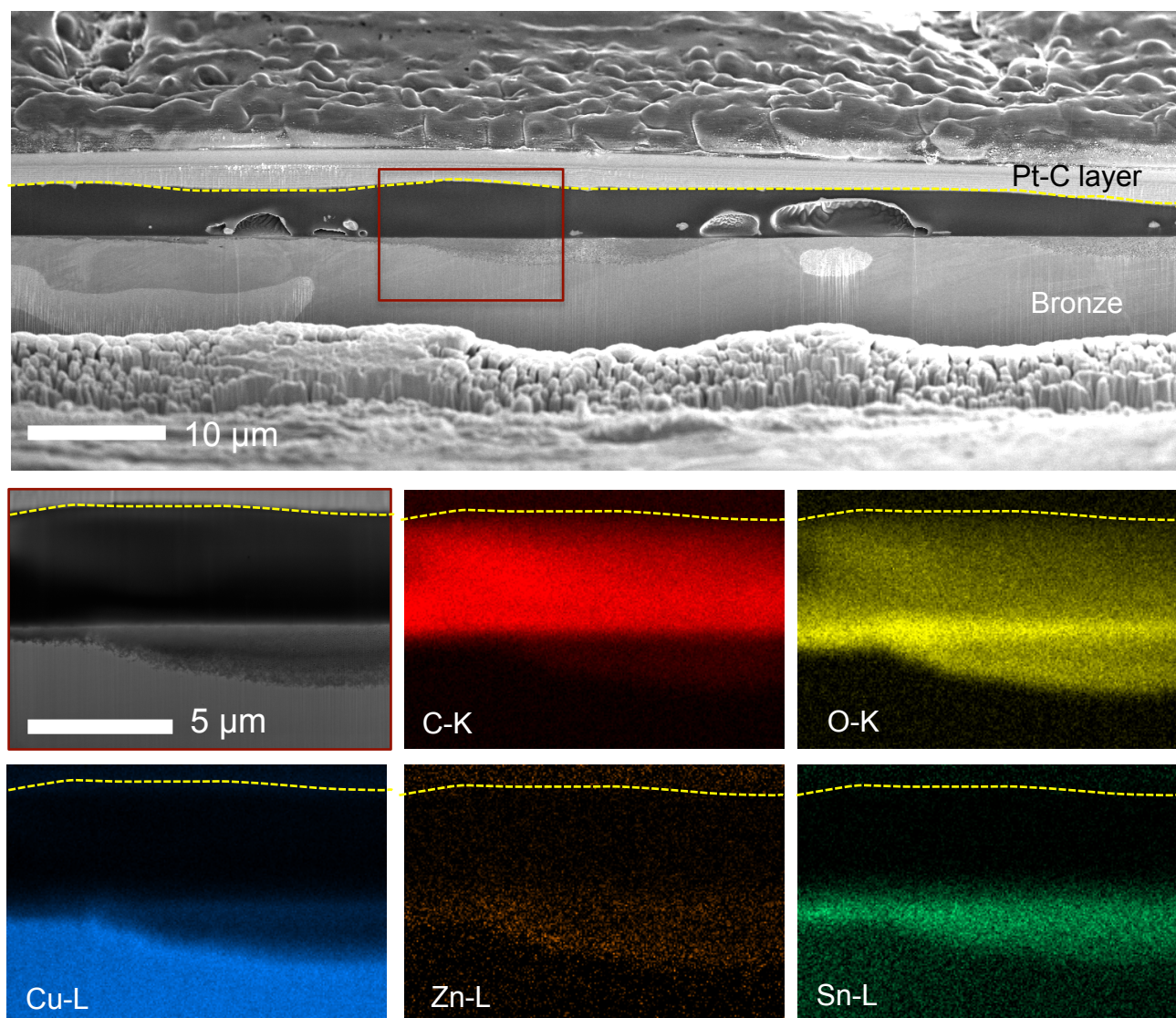
Figure 4.17: FIB cross-section of patinated Cu-Sn-Zn-Pb coated by Incralac® after Dropping. X-ray maps in correspondence of the red square show the distribution of the main elements in the coated system after ageing.

FIB cross-section of the PropS-SH+β-CD+MPT after Dropping did not reveal any corrosion attacks at the interface between the coating and the patinated substrate (Figure 4.18). Differently from Incralac® layer, this coating allows the formation of continuous layer and no porosity was detected. Such difference is likely connected to a different wettability of the patinated substrate by the coating formulations. In addition, x-ray maps reported in Figure 4.18 also highlighted the fact that the silane coating is able to fill up the porosities of the patina, inducing a better bond on the patinated substrate.
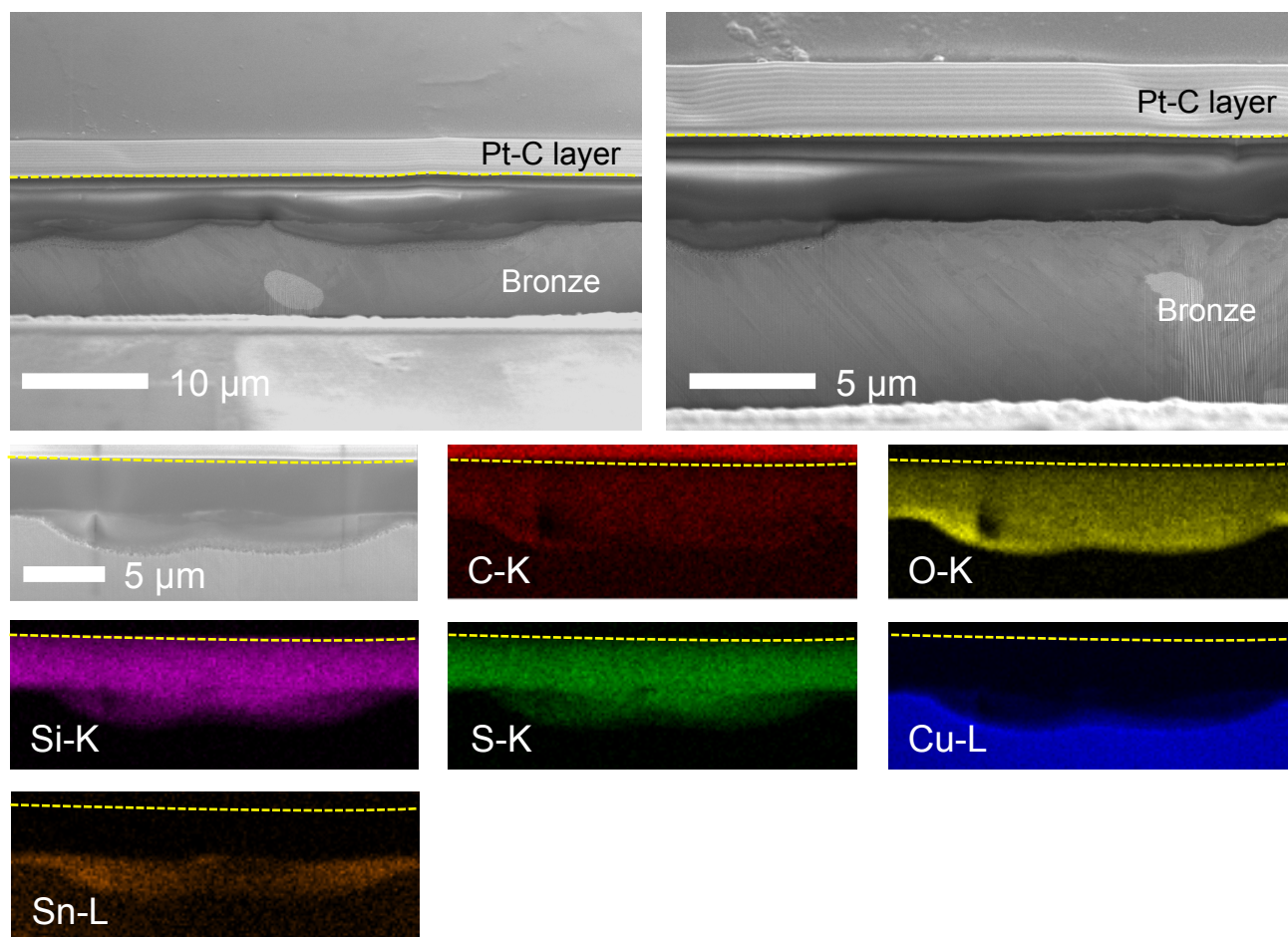
Figure 4.18: FIB cross-section of patinated Cu-Sn-Zn-Pb coated by PropS-SH+β-CD+MPT after Dropping. X-ray maps of the cross-section showing the distribution of the main elements in the coated system after ageing (Zn is not reported due to the not well-resolved EDS maps).

Finally, Investigation of the cross-section of the FA-MS coated sample is illustrated in Figures 4.18, as well as x-ray maps recorded in a representative portion of the *in situ* FIB cross-section. FA-MS is highly sensitive to the electron beam. Thus during the FIB session, the coating also showed some peeling and degradation due to electron and ion beam. The FIB cross-section showed the corrosion layer relative to the patination process and revealed also some coating accumulation characterised by higher coating thickness relative to some shrinkage porosity in the bronze substrate. Generally the FA-MS layer is thin, characterised by a mean thickness of 2 μm, except in correspondence of the coating accumulation areas, where the thickness ranges from 5.5 to 7 μm. In addition, the coating layer showed few porosities and the coating/substrate interface followed the substrate morphology, but it also revealed some nano-porosities of the coating. As previously pointed out from XPS measurements as well as surface observation, x-ray maps highlight a chemical heterogeneity of the coating, showing a F enrichment in the internal part of the FA-MS layer.
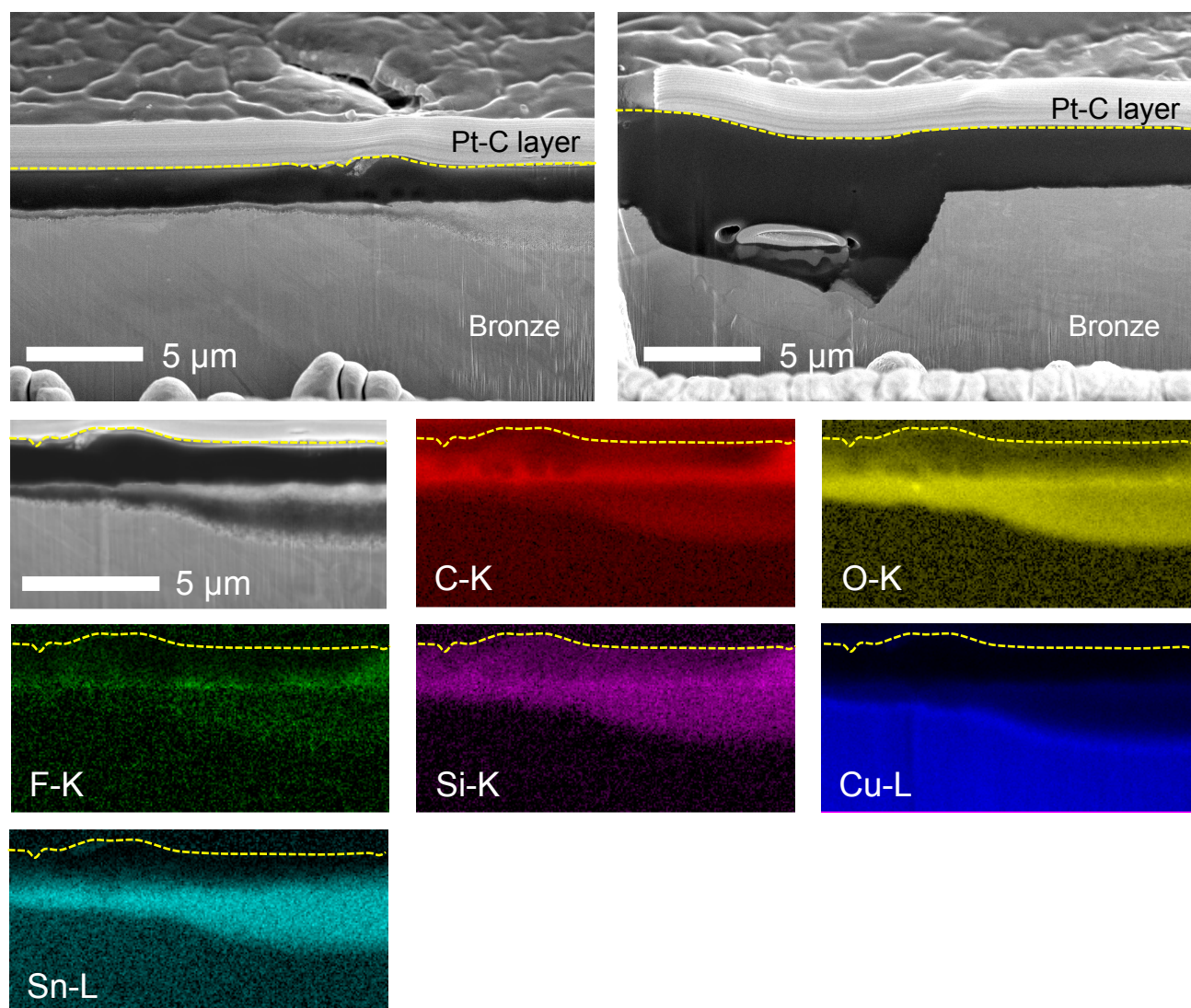
Figure 4.19: FIB cross-section of patinated Cu-Sn-Zn-Pb coated by FA-MS after Dropping. X-ray maps in correspondence of the cross-section showing the distribution of the main elements in the coated system after ageing (Zn is not reported due to the not well-resolved EDS maps).

These observations suggest that both the silane and the FA-MS coatings efficiently act as a barrier layer, while Incralac® layer exhibit lower durability due to the presence of micro-porosities, even if all the coatings exhibit very high and comparable inhibiting efficiency in terms of metal release.

4.5. Other result from B-IMPACT project

To present an overview of other results about the selected coatings applied on patinated Cu-Sn-Zn-Pb bronze achieved in the B-IMPACT project, results from the electrochemical tests performed by I-UniFE (Italy) and S-ZAG (Slovenia) reported in the B-IMPACT Deliverable 2.1 – Proposal of candidate protection systems for patinated bronze and B-IMPACT Deliverable 2.2 – Protection efficiency report for eco-friendly coatings [120,135] and from the Occupational Exposure tests performed by I-ECAM and reported in B-IPACT Deliverable 3.3 – Assessment of TLW/TWA and STEL [137] are reported in paragraph 4.5.1 and 4.5.2, respectively.

4.5.1. Electrochemical tests

In the project deliverables [120,135], the protection efficiency of the selected surface treatments was investigated by monitoring the time evolution of the polarization resistance R_p and corrosion E_{cor} values. The results obtained during 30 days of continuous exposure to concentrated acid rain ARX10 are profusely discussed in [120,135] and only the results recorded for the plain and charged PropS-SH coatings, as well as FA-MS, applied on patinated Cu-Sn-Zn-Pb are reported in this paragraph. In particular, Figure 4.20 reported the trends of R_p as a function of immersion time and polarization curves of uncoated and coated sample by plain and charged PropS-SH costing. As regards the uncoated patinated Cu-Sn-Zn-Pb, the measured R_p values showed a slight increase during the initial time of the exposure until 8 days of immersion. Then, they decreased until the end of exposure (Figure 4.20, black line). This indicates that the precipitation of corrosion products on the surface only partially protects the metallic substrate. Regarding the exposure of the samples coated by Incralac® (Figure 4.20, dash line), the R_p values continuously decreased as a function of immersion time, indicating that this coating well adhered on patinated Cu-Sn-Zn-Pb substrate and offered good protection, but the slow penetration of the aggressive solution and dissolved oxygen partially impaired its performance. However, both the plain and the charged PropS-SH coatings applied by spraying determined some improvements in the protective efficiency of the patinated Cu-Sn-Zn-Pb, mainly due to an increase of the coating thickness compared to the plain PropS-SH applied by dip-coating (Figure 4.20, blue line). In particular, all the sprayed silane coatings (Figure 4.20, green lines) exhibited R_p values one order of magnitude higher than the same coating obtained by dip-coating.

The polarization curves recorded on the selected coatings after 30 days of immersion reported in Figure 4.20b and d show that only PropS-SH+β-CD+MPT exhibited E_{cor} values nobler than that of the blank. Incralac® appreciably inhibited the cathodic process, while both charged PropS-SH with FA and β-CD+MPT as well as FA-MS (here not reported) exhibited a more efficient barrier effect against both the cathodic and anodic process.
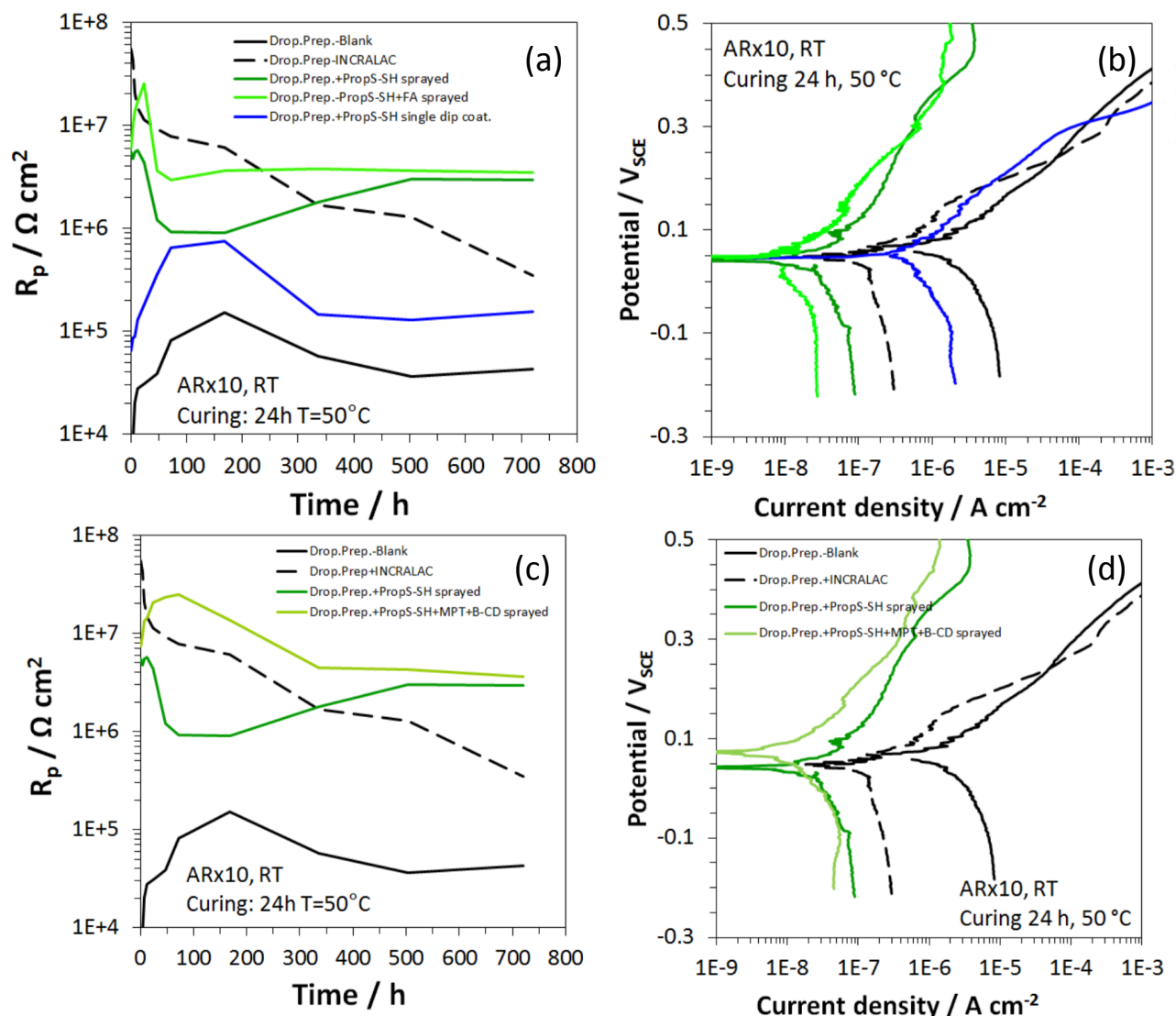
Figure 4.20: Electrochemical characterisation of uncoated and coated bronzes by different silane coatings. (a, c) Polarization resistance R_p and (b, d) corrosion potential values (E_{cor}) recorded during 30 days exposure to ARX10 [135].

Finally, in the B-IMPACT deliverables [120,135] E_{cor} and i_{cor} values deduced from the 30 days polarization curves and the final protective efficiency (PE), calculated using Equation 3.5, are reported (Table 4.7). These results showed that the final PE values for all the developed coatings are 99%, while for Incralac[®] PE value is 89%. So, the time evolution of the polarization curves stresses the excellent performances (higher than Incralac[®]) of the charger PropS-SH as well as of FA-MS during the continuous exposure to concentrated acid rain (ARX10).

Table 4.7:Parameters obtained from 30 days of polarization curves [135].

Samples	E_{cor} (V_{SCE})	i_{cor} $(\mu A\ cm^{-2})$ 30 days	PE (%)
Patinated Cu-Sn-Zn-Pb	0.065	1.0	-
Incralac®	0.047	0.11	89
PropS-SH+β-CD+MPT (spraying)	0.075	0.01	99
PropS-SH+FA (spaying)	0.040	0.01	99
FA-MS (brushing)	0.030	0.02	99

4.5.2. Eco-toxicity

Regarding eco-toxicity measurements, only values of the Exposure Limit (EL) of the selected coatings, reported in [137], are shown in this thesis (Table 4.8). The measurements performed by I-ECAM (Italy) and reported in the B-IMPACT deliverable [137] permit to rank the selected coatings on the basis of their occupational impact. So, the selected coatings were ranked as follows, from the safest to the most hazardous:

$$PropS\text{-}SH+\beta\text{-}CD+MPT \approx PropS\text{-}SH+FA > FA\text{-}MS >> Incralac^{®}$$

Considering that a coating must have an EL < 1 to be compliant, all the selected coatings performed better that the commercial reference Incralac® that showed an EL = 1.108. This is mainly due to the presence of toluene, methyl-acetate and other uncalibrated VOCs as n-hexane.

Table 4.8:Values of the Exposure Limit (EL) for the coatings selected for the protection of patinated Cu-Sn-Zn-Pb [137].

Coating	Exposure Limit (EL)
Incralac®	1.108
PropS-SH+β-CD+MPT	0.045
PropS-SH+FA	0.050
FA-MS	0.301

4.6. Conclusive remarks

The following conclusions could be drawn from the results presented in Chapter 4:

- The quaternary bronze artificial patinas produced by the dropping and Wet&Dry methods can be considered as representative aged surfaces for outdoor bronze monuments. Coupling morphology and elemental analysis of the surface and the cross-section of the artificially corroded samples allowed a fine physical and chemical characterization of the corrosion structure up to a few nm size. In particular, FIB milling on the SEM represents a promising scientific approach for bronze corrosion investigation.

- Dropping and Wet&Dry-aged bronze surfaces reveal general corrosion behaviour connected to the decuprification process, inducing internal oxidation and the preferential release of Cu and also Zn from the alloy. Both samples show layer thicknesses of a few μm in the anodic parts and few-nm-thick films in more cathodic parts, in the dendrite border close to the eutectoid. However, the corrosion layer on the samples achieved with the dropping method is more homogenous and thicker (2 μm). The corrosion layer produced by Wet&Dry highlighted a compact internal layer and porous external one of around 1 μm.

- A clear difference between the two ageing methods is the production of a slight erosion effect by the dropping and a corrosion deposit by the Wet&Dry. Mainly, the metal-oxygen compounds not well crystallised, as Cu_2O and Sn-O were observed on the corroded surfaces by the dropping test, due to runoff, whereas hydroxyl-sulphates and cuprite characterized the patinated surface produced by the Wet&Dry test. Chlorine is found in both samples but only in very minor amounts in the anodic areas, more located within the corrosion layer for the Dropping test and at the interface of the cuprous oxide/alloy for the Wet&Dry samples. Nano-porosities are evidenced in both corrosion structures: uniformly distributed throughout the whole thickness for the Dropping tests, and mainly located in the external part for the Wet&Dry samples. This evidence of nano-porosities confirmed the impact of the decuprification process and can be ascribed to Cu and Zn-selective dissolution accompanied to the formation of a tin-species network within the corroded structure, forming a porous layer more evidenced in the case of rainwater runoff.

- The assessment of the protectiveness of charged silane coatings (PropS-SH+β-CD+MPT and PropS-SH+FA) and FA-MS coating was carried out by a multi-scale approach. All the applied coatings produced continuous layers. However, Incralac® exhibits some uncovered areas, as well some micro-pores embedded within the coating layer. In addition, the application by spraying of both Incralac® and charged PropS-SH coatings on patinated Cu-Sn-Zn-Pb induce a colour variation closed to the limit of the acceptability for Cultural Heritage applications (ΔE* < 5), while FA-MS did not exhibit noticeable changes in terms of colour variations.

- After Dropping exposure, inhibiting efficiency in terms of metal release was found higher than 98% for all the coatings. These results are confirmed by the observation of surfaces and *in situ* FIB cross-sections that do not exhibit alterations and the precipitation of corrosion products in the interface between coating and patinated bronze.

- Based on the results from electrochemical tests, all the selected coatings offer a good protection to patinated Cu-Sn-Zn-Pb better than Incralac®, showing a more efficient barrier effect against both the cathodic and anodic process. Final protective efficiency (PE) values are 99% and 89% for the developed coatings and for Incralac®, respectively.

- Finally, the measurements from the occupational exposure test determine that the selected coatings (both charged silanes and FA-MS) exhibit a EL < 1, contrary to what measured for Incralac® (EL = 1.108). This indicates that all the developed coatings are non-toxic and non-hazardous for restorers and operators.

5. XPS STUDY ON THE INTERACTION OF SILANE COATING ON Cu-Sn-Zn-Pb-Sb

5.1. Thick PropS-SH coatings on quinary bronze

Starting from the most representative system of real outdoor bronzes, images of thick PropS-SH coatings on quinary bronze obtained by 1h immersion are shown in Figure 5.1 for both bare (left-hand side) and artificially patinated (right-hand side) samples. In Figures 5.1a and b, the low magnification tilted images of the free surface reveal different features when PropS-SH coating is applied on bare or patinated bronze, highlighting the influence of the substrate. In particular, they show that PropS-SH adapts tightly to the surface morphology of the substrate, so that a very smooth and planar surface is achieved on the polished alloy, while the initial rough morphology is still observed on the patinated sample.

SEM images of the micrometric cross-section slices prepared by FIB lift-out technique are reported in Figures 5.1c-f for the same samples. Figures 5.1c and d give a general view of bare and patinated bronze cross-sections respectively, while higher magnification images are reported in Figures 5.1e and f, so allowing a better identification of microstructural details and layer sequence. In both cases, the Pt-C overlayer (for protection during FIB milling) is visible above the organosilane coating.

The application of PropS-SH on bare bronze (Figures 5.1a, c and e) produces a rather homogeneous layer with an average thickness of about 0.3 μm. However, when PropS-SH is applied by 1h immersion on the uneven patinated bronze (Figures 5.1b, d and f), the coating fills up the localised corrosion areas forming a layer with variable thickness (dark grey in Figures 5.1d and f). Figure 5.1d shows a crater of corrosion preferentially developed within the brighter grain on the right-hand side corresponding to dendrite core, being the grain microstructure of the bronze highlighted thanks to the electron channelling contrast.
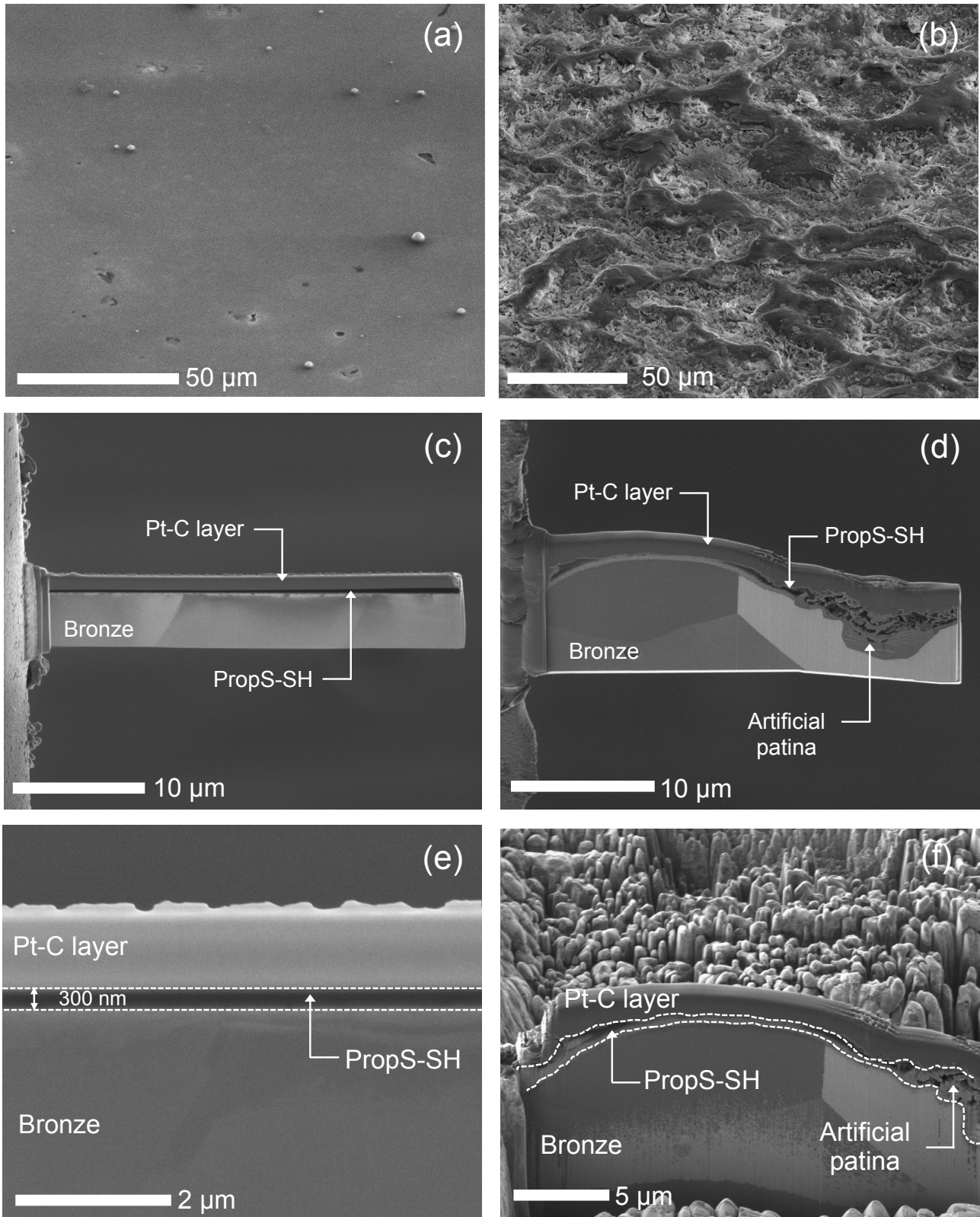
Figure 5.1: SEM observation of PropS-SH coatings on quinary bronze substrate. Left-hand side (a, c, e): bare bronze / Right-hand side (b, d, f): patinated bronze. (a, b) PropS-SH coating surfaces; (c, d, e, f) cross-sections prepared by FIB (Focused Ion Beam) lift-out technique [121].

In order to investigate more deeply the elemental distribution within the PropS-SH coating on quinary bronze, EDS and HR-SRPES maps of elemental distribution were collected in the same locations on the free surface of the coated bare bronze samples.

EDS maps are reported in Figure 5.2 for a typical area where the PropS-SH coating covers a shrinkage micro-cavity at the dendrite border, located in the centre of each image. Regarding the characteristic elements belonging to PropS-SH, C and O show a relatively homogeneous distribution, while Si and S exhibit locally higher intensities in correspondence with the shrinkage micro-cavity. Hence, the more intense signal of Si and of S is related to a possible accumulation of PropS-SH, filling up this cavity. In addition, due to the low thickness of the silane coating (~300 nm), also X-rays emission from bronze alloying elements is detected, revealing the microstructure of the as-cast bronze with Sn micro-segregation in the interdendritic space.
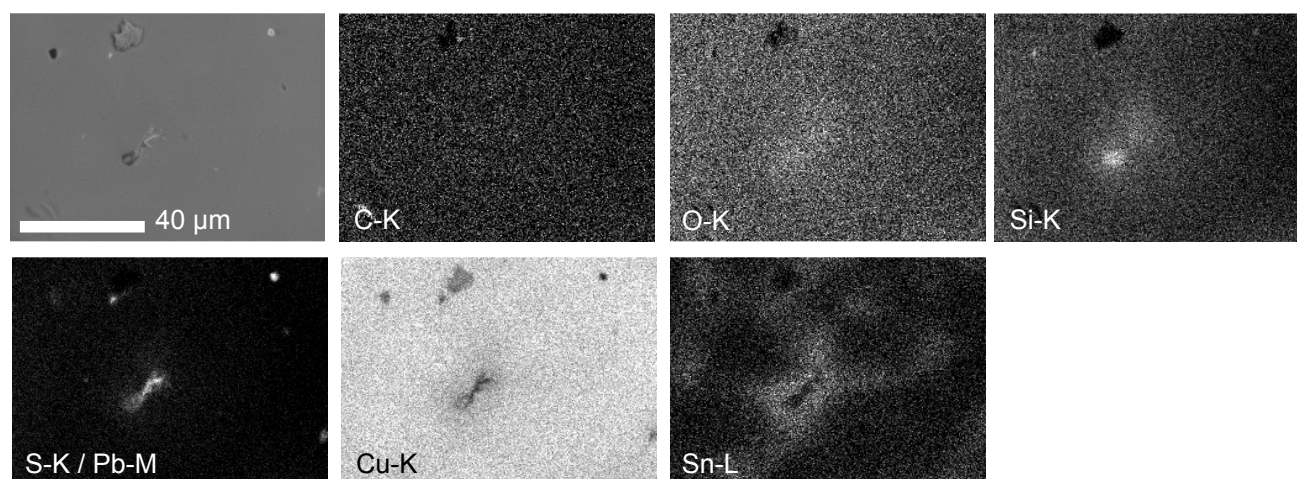
Figure 5.2: PropS-SH on bare quinary bronze, SEM/EDS analysis of the free surface: SE image and X-ray maps of the main elements (C, O, Si, S, Cu, Sn and Pb) [121].

HR-SRPES chemical imaging brings complementary information about coating elements distribution: it is worth noting that in the case of HR-SRPES only the top surface (a few nm) of the coating is investigated, while EDS results reveal the alloying element distribution underneath the coating as previously discussed.

Figure 5.3a reports the optical observation of the same area where EDS maps of Figure 5.2 were collected and where HR-SRPES maps of Figures 5.3b-d were recorded as well. It shows some colorimetric interference surrounding the central micro-porosity in the middle of the image. This could be linked to small variations of coating thickness according to a different elemental distribution on the surface, as revealed in Figures 5.3b-d, related to the HR-SRPES maps of C 1s, O 1s and Si 2p at a micrometric scale.
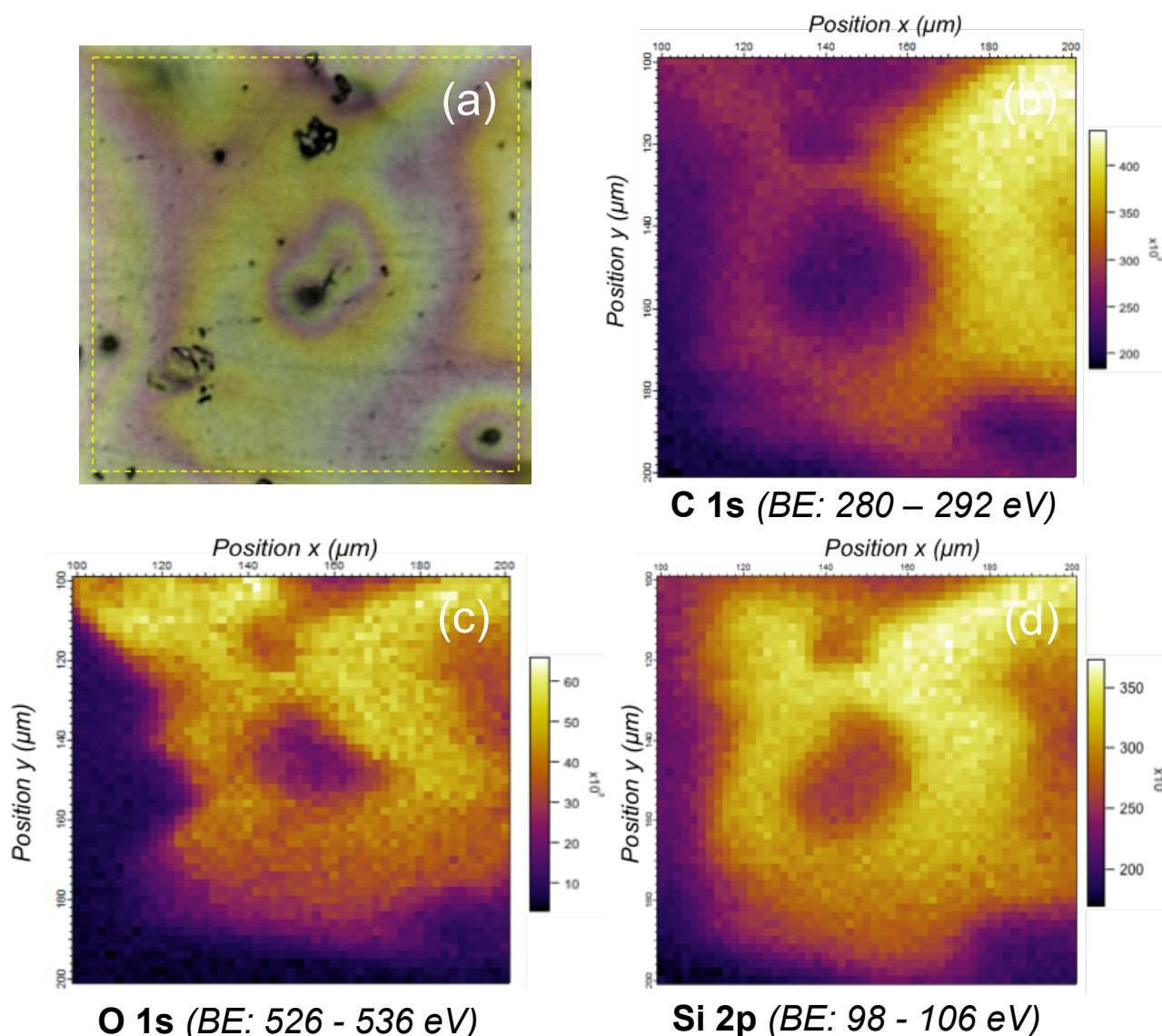
Figure 5.3: PropS-SH on bare quinary bronze, free surface: optical image (a) and HR-SRPES maps for C 1s, O1s and Si 2p (b-d). The optical image (a) shows the analysed area, corresponding to the same location of Figure 5.2: the yellow dashed square indicates the area covered by HR-SRPES maps (side of the square=100 μm) (b-d) [121].

In fact, these signals are rather strong in the area surrounding the cavity, while they are absent in the cavity itself. Conversely, EDS Si and O signals are more intense into the cavity than outside it and decrease towards the dendrite core, as shown by the Sn distribution map in Figure 5.2, highlighting microstructural features. These observations suggest that the organosilane coating accumulates at the bottom of the cavity (as shown by EDS signals, coming from a higher depth than HR-SRPES), replicating the surface topography, while it is not detectable in the upper volume of the cavity itself (as suggested by HR-SRPES signal from the uppermost layer) because the coating does not level up completely the surface. This is probably due to the relatively low viscosity of the adopted silane solution and to capillary effects, which allow its penetration into recessed features.

109

5.2. XPS analysis: PropS-SH-coated metals and alloys and uncoated quinary bronze

In order to deeply investigate the coating-substrate bonding system, which is very important for understanding PropS-SH protective properties both on bare and patinated bronze, XPS analyses on coated samples and on uncoated bare quinary bronze were performed, using a larger spot size than in HR-SRPES and taking into account very thin PropS-SH deposits on Cu, Sn, Cu8Sn and bare quinary bronze, so as to investigate the coating-substrate interface. Tests on ZrN and patinated quinary bronze, both coated by 1h immersion, and uncoated quinary bronze were also performed to investigate, respectively, the coating bulk, a sample more representative of a real coated system and the bronze substrate before coating application. Elemental Zn was not taken into consideration as a reference material, because in patinated bronze Zn is selectively dissolved in the environment, so that it is no more detected in patinas [18,122]. To help comprehension of the following results, Table 5.1 reports the values of XPS peak positions of the main elements detected on the top surfaces of the different PropS-SH coated samples in this study.

Table 5.1: Binding energies of the different chemical species detected in XPS core levels [121].

Element	Peak	Position (eV)	References
C 1s	CC, CH, C-Si	284.5	
	C-O, C-S	286.2	[52,53]
	C=O, O=C-O	288.3	
O 1s	-	531.8	[52,161]
Si 2p	C-Si-O, Si-O-Si	101.7	[52,53,161,162]
	Si-O (SiO$_2$)	103.2	
S 2p$_{3/2}$	S-C, S-Metal	162.5	[52,53,151–153]
	sulfates	168.5	
Cu 2p$_{3/2}$	Cu(0)	932.5[*]	[86,118,163,164]
	Cu (I)	933.1[**]	[51]
Zn 2p$_{3/2}$	Oxide	1022.1	[86,118]
Sn 3d$_{5/2}$	Metal	484.7	
	Sn(II)	485.9	[147,156–159]
	Sn(IV)	486.7	
Pb 4f$_{7/2}$	Oxide	138.7	[86,118]

[*] KE (Cu LMM) = 918.0 eV; α' = 1850.5 eV – Cu(0) component
[**] KE (Cu LMM) = 915.6 eV; α' = 1848.7 eV – Cu(I) component

5.2.1. ZrN (reference substrate)

The obtained XPS surveys are reported in Figure 5.4. Figure 5.4a refers to PropS-SH layer on ZrN and it shows intense peaks of the characteristic elements of the coating (C 1s, O 1s, Si 2p, S 2s and S 2p). No signal

from the substrate (Zr 3d and N 1s) is detected, suggesting that, as expected, the spectrum in Figure 5.4a is not affected by the substrate/coating interface and can be considered as a reference one for PropS-SH coating.
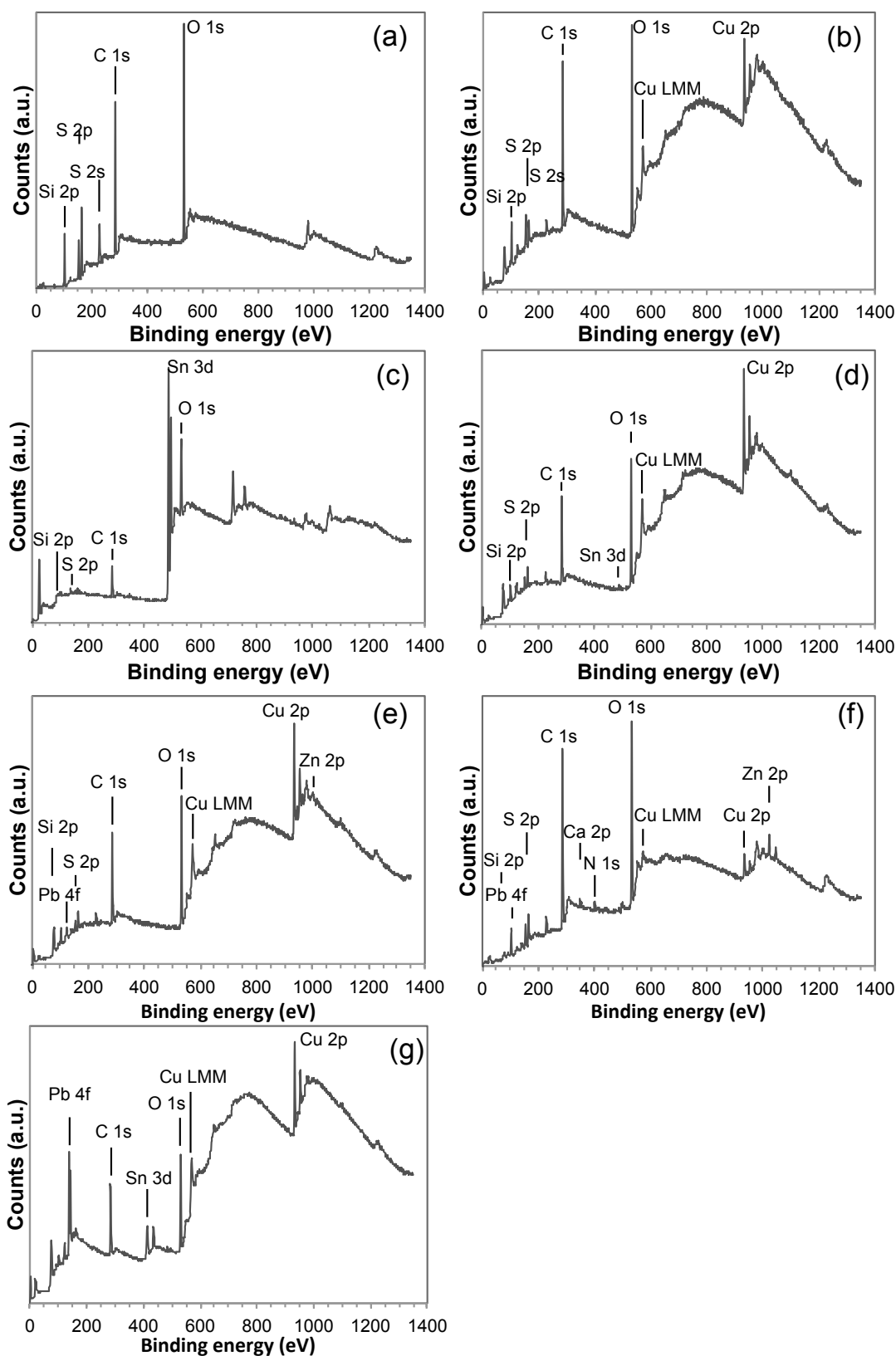
Figure 5.4: XPS surveys of PropS-SH layer on: (a) ZrN, (b) Cu, (c) Sn, (d) Cu8Sn, (e) bare quinary bronze, (f) patinated quinary bronze and (g) uncoated bare quinary bronze (BQ), (thin coatings in (b), (c), (d) and (e)) [121].

The core level spectra of C 1s, O 1s, Si 2p and S 2p are reported in Figure 5.5a-d, respectively.

C1s spectrum in Figure 5.5a shows a sharp peak centred at 284.5 eV (BE), typical of aliphatic chain (C-H bond) of PropS-SH and atmospheric compounds adsorbed on the surface. Characteristic contributions of silane layer are highlighted by O 1s and Si 2p levels at binding energies of 531.9 eV (O1s core level spectra of Figure 5.5b) and 101.8 eV (S2p core level spectra of Figure 5.5c). These BE values indicate a main contribution of the Si-O-Si bonds, suggesting a good grade of reticulation of the coating [52,161,162]. Figure 5.5d evidences that the contribution of S $2p_{3/2}$ is centred at 162.9 eV, representative of S-C bonds [151]. In particular, the analysis of S 2p signal takes into account the presence of a doublet structure of the core level with a spacing of 1.2 eV (S $2p_{1/2}$ - S $2p_{3/2}$ = 1.2 eV) and a theoretical intensity ratio of 2 (S $2p_{3/2}$/S $2p_{1/2}$=2). No evidence of unreacted thiol groups (-SH) usually occurring at around 163.5 eV (BE) [52,152] was observed in the S 2p core level, likely due to prevalent adsorption through metal-thiolate bonds [60].

Figure 5.5: XPS core levels of the characteristic PropS-SH elements on the different substrates (thin coatings on Cu, Sn, Cu8Sn, and Q): (a) C 1s, (b) O 1s, (c) Si 2p and (d) S 2p [121].

5.2.2. Pure Cu

XPS survey of the thin PropS-SH layer applied on pure Cu substrate is reported in Figure 5.4b. Characteristic elements of the coating (C 1s, O 1s, Si 2p, S 2s and S 2p) are clearly detected as previously observed for the coating reference, as well as the intense signal of the substrate (Cu 2p). In particular, Figure 5.5 shows the main contributions of C 1s, O 1s, Si 2p and S 2p, centred at binding energies of 284.5 eV, 531.9 eV, 101.7 eV and 162.6 eV, respectively. C 1s signal also shows some small contributions at higher binding energies (Figure 5.5a), that is at 286.2 eV and 288.3 eV, corresponding to C-S / C-O and O=C-O, respectively. The former C 1s contribution (C-S) is typical of the studied silane molecule, while the latter suggests that some PropS-SH oxidation occurs [56]. On this substrate, S 2p signal shows two different contributions: S $2p_{3/2}$ BE=162.6 eV, ascribed to S-Cu thiolate bond [52,53,153] or S-C, and BE=168.2 eV, mainly related to sulfate, as better distinguishable in Figure 5.5d. It is well known that the partial oxidation of the thiol groups can occur in the presence of oxygen gas contamination [149,150] and it is catalysed by the presence of multiple-valence cations (like Cu and Sn ions), among which Cu ions show high catalytic effects [149]. This justifies the presence of oxidized species on coated Cu, but not on coated ZrN, as from zirconium element only zirconium (IV) cations can be formed. It is significant that the thiol group oxidation occurs concurrently to the oxidation of silane aliphatic chain.

5.2.3. Pure Sn

XPS survey of coated pure Sn (Figure 5.4c) shows weaker peak intensities of the characteristic elements of PropS-SH, in comparison to pure Cu. In particular, contributions at higher BE for C 1s (BE = 286.2 and 288.3 eV) are more intense than those on Cu, indicating a higher degree of oxidation (Figure 5.5a). Figure 5.5 b shows that for O 1s a shoulder at BE=530.4 eV occurs, typical of oxide species linked to Sn. Si 2p and S 2p signals (Figure 5.5c and d) are with scarce intensity, noisy and characterized by broad peaks. For S 2p signal (Figure 5.5d), the contributions due to the S-Sn/S-C environment (BE=162.5 eV) and to SO_x (BE=168.5 eV) are comparable.

Figure 5.6a shows the characteristics of Sn 3d core level detected on coated Sn metal. Sn 3d exhibits three different contributions at 484.7 eV, 485.9 eV and 486.7 eV, corresponding to metallic Sn, Sn(II) oxide (SnO) and/or Sn(II)-S, and Sn(IV) oxide (SnO_2) with a possible $Sn-SO_x$ contribution, in good accordance with literature data [147,156–159]. Here the distinction between Sn(II) and Sn(IV) peaks has been performed assuming a FWHM value of 1.3 eV and 1.5 eV, respectively. These findings indicate the formation of a thinner PropS-SH coating on pure Sn compared to pure Cu substrate and suggest that the Sn oxidized species can have a considerable catalytic effect in the oxidation of thiol group inducing the formation of significant amounts of poorly soluble SO_x compounds.
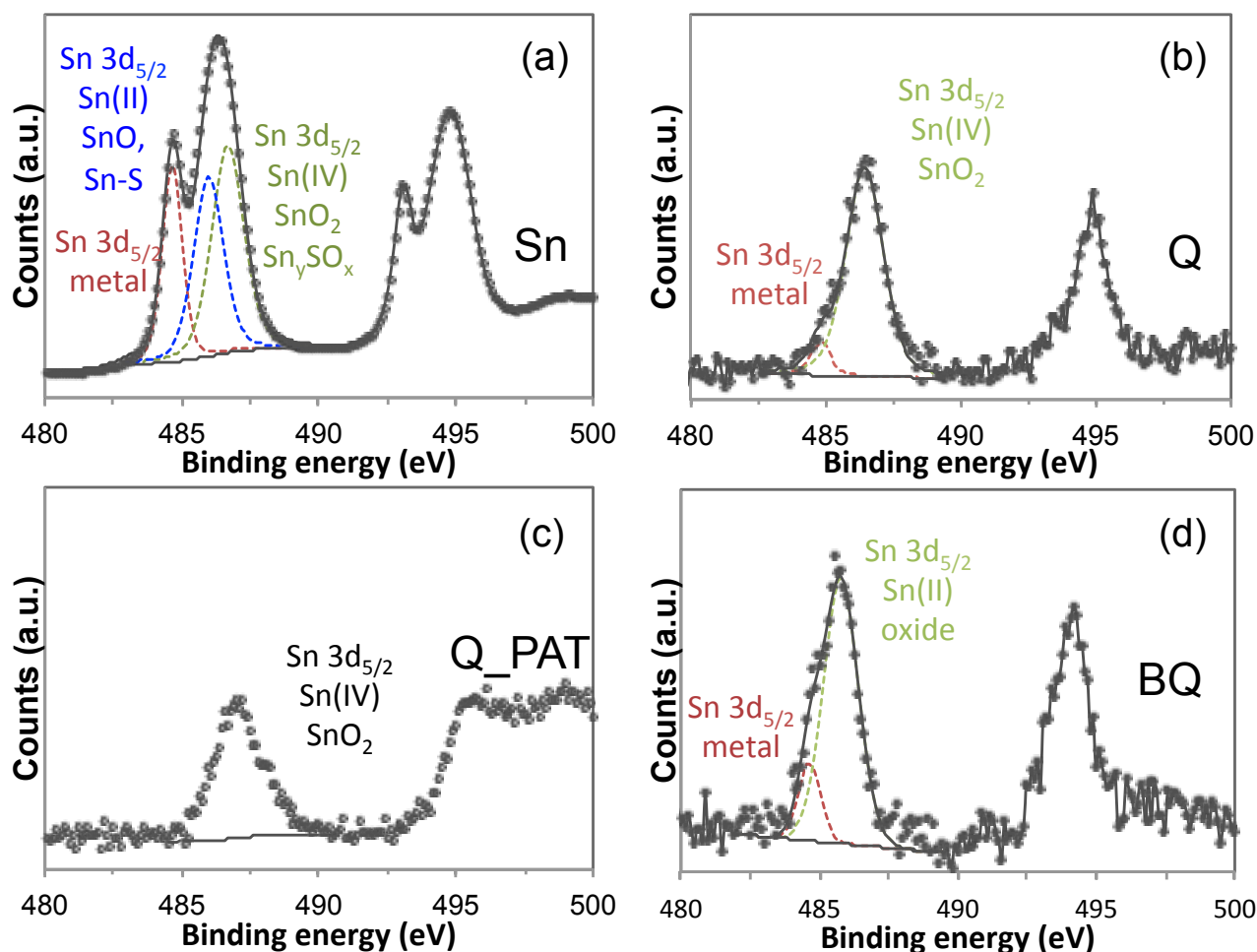
Figure 5.6: XPS core level of Sn 3d measured on (a) pure Sn coated with PropS-SH; (b) quinary (thin coating); (c) quinary patinated bronze and (d) uncoated bare quinary bronze (BQ) [121].

5.2.4. Cu8Sn and quinary bronze (Cu-Sn-Zn-Pb-Sb)

When a PropS-SH film is applied by fast dip-coating on bare bronze samples, the XPS survey spectra of Figures 4.15 d-e are recorded, showing similar features to those observed in Cu and Sn spectra (Figure 5.4 b-c). In particular, intense peaks belonging to PropS-SH are observed, but among the alloying elements of the substrates only Cu signal is clearly visible.

In Cu8Sn (Figure 5.4d), the Sn $3d_{5/2}$ level shows a very low and poorly resolved signal, with a main contribution at BE=486.4 eV, attributed to Sn(IV) oxide and only a small peak at BE=484.8 eV linked to metallic Sn, as reported in the literature [156]. In quinary bronze (Figure 5.4e), all alloying elements except Cu (Sn 3d, Zn 2p, Sb 3d, Pb 4f) exhibit undetectable or low intensity XPS peaks. In particular, Figures 6b show the Sn 3d core levels on this substrate which indicate the presence of both metallic and oxidised Sn(IV) species, at 484.7 eV and 486.7 eV respectively [34]. Pb $4f_{7/2}$ level centred at BE = 138.6 eV and Zn $2p_{3/2}$ level centred at BE = 1022.1 eV (core levels not shown) are linked to oxygen-containing species [86,118]. As some of these elements are in significant concentration in bronzes (*e.g.* tin in Cu8Sn), in general their absence or

negligible detection by XPS indicates that PropS-SH produces relatively abundant continuous coatings on bronze substrates.

Regarding the characteristic PropS-SH elements, Figure 5.5 evidences that the chemical environments for C 1s, O 1s, Si 2p and S 2p detected on both bare bronzes are corresponding to those on pure Cu substrate. This suggests that the minor alloying elements do not affect the coating-bronze bonds: the coating correctly adheres onto the substrates, with a similar binding mechanism, which is essentially due to the formation of metal-thiolate bonds, involving Cu and Sn atoms, the latter being at a relatively minor extent.

Also on coated bronzes, the oxidation of the thiol group in the coating occurs in conjunction with oxidation of the silane aliphatic chain, as already observed for pure Cu and Sn. The peculiar influence of Cu and bronze alloying elements on this degradation process is likely responsible of its occurrence on these substrates.

5.2.5. Quinary bronze vs. patinated quinary bronze

Figure 5.4f shows the XPS survey of thick coated patinated bronze surface. In contrast to the thin bare quinary bronze (Figure 5.4e), the characteristic elements of the coating (C 1s, O 1s, Si 2p and S 2p) are more clearly detected, while the characteristic peaks of the substrate, like Cu 2p, Zn 2p, Sn 3d and Pb 4f, are less intense. As far as Sn 3d core levels in the presence of these substrates (Figures 5.6b and c), it is clear that, while both metallic and oxidised Sn(IV) species are detected on bare quinary bronze at 484.7 eV and 486.7 eV, respectively, on patinated bronze reasonably only Sn(IV) species related to Sn-rich corrosion products are observed [34].

On coated patinated quinary bronze, some environmental elements linked to the corrosion process in acid rain solution are also recorded on the XPS survey, such as N 1s and Ca 2p centred at 400 eV and 347 eV, respectively (Figure 5.4f). The increase of -SO$_x$ contributions for S 2p is also linked to the formation of sulfates among the corrosion products. All the characteristic elements of the coating show peaks similar in position and concentration to those obtained on coated quinary bare bronze. However, O 1s peak is broader and shows, in addition, a contribution at higher BE (~ 534 eV), indicating a remarkable presence of oxide and/or hydroxide compounds linked to Cu and related to corrosion products on the top surface (Figure 5.5b).

5.2.6. Uncoated bare quinary bronze (BQ)

XPS survey of the uncoated bare quinary bronze (BQ) is reported in Figure 5.4g. As expected, the spectrum shows the characteristics contributions of the alloying elements (Pb 4f, Sn 3d and Cu 2p), except for Zn that was not detected. In particular, Figure 5.6d shows the Sn core level spectrum recorded on uncoated quinary bronze just after polishing and before coating application, highlighting the presence of a predominant peak at 485.7 eV connected to Sn(II) oxide and a minor peak compatible with Sn(0). Dip-coating in aerated silane

hydroalcoholic solution is likely responsible of further oxidation of the pre-existing Sn(II) oxide film into the oxidised Sn(IV) species, detected under the PropS-SH coating, as shown by Figure 5.6a.

5.2.7. Auger

Cu 2p core level and Auger spectra (Cu LMM) are reported in Figures 5.7a and b respectively, for coated pure Cu, bare bronzes (Cu8Sn and quinary bronze), patinated quinary bronze substrate and uncoated bare quinary bronze. A very similar chemical environment for Cu core levels is found for the coated samples. In particular, Cu 2p core levels show the typical features of the oxidation state of Cu (I) with just a very small shake-up satellite peak, more developed for quinary bronze after accelerated ageing by Dropping test. The Cu $2p_{3/2}$ peak is centred at 933.1 eV (BE), while the Auger Cu $L_3M_{4,5}M_{4,5}$ signal at 915.6 eV (KE), with modified Auger parameter (α'), is measured at around 1848.7 eV. These values well correspond to Cu(I) species, such as a mix of cuprous oxide and Cu(I)-S bonds [165]. For patinated quinary bronze coated by PropS-SH, Cu contribution is low and the Cu 2p core level, as well as the Auger signal, is noisy and not well resolved. Conversely, the uncoated bare quinary bronze shows a Cu environment slightly different. In particular, Cu 2p core level shows the features of a mix of Cu(0) and Cu(I) species, with the Cu $2p_{3/2}$ peak centred at 932.5 eV (BE). The Auger Cu $L_3M_{4,5}M_{4,5}$ signal at 918.0 eV (KE), with modified Auger parameter (α') measured at around 1850.5 eV, are characteristic of Cu(0) species, as reported in [163,164]. This confirms the fact that coating application is likely responsible of further oxidation of the pre-existing Cu(0) in Cu(I) species.
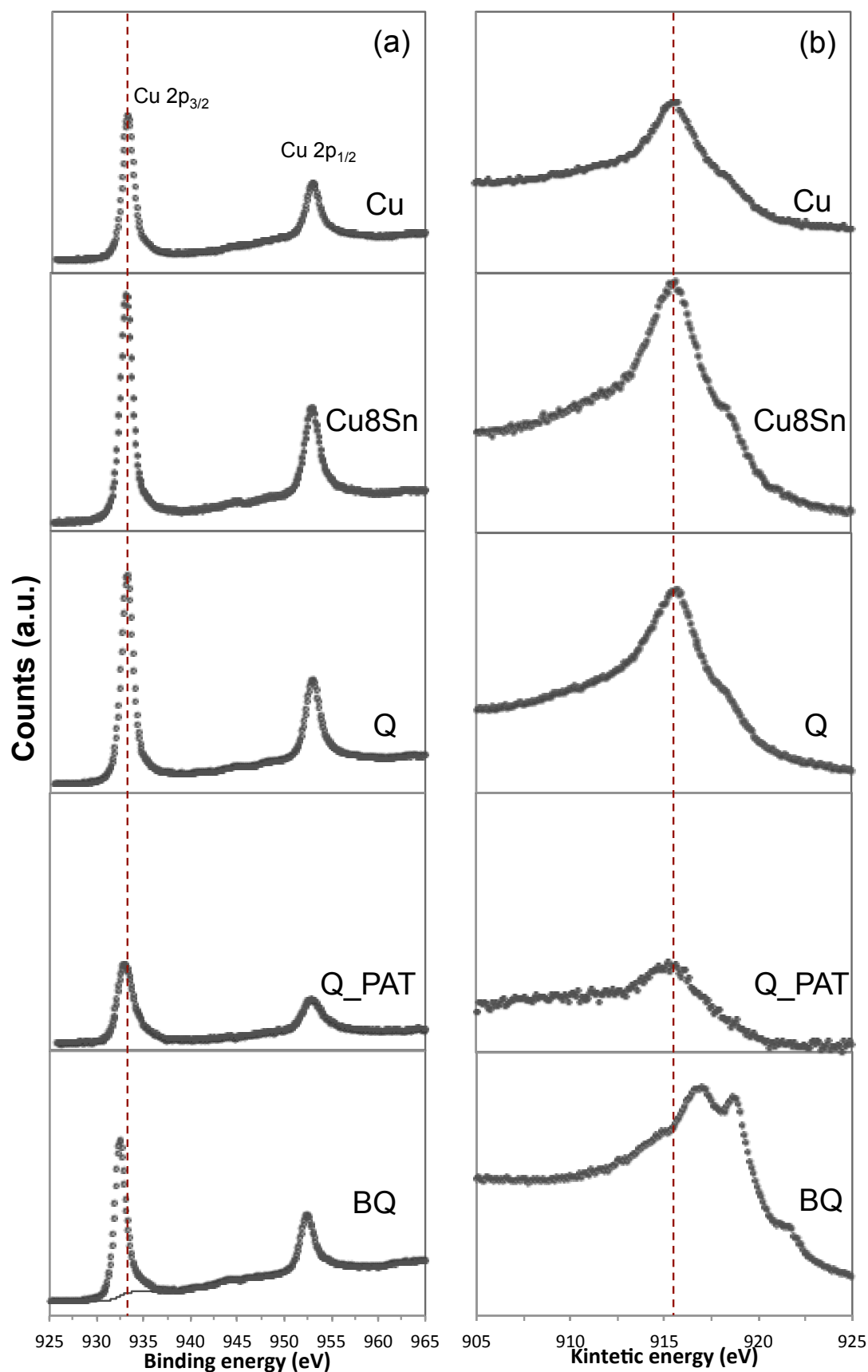
Figure 5.7: (a) Cu 2p core levels and (b) Cu-LMM Auger spectra measured on Cu, Cu8Sn and quinary (thin coatings), on quinary patinated bronze and on uncoated bare quinary bronze (BQ) (from the top to the bottom, respectively) [121].

5.2.8. XPS atomic quantification on the top surface of PropS-SH coated substrates

From the analysis of the XPS core levels, it is possible to evaluate the atomic concentration of the different elements on the coated surfaces. These values, together with their concentrations normalized with respect Si relative amount, are reported in Table 5.2.

On all samples, high C concentrations are detected but, due to surface C contamination, no meaningful trend among the samples is evident. O level always shows comparable atomic concentrations in all samples, except for PropS-SH applied on pure Sn, in which O concentration is higher (1.5 times higher than in the reference sample), due to abundant formation of tin oxides and sulphates. In general, the coated ZrN substrate shows the lowest O atomic concentration, because the coating is rather thick and the coating/material interface (where oxide accumulation may occur) cannot be investigated. On this reference substrate, the concentrations of the coating elements (C 1s, O 1s, S 2p) normalized to silicon are in very good agreement with the theoretical atomic ratios (O/Si=1.5, C/Si=3.0 and S/Si=1.0). This suggests that the coating reticulation is almost complete and no significant silane oxidation occurs.

On coated metallic substrates, Si concentrations decrease by passing from pure Cu to either bare or patinated bronze, to pure Sn, indicating a decreasing coating build-up, as the tin content of the substrate increases. Also total S atomic concentration decreases by passing from Cu and Cu-based alloys to Sn, but without a monotonic trend. Oxidation of the thiol group up to sulphate ion occurs at various extents on all bare metals and the low total S/Si ratios detected on Cu and bronze substrates, in comparison to the expected value of 1 (based on silane stoichiometry), suggest partial sulphate dissolution during dip-coating. Only on Sn substrate, the ratio (total S)/Si ratio is close to 1 (0.6+0.5), due to significant amount of insoluble sulphate species detected, likely linked to the formation of insoluble compounds with Sn(IV), as suggested by Sn core level spectrum. The concentration of S involved in S-Metal and C-S bonds, normalized to that of silicon, is particularly low in the case of Cu substrate, indicating that thiol oxidation in PropS-SH is more evident on pure Cu than on bronze or pure Sn.

Regarding the characteristic elements of the metallic substrates, Cu 2p signal is about double on coated bare bronze substrates in comparison to pure Cu, so confirming the lower average PropS-SH thickness on the former substrate types than on pure Cu. On patinated quinary bronze, where decuprification occurs due to selective corrosion, the lowest Cu concentration is detected. On this substrate, the relatively high sum of the alloying element content (> 1.3 at%) is a consequence of the decrease in Cu at%, but may be also connected to the non-uniform distribution of PropS-SH, which does not avoid the emergence of the rough surface patina.

Table 5.2: XPS atomic quantification on the top surface of PropS-SH coated substrates (at%). Each concentration value has been normalised to Si atomic content (/Si at%).

	C CC, C—H, C—Si	C C—O, C—S	C C=O, O=C-O	O	Si C—Si—O, Si—O—Si	Si SiO₂	S S—Metal, C-S	S Sulfate	Cu Cu(0)-Cu(I)	Cu Cu(I)	Zn Oxide	Sn Metal	Sn Sn(IV)	Sn Sn(II)	Pb Oxide
BQ															
at%	42.2	5.2	7.4	30.9	-	-	-	-	9.4	-	-	0.1	-	0.3	4.8
ZrN															
at%	47.3	-	-	22.9	16.3	-	13.5	-	-	-	-	-	-	-	-
Normalised (/Si at%)	2.9	-	-	1.4	1.0	-	0.8	-	-	-	-	-	-	-	-
Cu															
at%	43.0	3.4	3.1	25.4	13.2	-	5.5	0.5	-	5.9	-	-	-	-	-
Normalised (/Si at%)	3.3	0.3	0.2	1.9	1.0	-	0.4	0.04	-	0.4	-	-	-	-	-
Sn															
at%	25.8	3.3	4.9	36.1	4.1	-	2.5	1.9	-	-	-	5.3	8.9	7.2	-
Normalised (/Si at%)	6.3	0.8	1.2	8.8	1.0	-	0.6	0.5	-	-	-	1.3	2.2	1.8	-
Cu8Sn															
at%	38.5	3.2	4.7	25.6	8.6	-	6.4	0.5	-	12.4	-	0.1	0.1	-	-
Normalised (/Si at%)	4.5	0.4	0.5	2.9	1.0	-	0.7	0.06	-	1.4	-	0.01	0.01	-	-
Q															
at%	38.9	3.8	4.8	25.7	8.0	-	6.7	0.3	-	11.8	0.1	-	0.1	-	0.3
Normalised (/Si at%)	4.9	0.5	0.6	3.2	1.0	-	0.8	0.04	-	1.5	0.01	-	0.01	-	0.04
Q_PAT															
at%	40.5/7.6/4.7	7.5	4.7	24.4	7.9	2.0	5.8	1.1	-	1.6	1.0	-	0.2	-	0.1
Normalised (/Si at%)	4.1	0.8	0.5	2.5	1.0	-	0.6	0.1	-	0.2	0.1	-	0.02	-	0.01

5.3. Conclusive remarks

The following conclusions could be drawn from the results presented in Chapter 5:

- XPS technique allowed the collection of detailed information about the interaction of the organosilane coating (PropS-SH) with bronze including the role of the main alloying elements in artistic alloys (Sn, Zn and Pb). PropS-SH coatings tightly follow the morphology of the substrate on which they are applied. In particular, EDS and HR-SRPES maps on bare quinary bronze evidence that these coatings sink into shrinkage cavities, filling them up and forming a homogenous and continuous thin layer (< 500 nm). On patinated quinary bronze, the coating penetrates into the porosities apparently insulating the bronze substrate.

- 1h dip-coating applied to the ZrN substrate produces rather thick coatings, which allow the characterisation of the coating itself by XPS. Atomic quantification data related to the coating and normalized to Si signal are in good accordance with theoretical values, indicating that coating reticulation is almost complete and no silane oxidation occurs. More uniform and likely thicker silane layers form by passing from pure Sn to bronze to pure Cu. In all cases, the contribution of Cu- and (where present) Sn-thiolate bonds to silane adhesion has been recognized.

- An appreciable tendency of PropS-SH coating to oxidation is detected, with formation of sulfate and carboxylate groups. The extent of this phenomenon depends on the substrate nature: it is more evident on pure Cu than on bronze or pure Sn. It does not occur on ZrN. It likely takes place during the dip-coating step and appears to be favoured by the presence of multiple-valence cations.

6. PROTECTIVE COATINGS FOR BRONZES FOR CONTEMPORARY ART (Cu-Si-Mn)

6.1. Black patina (K$_2$S)

Macroscale observation of the black patina on Cu-Si-Mn bronze displays a rather homogeneous surface, black and dark grey in colour. The colour coordinates resulting from the average of six samples are: L*=24±1, a*=1.3±0.5, b*=2.1±0.9. SEM observation, however, indicates a noticeable surface roughness as shown in Figure 6.1, directly related to surface preparation (sand blasting) before patination. At micrometric scale, the patina surface consists of micrometric grains, also including some large particles of silica embedded in the metallic surface.

Grazing angle X-ray diffraction reveals the presence of orthorhombic chalcocite (Cu$_2$S – JCPDS PDF 00-033-0490) and Cu oxide (Cu$_2$O – JCPDS PDF 01-071-3645), and also confirms the presence of some quartz (SiO$_2$ – JCPDS PDF 01-089-1961). A representative FIB cross-section of the black patina is shown in Figure 6.1a.
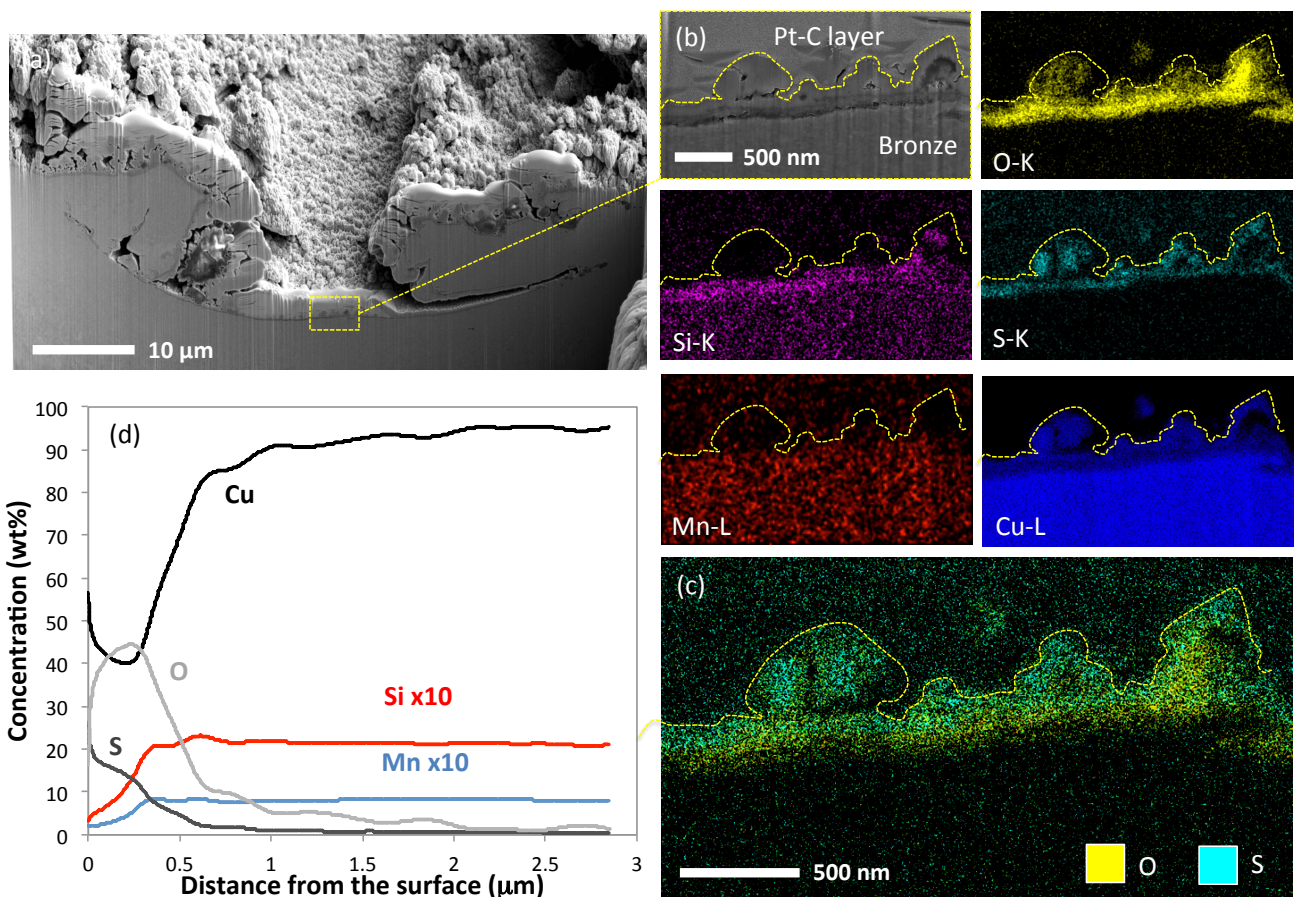
Figure 6.1: Cross-section of "as-supplied" black patina (K$_2$S) on Cu-Si-Mn bronze: (a) in situ FIB cross-section of representative portion of the sample; (b) X-ray maps (C, O, Si, S, Cu) of the black patina; (c) superimposition of O (yellow) and S (cyan) EDS signal to highlight the layered structure of the patina; (d) GD-OES concentration profiles of S and alloying elements (Cu, Si and Mn) measured from the free surface. In order to improve the readability of the image, the GD-OES concentration profiles for Si and Mn were amplified 10 times (x10) [136].

The influence of sand blasting is clearly visible, producing scratches about 10 µm wide and thin cracks in the surface layer of strain hardened bronze. The black patina displays a variable thickness, ranging from 500 nm to about 3 µm. It is characterised by a two-layer structure (Figure 6.1b and c): an internal cuprous oxide layer covered by an external one consisting of cuprous sulphide. The internal oxide, thin and regular, is directly related to the surface heating during the patination process, before the application of the potassium sulphide solution. The external cuprous sulphide formed mainly small dendritic crystals. GD-OES measurements reported in Figure 6.1d confirm the FIB observation, as the profiles reveal a patina layer exhibiting an external part rich in S content and an inner part very rich in oxygen element with lower or no S element. It is also evidenced that the layer is very thin with a thickness lower than 1 µm.

6.2. Surface characterisation of the coated samples

The preliminary optical investigation confirmed the relative homogeneity of all coatings produced by spraying at a macroscale level. As shown in Table 6.1, no remarkable colour variation is induced by the coatings, as the ΔE* values were 2.9 and 3.8 for Incralac® and PropS-SH, respectively.

Table 6.1:Colour variation measurements in CIELab 1976 colour space induced by coating application. Standard deviation values are reported in bracket [136].

	$\Delta a*$	$\Delta b*$	$\Delta L*$	$\Delta E*$
Incralac®	-0.5(0.2)	-1.2(1.4)	2.0(1.7)	**2.9(1.2)**
PropS-SH	-0.2(0.4)	-1.0(0.4)	3.8(0.4)	**3.8(0.3)**

The morphology of the coated patinated surfaces on Cu-Si-Mn bronze is displayed in Figure 6.2.

The application of Incralac® and PropS-SH coatings induced the formation of a continuous layer, masking the rough morphology of the black patina previously detailed. However, the surface coated by Incralac® (Figure 6.2, left column) reveals a very thin coating layer on areas hardly reachable by the spray jet, characterised by visible Cu sulphide crystals embedded within the polymer with some external micro-porosities. Conversely, the coating layer produced by PropS-SH is more homogeneously distributed. As shown in Figure 6.2 (right column) at higher magnification, the polymer forms a continuous network, well embedding the Cu sulphide crystallites of the black patina. These differences are related to a different surface wettability afforded by the two coating formulations on the patinated surface, as confirmed by simple capillary rise measurements performed after 15 minutes of partial immersion of patinated bronze sheets in 2 mm head of the coating formulations, followed by sheet drying. The capillary rise in this short exposure time was about 5 mm for Incralac® and 8.5 mm for PropS-SH. The higher wettability of PropS-SH is likely due to the high chemical affinity between the thiol group and Cu cations in the patina [67] and determines an easier access of the silane solution into surface cavities, due to capillary forces.
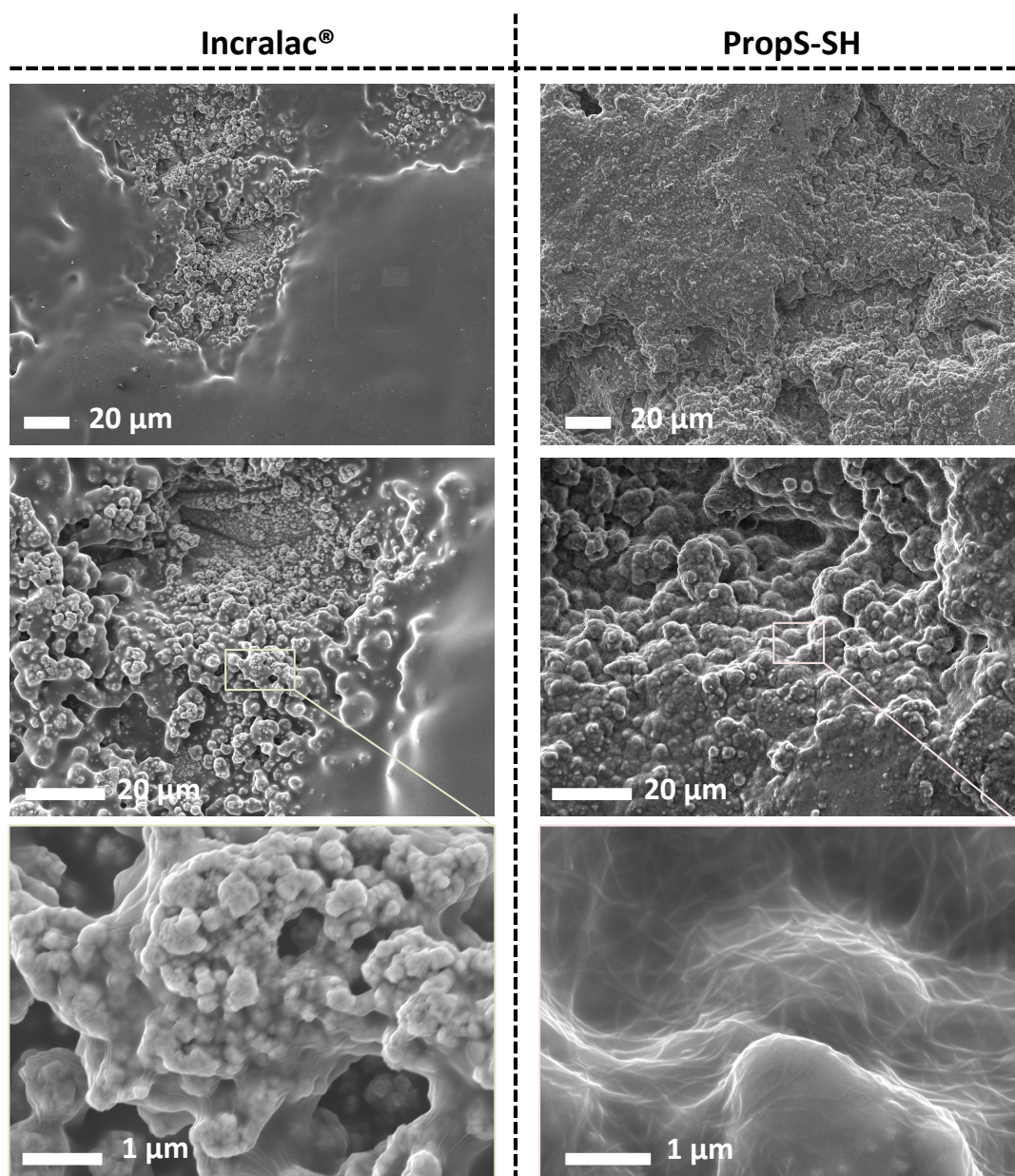
Incralac®	PropS-SH

Figure 6.2: Incralac® and PropS-SH surfaces on K₂S-patinated bronze, at different magnifications. SEM observation (SEI) [136].

The XPS surface analysis of the two coatings applied on black patina are reported in Table 6.2. Results were obtained after a slight Ar⁺ etching for limiting the detection of C pollution. For Incralac®, the top surface mainly consists of C and O with a minor contribution of N and Si elements. In particular, C 1s showed an intense peak centred in BE=284.6±0.1 eV, characteristic of C-C and C-H chains of methyl-methacrylate and ethyl-methacrylate, present in the coating formulation, and two minor peaks at BE=286.3±0.1 eV and BE=288.5±0.1 eV, linked to C-O and O-C=O species, respectively. In addition, O 1s is mainly linked to C 1s. This is also confirmed by the atomic quantification reported in Table 6.2, in which the O element present in the coating is completely linked to C, with a C/O atomic ratio of about 1. N was detected in low concentration (N 1s, BE=399.5±0.1 eV) highlighting the presence of BTA corrosion inhibitor within the organic layer, as reported in [85,86,148].

Table 6.2: *XPS atomic quantification (at%) of Incralac® and PropS-SH coatings before and after Dropping test. The XPS measurements are carried out after Ar⁺ sputtering (200 eV for 30s).*

	C 1s			N 1s	O 1s	Si 2p		S 2p		Cu 2p
	CC, CH, CN, C-Si	C-O, C-S	C=O, O-C=O	N-C, N-O		O-Si-C Si-O-Si	SiO_2	C-S	Sulphates	Cu(I)
Incralac®					*Before ageing*					
Peak BE (eV)	284.7	286.2	288.5	399.6	532.4	101.9	-	-	-	-
at%	61.0	10.4	8.9	0.5	18.6	0.6	-	-	-	-
PropS-SH										
Peak BE (eV)	284.7	286.3	288.2	399.2	532.4	102.4	103.4	163.2	168.1	-
at%	37.4	3.8	0.7	0.3	31.1	14.6	3.2	8.1	0.9	-
					After dropping					
Incralac®										
Peak BE (eV)	284.7	286.4	288.5	399.6	532.4	102.3	-	-	-	932.9*
at%	59.0	8.2	11.2	1.1	19.3	1.0	-	-	-	0.3
PropS-SH										
Peak BE (eV)	284.7	286.3	288.2	400.2	532.2	102.1	103.4	163.2	168.1	932.9*
at%	39.4	4.6	3.4	1.4	30.7	8.3	4.6	4.6	2.8	0.2

* KE (Cu LMM) = 915.8 eV; α' = 1848.7 eV Cu(I) - component.

Regarding the top surface of PropS-SH, the main elements detected are C, O, Si and S, as expected. In particular, C 1s showed an intense peak at BE=284.6±0.1 eV characteristic of the aliphatic chain of the coating and also two other small contributions (BE=286.3±0.1 eV and BE=288.2 eV) linked to C-S/C-O and O-C=O species, respectively. An intense Si 2p peak was observed at BE=102.3±0.1 eV, ascribed to the silane (C-Si-O and Si-O-Si), as detailed in [52,53]. A small concentration of SiO$_2$ (BE=103.4±0.1 eV) was also found. The analysis of S 2p signal takes into account the presence of a doublet structure of the core level with a spacing of 1.2 eV (S 2p$_{1/2}$ - S 2p$_{3/2}$ = 1.2 eV) and a theoretical intensity ratio of 2 (I(S 2p$_{3/2}$) / I(S 2p$_{1/2}$) = 2). In particular, S 2p peak is centred at BE=163.3±0.1 eV, characteristic of S-C bonds and thiol groups and presents a minor contribution centred at BE=168.1±0.1 eV, to be ascribed to the presence of sulphate groups [52,53,151–153], as highlighted in Figure 6.3 (dashed line). O-C=O and sulphate bonds are connected to a limited oxidation of the coating, as already observed on organic thiol compounds, like for PropS-SH exposed to the atmosphere [56,121,149,150]. It is unclear if also the small concentration of SiO$_2$ (peak at BE=103.4±0.1 eV) could be related to silane oxidation or to a contamination in the original silane monomer commercial product.
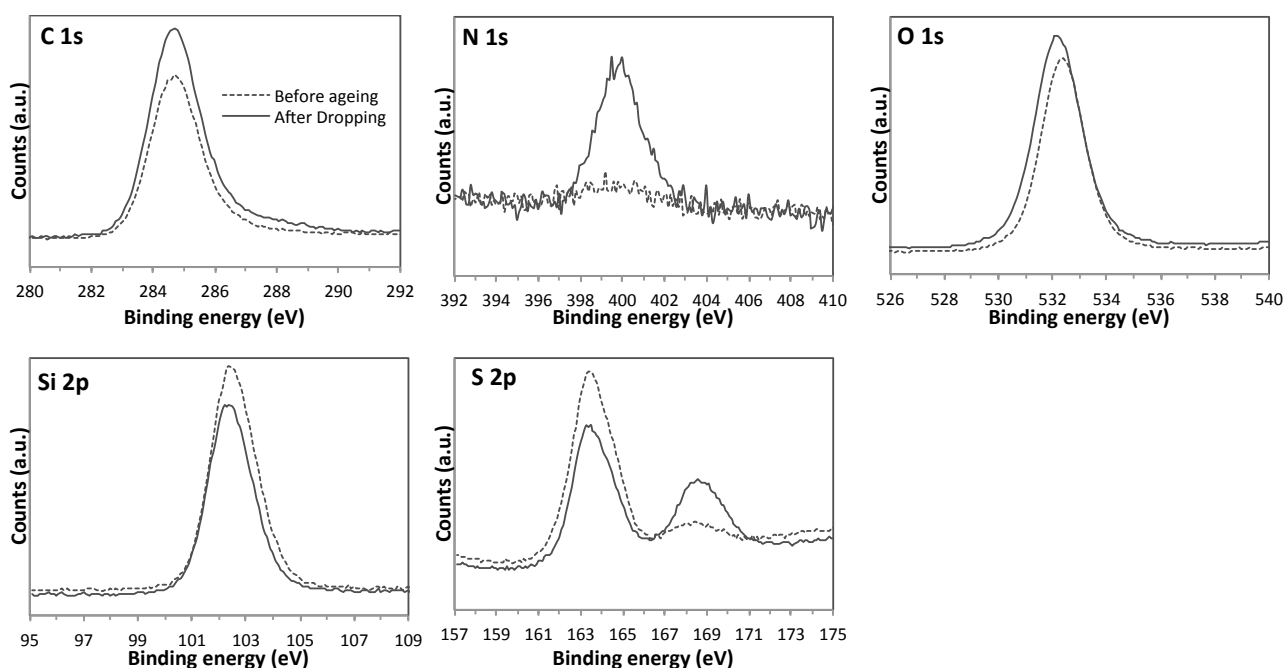
Figure 6.3: XPS measurements on PropS-SH surface before (dash line) and after ageing by Dropping [136].

From the atomic quantification reported in Table 6.2, the calculated atomic ratios are Si/C=0.35, Si/O=0.47 and Si/S=1.60, by considering only the concentration of Si 2p centred in the representative value for silane at BE=102.3 eV. These values agree quite well with the theoretical values: Si/C=0.33, Si/O=0.67 and Si/S=1.00, indicating that the Ar$^+$ ion sputtering is rather efficient in removing contamination without damaging the polymer. However, lower Si/O and higher Si/S ratios than the theoretical ones are found. The former difference is linked to the additional contribution of SiO$_2$ species found on this coated substrate, while the

latter one is likely due to a loss of sulphur from the silane top layer after thiol group oxidation to a volatile sulphur oxide [121].

6.3. Assessment of the coatings protectiveness: inhibiting efficiency after Dropping

The gravimetric measurements recorded during accelerated ageing by Dropping as a function of Time of Wetness (ToW), are reported in Figure 6.4. These results confirm the protective barrier effect of both coatings. Thus, while uncoated bronze exhibits a marked linear trend (R^2 = 0.997) of mass decrease with ToW, the coated samples only reveal a very limited mass decrease. However, at the end of the ageing test, a slight weight increase was measured for Incralac[®]. This has to be linked to localised corrosion at the coating/substrate interface, as detailed later, locally inducing corrosion deposits.
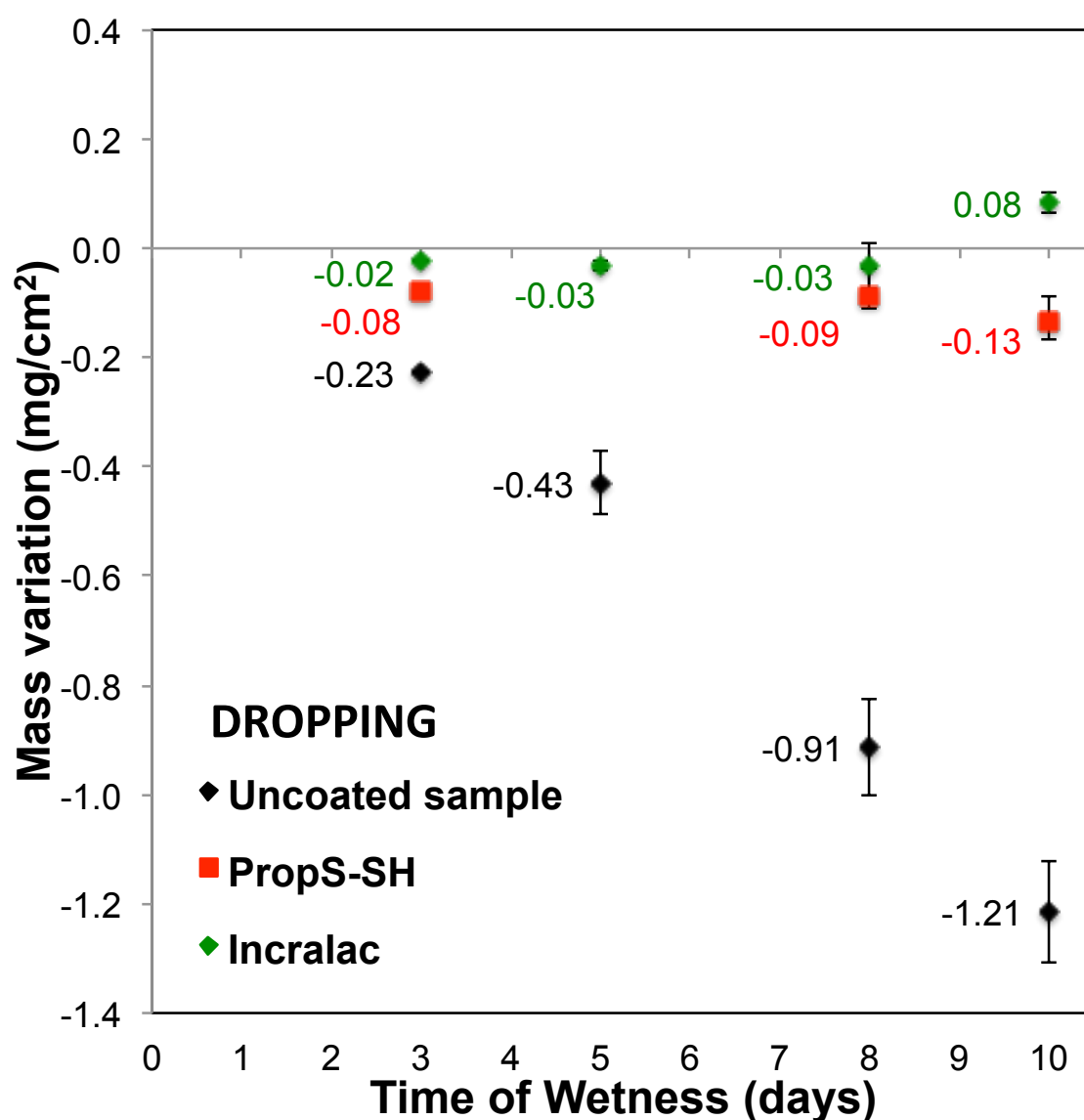
Figure 6.4: Mass variation for the uncoated (black line) and coated patinated bronze samples (PropS-SH in red and Incralac[®] in green) during accelerated ageing by Dropping test [136].

The evolution of Cu, Mn and Si cations release in the weathering solutions was measured as a function of ToW.
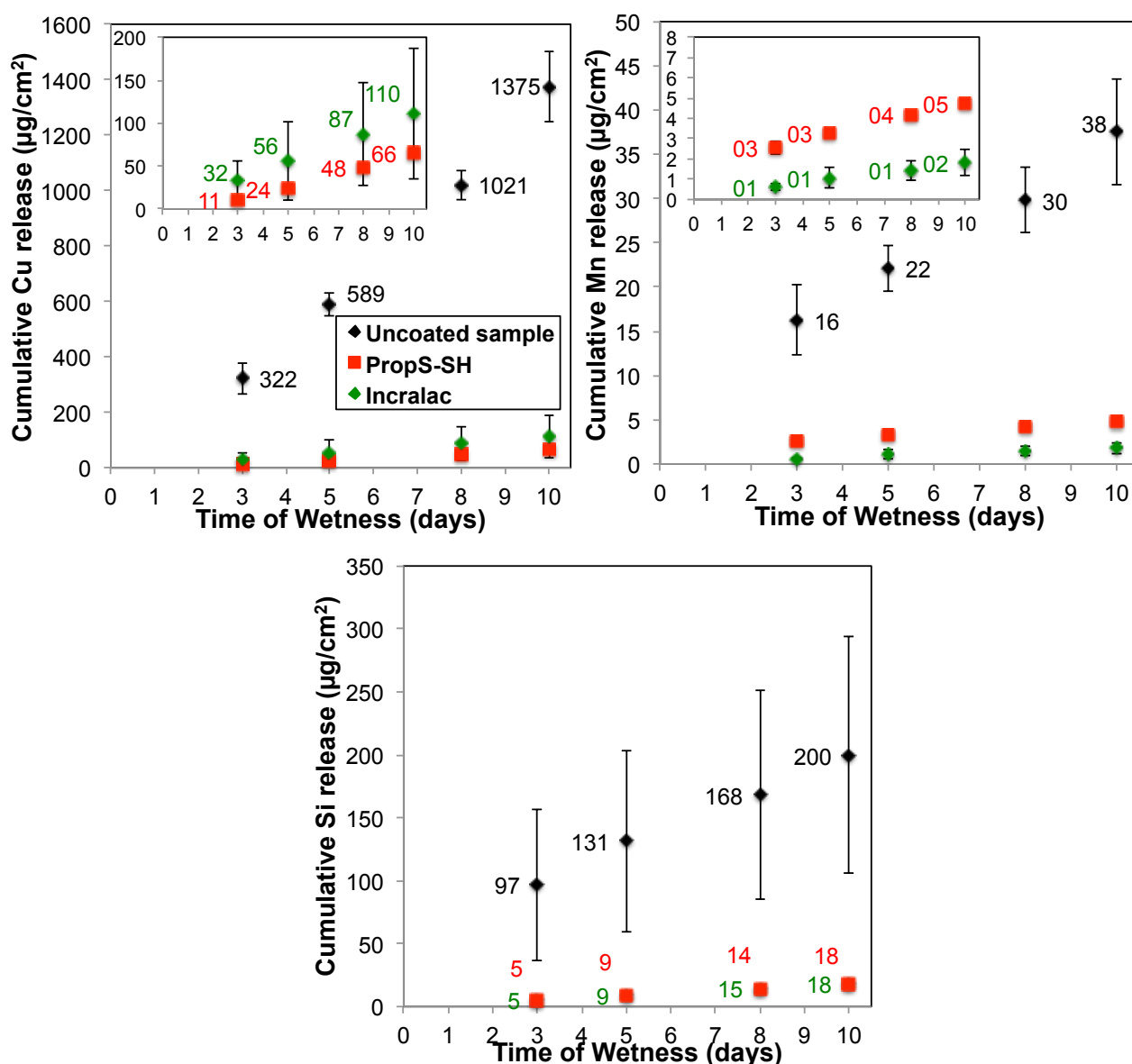
Figure 6.5: Cumulative Cu, Mn and Si ions release (µg/cm²) from patinated bronzes (coated and uncoated) in weathering synthetic solution, as a function of exposure time, for a total Time of Wetness (ToW) of 10 days of Dropping test [136].

Results are given in Figure 6.5, which shows that linear Cu and Mn ion release trends were detected. In the case of uncoated samples, Cu/Mn and Cu/Si concentration ratios (about 36 and 6, respectively) are much lower than in the alloy (around 96 and 31), likely due to slight local Cu species precipitation. This result highlights that the Dropping test always leads to a significant leaching of the surface of the uncoated, K_2S-patinated bronze, inhibiting the formation of a protective barrier layer of Cu-based corrosion products.

The coated samples displayed a lower dissolution rate of Cu and Mn by comparison to the uncoated ones. Regarding Si, for both PropS-SH and Incralac® coated samples, the concentrations of dissolved species were

always found under the Limit of Detection (LoD < 18 ppb) in the weathering solutions. Considering the relatively high Si LoD due to the analytical technique applied, a conservative approach was adopted, by assuming concentrations lower than LoD to be equal to ½ LoD. Therefore, for coated samples, Si concentrations equal to ½ LoD were used to estimate Si release reported in Figure 6.5. Overall, the results given in Figure 6.5 highlight a clear difference between uncoated and coated samples, with much smaller dissolution rates on coated samples, clearly confirming the high protectiveness of these coatings. Inhibiting efficiency values η, calculated in accordance with Equation 3.1, quantify these differences. In particular, Incralac® afforded an average η_{Cu} of 92, η_{Mn} of 95 and η_{Si} of 91%, while PropS-SH showed an average η_{Cu} of 95, η_{Mn} of 87 and η_{Si} of 91%, confirming an excellent equivalent protective performance of these coatings.

6.4. Surface examination after Dropping

The surface examination of uncoated patinated Cu-Si-Mn samples after ageing by Dropping indicates a more extensive degradation by comparison to the coated ones, as already pointed out by gravimetric and metal release data. As shown in Figure 6.6a, the uncoated samples revealed the formation of corrosion products linked to a slight evolution of the black patina.
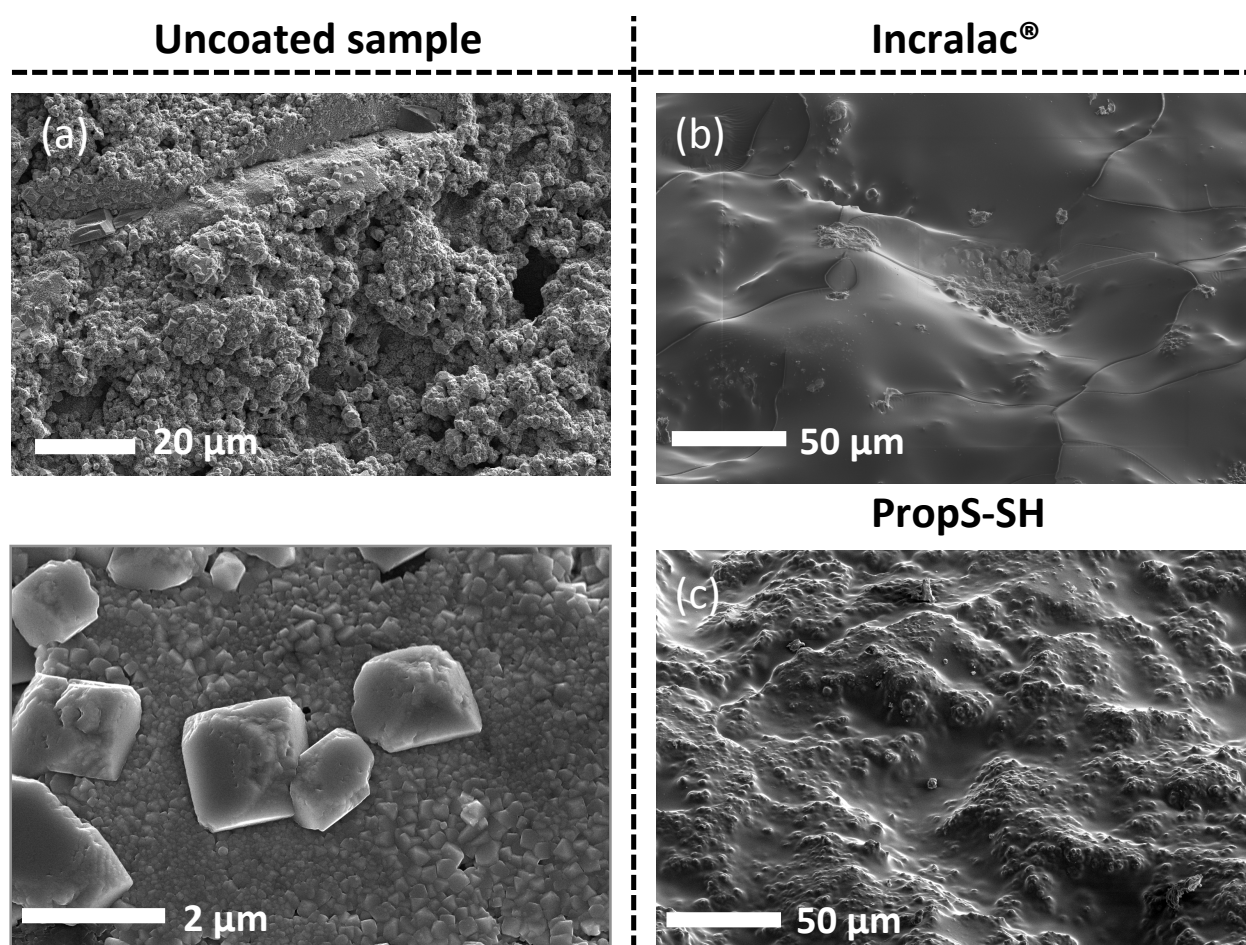
Figure 6.6: Surface morphology after Dropping: (a) Uncoated patinated bronze; (b) Patinated bronze coated by Incralac® (c) Patinated bronze coated by PropS-SH [136].

128

Due to runoff and high Cu ions release in the ageing solution, the initial rough surface is still observable but partially masked by the formation of a new layer of cubic crystallites.

XRD measurements confirmed that these Cu species essentially consist of cuprous oxide (Cu_2O JCPDS PDF 01-071-3645) but also of orthorhombic Cu_2S (JCPDS PDF 00-033-0490) and residual quartz particles due to sandblasting (JCPDS PDF 01-089-1961). No hydroxysulphate salts were identified. For the coated samples (Figures 6.6 b and c), no pronounced differences were observed compared to the surfaces before ageing (Figure 6.2). However, Incralac® coating exhibits surface cracks under Dropping exposure (Figure 6.6b) which are not observed for PropS-SH (Figure 6.6c). Furthermore, surface alterations appeared in areas exhibiting lower thickness of the protective coatings. For Incralac®, this occurs in correspondence with recessed areas (*e.g.* bottom of sand-blasting grooves) while for PropS-SH (*i.e.* for the surface treatment with higher penetration capability), this occurs on raised areas (*i.e.* upper part of grooves).

In addition, colour measurements reported in Table 6.3 revealed that the appearance of the uncoated black patinated bronze always showed marked colour variations induced by Dropping ($\Delta E^* \sim 9$), mainly due to an increase in lightness ($\Delta L^* \sim 7.5$) and to chromatic variations towards blue. On the contrary, the coated samples do not significantly change during the ageing test ($\Delta E^* < 3$). This confirms no evident visual alteration of the coatings in the test conditions, especially for PropS-SH coating, which has to be related to a good protectiveness, without patina evolution and formation of corrosion products.

Table 6.3: Colour variation measurements in CIELab 1976 colour space induced by accelerated ageing (Dropping test). Standard deviation values are reported in brackets [136].

	*Δa**	*Δb**	*ΔL**	*ΔE**
Uncoated sample	-0.9(0.7)	-4.1(2.2)	7.5(1.6)	**8.8(1.6)**
Incralac®	-0.3(0.5)	-0.8(1.0)	-0.4(1.1)	**1.2(1.2)**
PropS-SH	-0.4(0.2)	-0.20(0.03)	0.5(0.3)	**0.7(0.2)**

The influence of Dropping on Incralac® chemistry was analysed by XPS measurements (Figure 6.3). Atomic quantification measured on the top surface of the coating after ageing is reported in Table 6.2. These results show that no significant variation occurred, except a slight increase in N 1s, Si 2p. In parallel, on the top surfaces of PropS-SH, no strong differences in the environment of the main elements (C 1s, O 1s, Si 2p, S 2p and Cu 2p), as shown in Figure 6.3 when comparing the reported core levels before (dash line) and after the Dropping test. This confirms that no marked modification of the coating surface chemistry occurred after ageing. In particular as detailed in Table 6.2, Dropping induced an increase in N 1s contribution, to be ascribed to the presence of nitrate species due to the effect of the acid rain solution on the top surfaces. In addition, an increase of –SO_x species at BE=168.1±0.1 eV for S 2p was detected, related to the oxidation of silane coatings and to the presence of sulphates among the corrosion products, as observed in a previous study

[121]. However, even if Cu 2p signal slightly increased after Dropping, Cu was always present in very low concentrations and the signal was noisy and not well resolved.

Investigation of the microstructure of the coating/patina/bronze after the ageing test was performed by FEG-SEM observation of *in situ* FIB cross-sections. The results for uncoated samples are shown in Figure 6.7.
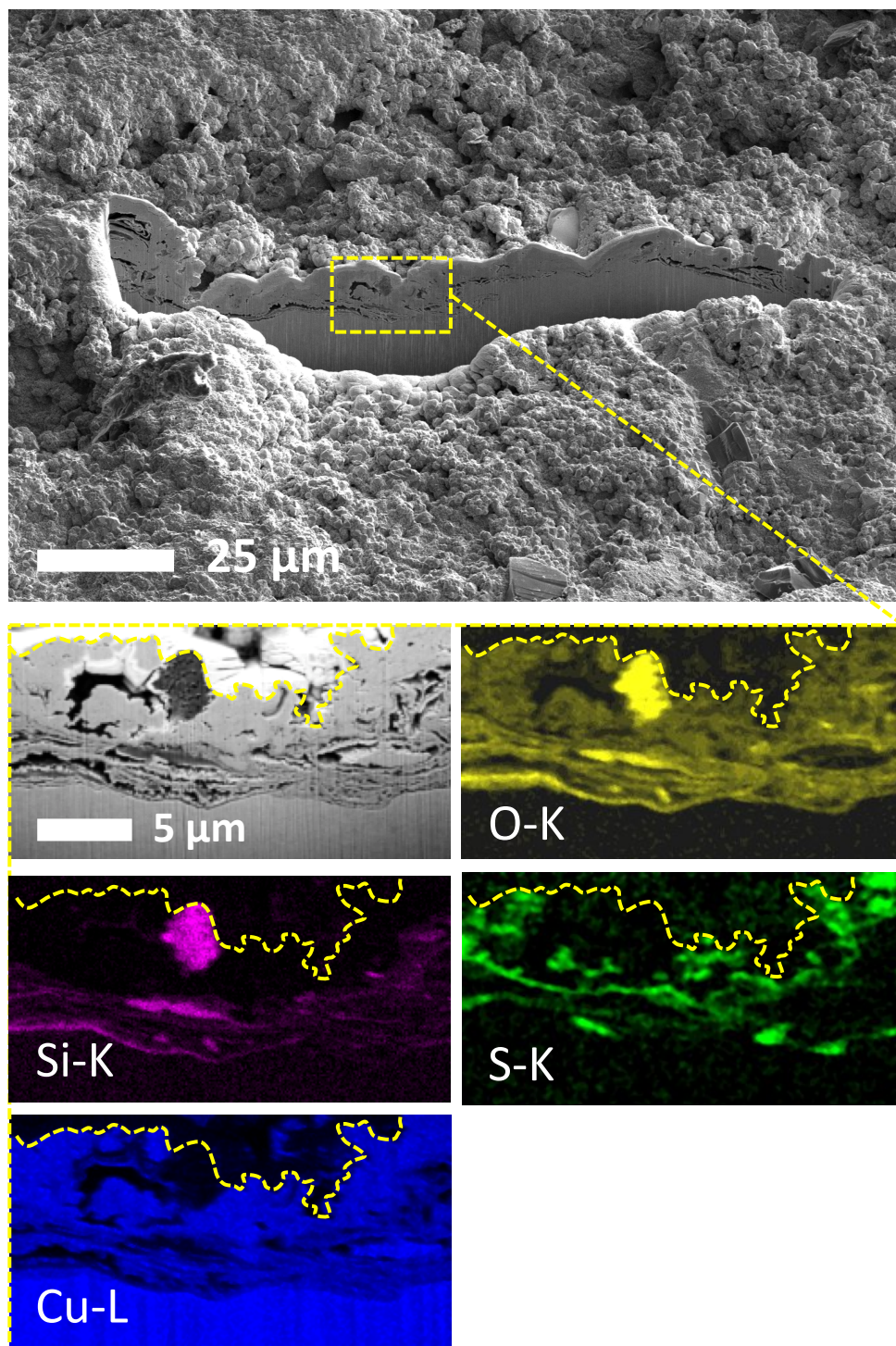
Figure 6.7: FIB cross-section of the uncoated patinated bronze after Dropping. X-ray maps of both the cross-sections show the distribution of O, Si, S, Cu (Mn is not reported as the EDS map is not well-resolved). Pt-C layer was applied before FIB milling in order to protect the top surface of the cross-section [136]*.*

By comparison with the examination before ageing reported in Figure 6.1, the corrosion process induced a modification of the patina structure. A preferential dissolution of Cu elements is observed, producing numerous voids and exfoliations within the corrosion-modified surface patina. This is accompanied by a relative enrichment in Si and O elements, forming an inner corrosion layer.

Therefore, as illustrated in Figure 6.7, a decuprification process may take place here, characterized by the internal oxidation of the alloy with a preferential dissolution of Cu ions and a relative enrichment in oxidised Si element. This phenomenon may be analogous to the corrosion behaviour highlighted for tin bronze [34], where selective dissolution of Cu, due to internal oxidation, induces selective enrichment in the stable oxidised alloying element such as Sn. However, further work is required to investigate the corrosion behaviour of the Cu-Si-Mn alloy itself. The cross-section observation also showed that S element, belonging to the original sulphide-containing black patina, is still present in the inner layer.

As regards the coated samples, FIB cross-section observations are reported in Figures 6.8 and 6.9 for Incralac® and PropS-SH, respectively. In general, the coatings fully cover the black patina, filling up the porosities within black Cu sulphide crystallites. However, for both coatings, the polymer layer is not homogenous in thickness. It is ranging from about 150 nm (Figures 6.8a and 6.9a) to about 10 µm for Incralac® and 7 µm for PropS-SH (Figures 6.8b and 6.9b respectively). However, the variations of thickness in Incralac® are conversely disposed to those of PropS-SH. In fact, Incralac® is thicker on the raised areas of the patinated bronze (*i.e.* on the top areas of sand-blasting grooves) and very thin in the lower recessed parts. The opposite occurs for PropS-SH film. This microstructure characterisation confirms the previous observations performed before ageing.

Figure 6.8 also shows that large pores are entrapped inside Incralac®, with diameters ranging from 1 to several µm, sometimes in contact with the black patina. Conversely, PropS-SH (Figure 6.9) is dense and well adherent to the underlying black patina.

Such differences are connected to a different wettability of the surface patina by the coating formulations. In fact, the high affinity of the thiol groups with the Cu cations of the patina is expected to particularly favour the penetration of PropS-SH hydrolysed solution inside the patina pores and cavities, by the contribution of capillary forces.
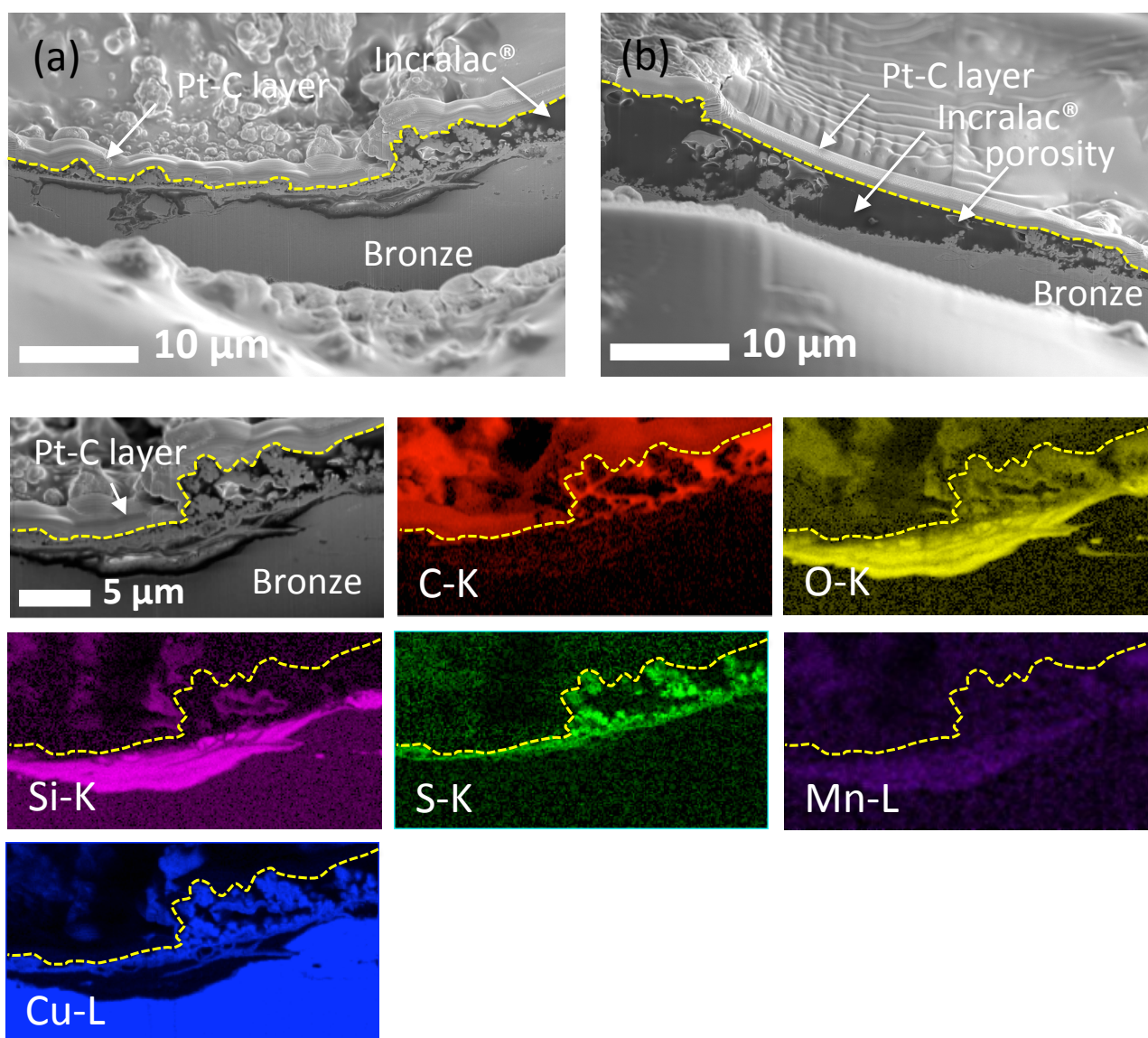
Figure 6.8: FIB cross-section of the patinated bronze coated by Incralac® after ageing by Dropping, in correspondence of (a) a thinner part (recessed parts) and (b) coating thicker part, corresponding to raised areas of the patinated bronze, i.e. on the top of grooves induced by sand-blasting). X-ray maps on cross-section revealing the distribution of the main elements in the coated system (right detailed part of (a)). Pt-C layer was applied before FIB milling in order to protect the top surface of the cross-section [136].

Because of these thickness variations, corrosion started within the thinnest coating areas, inducing localised corrosion attack: on the recessed areas for Incralac® and on raised areas for PropS-SH. For Incralac®, this is shown in Figure 6.8a (SEM image), and by the X-ray maps of C and O elements (coating polymer) as well as of Si, Cu and Mn (patina system), always in Figure 6.8. The corrosion, developed at the bronze/black patina interface, produces an internal corrosion layer under the Cu sulphide crystallites of the initial patina, as clearly highlighted by the presence of oxygen in Figure 6.8. The O map, together with those of S and Cu, clearly shows that, as for the uncoated sample (Figure 6.7), a decuprification process occurred, which is characterised by a marked Cu dissolution (low Cu signal) and a relative enrichment in Si (high Si signal) and, to a lower extent, in Mn.
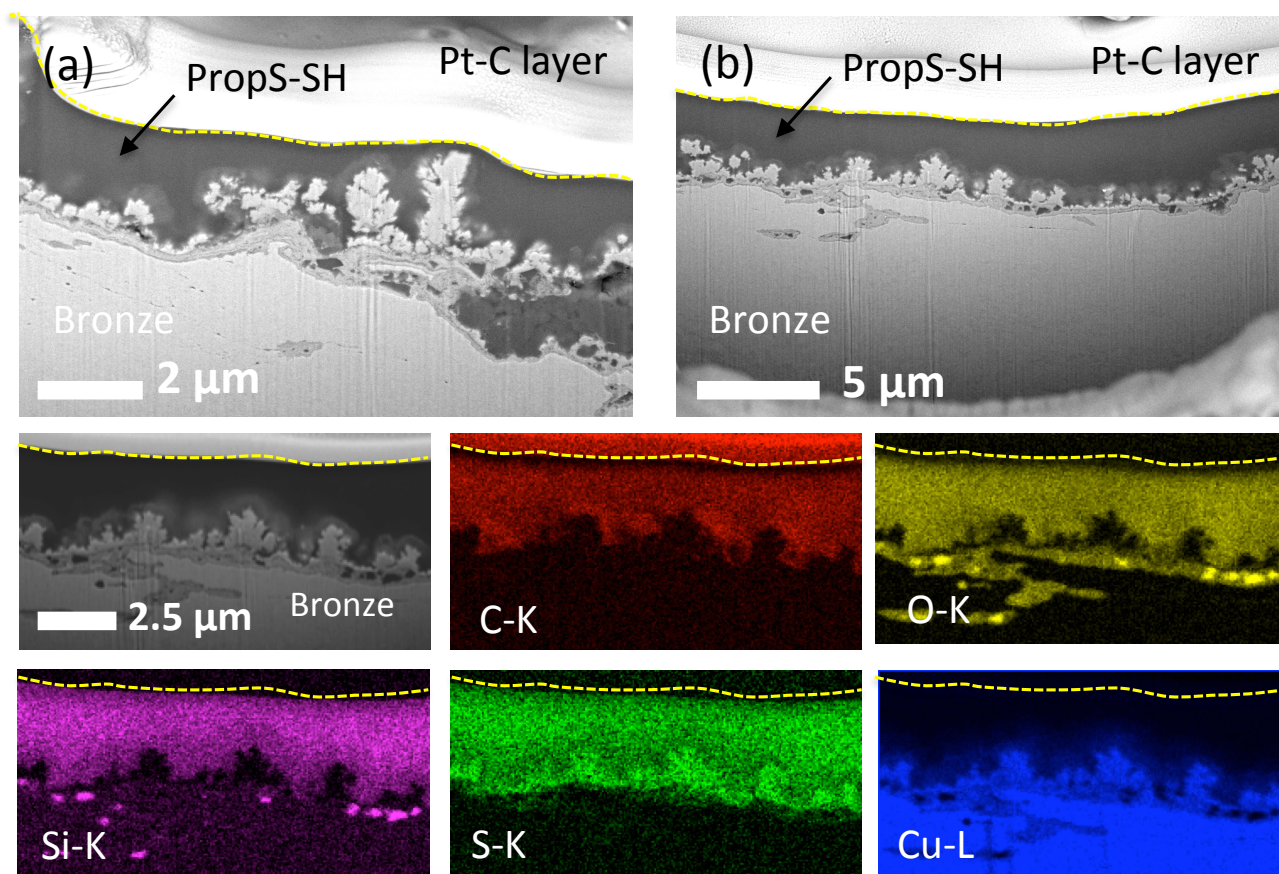
Figure 6.9: FIB cross-section of the patinated bronze coated by PropS-SH after ageing by Dropping, in correspondence of (a) thin part (raised area of the patinated bronze surface), and (b) thick part located in the recessed parts of the patinated bronze surface. X-ray maps on cross-section of the main elements located within the coated system after ageing. Pt-C layer was applied before FIB milling in order to protect the top surface of the cross-section [136].

FIB cross-section of the PropS-SH coating after Dropping did not reveal a corrosion attack at the coating-substrate interface (Figure 6.9). The double-layer structure of the initial black patina (previously reported in Figure 6.1) is clearly conserved. This indicates that also when deposited as a thin layer, PropS-SH was able to protect the substrate from corrosion. X-ray maps of the aged PropS-SH layer on black patina (Figure 6.9) also confirm that, after ageing by Dropping, the film is not affected by corrosion and maintains a homogenous chemical composition.

These findings suggest that, even if the two coatings exhibit very low and comparable metal releases from the substrate, in terms of η_{Cu}, η_{Mn} and η_{Si} values (c.f. paragraph 6.3), only PropS-SH efficiently prevents alloy decuprification. Instead, Incralac® cannot avoid the formation of Si-enriched layers under the patina, related to localised corrosion in thinner areas of the coating.

6.5. Other result from B-IMPACT project

To present an overview of other results about the PropS-SH and Incralac® coatings applied on patinated Cu-Si-Mn bronze achieved in the B-IMPACT project, results from the electrochemical tests performed by I-

133

UniFE (Italy) and S-ZAG (Slovenia) reported in B-IMPACT Deliverable 2.1 – Proposal of candidate protection systems for patinated bronze and B-IMPACT Deliverable 2.2 – Protection efficiency report for eco-friendly coatings [120,135] and from the Occupational Exposure tests performed by I-ECAM and reported in B-IPACT Deliverable 3.3 – Assessment of TLW/TWA and STEL [137] are reported in paragraph 6.5.1 and 6.5.2, respectively.

6.5.1. <u>Electrochemical tests</u>

In B-IMPACT deliverables [120,135], the protection efficiency of the PropS-SH and Incralac® treatments, applied either by dip-coating or by spraying, was investigated by monitoring the time evolution of the polarisation resistance R_p and corrosion potential E_{cor} values. It was reported the results obtained during 30 days of continuous exposure to concentrated acid rain ARX10 and are shown in Figures 6.10a and 6.10b.

As regards the uncoated K_2S-patinated bronze, the measured R_p values showed a slight increase from 11 kΩ cm^2 to 28 kΩ cm^2, during the initial 24 h. Then, despite some fluctuations, they decreased down to 7.9 kΩ cm^2 at the end of the exposure (Figure 6.10a). The corresponding E_{cor} values evolved from -0.07 V after 1 h immersion to more active values (-0.14 V_{SCE}) after 24 h and then continuously increased up to 0.007 V_{SCE}, at the end of test (Figure 6.10b). The relatively low and slightly decreasing R_p values indicate that the K_2S-patina could offer only a partial protection to the bronze substrate and that the influence of immersion time on bronze corrosion rate is limited.

During the first week of exposure, PropS-SH-coated bronze specimens obtained by dip-coating exhibited R_p values of about one order of magnitude greater than those recorded on the blank. Then, the R_p values tended to decrease slowly, although they always remained well higher than those of the blank (about 47 kΩ cm^2, after 30 days). Despite, as above mentioned, the dip-coating application method produced Incralac® coatings with specific weights much higher (5.6 g m^{-2} on average) than those of silane coatings (1.6 g m^{-2} on average), the former surface treatment on patinated bronze determined only slightly higher R_p values, with similar time evolution and final average R_p values of 65 kΩ cm^2 (Figure 6.10a).

It was suggested that that both PropS-SH and Incralac® applied by dip-coating adhere on patinated bronze and offer a good protection, but the slow penetration of the aggressive solution and dissolved oxygen partially impairs their performances. To assess and compare the performance of silane and Incralac®, sprayed coatings of the same specific weight of about 6g m^{-2} (and hence comparable thickness) were then tested, as reported in [120,135].

Figure 6.10a shows that the spraying method determined some improvements in comparison to dip-coating, much more noticeable in the case of PropS-SH, which afforded R_p values one order of magnitude higher than those obtained by dip-coating, due to the increase of its thickness.

(a)

(b)

(c)

(d)

(e)

(f)
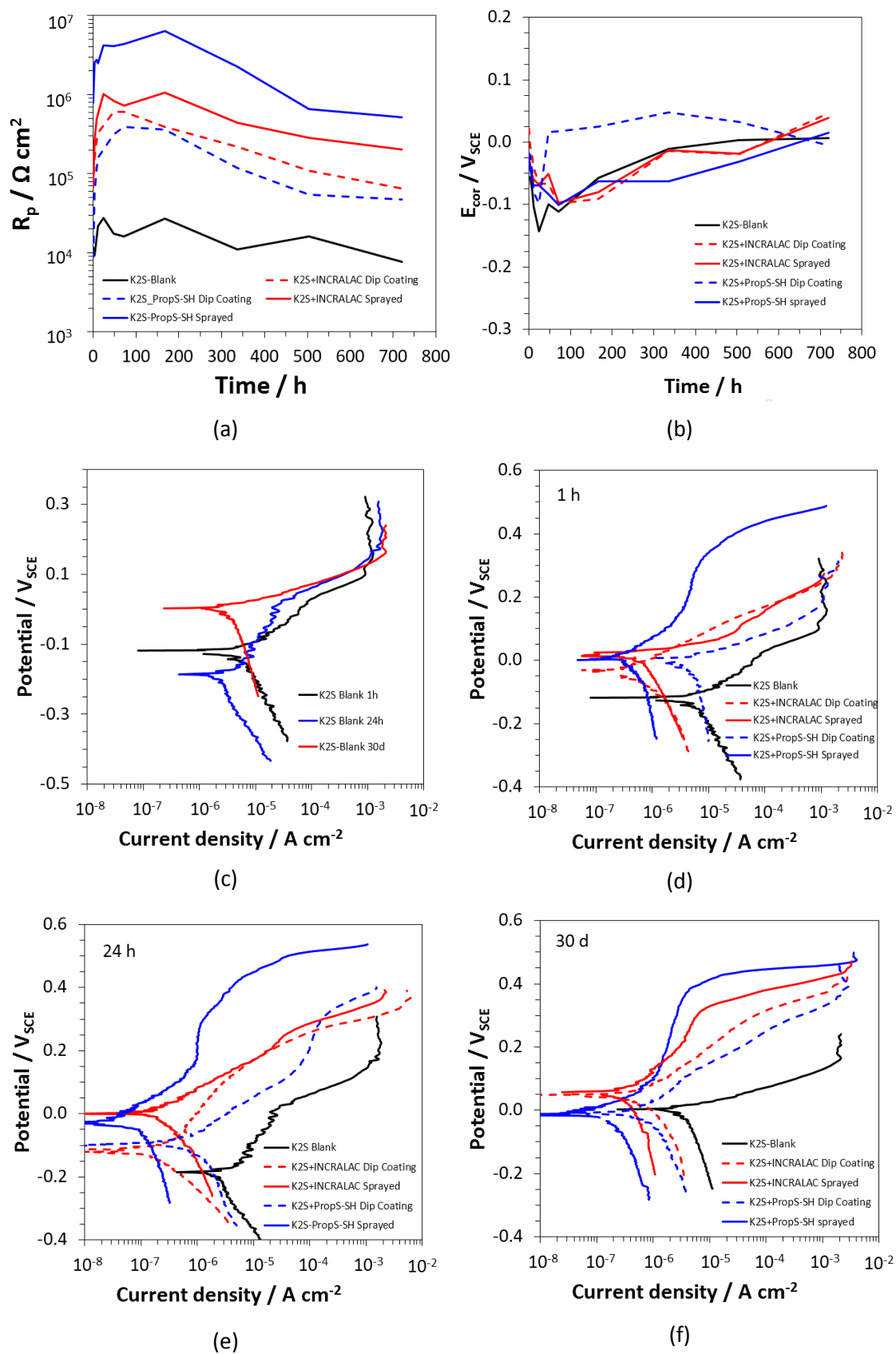
Figure 6.10: Electrochemical characterization of uncoated and coated bronzes. Polarization resistance (a) and corrosion potential (b) values recorded during 30 days exposure to ARX10. Polarization curves recorded on uncoated specimens at different immersion times (c) and on uncoated and coated specimens after 1 hour (d), 24 h (e) and 30 days (f) of exposure to ARX10 [135,136].

The polarization curves were also recorded at different exposure times on uncoated specimens and are reported in Figure 6.10c. They highlighted relatively high initial anodic slopes of about 0.12 V/decade, after 1 h, and 0.24 V/decade, after 24 h of exposure. In this period, the cathodic polarization curve of oxygen reduction tended to shift towards lower current densities. Instead, at the end of the exposure period (30 days), the anodic slope significantly decreased to about 0.06 V/decade, while the cathodic currents again accelerate. It was suggested that at first the patina behaved like a passive film, which initially became more compact and protective, likely due to the precipitation of insoluble corrosion products in the patina pores, likely related to cuprous oxide. Then, at the end of the exposure period, prevalent formation of soluble corrosion products appeared to occur because patinated bronze exhibited an active corrosion behaviour, meaning that the patina was no more protective [120,135].

The polarization curves recorded on PropS-SH and Incralac® produced by dip-coating and by spraying after 1 h, 24 h and 30 days of immersion are shown in figures 6.10d, e and f, respectively. After 1 h exposure (Figure 6.10d), all coated bronze specimens showed E_{cor} values nobler than that of the blank. However, in the case of silane surface treatment applied by dip-coating (1.6 g m^{-2}), a negligible inhibition of the corrosion current (i_{cor}) was achieved, while the other thicker coating types offered a significant protectiveness. In particular, regardless the application method, Incralac® appreciably inhibited the cathodic process, while PropS-SH applied by spraying exhibited a more significant barrier effect, against both the cathodic and the anodic process. After 24 h of exposure (Figure 6.10e), a marked i_{cor} reduction was observed on all coated samples in comparison to their performances at shorter immersion times, again more evident in the case of sprayed silane.

Table 6.4: Corrosion potential (E_{cor}) and current density (i_{cor}) parameters and Protection efficiency (PE) obtained from 30 days polarization curve measurements [135,136].

Sample	E_{cor} (V$_{SCE}$)	i_{cor} ($\mu A\ cm^{-2}$) 30 days	PE (%)
K$_2$S-patinated bronze	0.003	4.0	-
Incralac® Dip-coating	0.058	0.69	83
Incralac® Sprayed	0.056	0.45	89
PropS-SH Dip-coating	-0.015	0.72	82
PropS-SH Sprayed	-0.009	0.10	97

It was stated that this coating was the most efficient to hinder both the cathodic and the anodic reactions of the corrosion process and afforded i_{cor} values as low as 3×10^{-8} A/cm^2. At the end of the exposure period (Figure 6.10f), on all specimen types the corrosion process was slightly speeded up, but still important final protective efficiencies (PE) were measured applying Equation 3.5, particularly in the case of sprayed PropS-SH. So,

Table 6.4, collecting the E_{cor} and i_{cor} parameters deduced from the 30 day polarization curves, showed that final PE of sprayed silane is 97%, while those of Incralac® are 83 and 89%, in the case of dip-coating or spraying application methods, respectively. The time evolution of the polarization curves stresses the excellent performances of sprayed PropS-SH during the continuous exposure to concentrated acid rain (ARX10) [120,135].

6.5.2. Eco-toxicity

B-IMPACT deliverable 3.3 reports the values of the Exposure Limit (EL) of PropS-SH coating that was 0.019 [137]. Compared to Incralac® that shows a value of EL of 1.108, as reported in Table 4.7, also plain PropS-SH performed better than the commercial reference Incralac®. So, it was concluded that all the selected coatings in the B-IMPACT project showed low toxicity values and could be considered as non-hazardous protective coatings [137].

6.6. Conclusive remarks

The assessment of the protectiveness of 3-mercapto-propyl-trimethoxysilane (PropS-SH) coating applied on patinated Cu-Si-Mn bronze was carried out. The following main conclusions can be drawn from this work:

- The K_2S patina on silicon bronze forms a double-layer structure: an internal cuprous oxide layer, directly related to surface heating during the first step of the patination, covered by an external one consisting mainly of cuprous sulphide developing small coalesced crystals, identified by XRD and *in situ* FIB cross-section.

- Based on results from electrochemical tests, PropS-SH and Incralac® applied by spraying offer a good protection to patinated bronze, better than that by dip-coating, particularly in the case of PropS-SH. With the former application method, final protective efficiency (PE) values are 97 and 89% for silane and Incralac®, respectively.

- Incralac® and PropS-SH coatings applied by spraying produce continuous layers. However, Incralac® coating does not completely penetrate within patina cavities, whereas PropS-SH coating is found to cover more homogenously the patinated surface. The top surface of Incralac® mainly contains C atoms involved in C-C and C-H bonds and O atoms from C-O and O-C=O bonds, as expected for a methyl-methacrylate / ethyl-methacrylate copolymer. N is also detected to be ascribed to the presence of BTA corrosion inhibitor within the organic layer. On the top surface of PropS-SH, C, O, Si and S elements are mainly detected, with atomic ratios in agreement with the theoretical values. Dropping tests (artificial accelerated ageing) did not induce strong variation in the chemistry of both top coating layers, indicating a good stability of the polymer/patina system under ageing conditions.

- Inhibiting efficiency in terms of metal release of Incralac® and PropS-SH show η_{Cu} values of 92 and 95 (RSD about 15%), η_{Mn} of 95 and 87, respectively, and an estimated η_{Si} of 91% for both,

suggesting excellent coating performance. Furthermore, based on cross-section observations, PropS-SH also prevents the accumulation of insoluble corrosion products under the patina, while Incralac® cannot avoid the formation of a silicon-enriched corrosion product suggesting the onset of decuprification.

Conclusions

IN **CHAPTER 7**, CONCLUSIONS ARE SUMMARIZED AND PERSPECTIVES FOR THE FUTURE RESEARCH ARE ALSO REPORTED.

7. GENERAL CONCLUSIONS AND FUTURE RESEARCH

The assessment of the protectiveness of innovative, non-hazardous coatings tailored for the conservation of outdoor bronze Cultural Heritage was achieved in this study. The multi-analytical approach adopted allowed a coherent and consistent investigation of the performance of the selected coatings under simulated ageing conditions, representative of the outdoor exposure. All the investigated protective coatings, developed for the protection of both traditional quaternary bronze alloy (Cu-Sn-Zn- Pb) and ternary alloy (Cu-Si-Mn) used for contemporary art, show outstanding protective performance compared to the uncoated samples. In addition, the protective performance of the selected treatments were also compared to the commercial product Incralac[®], considered as the reference treatment as one of the most used product for the conservation of outdoor bronzes. Electrochemical approach, accelerated ageing, morphological and structural characterisation of the coated substrates before and after ageing were discussed in this thesis, as well as data about the eco-toxicity of the investigated treatments.

The selected coatings were tested on both the bronze substrates in patinated conditions, representative of the natural patinas on quaternary Cu-Sn-Zn-Pb bronze and of the aesthetical black patina (K_2S aqueous solution) on the Cu-Si-Mn, usually applied by artistic foundries. The characterisation of both patinated substrates showed different features, therefore the development of the protective treatments had taken into account the morphological and structural features of the different patinas. On one hand, the artificial patinas on Cu-Sn-Zn-Pb produced by the artificial ageing of Dropping (ToW=37 days) was not homogenous as mainly dendrite cores were corroded and a thin layer of few microns characterised by nano-porosity was achieved, as discussed in paragraph 4.1. This substrate simulating the real patinas of outdoor exposure of unsheltered geometries was also compared to the ones produced by Wet&Dry test, representative of sheltered exposure. So, similar corrosion behaviour was revealed by the characterization of Dropping and Wet&Dry-aged bronze surfaces, characterised by the internal oxidation and decuprification process. However, the corrosion layer on the samples produced with Dropping is thicker and a slight erosion effect was also detected. So both the artificial patinas well represented the main features of the real corroded substrates of outdoor bronzes and patinated Cu-Sn-Zn-Pb substrates obtained by Dropping were selected as representative substrates for the application of the selected treatments. On the other hand, the K_2S patina on Cu-Si-Mn bronze is characterised by a developed surface roughness and porosity. It forms a double-layer structure: an internal cuprous oxide layer, directly related to surface heating during the first step of the patination, covered by an external one consisting mainly of cuprous sulphide developing small coalesced crystals, as reported in paragraph 6.1.

From a methodological point of view, the important achievement of this study was the implementation of the Dropping device for the patination of a large set of samples in the same experimental conditions. The standardisation of representative aged surfaces equivalent to natural bronze patinas is a fundamental point for justifying the performance of conservation treatments, such as, for example, when designing the efficiency of protective coatings. To this aim, the implemented method in relation to artificially aged bronze patinas

representative of naturally aged outdoor bronzes was developed, essential for the reproducible evaluation of conservation treatments. The scale up set for the Dropping test device allowed the ageing of a batch of 52 samples under the same experimental conditions. However, considerations of the effect of the experimental set up initially defined in the earliest papers [34,35,61] have to be taken into account, such as the bronze composition. In particular, tin content in as-cast bronzes seems to play an important role in corrosion behaviour. As well-known for bronze alloys [114], the formation and proportion of eutectoid including delta phase is also related to the cooling rate. Thus in as-cast condition, the formation of eutectoid is observed at around 6-8 wt% Sn for industrial and artistic bronzes, quite far from the maximum Sn solubility in Cu solid solution (15.8 wt%). In this study, the Sn content of the bronze was around 7 wt%, higher than in [34,35], which was 4.4 wt%, and the presence of delta phase in the interdendritic eutectoid is quite important as evidenced by surface observation [121]. So, the presence of the Sn-rich δ phase, chemically more stable, is probably enhancing the general stability of the bronze. This could explain the less-effective corrosion impact of both ageing tests (Dropping and Wet&Dry) observed in comparison to the previous studies [34,35]. Furthermore, for the Dropping test, the drop dimension, the drop fall height, the average flow rate and the alternate wet and dry cycles are fundamental parameters for optimising the mechanical effect of runoff. Also, the less evident erosion effect observed in this study for the dropping test in comparison to the more pronounced alteration in the reference study [34] could also be ascribed to the feebler impact due to the greater dimension of drops used for batch making. In this context, additional improvements could be performed for providing fully controlled ageing standards for outdoor bronze, such as including the impact of the tin concentration or the wetting condition on the corrosion rate for improving the time schedule as well as the phenomenon amplitude.

In chapter 4, the assessment of the protectiveness of charged silane coatings (PropS-SH+β-CD+MPT and PropS-SH+FA) and fluoropolymers (FA-MS) shows that all the applied coatings produced continuous layers and exhibited similar inhibiting efficiencies in terms of metal release compared to Incralac®. In addition, from the electrochemical point of view, the selected coatings offer a better protection to patinated Cu-Sn-Zn-Pb than Incralac®, showing a more efficient barrier effect against both the cathodic and anodic process. Finally, the occupational exposure test determines that the selected coatings have low toxicity, as they exhibit a EL < 1, contrary to what measured for Incralac®. Considering all the qualitative physical properties of the selected coatings, such as colour changes, coverage ability, thickness homogeneity and porosity, as well as qualitative evaluation of the effect of accelerated ageing (Dropping) and electrochemical measurements, FA-MS was selected as the best protective treatment for the patinated Cu-Sn-Zn-Pb, mainly due to the low aesthetical impact during coating application, while charged silane coatings induces a colour variation close to the limit of acceptability for Cultural Heritage applications.

Chapter 5 demonstrates that XPS technique is a powerful tool for the study of interaction of coatings with the patinated bronze substrate. The influence of the main alloying elements of a quinary bronze alloy (Cu-Sn-Zn-

Pb-Sb) was discussed to understand the interaction with the organosilane coating (PropS-SH). Simpler substrates, such as pure Cu and Sn, a binary Cu-Sn alloy and an inert sample were analysed by XPS after the application of PropS-SH coating. Coupling conventional XPS technique with High resolution-Synchrotron Radiation XPS device (HR-SRPES) carried out at Antares beamline at the Synchrotron Soleil (Saint Aubin, France), it was found that the coating tightly follow the morphology of the substrate on which they are applied and on patinated quinary bronze, the coating penetrates into the porosities apparently insulating the bronze substrate. Finally, in all the substrates the contribution of thiolate bonds to silane adhesion has been observed and more uniform silane layer forms by passing from pure Sn to bronze to pure Cu.

In chapter 6, the results about the protective assessment of protective coatings for the conservation of black patinated (K_2S) Cu-Si-Mn bronze alloy were discussed. For this rough patinated substrate, PropS-SH shows outstanding properties compared to both uncoated samples and Incralac® performance. Regarding electrochemical tests both the coatings applied by spraying offer a good protection to patinated bronze, better than that by dip-coating, particularly in the case of PropS-SH. With the former application method, final protective efficiency (PE) values are 97 and 89% for silane and Incralac®, respectively. Similar trend was also recorded by the measurement of the inhibiting efficiency in terms of metal release and particularly PropS-SH also prevents the accumulation of insoluble corrosion products under the patina, while Incralac® cannot avoid the formation of a silicon-enriched corrosion product suggesting the onset of decuprification.

The results achieved in this study also allowed the final actions of B-IMPACT project. In particular, the selection of the treatment for both the patinated bronze substrates (FA-MS for Cu-Sn-Zn-Pb and PropS-SH for Cu-Si-Mn) was necessary in the phase of the pre-industrialisation process and validation of coating application. In particular, a B-IMPACT test-kit containing a bronze object, PropS-SH coating and instructions for application, was prepared (Figure 7.1) and sent to selected end-users (restorers, artistic foundries, …) for testing. The end-users were required to fill up an on-line questionnaire. The feedbacks from the end-users highlight a very positive performance of the coating in general. Some comments were reported about the smell of the coating released during application and scattered feedbacks about the visual appearance were recorded.

Figure 7.1: B-IMPACT test-kit (bronze object, selected coating, instruction for application) sent to selected end-users and a print screen of the on-line questionnaire [167].

143

Finally, in order to monitor the long-term durability of both the selected coatings, two identical bronze object depicting the Slovenian poet France Prešeren (1800-1849) were supplied by the artistic foundry Livartis d.o.o. (subcontractor of the B-IMPACT project) and installed in the park of ZAG Institute (March 2017). The objects were made of the same alloys used for the samples of this study: Cu-Sn-Pb-Zn bronze without artificial patination and Cu-Si-Mn alloy already supplied black-patinated (K_2S). In the first case, FA-MS will be applied when the bronze will be naturally patinated, while on black-patinated object PropS-SH was applied at the moment of installation. Durability and protective performance of the coatings will be monitored by checking the visual appearance and by characterisation with a portable X-Ray Fluorescence (XRF). As revealed Figure 7.2, the traditional quaternary bronze object showed only some traces of the natural patina after more than 5 months of outdoor exposure. FA-MS coating will be applied only when the object surface will be more homogenously patinated.

Figure 7.2: Evaluation of surface evolution of the Cu-Sn-Zn-Pb object after more than 150 days after installation (FA-MS coating has not been applied yet) [168]*.*

Conversely, the black patinated Cu-Si-Mn object already coated by PropS-SH did not reveal any visual changes after the first 5 months of outdoor exposure. The test is still in progress and the main observation about the performances of both the coatings will be reported also in the future in order to fulfil the understanding in terms of long-term durability of the selected B-IMPACT coatings.

Figure 7.3: Visual appearance evolution of the coated black-patinated object by PropS-SH at the moment of the installation, after 3 days and after more than 150 days after installation. No appreciable visual difference were observed in more than 5 months of outdoor exposure [168].

To conclude, a consistent understanding about the protectiveness of different innovative, non-hazardous coatings was achieved thanks to a systematic and multi-analytical approach. However, some aspects could be furtherly investigated. In particular, the influence of acid rain was investigated as the main responsible of the mechanism of decay of outdoor bronzes. As pointed out in the introduction, the atmosphere is a very complex media and several factors can play a role in the mechanism of decay of metallic Cultural Heritage. For this reason, the synergistic action of different air pollutants, such as particulate matters (PM) and UV radiation should be deeply investigated, in order to complete the assessment of the performance of the selected coatings. As in this study organic polymers were investigated, the influence of temperature should be also considered as one of the parameter acting in synergism with the other environmental constituents. A broad investigation on the influence of these main environmental pollutants will fulfil the scientific understanding about the mechanisms of decay of bronze substrates and of promising protective treatments to be used for conservation. In addition, for engineer practice it would be possible to develop an implemented systematic method to evaluate innovative protective coatings, considering the synergistic action of the main aggressive constituents present in atmosphere.

Finally, one of the requirements for protective treatment for conservation coatings is the removability of the coatings. In this study, only some literature data are reported about this aspect. It is known that fluoropolymers may be easily removed by polar solvents, such as acetone [75]. So, a specific study about the removability and consequently the re-applicability of the selected coatings will be carried out in order to verify all the requirements for the acceptability of the selected coatings for conservation practice.

References

[1]   M-ERA.NET Transnational Call 2013 - B-IMPACT project - Full proposal, 2013.

[2]   D. Watkinson, Preservation of Metallic Cultural Heritage, in: Shreir's Corros., Tony, J.A., Elsevier: Oxford, 2010: pp. 3307–3341.

[3]   Appelbaum, Conservation Treatment Methodology, Elsevier: Oxford, 2007.

[4]   International Standard BS EN ISO 8044:2015 Corrosion of metals and alloys. Basic terms and definitions, 2015.

[5]   S.S. Shreir, Corrosion 1 Metal/Environment reactions, Newnes-Butterworths, 1976.

[6]   Pratical Use of E-pH Diagrams, in: ASM Handbook, Vol. 13A, Corros. Fundam. Test. Prot., 2005.

[7]   G. Bianchi, F. Mazza, Corrosione e protezione dei metalli, Associazione italiana di metallurgia, 2000.

[8]   D.E. Tyler, W.T. Black, Introduction to Copper and Copper Alloys, in Properties and Selection: Nonferrous Alloys and Special-Purpose Materials, in: ASM Hand Vol. 2, ASM Int., 1990.

[9]   Casting of Copper and Copper Alloys Casting, Vol 15, in: ASM Handbook, ASM Int., 2008: pp. 1026–1048.

[10]   U.S. General Services Administration, http://www.gsa.gov/portal/content/111994.

[11]   D.A. Scott, Metallography and microstructure in ancient and historic metals, Getty publications, 1992.

[12]   Cu (Copper) Binary Alloy Phase Diagrams, Alloy Phase Diagrams, in: Vol 3, ASM Handbook, ASM Int., 2016: pp. 304–326.

[13]   https://www.doitpoms.ac.uk/miclib/micrograph.php?id=485.

[14]   J. Watt, J. Tidblad, V. Kucera, R. Hamilton, The effects of air pollution on cultural heritage, Springer, 2009.

[15]   European Environment agency, EEA Report, Air quality in Europe — 2016 report, 2016.

[16]   L. Robbiola, J.M. Blengino, C. Fiaud, Morphology and mechanisms of formation of natural patinas on archeological Cu-Sn alloys, Corros. Sci. 40 (1998) 2083–2111.

[17]   L. Robbiola, H.P. Hurtel, Nouvelle contribution à l'étude des mécanismes de corrosion des bronzes de plein air: caractérisation de l'altération de bronzes de Rodin, (1991) 809–823.

[18]   C. Chiavari, K. Rahmouni, H. Takenouti, S. Joiret, P. Vermaut, L. Robbiola, Composition and electrochemical properties of natural patinas of outdoor bronze monuments, Electrochim. Acta. 52 (2007) 7760–7769. doi:10.1016/j.electacta.2006.12.053.

[19]   L. Robbiola, K. Rahmouni, C. Chiavari, C. Martini, D. Prandstraller, A. Texier, et al., New insight into the nature and properties of pale green surfaces of outdoor bronze monuments, Appl. Phys. A Mater. Sci. Process. 92 (2008) 161–169. doi:10.1007/s00339-008-4468-4.

[20]   H. Strandberg, Reactions of copper patina compounds - I. Influence of some air pollutants, Atmos. Environmenr. 32 (1998) 3511–3520.

[21]   T.E. Graedel, K. Nassau, J.P. Franey, Copper patinas formed in the atmosphere—I. Introduction, Corros. Sci. 27 (1987) 639–657. doi:https://doi.org/10.1016/0010-938X(87)90047-3.

[22]   D. de la Fuente, J. Simancas, M. Morcillo, Morphological study of 16-year patinas formed on copper in a wide range of atmospheric exposures, Corros. Sci. 50 (2008) 268–285. doi:10.1016/j.corsci.2007.05.030.

[23]   Y.S. Hedberg, J.F. Hedberg, G. Herting, S. Goidanich, I.O. Wallinder, Critical Review: Copper Runoff from Outdoor Copper Surfaces at Atmospheric Conditions, Environ. Sci. Technol. 48 (2014) 1372–1381. doi:10.1021/es404410s.

[24]   M. Morcillo, T. Chang, B. Chico, D. De Fuente, I. Odnevall Wallinder, J.A. Jiménez, et al., Characterisation of a centuries-old patinated copper roof tile from Queen Anne' s Summer Palace in Prague, Mater. Charact. 133 (2017) 146–155. doi:10.1016/j.matchar.2017.09.034.

[25]   A. Krätschmer, I. Odnevall Wallinder, C. Leygraf, The evolution of outdoor copper patina, Corros. Sci. 44 (2002) 425–450. doi:10.1016/S0010-938X(01)00081-6.

[26]   C. Chiavari, E. Bernardi, C. Martini, L. Morselli, F. Ospitali, L. Robbiola, et al., Predicting the corrosion behaviour of outdoor bronzes: assessment of artificially exposed and real outdoor samples, Met. 2010 Proc. Interim Meet. ICOM-CC Met. Work. Group, Oct. 11-15, 2010, Charleston, South Carolina, USA. (2011) 218–226.

[27]   L. Robbiola, C. Fiaud, S. Pennec, New model of outdoor bronze corrosion and its implications for conservation, in: ICOM Comm. Conserv. Tenth Trienn. Meet., August 199, Washington DC, USA, 1993: pp. 796–802.

[28]   S. Jouen, B. Hannoyer, A. Barbier, J. Kasperek, M. Jean, A comparison of runoff rates between Cu, Ni, Sn and Zn in the first steps of exposition in a French industrial atmosphere, Mater. Chem. Phys. 85 (2004) 73–80. doi:10.1016/j.matchemphys.2003.12.008.

[29]   V. Alunno Rossetti, M. Marabelli, Analyses of the patinas of a gilded horse of St Mark's Basilica in Venice: corrosion mechanisms and conservation problems, Stud. Conserv. 21 (1976) 161–170.

[30]   T. Chang, I. Odnevall Wallinder, D. de la Fuente, B. Chico, M. Morcillo, J. Welter, et al., Analysis of Historic Copper Patinas . Influence of Inclusions on Patina Uniformity, Materials (Basel). 10 (2017) 1–13. doi:10.3390/ma10030298.

[31]   T. Kosec, H. Otmacic Curkovic, A. Legat, Investigation of the corrosion protection of chemically and electrochemically formed patinas on recent bronze, Electrochim. Acta. 56 (2010) 722–731. doi:10.1016/j.electacta.2010.09.093.

[32]   P. Eriksson, L.G. Johansson, J. Gullman, A laboratory study of corrosion reactions on statue bronze, Corros. Sci. 34 (1993) 1083–1097. doi:http://dx.doi.org/10.1016/0010-938X(93)90290-W.

[33]   S. Goidanich, I.O. Wallinder, G. Herting, C. Leygraf, Corrosion induced metal release from copper based alloys compared to their pure elements, Corros. Eng. Sci. Technol. 43 (2008) 134–141. doi:10.1179/174327808X286383.

[34]   E. Bernardi, C. Chiavari, B. Lenza, C. Martini, L. Morselli, F. Ospitali, et al., The atmospheric corrosion of quaternary bronzes: The leaching action of acid rain, Corros. Sci. 51 (2009) 159–170. doi:10.1016/j.corsci.2008.10.008.

[35]   C. Chiavari, E. Bernardi, C. Martini, F. Passarini, F. Ospitali, L. Robbiola, The atmospheric corrosion of quaternary bronzes: The action of stagnant rain water, Corros. Sci. 52 (2010) 3002–3010.

doi:10.1016/j.corsci.2010.05.013.

[36]   J. Wolfe, R. Grayburn, A review of the development and testing of Incralac lacquer A review of the development and testing of Incralac lacquer, J. Am. Inst. Conserv. (2017) 1–20. doi:10.1080/01971360.2017.1362863.

[37]   http://www.conservationsupportsystems.com/product/show/incralac-solvent-based/metal-coatings.

[38]   J. Wolfe, R. Grayburn, H. Khanjian, A. Heginbotham, A. Phenix, Deconstructing Incralac : A formulation study of acrylic coatings for the protection of outdoor bronze sculpture, in: ICOM-CC 18th Trienn. Conf. (2017, Copenhagen), 2017: pp. 1–9.

[39]   L.B. Brostoff, E. De La Rie, Research into protective coating systems for outdoor bronze sculpture and ornamentation, in: Conférence Int. Sur La Conserv. Des Métaux, 1997: pp. 242–244.

[40]   J. Kim, K. Chang, T. Isobe, S. Tanabe, Acute toxicity of benzotriazole ultraviolet stabilizers on freshwater crustacean (Daphnia pulex), J. Toxicol. Sci. 36 (2011) 247–251.

[41]   C.J. McNamara, M. Breuker, M. Helms, T.D. Perry, R. Mitchell, Biodeterioration of Incralac used for the protection of bronze monuments, J. Cult. Herit. 5 (2004) 361–364. doi:10.1016/j.culher.2004.06.002.

[42]   C. Li, Biodeterioration of Acrylic Polymers Paraloid B-72 and B-44 : Report on Field Trials, Anatol. Archeol. Stud. 15 (2006) 283–289.

[43]   D.L. Moffett, Wax coatings on ethnographic metal objects: Justifications for allowing a tradition to wane, J. Am. Inst. Conserv. 35 (1996) 1–7.

[44]   C.A. Grissom, N. Grabow, C.S. Riley, A.E. Charola, Evaluation of coating performance on silver exposed to hydrogen sulfide, J. Am. Inst. Conserv. 52 (2013) 82–96.

[45]   T. Jaeger, Short communication removal of paraffin wax in the re-treatment of archaeological iron, J. Am. Inst. Conserv. 47 (2008) 217–223.

[46]   N. Swartz, T.L. Clare, On the protective nature of wax coatings for culturally significant outdoor metalworks: microstructural flaws, oxidative changes, and barrier properties, J. Am. Inst. Conserv. 54 (2015) 181–201.

[47]   F. Zucchi, V. Grassi, A. Frignani, G. Trabanelli, C. Monticelli, Octadecyl-trimethoxy-silane film formed on copper in different conditions, Mater. Chem. Phys. 103 (2007) 340–344. doi:10.1016/j.matchemphys.2007.02.050.

[48]   F. Deflorian, S. Rossi, L. Fedrizzi, M. Fedel, Integrated electrochemical approach for the investigation of silane pre-treatments for painting copper, Prog. Org. Coatings. 63 (2008) 338–344. doi:10.1016/j.porgcoat.2008.03.005.

[49]   C. Rahal, M. Masmoudi, M. Abdelmouleh, R. Abdelhedi, An environmentally friendly film formed on copper: Characterization and corrosion protection, Prog. Org. Coatings. 78 (2015) 90–95. doi:10.1016/j.porgcoat.2014.09.018.

[50]   R.J. Tremont, D.R. Blasini, C.R. Cabrera, Controlled self-assembly of mercapto and silane terminated molecules at Cu surfaces, J. Electroanal. Chem. 556 (2003) 147–158. doi:10.1016/S0022-0728(03)00340-1.

[51]   F. Zucchi, A. Frignani, V. Grassi, G. Trabanelli, M. Dal Colle, The formation of a protective layer of 3-mercapto-propyl-trimethoxy-silane on copper, Corros. Sci. 49 (2007) 1570–1583.

doi:10.1016/j.corsci.2006.08.019.

[52] F. Sinapi, S. Julien, D. Auguste, L. Hevesi, J. Delhalle, Z. Mekhalif, Monolayers and mixed-layers on copper towards corrosion protection, Electrochim. Acta. 53 (2008) 4228–4238. doi:10.1016/j.electacta.2007.12.061.

[53] Y.S. Li, W. Lu, Y. Wang, T. Tran, Studies of (3-mercaptopropyl)trimethoxylsilane and bis(trimethoxysilyl)ethane sol-gel coating on copper and aluminum, Spectrochim. Acta - Part A Mol. Biomol. Spectrosc. 73 (2009) 922–928. doi:10.1016/j.saa.2009.04.016.

[54] A. Balbo, A. Frignani, C. Monticelli, Influence of nanoparticles on the inhibiting efficiency of organosilane coatings on bronze. Part 1: Electrochemical characterization, in: Eurocorr 2012 (EFC Event n.330), EFC, London, UK, 2012: p. 1–8 (Paper: 1524).

[55] A. Balbo, C. Chiavari, C. Martini, C. Monticelli, Effectiveness of corrosion inhibitor films for the conservation of bronzes and gilded bronzes, Corros. Sci. 59 (2012) 204–212. doi:10.1016/j.corsci.2012.03.003.

[56] C. Chiavari, A. Balbo, E. Bernardi, C. Martini, F. Zanotto, I. Vassura, et al., Organosilane coatings applied on bronze: Influence of UV radiation and thermal cycles on the protectiveness, Prog. Org. Coatings. 82 (2015) 91–100. doi:10.1016/j.porgcoat.2015.01.017.

[57] C. Chiavari, A. Balbo, E. Bernardi, C. Martini, M.C. Bignozzi, M. Abbottoni, et al., Protective silane treatment for patinated bronze exposed to simulated natural environments, Mater. Chem. Phys. 141 (2013) 502–511. doi:10.1016/j.matchemphys.2013.05.050.

[58] W.J. van Ooij, D. Zhu, M. Stacy, A. Seth, T. Mugada, J. Gandhi, et al., Corrosion Protection Properties of Organofunctional Silanes—An Overview, Tsinghua Sci. Technol. 10 (2005) 639–664. doi:10.1016/S1007-0214(05)70134-6.

[59] H. Fan, S. Li, Z. Zhao, H. Wang, Z. Shi, L. Zhang, Inhibition of brass corrosion in sodium chloride solutions by self-assembled silane films, Corros. Sci. 53 (2011) 4273–4281. doi:10.1016/j.corsci.2011.08.039.

[60] M. Kozelj, A.S. Vuk, I. Jerman, B. Orel, Corrosion protection of Sunselect, a spectrally selective solar absorber coating, by (3-mercaptopropyl)trimethoxysilane, Sol. Energy Mater. Sol. Cells. 93 (2009) 1733–1742. doi:10.1016/j.solmat.2009.05.023.

[61] C. Chiavari, E. Bernardi, A. Balbo, C. Monticelli, S. Raffo, M.C. Bignozzi, et al., Atmospheric corrosion of fire-gilded bronze: corrosion and corrosion protection during accelerated ageing tests, Corros. Sci. 100 (2015) 435–447. doi:http://dx.doi.org/10.1016/j.corsci.2015.080.013.

[62] D. Zhu, W.J. Van Ooij, Corrosion protection of metals by water-based silane mixtures of bis-[trimethoxysilylpropyl]amine and vinyltriacetoxysilane, Prog. Org. Coatings. 49 (2004) 42–53. doi:10.1016/j.porgcoat.2003.08.009.

[63] F. Zucchi, V. Grassi, A. Frignani, G. Trabanelli, Inhibition of copper corrosion by silane coatings, Corros. Sci. 46 (2004) 2853–2865. doi:10.1016/j.corsci.2004.03.019.

[64] Y.S. Li, W. Lu, Y. Wang, T. Tran, Studies of (3-mercaptopropyl)trimethoxylsilane and bis(trimethoxysilyl)ethane sol-gel coating on copper and aluminum, Spectrochim. Acta - Part A Mol. Biomol. Spectrosc. 73 (2009) 922–928. doi:10.1016/j.saa.2009.04.016.

[65] A. Balbo, A. Frignani, C. Monticelli, Influence of nanoparticles on the inhibiting efficiency of organosilane coatings on bronze. Part 1: Electrochemical characterization, in: Eurocorr 2012 (EFC

Event n.330), EFC, London, UK (CD-ROM), Istanbul, Turkey, 2012: p. 1–8 (Paper 1524).

[66] G. Gupta, S.S. Pathak, A.S. Khanna, Anticorrosion performance of eco-friendly silane primer for coil coating applications, Prog. Org. Coatings. 74 (2012) 106–114. doi:10.1016/j.porgcoat.2011.11.023.

[67] J. Bao, Q. Wang, X. Liu, L. Ding, Site-selective deposition of copper by controlling surface reactivity of SAMs with UV-irradiation, Surf. Sci. 602 (2008) 2250–2255. doi:10.1016/j.susc.2008.05.005.

[68] H. Zhao, R.K.Y. Li, A study on the photo-degradation of zinc oxide (ZnO) filled polypropylene nanocomposites, Polymer (Guildf). 47 (2006) 3207–3217. doi:10.1016/j.polymer.2006.02.089.

[69] A.P. Kumar, D. Depan, S.T. Tomer, S.R. P, Nanoscale particles for polymer degradation and stabilization — Trends and future perspectives, Prog. Polym. Sci. 34 (2009) 479–515. doi:10.1016/j.progpolymsci.2009.01.002.

[70] D.K. Hwang, J.H. Moon, Y.G. Shul, K.T. Jung, D.H. Kim, D.W. Lee, Scratch Resistant and Transparent UV-Protective Coating on Polycarbonate, J. Sol. 26 (2003) 783–787.

[71] X.D. Chen, Z. Wang, Z.F. Liao, Y.L. Mai, M.Q. Zhang, Roles of anatase and rutile TiO2 nanoparticles in photooxidation of polyurethane, Polym. Test. 26 (2007) 202–208. doi:10.1016/j.polymertesting.2006.10.002.

[72] M. Pilz, H. Romich, Sol-Gel Derived Coatings for Outdoor Bronze Conservation, Hournal Sol-Gel Sci. Technol. 8 (1997) 1071–1075.

[73] V. Balek, Z. Málek, B. Cásenský, D. Niznanský, J. Šubrt, E. Vecerníková, et al., A new approach to characterization of barrier properties of ORMOCER protective coatings, J. Sol-Gel Sci. Technol. 8 (1997) 591–594. doi:10.1007/BF02436905.

[74] E. Joseph, P. Letardi, R. Mazzeo, S. Prati, M. Vandini, Innovative treatments for the protection of outdoor bronze monuments, in: Met. 2007, Rijksmuseum, Amsterdam, 2007: pp. 71–77.

[75] R.A. Iezzi, S. Gaboury, K. Wood, Acrylic-fluoropolymer mixtures and their use in coatings, Prog. Org. Coatings. 40 (2000) 55–60. doi:10.1016/S0300-9440(00)00117-X.

[76] G. Bierwagen, T.J. Shedlosky, K. Stanek, Developing and testing a new generation of protective coatings for outdoor bronze sculpture, Prog. Org. Coatings. 48 (2003) 289–296. doi:10.1016/j.porgcoat.2003.07.004.

[77] M. Albini, C. Chiavari, E. Bernardi, C. Martini, L. Mathys, E. Joseph, Evaluation of the performances of a biological treatment on tin-enriched bronze, Environ. Sci. Pollut. Res. (2016) 1–10. doi:10.1007/s11356-016-7361-2.

[78] M. Albini, Fungal biogenic patina: optimization of an innovative conservation treatment for copper-based artefacts, University of Neuchatel, Swiss, 2017.

[79] G. Giuntoli, L. Rosi, M. Frediani, B. Sacchi, B. Salvadori, S. Porcinai, et al., Novel coatings from renewable resources for the protection of bronzes, Prog. Org. Coatings. 77 (2014) 892–903. doi:10.1016/j.porgcoat.2014.01.021.

[80] M. Matteini, Interventi di conservazione dei bronzi in ambiente urbano - tecniche innovative di inibizione della corrosione, in: Sci. E Beni Cult. XXXI, 2015: pp. 253–263.

[81] F. Faraldi, E. Angelini, C. Riccucci, A. Mezzi, D. Caschera, S. Grassini, Innovative diamond-like carbon coatings for the conservation of bronzes, Surf. Interface Anal. 46 (2014) 764–770. doi:10.1002/sia.5367.

[82]   R. Grayburn, Z.E. Voras, C.M. Goodwin, M.C. Liu, T.P. Beebe, A. Phenix, Ion probe techniques to measure the distribution of substrate elements in coatings for copper alloys, Prog. Org. Coatings. 111 (2017) 267–272. doi:10.1016/j.porgcoat.2017.06.016.

[83]   T. Kosec, A. Legat, I. Miloev, The comparison of organic protective layers on bronze and copper, Prog. Org. Coatings. 69 (2010) 199–206. doi:10.1016/j.porgcoat.2010.04.010.

[84]   K. Rahmouni, H. Takenouti, N. Hajjaji, A. Srhiri, L. Robbiola, Protection of ancient and historic bronzes by triazole derivatives, Electrochim. Acta. 54 (2009) 5206–5215. doi:10.1016/j.electacta.2009.02.027.

[85]   T. Kosec, D.K. Merl, I. Milošev, Impedance and XPS study of benzotriazole films formed on copper, copper-zinc alloys and zinc in chloride solution, Corros. Sci. 50 (2008) 1987–1997. doi:10.1016/j.corsci.2008.04.016.

[86]   A. Galtayries, A. Mongiatti, P. Marcus, C. Chiavari, Surface characterisation of corrosion inhibitors on bronzes for artistic casting, Corros. Met. Herit. Artefacts Investig. Conserv. Predict. Long Term Behav. 48 (2007) 335–351. doi:10.1533/9781845693015.335.

[87]   J.E. Fagel Jr, G.W. Ewing, The Ultraviolet Absorption of Benzotriazole1a, J. Am. Chem. Soc. 73 (1951) 4360–4362.

[88]   M.P. Casaletto, C. Cirrincione, A. Priviter, V. Basilissi, A Sustainable Approach to the Conservation of Bronze Artworks by Smart Nanostructured Coatings, in: Proc. Interim Meet. ICOM-CC Met. Work. Gr., 2016: pp. 144–152.

[89]   M. Wadsak, I. Constantinides, G. Vittiglio, A. Adriaens, K. Janssens, M. Schreiner, et al., Inhibiting effect of 4-methyl-1-p-tolylimidazole to the corrosion of bronze patinated in sulphate medium, J. Cult. Herit. 37 (2013) 7491–7502. doi:10.1016/j.electacta.2011.06.107.

[90]   B. Salvadori, A. Cagnini, M. Galeotti, S. Porcinai, S. Goidanich, A. Vicenzo, et al., Traditional and innovative protective coatings for outdoor bronze : Application and performance comparison, J. Appl. Polym. Sci. 460112 (2017) 1–12. doi:10.1002/app.46011.

[91]   K. Marusic, H. Otmacic-Curkovic, S. Horvat-Kurbegovic, H. Takenouti, E. Stupnisek-Lisac, Comparative studies of chemical and electrochemical preparation of artificial bronze patinas and their protection by corrosion inhibitor, Electrochim. Acta. 54 (2009) 7106–7113. doi:10.1016/j.electacta.2009.07.014.

[92]   H. Otmacic Curkovic, T. Kosec, K. Marusic, A. Legat, An electrochemical impedance study of the corrosion protection of artificially formed patinas on recent bronze, Electrochim. Acta. 83 (2012) 28–39. doi:10.1016/j.electacta.2012.07.094.

[93]   S. Varvara, R. Bostan, O. Bobis, G. Luiza, V. Mena, R.M. Souto, Applied Surface Science Propolis as a green corrosion inhibitor for bronze in weakly acidic solution, Appl. Surf. Sci. 426 (2017) 1100–1112. doi:10.1016/j.apsusc.2017.07.230.

[94]   E. Cano, D. Lafuente, D.M. Bastidas, Use of EIS for the evaluation of the protective properties of coatings for metallic cultural heritage: A review, J. Solid State Electrochem. 14 (2010) 381–391. doi:10.1007/s10008-009-0902-6.

[95]   P. Letardi, B. Salvadori, M. Galeotti, A. Cagnini, S. Porcinai, A. Santagostino Barbone, et al., An in situ multi-analytical approach in the restoration of bronze artefacts, Microchem. J. 125 (2016) 151–158. doi:10.1016/j.microc.2015.11.018.

[96]   E. Bescher, J.D. Mackenzie, Sol-gel coatings for the protection of brass and bronze, J. Sol-Gel Sci. Technol. 26 (2003) 1223–1226. doi:10.1023/A:1020724605851.

[97]   W. Sperotto, E. Tedesco, B-IMPACT Deliverable 3.1 - Survey report on toxicity, 2015.

[98]   OECD Guidelines for the testing of Chemicls - http://www.oecd.org/chemicalsafety/testing/oecdguidelinesforthetestingofchemicals.htm, (1994).

[99]   C.A.M. Broers, J. Lappalainen, New developments in the bioluminescence assay, (2004).

[100] S. Parvez, C. Venkataraman, S. Mukherji, A review on advantages of implementing luminescence inhibition test (Vibrio fischeri) for acute toxicity prediction of chemicals, Environ. Int. 32 (2006) 265–268.

[101] M. Farré, D. Barceló, Toxicity testing of wastewater and sewage sludge by biosensors, bioassays and chemical analysis, TrAC Trends Anal. Chem. 22 (2003) 299–310.

[102] C.R. Janssen, G. Persoone, Rapid toxicity screening tests for aquatic biota 1. Methodology and experiments with Daphnia magna, Environ. Toxicol. Chem. 12 (1993) 711–717.

[103] M.A. Lewis, Chronic and sublethal toxicities of surfactants to aquatic animals: a review and risk assessment, Water Res. 25 (1991) 101–113.

[104] D.G. Crosby, R.K. Tucker, Toxicity of aquatic herbicides to Daphnia magna, Science (80). 154 (1966) 289–291.

[105] R.W. Andrew, K.E. Biesinger, G.E. Glass, Effects of inorganic complexing on the toxicity of copper to Daphnia magna, Water Res. 11 (1977) 309–315.

[106] K.M. Newton, Toxicity of binary metal mixtures to freshwater aquatic organisms: Experimental design, acute and chronic effects, (2015).

[107] J. Cristale, A.G. Vázquez, C. Barata, S. Lacorte, Priority and emerging flame retardants in rivers: occurrence in water and sediment, Daphnia magna toxicity and risk assessment, Environ. Int. 59 (2013) 232–243.

[108] C. Wang, C. Liang, H. Yeh, Aquatic acute toxicity assessments of molybdenum (+ VI) to Daphnia magna, Chemosphere. 147 (2016) 82–87.

[109] L.A. V De Luna, T.H.G. Da Silva, R.F.P. Nogueira, F. Kummrow, G.A. Umbuzeiro, Aquatic toxicity of dyes before and after photo-Fenton treatment, J. Hazard. Mater. 276 (2014) 332–338.

[110] A. Parrella, M. Kundi, M. Lavorgna, E. Criscuolo, C. Russo, M. Isidori, Toxicity of exposure to binary mixtures of four anti-neoplastic drugs in Daphnia magna and Ceriodaphnia dubia, Aquat. Toxicol. 157 (2014) 41–46.

[111] X. Wu, N. Chou, D. Lupher, L.C. Davis, Benzotriazoles: toxicity and degradation, in: Conf. Hazard. Waste Res. Kansas City, MO, 1998.

[112] D.A. Pillard, J.S. Cornell, D.L. DuFresne, M.T. Hernandez, Toxicity of benzotriazole and benzotriazole derivatives to three aquatic species, Water Res. 35 (2001) 557–560.

[113] M.L. Young, S. Schnepp, F. Casadio, A. Lins, M. Meighan, J.B. Lambert, et al., Matisse to Picasso : a compositional study of modern bronze sculptures, (2009) 171–184. doi:10.1007/s00216-009-2938-y.

[114] R.N. Caron, R.G. Barth, D.E. Tyler, Metallography and Microstructures of copper and its alloys, in:

Metallogr. Microstruct. Vol 9, ASM Handb., ASM International, 2004: pp. 775–788.

[115] A. Cohen, Properties of Cast Copper Alloys, Properties and Selection: Nonferrous Alloys and Special-Purpose Materials, in: Vol 2, ASM Handbook, ASM Int., 1990: pp. 356–391.

[116] P.D. Weil, A review of the history and practice of patination, Corros. Met. Artifacts A Dialogue Between Conserv. Archaeol. Corros. Sci. 479 (1977) 77.

[117] R. Hughes, Artificial patination, Butterworth-Heinemann Oxford, 1993.

[118] G. Masi, C. Chiavari, J. Avila, J. Esvan, S. Raffo, M.C. Bignozzi, et al., Corrosion investigation of fire-gilded bronze involving high surface resolution spectroscopic imaging, Appl. Surf. Sci. 366 (2016) 317–327. doi:10.1016/j.apsusc.2016.01.101.

[119] P. Marcus, F. Mansfeld, Analytical methods in corrosion science and engineering, CRC press, 2005.

[120] A. Balbo, C. Monticelli, N. Gartner, T. Kosec, E. Fabjan, B-IMPACT Deliverable 2.1 - Proposal for cadidate protection systems for patinated bronze, 2016.

[121] G. Masi, A. Balbo, J. Esvan, C. Monticelli, J. Avila, L. Robbiola, et al., X-ray Photoelectron Spectroscopy as a tool to investigate silane-based coatings for the protection of outdoor bronze: The role of alloying elements, Appl. Surf. Sci. 433 (2018). doi:10.1016/j.apsusc.2017.10.089.

[122] E. Bernardi, C. Chiavari, C. Martini, L. Morselli, The atmospheric corrosion of quaternary bronzes: An evaluation of the dissolution rate of the alloying elements, Appl. Phys. A Mater. Sci. Process. 92 (2008) 83–89. doi:10.1007/s00339-008-4451-0.

[123] C. Chiavari, E. Bernardi, D. Cauzzi, S. Volta, M.C. Bignozzi, B. Lenza, et al., Influence of natural patinas of outdoor quaternary bronzes on conservation treatments, Met. 2013 Proc. Interim Meet. ICOM-CC Met. Work. Gr. (2013) 159–168.

[124] G. Masi, J. Esvan, C. Josse, C. Chiavari, E. Bernardi, C. Martini, et al., Characterization of typical patinas simulating bronze corrosion in outdoor conditions, Mater. Chem. Phys. 200 (2017) 308–321. doi:10.1016/j.matchemphys.2017.07.091.

[125] G. Graziani, E. Sassoni, G.W. Scherer, E. Franzoni, Resistance to simulated rain of hydroxyapatite- and calcium oxalate-based coatings for protection of marble against corrosion, Corros. Sci. 127 (2017) 168–174. doi:10.1016/j.corsci.2017.08.020.

[126] W. Mokrzycki, M. Tatol, Color difference Delta E - A survey, Mach. Graph. Vis. 20 (2011).

[127] L.A. Giannuzzi, F.A. Stevie, A review of focused ion beam milling techniques for TEM specimen preparation, Micron. 30 (1999) 197–204. doi:https://doi.org/10.1016/S0968-4328(99)00005-0.

[128] R. Jenkins, R.L. Snyder, Introduction to X-ray Powder Diffractometry, Volume 138, Chem. Anal. a Ser. Monogr. Anal. Chem. Its Appl. (1996).

[129] D.S. Sivia, Elementary scattering theory: for X-ray and neutron users, Oxford University Press, 2011.

[130] J.M. Madariaga, Analytical chemistry in the field of cultural heritage, Anal. Methods. 7 (2015) 4848–4876.

[131] G.D. Smith, R.J.H. Clark, Raman microscopy in archaeological science, J. Archaeol. Sci. 31 (2004) 1137–1160.

[132] SOLEIL Synchrotron - how does it work? https://www.synchrotron-soleil.fr/en/about-us/what-

soleil/soleil-3-questions.

[133] J. Avila, I. Razado-Colambo, S. Lorcy, B. Lagarde, J. Giorgetta, F. Polack, et al., ANTARES, a scanning photoemission microscopy beamline at SOLEIL, J. Phys. Conf. Ser. 425 (2013) 192023. doi:10.1088/1742-6596/425/19/192023.

[134] J. Avila, I. Razado-Colambo, S. Lorcy, J. Giorgetta, F. Polack, M.C. Asensio, Interferometer-controlled soft X-ray scanning photoemission microscope at SOLEIL, J. Phys. Conf. Ser. 425 (2013) 132013. doi:10.1088/1742-6596/425/13/132013.

[135] K. Tadeja, C. Monticelli, B-IMPACT Deliverable 2.2 - Protection efficiency report for eco friendly coatings, 2016.

[136] G. Masi, C. Josse, J. Esvan, C. Chiavari, E. Bernardi, C. Martini, et al., Evaluation of the protectiveness of an organosilane coating on patinated Cu-Si-Mn bronze for contemporary art, Corros. Sci., submitted on the 22/12/2017.

[137] E. Tedesco, W. Sperotto, F. Benetti, B-IMPACT Deliverable 3.3 - Assessment of TLW/TWA and STEL, 2017.

[138] I. Odnevall Wallinder, C. Leygraf, A study of copper runoff in an urban atmosphere, Corros. Sci. 39 (1997) 2039–2052.

[139] F. Ospitali, C. Chiavari, C. Martini, E. Bernardi, F. Passarini, L. Robbiola, The characterization of Sn-based corrosion products in ancient bronzes: A Raman approach, J. Raman Spectrosc. 43 (2012) 1596–1603. doi:10.1002/jrs.4037.

[140] V. Hayez, V. Costa, J. Guillaume, A. Hubin, Micro Raman spectroscopy used for the study of corrosion products on copper alloys : study of the chemical composition of artificial patinas used for restoration purposes, Analyst. 130 (2005) 550–556. doi:10.1039/b419080g.

[141] M.C. Bernard, S. Joiret, Understanding corrosion of ancient metals for the conservation of cultural heritage, Electrochim. Acta. 54 (2009) 5199–5205. doi:10.1016/j.electacta.2009.01.036.

[142] P. Colomban, A. Tournié, M. Maucuer, P. Meynard, On-site Raman and XRF analysis of Japanese/Chinese bronze/brass patina – the search for specific Raman signatures, J. Raman Spectrosc. 43 (2012) 799–808. doi:10.1002/jrs.3095.

[143] S.K. Chawla, N. Sankarraman, J.H. Payer, Diagnostic Spectra for XPS analysis of Cu-O-S-H compounds.pdf, J. Electron Spectros. Relat. Phenomena. 61 (1992) 1–18.

[144] V. Hayez, A. Franquet, A. Hubin, H. Terryn, XPS study of the atmospheric corrosion of copper alloys of archaeological interest, Surf. Interface Anal. 36 (2004) 876–879. doi:10.1002/sia.1790.

[145] M.C. Squarcialupi, G.P. Bernardini, V. Faso, A. Atrei, G. Rovida, Characterisation by XPS of the corrosion patina formed on bronze surfaces, J. Cult. Herit. 3 (2002) 199–204. doi:10.1016/S1296-2074(02)01179-2.

[146] M. Chan, A. Capek, D.A. Brill, S.J. Garrett, Characterization of the patina formed on a low tin bronze exposed to aqueous hydrogen sulfide, Surf. Interface Anal. 46 (2014) 433–441. doi:10.1002/sia.5520.

[147] L. Robbiola, T.T.M. Tran, P. Dubot, O. Majerus, K. Rahmouni, Characterisation of anodic layers on Cu-10Sn bronze (RDE) in aerated NaCl solution, Corros. Sci. 50 (2008) 2205–2215. doi:10.1016/j.corsci.2008.06.003.

[148] L. Tommesani, G. Brunoro, A. Frignani, C. Monticelli, M. Dal Colle, On the protective action of

1,2,3-benzotriazole derivative films ageinst copper corrosion, 39 (1997) 1221–1237.

[149] G.A. Bagiyan, I.K. Koroleva, N. V Soroka, A. V Ufimtsev, Oxidation of thiol compounds by molecular oxygen in aqueous solutions, Russ. Chem. Bull. 52 (2003) 1135–1141. doi:10.1023/A:1024761324710.

[150] W. Sui, W. Zhao, X. Zhang, S. Peng, Z. Zeng, Q. Xue, Comparative anti-corrosion properties of alkylthiols SAMs and mercapto functional silica sol-gel coatings on copper surface in sodium chloride solution, J. Sol-Gel Sci. Technol. 80 (2016) 567–578. doi:10.1007/s10971-016-4108-y.

[151] M. Finšgar, 2-Mercaptobenzimidazole as a copper corrosion inhibitor: Part II. Surface analysis using X-ray photoelectron spectroscopy, Corros. Sci. 72 (2013) 90–98. doi:10.1016/j.corsci.2013.03.010.

[152] Z. Mekhalif, L. Massi, F. Guittard, S. Geribaldi, J. Delhalle, X-Ray photoelectron spectroscopy study of polycrystalline zinc modified by n -dodecanethiol and 3-perfluorooctyl-propanethiol, 405 (2002) 186–193.

[153] F. Sinapi, I. Lejeune, J. Delhalle, Z. Mekhalif, Comparative protective abilities of organothiols SAM coatings applied to copper dissolution in aqueous environments, Electrochim. Acta. 52 (2007) 5182–5190. doi:10.1016/j.electacta.2006.12.087.

[154] C. Ni, Z. Zhang, M. Wells, T.P. Beebe, L. Pirolli, L.P.M. De Leo, et al., Effect of film thickness and the presence of surface fluorine on the structure of a thin barrier film deposited from tetrakis-(dimethylamino)-titanium onto a Si(100)-2 × 1 substrate, 515 (2006) 3030–3039. doi:10.1016/j.tsf.2006.08.046.

[155] I. Mabille, A. Bertrand, E.M.M. Sutter, C. Fiaud, Mechanism of dissolution of a Cu-13Sn alloy in low aggressive conditions, Corros. Sci. 45 (2003) 855–866. doi:10.1016/S0010-938X(02)00207-X.

[156] L. Kövér, Z. Kovács, R. Sanjinés, G. Moretti, I. Cserny, G. Margaritondo, et al., Electronic structure of tin oxides: High-resolution study of XPS and Auger spectra, Surf. Interfa. 23 (1995) 461–466. http://onlinelibrary.wiley.com/doi/10.1002/sia.740230705/full (accessed May 30, 2016).

[157] P. Sinsermsukakul, L. Sun, S. Lee, H. Park, S. Kim, C. Yang, et al., Overcoming efficiency limitations of SnS-based solar cells, Adv. Energy Mater. (2014) 1400496. http://faculty.chemistry.harvard.edu/files/gordon/files/prasertadvenergymater2014.pdf (accessed June 1, 2016).

[158] J.A. Rodriguez, T. Jirsak, S. Chaturvedi, J. Hrbek, Surface chemistry of SO2 on Sn and Sn/Pt(111) alloys: Effects of metal- metal bonding on reactivity toward sulfur, J. Am. Chem. Soc. 120 (1998) 11149–11157. doi:10.1021/ja982174a.

[159] M. Hutchison, P. Zhou, K. Ogle, J. Scully, Enhanced Electrochemical Cu Release from Commercial Cu-Sn Alloys: Fate of the Alloying Elements in Artificial Perspiration, Electrochim. Acta. (2017). doi:10.1016/j.electacta.2017.04.092.

[160] G. Masi, L. Robbiola, J. Esvan, C. Chiavari, C. Monticelli, A. Balbo, et al., Corrosion protection of outdoor bronze : historical quaternary alloy and modern alloy with artificial patination, in: EUROCORR 2016, Adv. Link. Sci. to Eng. Eur. Fed. Corros. Event No. 390, Montpellier, Fr. Vol. Proc. (USB Device), Pap. N. 57297, 2016: pp. 1–9.

[161] F. Sinapi, J. Delhalle, Z. Mekhalif, XPS and electrochemical evaluation of two-dimensional organic films obtained by chemical modification of self-assembled monolayers of (3-mercaptopropyl) trimethoxysilane on copper surfaces, Mater. Sci. 22 (2002) 345–353. doi:10.1016/S0928-4931(02)00210-2.

[162] P.M. Dietrich, S. Glamsch, C. Ehlert, A. Lippitz, N. Kulak, W.E.S. Unger, Synchrotron-radiation XPS analysis of ultra-thin silane films : Specifying the organic silicon, Appl. Surf. Sci. 363 (2016) 406–411.

[163] C. Debiemme-Chouvy, F. Ammeloot, E.M.M. Sutter, X-ray photoemission investigation of the corrosion film formed on a polished Cu-13Sn alloy in aerated NaCl solution, Appl. Surf. Sci. 174 (2001) 55–61.

[164] S. Colin, E. Beche, R. Berjoan, H. Jolibois, A. Chambaudet, An XPS and AES study of the free corrosion of Cu-, Ni- and Zn-based alloys in synthetic sweat, Corros. Sci. 41 (1999) 1051–1065. doi:10.1016/S0010-938X(98)00141-3.

[165] F. Zucchi, A. Frignani, V. Grassi, G. Trabanelli, M. DalColle, The formation of a protective layer of 3-mercapto-propyl-trimethoxy-silane on copper, Corros. Sci. 49 (2007) 1570–1583. doi:10.1016/j.corsci.2006.08.019.

[166] N. De Cristofaro, F. Gallese, G. Laguzzi, L. Luvidi, Selection of bronze alloys with reduced lead content suitable for outdoor sculptures production, Mater. Chem. Phys. 132 (2012) 458–465. doi:10.1016/j.matchemphys.2011.11.053.

[167] N. Gartner, T. Kosec, B-IMPACT Deliverable 0.4 - Final progress report, 2017.

[168] 2017, B-IMPACT Facebook page, https://www.facebook.com/b.impact.project/photos/.

List of Tables

List of Figures

List of publications and conference presentations

JOURNAL PAPERS

- **G. Masi**, C. Chiavari, J. Avila, J. Esvan, S. Raffo, M.C. Bignozzi, M.C Asensio, L. Robbiola, C. Martini, *Corrosion investigation of fire-gilded bronze involving high surface resolution spectroscopic imaging,* Applied Surface Science 366 (2016) 317-327, ISSN:0169-4332.

- **G. Masi**, J. Esvan, C. Josse, C. Chiavari, E. Bernardi, C. Martini, M.C. Bignozzi, N. Gartner, T. Kosec, L. Robbiola, *Characterisation of typical patinas simulating bronze corrosion in outdoor conditions*, Materials Chemistry and Physics 200 (2017) 308-321, ISSN: 0254-0584.

- **G. Masi,** A. Balbo, J. Esvan, C. Monticelli, J. Avila, L. Robbiola, E. Bernardi, M.C. Bignozzi, M.C Asensio, C. Martini, C. Chiavari, *X-ray photoelectron spectroscopy as a tool to investigate silane-based coatings for the protection of outdoor bronze: the role of alloying elements*, Applied Surface Science 433 (2018) 468-479, ISSN: 0169-4332.

- **G. Masi**, C. Josse, J. Esvan, C. Chiavari, E. Bernardi, C. Martini, M. C. Bignozzi, C. Monticelli, F. Zanotto, A. Balbo, E. Svara Fabjan, T. Kosec, L. Robbiola, *Evaluation of the protectiveness of an organosilane coating on patinated Cu-Si-Mn bronze for contemporary art*, submitted to Corrosion Science on the 22nd December 2017.

CONFERENCE PROCEEDINGS

- **G. Masi**, L. Robbiola, C. Chiavari, J. Esvan, C. Josse, E. Bernardi, C. Martini, M.C. Bignozzi, *Characterisation of quaternary bronze artificial patinas for outdoor Cultural Heritage applications,* published as abstract in Journal of Applied Biomaterials & Functional Materials, 2016, 14 XIII National Congress AIMAT, Ischia Porto, Italy, 13th - 15th July 2016, **oral presentation**.

- **G. Masi**, L. Robbiola, J. Esvan, C. Chiavari, C. Monticelli, A. Balbo, E. Bernardi, M.C. Bignozzi, C. Martini, *Corrosion protection of outdoor bronze: historical quaternary alloy and modern alloy with artificial patination,* published in the EUROCORR 2016 Proceedings (USB flash driver) (2016) Paper n. 57297, 1-9, International EFC's Conference EUROCORR 2016, Montpellier, Francia, 11th – 15th September 2016, **oral presentation**.

- C. Chiavari, **G. Masi**, A. Balbo, C. Monticelli, J. Avila, J. Esvan, L. Robbiola, E. Bernardi, M.C. Bignozzi, M.C. Asensio, C. Martini, *Outdoor bronze corrosion: nanoscale XPS investigation of silane-based protective coatings*, published in the EUROCORR 2016 Proceedings (USB flash driver) (2016) Paper n. 57367 1-12, International EFC's Conference EUROCORR 2016, Montpellier, Francia, 11th – 15th September 2016, **poster**.

- **G. Masi**, C. Martini, E. Bernardi, M.C. Bignozzi, C. Monticelli, A. Balbo, F. Zanotto, M. Aufray C. Josse, J. Esvan, L. Robbiola, C. Chiavari, *Protectiveness of different silane coatings on patinated ancient and modern bronzes: Part 2,* published in the EUROCORR 2017 Proceedings (USB flash driver) (2017) Paper n. 95722 1-9, International EFC's Conference EUROCORR 2017, Prague, Czech Republic, 3rd - 7th September 2017.

- **G. Masi**, C. Josse, J. Esvan, E. Bernardi, C. Martini, M.C. Bignozzi, L. Škrelp, E. Š. Fabjan, T. Kosec, M. Aufray, L. Robbiola, C. Chiavari, *Micro-characterisation of innovative organic coatings for the protection of outdoor bronze monuments*, published in the EUROCORR 2017 Proceedings (USB flash driver) (2017) Paper n. 95587 1-9, International EFC's Conference EUROCORR 2017, Prague, Czech Republic, 3rd - 7th September 2017, **oral presentation**.

CONFERENCE ABSTRACTS

- C. Chiavari, E. Bernardi, J. Esvan, **G. Masi**, M.C. Bignozzi, J. Avila, M.C. Asensio, C. Martini, *Fire-gilded bronze: investigation of the corrosion mechanism by synchrotron radiation (nanoscale XRF and XPS),* European Materials Research Society (EMRS) Spring meeting 2015, Lille, France, 11th - 15th May 2015 (invited lecture).

- C. Chiavari, E. Bernardi, J. Esvan, **G. Masi**, M.C. Bignozzi, J. Avila, M.C. Asensio, C. Martini, *Bronzi dorati: studio dei meccanismi di corrosione attraverso la radiazione di sincrotrone (nanoscale XPS),* National Conference on Corrosion and Corrosion Protection 2015 (organised by the Italian Metallurgy Society, AIM) - XI Edition, Ferrara, Italy, 15th - 17th June 2015.

- M. Aufray, M. Babnik, A. Balbo , E. Bernardi , M.C. Bignozzi, C. Chiavari, J. Esvan₁ , N. Gartner, M. Girotto, V. Grassi, C. Josse, B. Kamšek, M. Kete, T. Koršič, T. Kosec, L. Marchin, C. Martini, **G. Masi**, C. Monticelli, D. Perez, L. Robbiola, E. Švara, L. Škrlep, W. Sperotto, L. Valente, F. Zanotto, *Development of eco-friendly and non-hazardous outdoor bronze protective coatings – first year achievements of B-IMPACT project,* Workshop "New strategies for the conservation of metallic Cultural Heritage", Paris, France 11th -12th April 2016.

- C. Chiavari, E. Bernardi, L. Robbiola, J. Esvan, **G. Masi**, S. Raffo, M.C. Bignozzi, J. Avila, M.C. Asensio, C. Martini, *Bronzi dorati: studio dei meccanismi di corrosione attraverso la radiazione di sincrotrone (XPS su nanoscala),* XVI National Conference Environmental and Cultural Heritage Chemistry, Lecce, Italy, 26th - 29th June 2016, **poster**.

- C. Chiavari, E. Bernardi, **G. Masi**, M.C. Bignozzi, C. Martini, *Bronzi dorati: studio dei meccanismi di corrosione attraverso la radiazione di sincrotrone (XPS su nanoscala),* 36° National Conference Italian Metallurgy Society (AIM), Parma, Italy, 21st - 23th September 2016.

- M. Aufray, M. Babnik, A. Balbo, E. Bernardi, M.C. Bignozzi, C. Chiavari, J. Esvan, N. Gartner, M. Girotto, V. Grassi, C. Josse, B. Kamsek, M. Kete, T. Korsic, T. Kosec, L. Marchin, C. Martini, **G. Masi**, C. Monticelli, D. Perez, L. Robbiola, L. Skrlep, W. Sperotto, L. Valente, F. Zanotto, *B-IMPACT: a new project for the development of eco-friendly and non-hazardous outdoor bronze protective coatings*, International Conference ICOM-CC Metals 2016, New-Dehli, India, 26th - 30th September 2016, ISBN: 978-92-9012-418-4, **poster**.

- **G. Masi**, C. Martini, E. Bernardi, M.C. Bignozzi, C. Monticelli, A. Balbo, F. Zanotto, M. Aufray, J. Esvan, L. Robbiola, C. Chiavari, *Sviluppo di rivestimenti a base di silani per la protezione del bronzo patinato in condizioni che simulano l'esposizione all'aperto,* National Conference on Corrosion and Corrosion Protection 2017 (organised by the Italian Metallurgy Society, AIM) - XII Edition, Milano, Italy, 28th - 30th June 2017, **oral presentation**.

- C. Monticelli, V. Grassi, C. Martini, C. Chiavari, G. Mavilla, **G. Masi**, E. Bernardi, A. Balbo, *Protettività di diversi tipi di rivestimenti a base di silvani per bronzi patinati,* National Conference on Corrosion and Corrosion Protection 2017 (organised by the Italian Metallurgy Society, AIM) - XII Edition, Milano, Italy, 28th - 30th June 2017, **poster**.

- C. Monticelli, V. Grassi, C. Martini, C. Chiavari, G. Mavilla, F. Zanotto, **G. Masi**, E. Bernardi, A. Balbo, *Protectiveness of different silane coatings on patinated ancient and modern bronzes: Part 1,* International EFC's Conference EUROCORR 2017, Prague, Czech Republic, 3rd - 7th September 2017.

- T. Kosec, E. Švara, L. Škrlep, N. Gartner, E. Bernardi, M.C. Bignozzi, C. Chiavari, C. Martini, **G. Masi**, J. Esvan, L. Robbiola, *Development of eco-friendly and non-hazardous outdoor bronze protective coatings,* International EFC's Conference EUROCORR 2017, Prague, Czech Republic, 3rd - 7th September 2017.

- M. Aufray, M. Babnik, A. Balbo, E. Bernardi, M.C. Bignozzi, C. Chiavari, J. Esvan, N. Gartner, M. Girotto, V. Grassi, C. Josse, B. Kamsek, M. Kete, T. Korsic, T. Kosec, L. Marchin, C. Martini, **G. Masi**, C. Monticelli, D. Perez, L. Robbiola, L. Skrlep, W. Sperotto, L. Valente, F. Zanotto, *B-IMPACT: a new project for the development of eco-friendly and non-hazardous outdoor bronze protective coatings*, XXVI National Conference of the Italian Chemistry Society (SCI), Paestum, Italy, 10th - 14th September 2017.

<div align="right">PROJECT DELIVERABLES</div>

- **G. Masi**, L. Robbiola, B-IMPACT Deliverable D 1.1 - *Characterisation of patinated samples*, finalised the 4th May 2016.

- **G. Masi**, E. Bernardi, C. Chiavari, C. Martini, L. Robbiola, B-IMPACT Deliverable D 4.1 - *Technical report on the assessment of surface treatment protectiveness*, finalised the 30th March 2017.

Curriculum vitae

<div align="right">PERSONAL INFORMATION</div>

Surname e Family name: Giulia Masi
Date and place of birth: 15/09/1988 Bologna, Italy
Nationality: Italian

<div align="right">PERSONAL CONTACTS</div>

E-mail: giu.masi88@gmail.com | giulia.masi5@unibo.it
Web: https://www.unibo.it/sitoweb/giulia.masi5 | https://www.researchgate.net/profile/Giulia_Masi

<div align="right">EDUCATION AND GRANTS</div>

November 2017 - ongoing
University of Bologna
Postdoctoral Research Associate
in the department of Civil, Chemical, Environmental and Materials Engineering (2 years fellowship)
Supervisor: Prof. Maria Chiara Bignozzi
Research project: *"Study of corrosion resistance and development of protective methods for metallic alloys for industrial and cultural heritage application."*

November 2014 - November 2017 (Expected date for Doctoral degree: May 2018)
University of Bologna, Italy
PhD student with Grant
in the department of Civil, Chemical, Environmental and Materials Engineering
XXX cycle, A.Y. 2017-2018
Curriculum: Materials Engineering and Industrial Biotechnologies | Disciplinary Sector: ING-IND/22 Materials Science and Technology
Supervisor: Prof. Maria Chiara Bignozzi | Co-supervisors: Dr. Cristina Chiavari, Dr. Elena Bernardi, Prof. Carla Martini, Dr. Luc Robbiola
PhD thesis: *"Atmospheric corrosion of outdoor bronze: mechanism of decay and conservation strategies"*, within the European Project B-IMPACT (Bronze-IMproved non-hazardous PAtina CoaTings)

January 2017 - April 2017
Université de Toulouse II - Jean Jaurès, Toulouse, France
"Marco Polo" Scholarship (II Session, 2016)
for a visiting period funded by the University of Bologna, as Visiting Student Research Collaborator to the Laboratoire TRACES (UMR 5608)
Supervisor: Dr. Luc Robbiola
February 2016 - May 2016
Université de Toulouse II - Le Mirail, Toulouse, France

Visiting Student research Collaborator
at the Laboratoire TRACES (UMR 5608)
Supervisor: Dr. Luc Robbiola

January 2015
University of Bologna, Italy
Professional Engineering License in Civil and Environmental Engineering
School of Engineering and Architecture (II Session, 2014)

April 2014 - October 2014
University of Bologna, Italy
Attending Graduate Student
to the Department of Civil, Chemical, Environmental and Materials Engineering (DICAM)
Supervisor: Prof. Maria Chiara Bignozzi

September 2007 - March 2014
University of Bologna, Italy
Master Degree in Building Engineering/Architecture
graded: 108/110
School of Engineering and Architecture
Master Degree Thesis (defended the 18th March 2014) in "Chemistry and Technology for Building Materials" entitled *"The influence of short fibres and foaming agents on the physical and thermal behaviour of geopolymer composites for building engineering"*, in collaboration with the Geopolymer Centre Group at the Curtin University (Perth, Western Australia)
Supervisor: Prof. Maria Chiara Bignozzi | Co-supervisors: Dr. Stefania Manzi, Prof. Arie van Riessen, Dr. William Rickard

October 2013 - January 2014
University of Bologna, Italy
Internship, *"Study of geopolymer porosity for applications in Civil Engineering"*
to the Department of Civil, Chemical, Environmental and Materials Engineering
Supervisor: Prof. Maria Chiara Bignozzi

March 2013 - October 2013
Curtin University, Perth, Western Australia
Study grant FOR FINAL Dissertation and RESEARCH ABROAD (II Session, 2012),
funded by the School of Engineering and Architecture of the University of Bologna, Italy
for a Visiting period (7 months) to the Geopolymer Centre Group.
Supervisor: Prof. Arie van Riessen | Co-Supervisor: Dr. William Rickard